


UNIVERSITÁ DEGLI STUDI DI MILANO &
UNIVERSITÁ CATTOLICA DEL SACRO CUORE

SCUOLA DI DOTTORATO IN
FISICA, ASTROFISICA E FISICA APPLICATA

DIPARTIMENTO
MATEMATICA E FISICA

DOTTORATO DI RICERCA IN
FISICA, ASTROFISICA E FISICA APPLICATA
Ciclo XXVII

Probing oxide heterostructure interfaces through angle resolved and resonant electron spectroscopies

Settore scientifico disciplinare FIS/03

Coordinatore: Prof. Marco Bersanelli
Tutore: Prof. Luigi Sangaletti

Tesi di Dottorato di:
Gabriele Salvinelli

Anno Accademico 2013-2014

Dedicated to my wife.

"La scienza conduce a un punto oltre il quale non ci può più guidare;
e l'uomo, giunto a questo punto, è necessitato a cercare un'altra guida,
che non trova se non sostituendo alla conoscenza scientifica la fede religiosa.
Scienza e Religione non sono in contrasto, ma hanno bisogno l'una dell'altra
per completarsi nella mente di un uomo che pensa seriamente." (Max Plank)

"Benedetta sii tu, Materia universale.
Durata senza limiti, Etere senza sponde
- triplice abisso di stelle, di atomi e di generazioni -
tu che superando e dissolvendo le nostre anguste misure
ci riveli le dimensioni di Dio."
(Teilhard de Chardin)

Contents

Introduction

In the recent years, devices have become smaller and faster, more powerful and efficient, as well as cheaper. However, the size of the building blocks of the current electronics - i.e. the transistors - is quickly approaching the limits of manufacture and the need of a new generation of devices based on novel mechanisms appears to be essential [1]. In this scenario, well-defined interfaces between oxide materials have produced novel electronic systems displaying a spectacular variety of properties with promising potentialities for future devices, such as colossal magnetoresistance, high-temperature superconductivity, magnetism at the interface between non magnetic oxides, as well as two-dimensional electron gas (2DEG) between two oxide insulators [2]. Because of their chemical complexity, the quality of oxide materials was believed to be lower with respect to the conventional semiconductors, but the recent advances in growth techniques based on pulsed laser deposition (PLD) or molecular beam epitaxy (MBE) have retracted this viewpoint, opening to the fabrication of oxide interfaces with the same atomic precision as semiconductors [3, 4]. At the same time, however, the rich electronic phases exhibited by heterojunctions involving transition metal oxides, which are dominated by the highly interacting electrons in *d*-orbitals, may be the result of a subtle balance of minute perturbations [3]. Even though the thin film growth technology has been suitably tailored for oxide compounds, a central issue remains the sample quality, where the control of defects may play a key role towards a future step of technology [4].

In this context, interfaces between perovskite oxides can display properties at the nanometer scale that are qualitatively different from their single building blocks, allowing one to engineer novel functionalities through the growth of epitaxial heterostructures. Indeed, the discovery of a 2DEG at the interface

between lanthanum aluminate, $LaAlO_3$, and strontium titanate, $SrTiO_3$, [5, 6] has disclosed unexpected perspectives in the physics of oxide-based junctions. So far, a large number of studies have attempted to determine the physical properties of the 2DEG and to develop novel devices based on the capability to control the interface properties through chemical interactions at the surface, suitable materials combination, or strain engineering [7]. The study of the electronic properties of the $LaAlO_3/SrTiO_3$ heterojunction can thus provide fundamental information to understand the origin of the relevant physical phenomena observed in these systems, while the profiling of energy-level alignment across the interface would disclose the basic information for the design, characterization, and tuning of devices based on the intrinsic electric fields arising at the interface, such as photovoltaics [8, 9] and field-effect transistors [10], as well as devices based on tunable conductivity and charge writing [11, 12].

In non-oxide semiconductors, the relaxation of polar discontinuity in heterointerfaces is usually achieved by an atomic reconstruction process [5], where the interface stoichiometry is altered by interdiffusion, point defect, and dislocation and in general by a structural roughening. In oxides, the possibility of multiple valence ions allows even an electronic reconstruction that, in the $LaAlO_3/SrTiO_3$ case, should move electrons from the surface to the empty Ti *d*-levels. Nevertheless, both atomic and electronic reconstructions could be present in oxide interfaces and the possibility to probe non-destructively the cation depth profiles across the junction would provide further details useful to understand the oxide physics. Indeed, the latter is also valid for less-ordered systems, i.e. amorphous thin films, in which the interfacial electronic properties can be driven by complex substitutional effects across the interface, such as stoichiometry gradients, vacancies and cation interdiffusion. This is the case of many ultrathin interfaces that are playing a key role in the development of new architectures to be tested in photovoltaic (PV) applications. Also in this field, novel devices can be engineered provided that the capability to control interfaces at the nanoscale is demonstrated. Among the most popular solar cells, electrochemical PV cells display a stack of interfaces with different thickness and chemical properties, from the front contact to the back electrode. The front contact constitutes itself an interface where a transparent conducting oxide (TCO) layer is usually matched with a nanosized blocking layer (BL). The quality of this interface may have relevant consequences on the overall cell performances.

The combination of chemical and structural information on a local scale (i.e. at the interface and the nearby few layers) can be obtained by an effective modeling of angle-resolved x-ray photoemission data, which constitutes the common thread of this study through two kinds of samples: the epitaxial $LaAlO_3/SrTiO_3$ interface and the $Cd_xSn_yO_z/TiO_2$ heterojunction for solar cell applications. In this thesis different x-ray photoelectron spectroscopy techniques have been used, such as XPS, AR-XPS, XAS, ResPES, μ-XPS, XPEEM and XASPEEM. The experiments were carried out at the BACH and NANOSPECTROSCOPY beamlines at the ELETTRA synchrotron radiation facility, as well as at the ILAMP laboratories within the Univeristà Cattolica del Sacro Cuore. The experimental data have been modeled by using the BriXias code, which is a package designed within the ILAMP laboratories to properly load, manipulate, analyze and modellize XPS signals on complex multilayer structures. Thus, the present study represents also an opportunity to apply this recent code and verify its potentialities on complex oxide heterointerfaces which can host cation disorder across the nominal junction.

In Chapter 1 the fundamentals of XPS, XAS and RePES experiments are presented, as well as a brief introduction of the PEEM and MEM techniques. In addition, an overview of the BriXias features is introduced, in particular considering the effective approach in modeling the photoemission intensity.

In Chapter 2 the heterojunctions between an amorphous $Cd_xSn_yO_z$ transparent conductive oxide and different thin films of TiO_2 anatase are studied by XPS and angle-resolved XPS. The aim is to probe non-destructively the depth profile for each atomic species across the junction, which exhibits a bulk stoichiometry gradient superimposed to a cation interdiffusion, and then reveal the band offset at the interface in order to relate the results to the overall efficiency of the solar cells in which the aforementioned heterojunctions have been applied.

In Chapter 3 the $LaAlO_3/SrTiO_3$ interface is investigated by XPS, XAS, ResPES, XPEEM, XASPEEM, MEM and μ-XPS techniques. A characterization of the chemical properties of the samples is carried out by XPS, with a special attention on the Ti^{4+}/Ti^{3+} ratio with respect to the interfacial carrier density. Then, the reconstruction of the band diagram at the junction is achieved by combining data from XPS and ResPES experiments, whereas XPEEM, MEM and XASPEEM measurements evidence a lateral chemical homogeneity in the nanometer scale. Furthermore, by using high-flux synchrotron

radiation, a reduction process of the Ti atoms is shown in relation with the exposure time, while a sample regeneration is evidenced via O_2 exposure.

In Chapter 4 the structural composition of the $LaAlO_3/SrTiO_3$ heterointerface is studied by AR-XPS to disclose possible cation interdiffusion, vacancies, sub-stoichiometry processes across the junction. Several models are compared with one another to justify the experimental data and some remarks about the the AR-XPS method are presented concerning the special case under investigation.

Chapter 1

Experimental and theoretical details

1.1 X-ray Photoelectron Spectroscopy

X-ray photoelectron spectroscopy (XPS) is one of the most powerful tool to investigate the composition and the electronic structure of matter, developed by Kai Siegbahn, who received the Nobel Prize in 1981, on the basis of the photoelectric effect first evidenced by Hertz in 1891 and later explained by Einstein in 1905 [13].

An XPS experiment involves exposing the specimen to be studied to an x-ray with energy $h\nu$, and then observing the resultant emission of photoelectrons. From the conservation of total energy, the kinetic energy of the electron photoemitted from a core-level to the vacuum can be described as

$$h\nu = E_B^V + E_k + V_c + V_{bias} \tag{1.1}$$

where $h\nu$ is the photon energy, E_B^V is the binding energy of a given electron relative to the vacuum level of the sample, E_k is the kinetic energy of the emitted electron just as it leaves the sample, V_{bias} is bias potential that may be placed between the sample and the spectrometer, while V_c is the charging potential produced by any net imbalance between charge input and output [14].

For insulating samples, the charging effect can cause an energy level shift from the values corresponding to the limiting situation where non charging occurs. A detailed analysis of the charging effect [15] shows the several difficulties to predict the V_c value in a real experiment, because various sources of electrons may partially compensate the positive charges left by the photoelectron emission process. For metals, (*i*) the positive charging may be spontaneously compensated for by the conduction electrons of the sample-holder from the ground contact; this makes the conductors non-charging, but for insulators the latter charge balance is lower and some other effects can happen. An example (*ii*) is the radiation induced conductivity typical of thin films, which is the generation of electron/hole pairs by the absorption of x-ray. In this situation, the electric field associated with the surface potential drives the electrons towards the surface, where they can partially recombine with the positive charges in excess, and the holes to the metallic sample-holder, where they may recombine with the conduction electrons. In addition, when films are even thinner and the x-ray reaches the substrate, (*iii*) also the photoelectrons from the substrate to the specimen may decrease the charging effect, as similarly happens when the photoelectrons - and secondary electrons - which are emitted from the x-ray tube windows, reach the sample surface. Nevertheless, some practical solutions can be applied to reduce charging effects, for example the increase of temperature of oxide-samples about 200°C, which suppresses charging favoring the charge detrapping process, or the application of a bias V_{bias} to the sample-holder with respect to the analyzer, or even the use of a flood gun which directly irradiates the positive charged surface of the specimen by low energy electrons. In any case, however, a zero surface potential, which cancels the laterally distributed positive charges (especially in small spot XPS), is difficult to be obtained without a precise knowledge of V_c.

Assuming both V_c and V_{bias} equal to zero, the simplest possible case consists of a conductive solid material in electrical connection with the spectrometer. In this way, a fixed potential during photoemission is maintained due to the thermodynamic equilibrium between the specimen and the spectrometer, which requires their Fermi levels (or chemical potentials) to be equal, as displayed in Figure 1.1. Therefore, defining the work function Φ for a solid as the energy separation between the vacuum level and the Fermi level, it follows that the respective vacuum levels for specimen and spectrometer are different,

in such a way that an electron passing from the surface of the specimen into the spectrometer undergoes an accelerating, or retarding, potential equal to $\Phi_s - \Phi_{spect}$, where Φ_s and Φ_{spect} are the work functions for the specimen and the spectrometer, respectively. Thus, eq. (1.1) can be written as

$$h\nu = E_B^F + E_k^{'} + \Phi_{spect} \tag{1.2}$$

with

$$E_B^F = E_B^V - \Phi_s \qquad \text{and} \qquad E_k^{'} = E_k + \Phi_s - \Phi_{spect} \tag{1.3}$$

where E_B^F is the binding energy relative to the Fermi level and $E_k^{'}$ is the kinetic energy inside the spectrometer. If the work function Φ_s is provided by some other technique, vacuum-referenced binding energies can then be obtained [16]. Furthermore, if for metallic samples the Fermi energy can be easily recognized as the cut-off energy at high kinetic energy, for insulating (semiconducting) samples the positioning of the Fermi level is non trivial, because it lies somewhere between the filled valence bands and the empty conduction bands. In such a situation, a metallic reference - e.g. a gold clip - in ohmic contact with the sample is generally used to retrieve the Fermi level, even though possible charging effects may negatively affect this evaluation [16].

In summary, an XPS experiment consists of collecting the number of photoelectrons as a function of their kinetic energy (i.e. a spectrum) by an electron analyzer; in such a way, the energy of the resulting peaks in the spectrum can be related to specific core levels of the atoms or to secondary Auger electrons induced by the core-hole, whereas the step-like background is generated by the inelastic scattering of photoelectrons. When a core level has a symmetry different with respect to the spherical s, a split into two components due to the spin-orbit interaction is detected. In this case, each component is characterized by the quantum number of total angular momentum $j = l \pm s$, where l and s are the orbital angular momentum and the spin angular momentum, respectively. The energy splitting ΔE_j is typical of the atomic species involved and generally increases in relation with both the atomic number Z, for constant values of l and s, and with the decreasing of l to equal principal quantum number n, whereas the area ratio of the two components follows the ratio of the relative electron degeneracies as

$$R = \frac{2j_+ + 1}{2j_- + 1} \qquad \text{with} \quad j_\pm = l \pm s \quad . \tag{1.4}$$

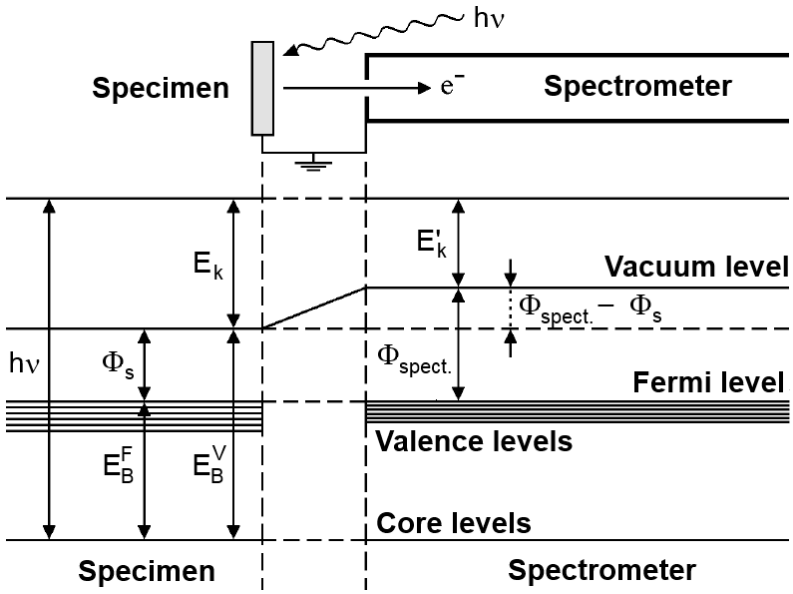

Figure 1.1: *Schematic of the energy levels of a metallic specimen in contact with a spectrometer. Adapted from Ref. [16].*

The XPS technique is generally used to identify both the sample composition and the bond ionicity degree, since the core-level energies are determined manly by the atomic species and even by the specific valence state of the atoms. Furthermore, despite of the penetration of x-ray reach a μm range, the probing depth[1] of the XPS ($\sim 2-3\ nm$) depends only on the scattering processes of electrons inside the matter and is generally approximated by $3\lambda_i$ for a direction of detection normal to the sample surface, where λ_i is the inelastic mean free path (IMFP). For $h\nu = 100 - 1000\ eV$ λ_i can be calculated by the empirical law [17]

$$\lambda_i(E_k) = \frac{A}{E_k^2} + B\sqrt{E_k} \tag{1.5}$$

where $A = 2170$ and $B = 0.365$ are constant values suitable for any kind of

[1]The present values are valid by using soft x-ray. Differently, for hard x-ray ($\sim 10\ keV$) the probing depth can be significantly enhanced up to 20 nm [18].

materials. However, a more accurate expression of λ_i in the photon range from 50 eV to 20 keV is the TTP-2M formula [19]

$$\lambda_i(\mathring{A}) = \frac{E_k}{\left\{E_p^2\left[\beta\ln(\gamma E_k) - \left(\frac{C}{E_k}\right) + \left(\frac{D}{E_k^2}\right)\right]\right\}} \tag{1.6}$$

with

$$E_p = 28.8\left(\frac{N_v\rho}{M}\right)^{\frac{1}{2}} \qquad \beta = -0.10 + \frac{0.944}{\left(E_p^2 + E_g^2\right)^{\frac{1}{2}}} + 0.069\rho^{0.1} \tag{1.7}$$

$$\gamma = \frac{0.191}{\sqrt{\rho}} \qquad C = 1.97 - \frac{0.91N_v\rho}{M} \qquad D = 53.4 - \frac{20.8N_v\rho}{M} \tag{1.8}$$

where N_v the number of valence electrons per atom/molecule, ρ is the density of materials, M is the atomic/molecular mass, E_p is the plasmon energy, while E_g is the band gap. In addition, Figure 1.2 shows the universal dependence of the mean escape depth as a function of the kinetic energy of photoelectrons.

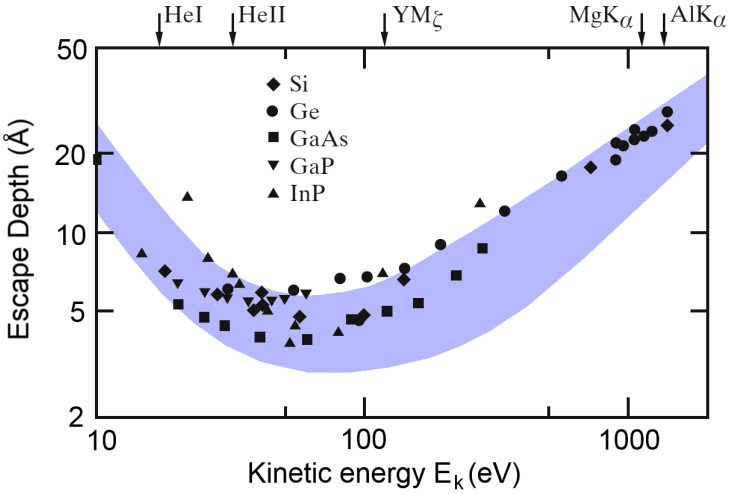

Figure 1.2: *The universal dependence of the escape depth on photoelectron kinetic energy for different solids, drawn as a shaded band that encompasses most of the existing experimental data. Adapted from Ref. [20].*

1.1.1 Three-step model

After Einstein received the Nobel Prize for his quantum theory of photoemission published in 1905, the photoemission process had been considered as a surface phenomenon for the following 50 years. Only in 1958 Spicer [21] developed a model in which the photoemission is treated as a bulk process. A more refined formalization was then published by Berglund and Spicer [22] in 1964. This approach was called *three-step model* because the photoemission process is subdivided into three consecutive and independent events:

- the photoemission from the atom, described by photoemission cross-sections [23, 24];
- the drift of the electron in the solid, based on the electronic IMFP [19];
- and the escape of the photoelectrons from the surface, described by the work-function.

Then, the total photoemission intensity is provided by the product of the three terms, i.e. the probability for the optical transition, the scattering probability for the traveling electrons, and the transmission probability through the surface potential barrier. The first step includes all the information about the electronic structure, the second step can be treated in terms of the IMFP, i.e. the probability that the excited electron reach the surface without scattering, whereas the third step is described by the transmission probability through the surface depending on the kinetic energy of the photoelectron and the material work function. However, a more accurate approach is the *one-step model* in which the photon absorption, the electron removal and the electron detection are described as a single process, thereby allowing for calculations of both the bulk and surface states, as well as evanescent states and surface resonances [25].

From a quantum-mechanics point of view, the photoemission process can be described by the transition probability w_{fi} for an optical excitation between the initial state Ψ_i^N with N electrons and one of the possible final states Ψ_f^N which is formed by the system of $(N-1)$ electrons (i.e. the ground state plus a core hole) and the photoemitted electron with kinetic energy E_k. Such a probability can be approximated by the Fermi's golden rule:

$$w_{fi} = \frac{2\pi}{\hbar}|\langle\Psi_f^N|H_{int}|\Psi_i^N\rangle|^2\delta(E_f^N - E_i^N - h\nu) \tag{1.9}$$

where the δ-Dirac accounts for the energy conservation between the initial $E_i^N = E_i^{N-1} - E_B^{\vec{k}}$ and final $E_f^N = E_f^{N-1} + E_k$ state energy of the N-particle system (where $E_B^{\vec{k}}$ is the binding energy of the photoelectron with kinetic energy E_k and momentum $\vec{k}$), whereas H_{int} is the matrix operator for the electron-photon interaction, which is usually approximated with the dipole operator $H_{int} = e \cdot \vec{r}$. Assuming the usual *sudden approximation*, in which the core-hole final state does not influence the photoelectron (i.e. the electron is instantaneously removed and the effective potential of the system changes discontinuously at that moment), we are allowed to factorize the wave functions for both the initial and final states. Thus, we can write

$$\Psi_f^N = \mathcal{A}\phi_f^{\vec{k}}\Psi_f^{N-1} \tag{1.10}$$

where $\mathcal{A}$ is the antisymmetric operator, which satisfies the Pauli principle, making the N-electron wave function antisymmetric under the exchange of the coordinates of any pair of electrons, $\phi_f^{\vec{k}}$ is the wave function of the photoelectron with momentum $\vec{k}$, while Ψ_f^{N-1} is the final state wave function for the system with $(N-1)$ electrons, which can be considered as an excited state with eigenfunction Ψ_m^{N-1} and energy E_m^{N-1}. In this way, the total transition probability is given by the sum over all possible excited states m. Then, we assume that the initial state is a single Slater determinant (in the Hartree-Fock formalism) defined as

$$\Psi_i^N = \mathcal{A}\phi_i^{\vec{k}}\Psi_i^{N-1} \tag{1.11}$$

where $\phi_i^{\vec{k}}$ is the wave function of a single electron, whereas Ψ_i^{N-1} is the wave function of the N-electrons system subtracted by one electron (but *not* the eigenfunction of the hamiltonian of $(N-1)$ electrons). At this point, we can write the matrix element of eq. (1.9) as

$$\langle \Psi_f^N | H_{int} | \Psi_i^N \rangle = \langle \phi_f^{\vec{k}} | H_{int} | \phi_i^{\vec{k}} \rangle \langle \Psi_m^{N-1} | \Psi_i^{N-1} \rangle \tag{1.12}$$

where $M_{f,i}^{\vec{k}} \equiv \langle \phi_f^{\vec{k}} | H_{int} | \phi_i^{\vec{k}} \rangle$ is the dipole matrix element of the single electron and $\langle \Psi_m^{N-1} | \Psi_i^{N-1} \rangle$ is the overlapping integral for the $(N-1)$ electrons. Then, the total photoemission intensity, i.e. $I = \sum \omega_{f,i}$, measured as a function of E_k is proportional to

$$I(E_{kin}) \propto \sum_{f,i} \left| M_{f,i}^{\vec{k}} \right|^2 \sum_m |c_{m,i}|^2 \delta(E_{kin} + E_m^{N-1} - E_i^N - h\nu) \tag{1.13}$$

where

$$|c_{m,i}|^2 = |\langle \Psi_m^{N-1} | \Psi_i^{N-1} \rangle|^2 \tag{1.14}$$

is defined as the probability to remove one electron from the state i and leave the system of $(N-1)$ electrons in the excited state m. Therefore, if $\Psi_i^{N-1} = \Psi_{m_0}^{N-1}$ for one particular state $m = m_0$, then the corresponding $|c_{m_0,i}|^2 = 1$ and $|c_{m,i}|^2 = 0$ for $m \neq m_0$; in this case, if $M_{f,i}^{\vec{k}} \neq 0$ it follows that the photoemission spectrum is a δ-Dirac at the Hartree-Fock orbital energy $E_B^{\vec{k}} = -\varepsilon_{\vec{k}}$ (i.e. the non-interacting particle case). Otherwise, if many $|c_{m,i}|^2 \neq 0$ as in the strongly correlated systems, the electron removal leads to a remarkable change of the effective potential where Ψ_i^{N-1} overlaps with many of the eigenstates Ψ_m^{N-1}, resulting into a photoemission spectrum which is no more a δ-Dirac but consists of a main line plus several satellites, according to the number of excited states m created in the process [25].

1.2 X-ray Absorption Spectroscopy

X-ray Absorption Spectroscopy (XAS) is a powerful technique to investigate the unoccupied electronic states in organic and inorganic systems, as well as crystalline and disordered solids, by measuring the x-ray total absorption cross-section of the specimen. According to the required experimental information or the specific application field, different notations are generally used, such as XANES (X-ray Absorption Near-Edge Structure) or NEXAFS (Near-Edge X-ray Absorption Fine Structure) - which measure the absorption cross section *near* the absorption edge of a specific elements - EXAFS (Extended X-ray Absorption Fine Structure) or SEXAFS (Surface Extended X-ray Absorption Fine Structure) - in which the absorption cross-section is collected for a wider energy range in order to retrieve information about the bonding lengths of the nearest-neighbor elements - and XMCD (X-ray Magnetic Circular Dichroism) or XLD (X-ray Linear Dichroism) - in which spectra collected with different x-ray polarizations provide local information about magnetism or ionic symmetry distortions.

In particular, the absorption of x-rays near the absorption edge of a specific element leads to the excitation of core electrons into unoccupied or continuum states, leaving behind a core vacancy as depicted in Figure 1.3. The detection

of this process can be probed either by monitoring the attenuation of the x-ray intensity passing through the sample or by measuring the intensity of secondary processes, i.e. Auger emission or x-ray fluorescence. Since the latter is favored for atomic number $Z \geq 35$, the Auger decay is generally used for light elements in two manners; *partial yield*, when only the electrons from a particular Auger decay channel are collected, and *total yield*, when all the emitted electrons from the specimen are detected.

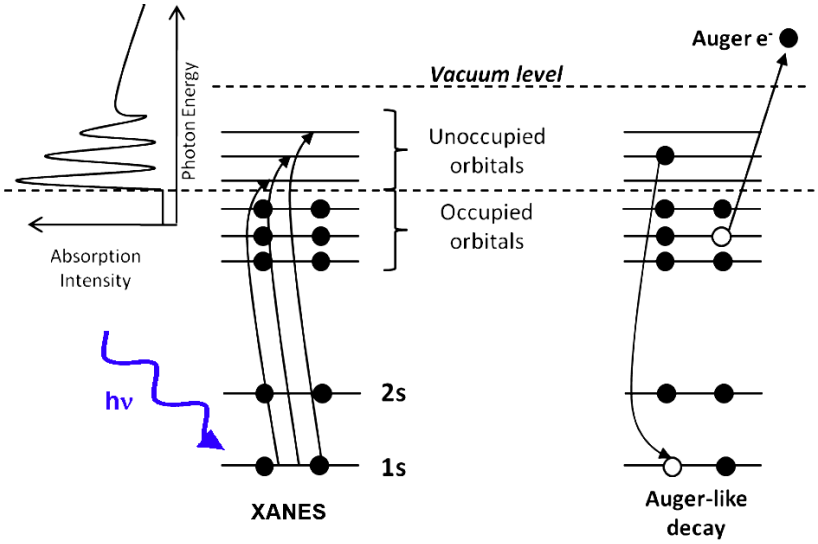

Figure 1.3: *Schematic of the XANES process; (left) the electron excitation due to the x-ray absorption and (right) the Auger decay.*

In first approximation, the x-ray absorption can be described as an electric dipole transition [26]. Using the Fermi's golden rule of eq.(1.9), the transition probability per unit time is given by

$$w_{fi} = \frac{e^2}{\hbar c}\frac{4\omega^3}{3c^2} n |\langle f|\mathbf{r}|i\rangle|^2 \delta(E_f - E_i - \hbar\omega) \tag{1.15}$$

where the first term $e^2/\hbar c$ is the fine structure constant α, the second term is proportional to the third power of the excitation frequency ω, while $|i\rangle$ and $|f\rangle$ are the initial and final state, respectively. Moreover, the transition probability

is proportional to the number of incident photons n, or the photon flux, which is defined as

$$F_n = n\frac{\omega^2}{\pi\hbar c^2} \quad . \tag{1.16}$$

Since the absorption cross section σ is defined as the transition probability normalized by the photon flux

$$\sigma = \frac{w_{fi}}{F_n} = \frac{4\pi\omega e^2}{3c}|\langle f|\mathbf{r}|i\rangle|^2\delta(E_f - E_i - \hbar\omega) \tag{1.17}$$

it follows that the cross section is directly proportional to the oscillator strength f as

$$\sigma = \frac{2\pi^2 e^2}{mc} f \tag{1.18}$$

with

$$f = \frac{2m\omega}{3\hbar}|\langle f|\mathbf{r}|i\rangle|^2\delta(E_f - E_i - \hbar\omega) \tag{1.19}$$

which is a dimensionless quantity. The present discussion follows Ref. [26] and omits the role of degeneracies for the initial and final states.

1.3 Resonant Photoemission Spectroscopy

Resonant photoelectron spectroscopy (ResPES) is a special case of the photoemission process in which the energy of the incident photon is tuned at the absorption edge of a specific element. As a result, a pronounced enhancement of the photoemission intensity relate to the valence band (VB) states occur as a manifestation of the quantum mechanical interference between the direct and indirect photoemission channels. Such element-selective effect is particularly useful to supply information on the local electronic structure for both molecular and crystalline specimens, especially for strongly interacting electron systems of transition metals, lanthanides and actinides, in which huge increases (giant resonances) in the photoemission cross section are revealed at a resonance condition [27].

In particular, below the absorption threshold of a selected element only the direct photoemission from the occupied electronic states contribute to the VB photoemission spectra, whereas the change of the photon energy across the x-ray absorption edge leads the system to an unstable excited state, in

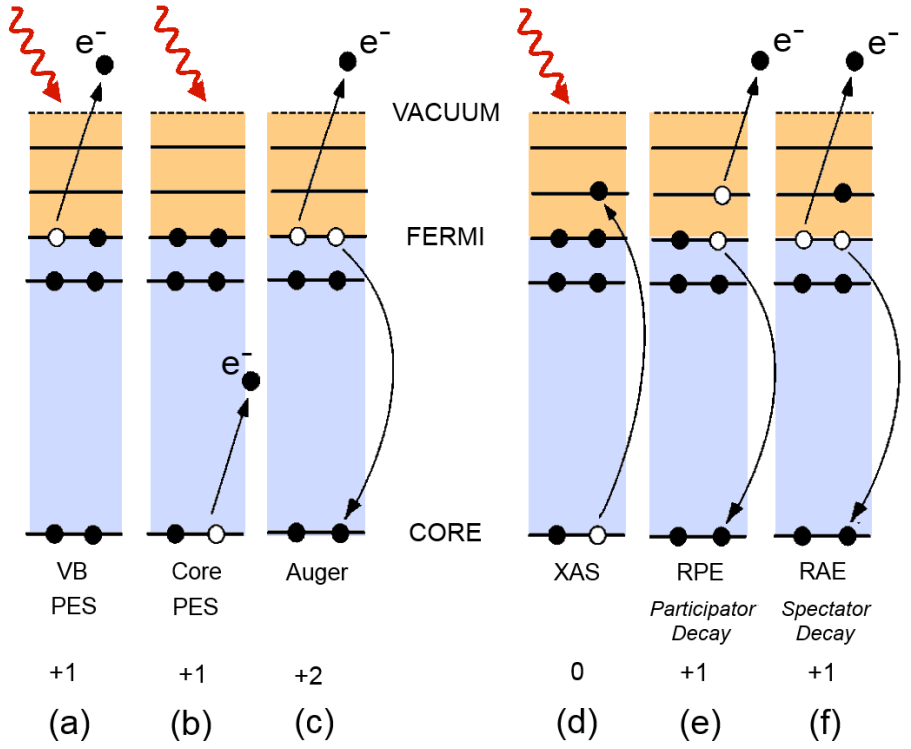

Figure 1.4: *Schematic of the electronic excitation/de-excitation processes in a ResPES experiment. Adapted from Ref. [28].*

which core electrons are promoted to different empty orbitals whence they may decay either by radiative or non-radiative processes. Figure 1.4 shows the main excitation and de-excitation channels related to the ResPES process. Panel (a) and (b) display the direct VB photoemission (VB-PES), as well as the core-level photoemission (Core-PES), where the core-hole may be filled by an outer shell electron, triggering a normal Auger decay, Figure 1.4 (c). In this case, the emitted electron exhibits a fixed kinetic energy which is independent of the photon energy.

When the photon is tuned at the absorption edge, the x-ray absorption induces the excitation of a core-electron into an empty state (XAS), Figure 1.4 (d),

from which the system proceeds involving a decay process of one VB electron, which removes the core-hole left behind and induces two different autoionization channels: in the *participator decay*, Figure 1.4 (e), the excited electron is emitted, leaving the system with a single valence vacancy. This final state is energetically equivalent of that of direct VB-PES and is generally referred to as *resonant photoemission* (RPE). Differently, in the *spectator decay*, Figure 1.4 (f), the excited electron remains in the normally unoccupied level while a valence electron is emitted, as in an Auger-like transition. For this reason, this channel is often called *resonant Auger* (RAE). The resulting final states of the normal Auger and the spectator autoionization process are similar apart from the localization of the promoted electron in an usually unoccupied orbital; thus, their spectral weights are similar in shape, but with an energy shift due to the different screening effects induced by the extra electron in the conduction band [28].

In summary, when the photon energy is at the absorption edge, the direct VB-PES and the RPE channels can interfere, increasing the total photoemission intensity. On the other hand, when the photon energy is increased above the absorption threshold, the autoionization process ultimately turns into the normal Auger emission and the interference effects are lost. In addition, the RAE emission is an $N-1$ electron final state that occurs at a photon energy close to a resonance, while the normal Auger emission is an $N-2$ electron final state found at constant kinetic energy. Therefore, if all spectra are aligned on the BE scale, the constant BE resonating features are those ascribed to RAE, while those apparently dispersing on the BE scale are the normal Auger [29].

1.3.1 Fundamental aspect of ResPES

In general, the ResPES intensity is given by the following expression [30]

$$w_{fi} = 2\pi \sum_{f} \left| \langle f|V_r|i\rangle + \sum_{m} \frac{\langle f|V_A|m\rangle\langle m|V_r|i\rangle}{E_i - E_m - \frac{i\Gamma_m}{2}} \right|^2 \delta(E_f - E_i) \tag{1.20}$$

where the left part of the matrix element represents the direct VB-PES, whereas the right part is the summation over the possible m intermediate core-excited states within the excitation/de-excitation channels. The initial-state $|i\rangle$ and

final-state $|f\rangle$ wave functions contain the incident photon and the emitted electron, respectively. V_r and V_A denote the radiative (dipole) and Coulomb (Auger) operators, respectively. Then, Γ_m is the core-level lifetime-induced width of state m, while the δ function ensures the energy conservation [28].

The simplest description of the resonant photoemission effect is provided by the Fano theory [31]. Considering non-degenerate states, the Hamiltonian is diagonalized into a subspace which consists of one discrete core-excited state ϕ with energy E_ϕ and one continuum $\psi(E)$ with states of energy E, such that

$$\langle\phi|\phi\rangle = 1 \quad , \quad \langle\psi(E)|\psi(E')\rangle = \delta(E-E') \quad , \quad \langle\psi(E)|\phi\rangle = 0 \quad . \tag{1.21}$$

In addition, the non-diagonal matrix elements $V(E)$ are between the discrete state and the continuum

$$\langle\psi(E)|\mathcal{H}|\phi\rangle = V(E) \tag{1.22}$$

$$\langle\psi(E)|\mathcal{H}|\psi(E')\rangle = E\ \delta(E-E') \tag{1.23}$$

$$\langle\phi|\mathcal{H}|\phi\rangle = E_\phi \tag{1.24}$$

so that the discrete energy level E_ϕ lies within the continuous range of values E. In the resonant photoemission process, ϕ is the core-excited intermediate state and $V(E)$ is the Auger matrix element for the decay step. The exact eigenfunctions of the continuum state $\Psi(E)$ can be expressed as

$$|\Psi(E)\rangle = a_E|\phi\rangle + \int dE'\ b_E(E')|\psi(E)'\rangle \tag{1.25}$$

where a_E and b_E can be obtained, by using the expressions (1.21)-(1.24), as

$$|a_E|^2 = \frac{|V(E)|^2}{\left[E-E_\phi-F(E)\right]^2+\pi^2|V(E)|^4} \tag{1.26}$$

$$b_E(E') = \left[\frac{1}{E-E'}+z(E)\delta(E-E')\right]V(E')a_E \tag{1.27}$$

with

$$F(E) = P \int dE' \, \frac{|V(E')|^2}{E - E'} \tag{1.28}$$

$$z(E) = \frac{E - E_\phi - F(E)}{|V(E)|^2} \quad . \tag{1.29}$$

The transition matrix element $\mathcal{T}$ to excite the state $\Psi(E)$ from the ground state Φ_g can then be expressed as

$$\langle \Psi(E)|\mathcal{T}|\Phi_g\rangle = a_E \langle \phi|\mathcal{T}|\Phi_g\rangle + \int dE' \, b_E(E') \langle \psi(E')|\mathcal{T}|\Phi_g\rangle \quad . \tag{1.30}$$

The ratio f between the transition probability $|\langle \Psi(E)|\mathcal{T}|\Phi_g\rangle|^2$ and the probability of the transition to the unperturbed continuum $|\langle \psi(E)|\mathcal{T}|\Phi_g\rangle|^2$ gives the Fano cross-section

$$f(\epsilon) = \frac{(q+\epsilon)^2}{1+\epsilon^2} \tag{1.31}$$

where the asymmetry parameter q is defined as

$$q = \frac{\langle \Phi|\mathcal{T}|\Phi_g\rangle}{\pi V(E) \langle \Psi(E)|\mathcal{T}|\Phi_g\rangle} \quad , \tag{1.32}$$

with the discrete state ϕ modified by an admixture of continuum states as

$$|\Phi\rangle = |\phi\rangle + P \int dE' \, \frac{V(E')}{E - E'} |\Psi(E')\rangle \tag{1.33}$$

Then, ϵ is defined as the reduced energy variable, given by

$$\epsilon = \frac{E - E_\phi - F(E)}{\pi |V(E)|^2} \quad , \tag{1.34}$$

which accounts for a shift of the discrete state ϕ at the resonance energy E_ϕ by the self-energy $F(E)$ - defined in eq. (1.28) - while the lifetime width of the discrete state ϕ is given by $\Gamma_m = \pi |V(E)|^2$ [27]. At this point, using the Fano formalism [26], the expression (1.20) can be simplified into

$$w = \sum_m |\langle f|V_r|i\rangle|^2 \, \frac{(q+\epsilon)^2}{1+\epsilon^2} \, \frac{E_m/\pi}{(E_f + E_i - E_m)^2 + \Gamma_m} \tag{1.35}$$

where the ResPES intensity is the direct VB-PES multiplied by the Fano cross-section $f(\epsilon) = (q+\epsilon)^2/(1+\epsilon^2)$. As shown in Figure 1.5 (a), the shape of the Fano profile $f(\epsilon)$ is determined by the asymmetry parameter q. The square of this parameter is proportional to the ratio between the strengths of the core level assisted (autoionization, RPE) process and the strength of the direct photoemission continuum over the core-hole width (VB-PES). The photoemission intensity decreases below the threshold and increases above due to the interference between the two channels [27]. With $q \gg 1$ a Lorentzian-like enhancement occurs, whereas with q values close to 1 implies more asymmetric Fano-profile with a minimum at $\epsilon = -1$ [32]. For $q = 0$ an antiresonance effect occurs, while for $q > 2$ high resonance effects can be seen; for instance, in the case of transition metals (TM) and rare heart (RE) the q factor can be rather high ($q > 3$) leading to pronounced resonant effects called *giant resonances*. Figure 1.5 (b) shows the experimental data of the valence band of nickel metal in comparison with the calculated a Fano profile for Fano lineshape $\Gamma_m = 0.35\ eV$ and $q = 2$ [27]

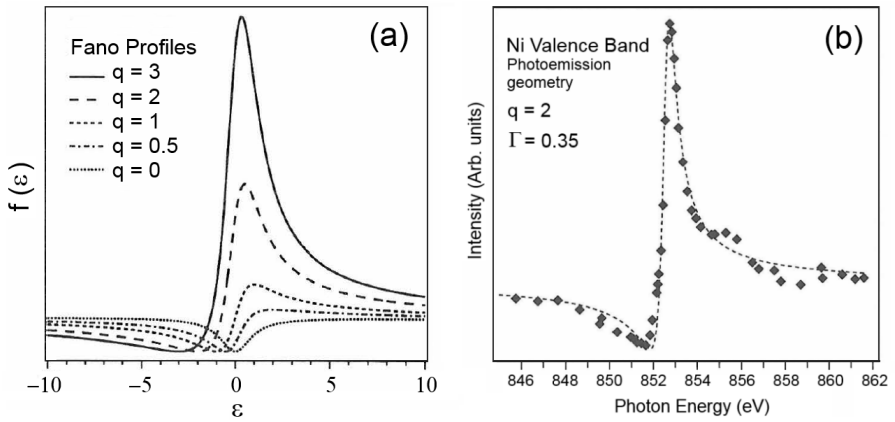

Figure 1.5: *(a) Characteristic Fano profiles for different q values. (b) A Fano-like profile in the Ni valence band; markers are the experimental data, dashed line is the calculated for* $q = 2$ *and* $\Gamma = 0.35$. *Adapted from Ref. [27].*

1.3.2 The case of Ti $L_{2,3}$ and La $M_{4,5}$ edge

Resonant photoemission spectroscopy experiments carried out by scanning the photon energy at the Ti $L_{2,3}$ edge provide the opportunity to emphasize titanium-related electronic states in the valence-band region up to the Fermi level (E_F) that would be otherwise missed by an off-resonance tuning of the photon energy. In this condition, for a $3d$ transition metal, the direct VB-PES channel

$$np^6 3d^n + h\nu \rightarrow np^6 3d^{n-1} + e^- \tag{1.36}$$

can interfere with the autoionization channel triggered by the creation of a core hole

$$np^6 3d^n + h\nu \rightarrow np^5 3d^{n+1} \rightarrow np^6 3d^{n-1} + e^- \quad . \tag{1.37}$$

These two processes with the same final states, i.e. the first-order direct VB-PES and the second-order RPE autoionization process, interfere with each other, resulting in asymmetry of the ResPES intensity as a function of the incident energy, the aforementioned *Fano shape* [26, 27]. The interference between these two channels gives rise to a resonant enhancement of the photoemission cross section of element-specific VB states at constant binding energy.

In a configuration interaction (CI) approach [33], the ground state (gs) of a Ti ion is described as

$$\Psi_{gs} = \alpha_0 |3d^n\rangle + \alpha_1 |3d^{n+1}\underline{L}^1\rangle + \alpha_2 |3d^{n+2}\underline{L}^2\rangle \tag{1.38}$$

(where $n = 0$ and $n = 1$ for Ti^{4+} and Ti^{3+} ions, respectively), while the final state of the x-ray absorption spectroscopy (XAS) process, i.e. the intermediate state (is) of the autoionization channel, is

$$\Psi_{is} = \beta_0 |\underline{2p}3d^{n+1}\rangle + \beta_1 |\underline{2p}3d^{n+2}\underline{L}^1\rangle + \beta_2 |\underline{2p}3d^{n+3}\underline{L}^2\rangle \tag{1.39}$$

and finally the photoemission channel (finale state, fs) is

$$\Psi_{fs} = \gamma_0 |3d^{n-1}\rangle + \gamma_1 |3d^n\underline{L}^1\rangle + \gamma_2 |3d^{n+1}\underline{L}^2\rangle \tag{1.40}$$

which can be reached either directly from the ground state or through autoionization from the intermediate state. The $|3d^{n-1}\underline{L}^1\rangle$ configuration is absent in the case of the Ti^{4+} ion. Here $\underline{L}$ and $\underline{2p}$ stand for an O $2p$ and a Ti $2p$ hole, respectively. The $|3d^n\underline{L}^m\rangle$-like configurations are those accounting for charge

transfer (CT) effects from the anion $2p$ to the transition metal (TM) $3d$ orbitals, providing a straightforward tool to consider the effect of Ti $3d$-O $2p$ bonding in CI calculations. The possibility to observe ResPES effects in the formally empty $3d$ shell of the Ti^{4+} cation is due to the presence of CT-like configurations, both in the initial and final states, whereas ResPES effects can also involve the ionic $|3d^1\rangle$ configuration in a Ti^{3+} cation.

The CIS (constant initial state) profile is collected by measuring the intensity profile of a selected photoemission peak (i.e., with constant binding energy) as the photon energy is scanned through the absorption threshold. As described in the previous paragraph for the case of a discrete level interfering with a continuum of states, the CIS line shape can be fit to the Fano profile $f(\epsilon)$ of eq. (1.31), where in this case the asymmetry strength parameter q can be written as

$$q = \frac{\langle \Psi_{3d}|\mathbf{r}|\Psi_{2p}\rangle}{\pi V_{CK}\langle \Psi_{E_k}|\mathbf{r}|\Psi_{3d}\rangle} \tag{1.41}$$

with Ψ_{3d} representing the $3d$ TM states in the valence band, and $\epsilon = (h\nu - h\nu_0)/\Gamma$ is the reduced energy parameter and $\Gamma = 2\pi V_{CK}^2$, V_{CK} being the matrix element of the Coster-Kronig transition occurring in the autoionization process. Usually, when the CIS is measured at the TM $2p$-$3d$ absorption threshold, the $\langle \Psi_{3d}|\mathbf{r}|\Psi_{2p}\rangle$ matrix element is quite large and the resulting CIS profile is very close to the absorption profile [34, 35].

The case of La is quite similar to that of Ti, and it can also be formally treated within a CI calculation scheme which includes CT configurations. CT effects are well known in core-level spectroscopy of ionic La compounds [36, 37], and are likewise expected in the final state of the valence-band photoemission. In the La case, the ground state (gs) of a La^{3+} ion can be treated as

$$\Psi_{gs} = \alpha_0|4f^0\rangle + \alpha_1|4f^1\underline{L}^1\rangle + \alpha_2|4f^2\underline{L}^2\rangle \tag{1.42}$$

while the final state of the XAS process, i.e. the intermediate state of the autoionization channel (is) is

$$\Psi_{is} = \beta_0|\underline{3d}4f^1\rangle + \beta_1|\underline{3d}4f^2\underline{L}^1\rangle + \beta_2|\underline{3d}4f^3\underline{L}^2\rangle \tag{1.43}$$

and finally the photoemission channel (finale state, fs) is

$$\Psi_{fs} = \gamma_0|4f^0\underline{L}^1\rangle + \gamma_1|4f^1\underline{L}^2\rangle \ . \tag{1.44}$$

1.4 X-ray Photoemission Electron Microscopy

Similarly to XPS, in photoemission electron microscopy (PEEM) information are carried out by the electrons photoemitted from the surface of solid materials, which are collected to generate an image which laterally resolves the photoemission signal. When x-rays are used as the exciting radiation, this technique is also called XPEEM and requires energy filtering of the emitted electrons; thereby photons with constant energy are used while the photoelectrons are energy filtered. The advantage of XPEEM is that the full spectral information guarantees a detailed chemical characterization of the imaged surface [38]. In addition, when high-brilliance third generation synchrotron radiation sources are used, lateral resolutions down to 20 nm at an energy resolution of a few tenths of an eV can be obtained, even though a further reduced lateral resolution of 2 nm with 0.1 eV can be reached as long as aberration-corrected instruments are implemented [39]. Moreover, with tunable photon energy, the experimental setup can work even in a XAS mode and is generally referred to as XAS-PEEM [38]. In some cases, the XPEEM setup is combined with low-energy electron microscopy (LEEM), which is used to monitor the surface structure and its dynamical evolution with higher spatial resolution, thereby forming a multimethod electron microscope called SPELEEM (spectroscopic photoemission and low-energy electron microscope), as the one operating at the NANOSPECTROSCOPY beamline at ELETTRA [40]. In this case, as shown in Figure 1.6, the sample can be probed by either x-ray photons or low-energy electrons provided by a LaB_6 source, sharing the same complex set of magnetic lenses and the electron analyzer used to generate the final magnified image. In a simplified description, the low-energy electron beam leaving the sample (photoemitted or scattered) is strongly accelerated by the electric field applied between the sample and the objective lens (~ 18 keV), producing a magnified image of the sample in the image plane at the beam separator before going through the transfer optics and then reaching the analyzer.

1.5 Mirror Electron Microscopy

Mirror electron microscopy (MEM) in ultra high vacuum (UHV) is a technique used to investigate the surface of specimens, such as the topography, the

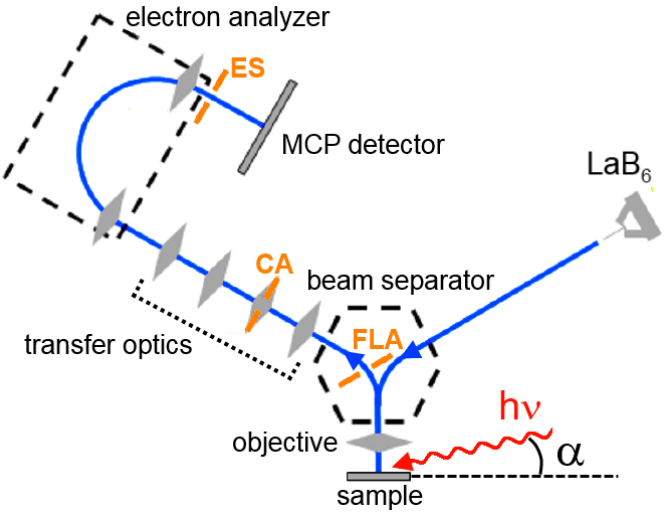

Figure 1.6: *Schematic of a SPELEEM setup. The electron path is traced in solid blue line, the field limiting aperture (FLA), contrast aperture (CA) and energy slit (ES) are marked in orange. Adapted from Ref. [40].*

electrical field variation due to work function differences, potential differences in electronic components (p-n junction, electronic circuits, etc) or magnetic stray fields [41]. Figure 1.7 depicts the working principle in the simplest configuration setup: accelerated electrons entering the retarding uniform field (E_0), which is slightly more negative than the accelerating voltage, are reflected on an equipotential surface in front of the sample (Sa), defined by the retarding potential V_0. Thus, the slow electrons near the sample (few eV of kinetic energy) are sensitive to the field disturbances due to geometrical, electrical or magnetic irregularities, providing information on the surface topography and the field distribution simultaneously. In this way, however, the image interpretation could result rather complicated if charging effects occur [42].

Furthermore, MEM exhibited a theoretical good resolution already at the beginning of the application of this technique in the '90s [41]. On the basis of geometrical-optical calculations for a monochromatic plane wave incident on a sinusoidal surface potential, a lateral resolution of $\delta = 2\ nm$ can be calculated

[41,43], even though the finite energy width and the divergence of every electron beam could cause a deterioration of the resolution up to 15 nm [41].

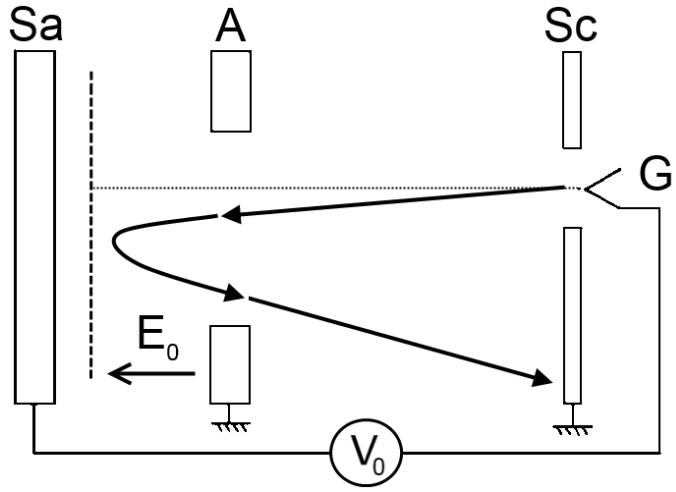

Figure 1.7: *Schematic of the MEM experiment: the electron beam coming from the gun (G) is reflected on an equipotential surface (dashed line), defined by the retarding potential (V_0) in front of the sample (Sa). Adapted from Ref. [42].*

1.6 Modeling for XPS: the BriXias code

The interface modeling based on the XPS peak angular dependence was carried out with the BriXias code [44]. This package is based on the IGOR Pro 6.3 programming language and has been developed mainly by G. Drera at the *Surface Science and Spectroscopy Laboratory*, I-LAMP Research Center, Università Cattolica del Sacro Cuore. It includes a computational engine, based on standard databases and state-of-the-art Monte Carlo (MC) code, designed to predict XPS spectra on complex multilayer structure, carefully considering the experimental geometry and the features of the X-ray source (energy and polarization). Moreover, the package allows an accurate element quantification at any geometry and photon energy, and is thus suitable to standard XPS laboratory, as well as complex synchrotron facilities. Since the practical accuracy

for relative element quantification is generally considered about $7 - 10\%$ [45], a careful XPS analysis must rely either on the comparison with reference samples - with proven composition and surface preparation by other techniques - or on specific sensitivity factors deduced by previous experiments carried out with the same instrumentation and similar data treatment. For this purpose, a fine calibration tool for the analyzer response is also included in the code (see Ref. [44] for a detailed description of the transmission function calibration method). At the same time, the BriXias package includes several tools for data manipulation, such as background removal (e.g., Shirley, iterated-Shirley [46], and Tougaard [47]), satellites line deconvolution and multiple curve peak fitting.

1.6.1 Effective XPS core-level intensity modeling

A variety of physical processes are known to play an important role in the XPS signal generation, such as elastic and inelastic scattering in the interior of the solid, surface excitations, and intrinsic excitations following the ionization that precedes the signal electron emission in XPS. Generally, such processes can occur repeatedly (multiple scattering) before the electron is ejected from the surface, giving rise to a complex combination of effects responsible for some important features observed in experimental spectra [48]. In XPS, the core-level peak intensity $I(E_k, \theta)$ of a selected layer at a depth d with a thickness t can be evaluated through the following formula:

$$I(E_k, \theta) = K \cdot \int_d^{d+t} \phi(E_k, \theta, z) dz \tag{1.45}$$

where $\phi(E_k, \theta, z)$ is the generic escape probability (known as the depth distribution function, DDF) of an electron generated at a depth z with a kinetic energy E_k at an angle θ with respect to the surface normal. K is a normalization constant, which includes the analyzer-dependent parameters, defined as

$$K = \frac{\sigma \rho}{4\pi} \left[1 - \frac{\beta}{4} \left(3\cos^2(\alpha) - 1 \right) \right] \tag{1.46}$$

where σ is the photoionization cross section [23, 24], ρ is the atomic density, β is the core-level asymmetry parameter and α is the angle between the direction of incidence of the photons and emission of the photoelectrons (see Figure 4.2 (a) for a schematic of all angles).

According to the Lambert-Beer law, the DDF function is usually approximated by a Poisson distribution [48] $\phi = \exp\left[-z/(\lambda_i \cdot \cos\theta)\right]$ where λ_i is the inelastic mean free path (IMFP) of the photoelectrons [19]. Such an approximation leads to a simple analytical expression for the peak areas, which is defined as straight line motion by Tilinin *et al.* [49]. However, this formulation may result in an overestimation of the top layer thickness, especially for thin overlayers. Indeed, different studies indicate that some electrons can change their direction of motion due to elastic scattering processes, thereby modify both the angular prediction, based on only inelastic collisions, and the depth distribution function, even for samples consisting of low atomic number elements [48,49]. As a result, the Monte Carlo technique has been widely used to achieve accurate evaluations in the effective study of transport processes [48, 50, 51].

On the basis of the algorithm described by Werner in Ref. [48], the BriXias package exploits MC DDF calculations which include both inelastic and elastic electronic scattering processes in the so-called transport approximation (TA) [52]. Although an accurate analytic DDF formulation can be written for homogeneous samples [53], the same is not possible for a generic multilayer sample [49]. Therefore, MC calculations of electron trajectories are needed for an effective treatment of the XPS peak θ-angular dependence, i.e. for angle-resolved XPS experiments in ultra-thin interfaces, as well as complex multilayered structures. For example, the first-published application of the BriXias code was carried out on an heterojunction formed by a networked layer of single-wall carbon nanotubes (SWCNT) and a Si (100) crystal [54], applied in hybrid photovoltaic (PV) cells. In this case, by an AR-XPS study a direct probe of the chemically inhomogeneous Si-O layer at the SWCNT/Si interface was evidenced, providing a non-destructive depth-profiling of a SWCNT/SiO_x/SiO_2/Si complex interface.

In this thesis, other applications on AR-XPS investigations of complex heterojunctions have been considered, such as the TiO_2/$Cd_xSn_yO_z$ interface, in which a Cd/Sn stoichiometry gradient has been evidenced along with a Ti-Sn cation exchange across the junction (see chapter 2), and the $LaAlO_3$/$SrTiO_3$ interface, where La-Al stoichiometry variations, multiple cation substitutions, cation-complexes vacancies and, in general, cation disorder at the junction may occur (see chapter 4).

Chapter 2

$Cd_xSn_yO_z/TiO_2$ heterojunctions for solar cell applications

The development of novel photovoltaic (PV) devices is based on ultrathin layers and buried interfaces which are engineered to optimize the PV efficiency [55, 56]. Among the most popular solar cells, electrochemical PV cells display a stack of interfaces with different thickness and chemical properties, from the front contact to the counter electrode [57]. The front contact constitutes itself an interface where a transparent conducting oxide (TCO) layer is usually matched with a nanosized blocking layer (BL). The quality of this interface may have relevant consequences on the overall cell performances [58–61] but the stoichiometry variations due to cation interdiffusion processes, which can be hosted at the junction, have been so far virtually neglected by a combined analysis of chemical and electronic properties.

In this chapter, on the basis of angle-resolved photoemission spectroscopies, cation interdiffusion and stoichiometry gradients have been identified at the interface between a nanosized TiO_2 (TO) blocking layer (BL) and a transparent conductive Cd-Sn amorphous oxide layer, which constitute the front contact of dye-sensitized solar cells (DSSC) recently developed by RF sputtering growth

of ultra-thin oxide layers [61,62]. In particular, as the TiO_2 thickness is known to affect the overall efficiency of the solar cell [61, 63–66], different BL thicknesses have been considered, with the aim to relate the physical properties of the interface with the cell performances. This heterojunction constitutes then a suitable opportunity to study complex stoichiometry profiles across the interface exploiting an effective analysis of the photoemission signal without having to model the photodiffraction effects distinctive for crystalline materials. In addition, on the basis of the band offset method developed by Kraut *et al.* [67, 68] and the non-destructive depth profiling obtained from the aforementioned analysis, the band diagrams across the junctions have been reconstructed and the results are discussed and related to the measured overall cell efficiencies in terms of charge injection and recombination. This chapter is based on the results recently published in Ref. [69].

The XPS data were collected with the Mg K_α-line ($h\nu = 1253.6\ eV$) of a dual-anode PsP X-ray source, running at a power of about 110 W. Photoelectrons were collected using a SCIENTA R3000 analyzer, operating in an ultra-high vacuum chamber with a base pressure of $2 \cdot 10^{-10}\ mbar$. The analyzer was properly calibrated according to the procedure described in Ref. [44].

2.1 Dye-sensitized solar cells and recombination processes

The seminal paper of Grätzel and O'Regan in 1991 [70] disclosed the opportunity to use molecular components in solar energy applications. Dye-sensitized solar cells have then become one of the most fascinating alternative with respect to the conventional thin-film silicon based cells, attracting a growing research activity during the past two decades. Besides the exciting features related to DSSCs - i.e. flexibility [71, 72], color and transparency - however, the operation principle of such solar cells has remained not entirely clear for years due to the complexity of the interactions between the internal components, especially at the oxide/dye/electrolyte interface. Different physical processes are still matter of debate, in particular the charge transport mechanisms [73, 74].

A schematic representation of the DSSC functioning is displayed in Figure 2.1. As a consequence of the photon absorption, the excited dye injects the elec-

tron in the conduction band of the mesoporous oxide material, then the electron is collected by the transparent conductive oxide (TCO) and transferred to the external load. Subsequently, the electron-deficient dye is regenerated by the mediator, an electrolyte usually in the form of an iodide/triiodide redox couple. When an electron is transferred to the dye, the oxidized mediator diffuses through the cell towards the counter electrode where it is regenerated.

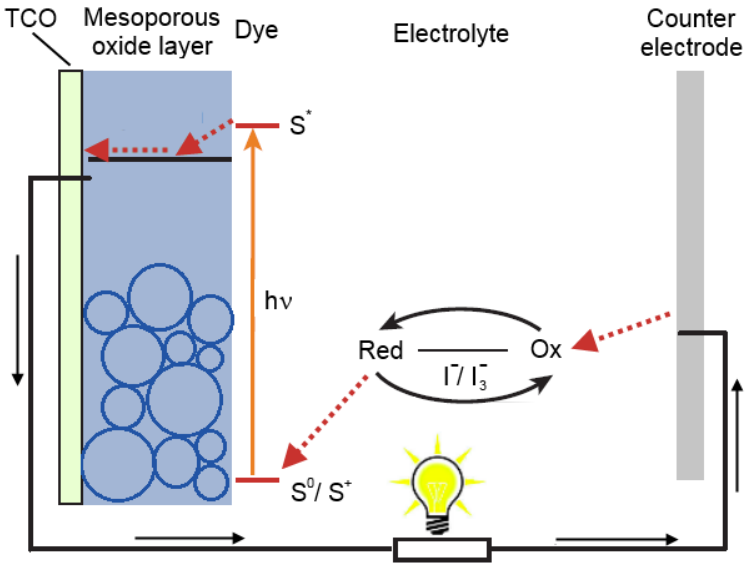

Figure 2.1: *Simplified representation of the DSSC operation principle. Adapted from Ref [73].*

In this scenario, the heart of the DSSC consists of the mesoscopic semiconductor oxide film. The most popular choice for this layer is generally TiO_2 in anatase phase, although alternative wide band-gap oxides can be used, such as ZnO [75], SnO_2 [76] or Nb_2O_5 [77, 78]. Typically the optimized structure is 10 μm thick with a porosity of 50-60% and is made of nanocrystalline particles with a grain size in the range of 10-80 nm to form high surface area transparent film which allows for dye chemisorption over a thousand times more than

that of a flat unstructured electrode of the same size [73, 74, 79]. In this way, the photoelectrode can be interpreted as a network of nanocrystals through which the electrons can percolate by hopping from one crystallite to the next one. However, this charge transfer mechanism is hampered by electronic trapping and detrapping effects which stem from the surface states of nanomaterials due to the presence of impurities, unsaturated bonds, deviation in the bond lengths or angle, whose origin and behavior are not clearly yet understood [80]. Even the morphology of the nanomaterials used in this layer is the focus of a fine research field to achieve better charge separation and transport [81], from nanoparticles [73, 82] to nanowires [75, 83] and nanotubes [72, 84]. Nevertheless the nanocrystalline structure has so far exhibited the absolute best performance in terms of overall efficiency in DSSCs up to 12.3% [85] and is predicted to exceed the limit of 15% in the next years [86].

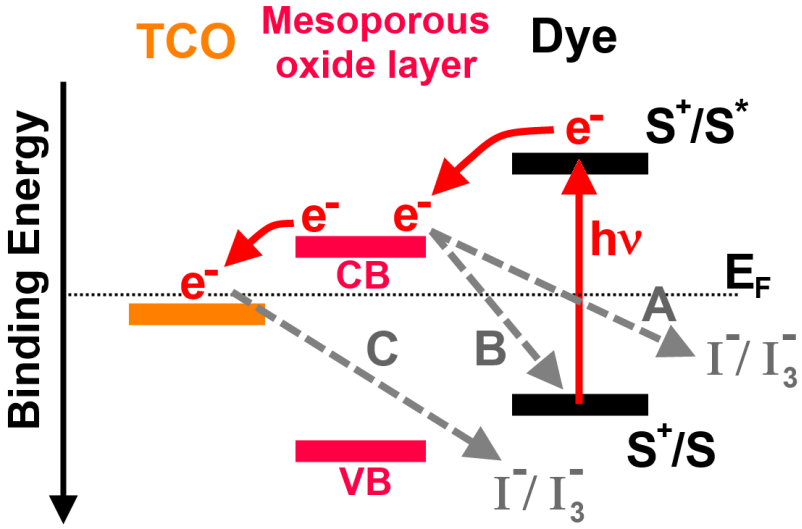

Figure 2.2: *Scheme for the main carrier recombination channels at the photoanode.*

Another factor which can deeply affect the cell efficiency is the interfacial recombination, that is the back flow of electrons to oxidized dyes or triiodide ions [74,79,87,88]. As displayed in Figure 2.2, two major sites of recombination can be identified: the mesoporous metal oxide nanoparticles/electrolyte and the TCO/electrolyte interfaces. In the first case, the electrons injected into the conduction band of the mesoporous metal oxide layer can recombine both with the triiodide ions (I_3^-) of the electrolyte (channel A) and the oxidized dye (channel B). The latter case can be neglected on the basis of time scale evaluations: in facts, it is known that the oxidized dye molecules are regenerated by the iodide ions faster (10^{-6} s) with respect to the electron back flow from the metal oxide conduction band (10^{-4} s) [74]. Channel A is instead one of the main factor decreasing the charge separation in DSSC governed by the electron trapping in surface states and depending on many parameters, such as light intensity, applied electrical potential and electrolyte composition [89]. This unintended reaction can be restrained by depositing a thin shell of insulating oxide, such as Nb_2O_5 [90], MgO [76], SiO_2 [91], ZrO_2 [92] and Al_2O_3 [93], even if the actual passivation of the mesoporous oxide layer seems to be related to specific features which the oxide thin film should present [88]. Channel C originates from the direct contact between the TCO collector and the electrolyte which penetrates through the pores of the nanoparticles film. An effective way to quench this recombination channel is to create a separator film between TCO and the electrolyte which is commonly called *Blocking Layer* (BL) [74, 94, 95], leading to an increase either in the photocurrent density [63, 96] or the open-circuit voltage [97] or both [62, 64, 87, 94]. Several studies account for the advantages due to the BL presence at the photoanodes, but its role is still debated because the resulting effects can be different on a case-by-case basis. Besides, the chemical composition, the crystal phase, the thickness and even the deposition method, for the most efficient BL, are not yet univocally defined.

2.2 Materials

In the frame of PV application, a non-stoichiometric amorphous cadmium-tin oxide $Cd_xSn_yO_z$ (CTO) thin film was obtained with a good compromise between electrical and optical properties, exhibiting low sheet resistance ($\sim 13\,\Omega/\square$) and high transparency ($> 80\%$ in the range 500-800 nm) [98] compa-

rable to other commercially available TCOs, like In_2O_3:Sn [99] Cd_2SnO_4 [100] and SnO_2:F [101]. Recently, the latter CTO was matched with an ultrathin TiO_2 BL, representing a reliable solution for DSSCs manufacturing as a front contact [61, 102].

The materials under investigation in this chapter are CTO/TiO_2 heterojunctions which were grown onto a Si (100) wafer, or glass substrates for the application in DSSCs, as described in details in Ref. [61] where the functional properties of the solar cells are completely specified. The samples considered in this chapter have been prepared by growing a 650 nm thick CTO film onto a clean Si substrate kept at 400°C in an inert (Ar) atmosphere for 2 hours at the constant pressure of $5 \cdot 10^{-3}$ $mbar$. Then, three different TiO_2 BL were deposited on CTO in an oxidizing atmosphere (Ar/O_2 equal to 90% - 10%) with three different deposition times; 15 min for CTO-TO15, 30 min for CTO-TO30 and 1h for CTO-TO60. As mentioned before, this kind of heterojunction was used as a front contact, but the reasons of employing this in DSSCs as carrier collector can be realized only considering the discovery of the transparent conductive oxides.

2.2.1 Transparent conductive oxide

A TCO is a material, usually in the form of thin film, which exhibits high optical transmittance and high electrical conductivity at the same time. This combination of properties is usually impossible to achieve in intrinsic or undoped oxides, therefore it is obtained by way of non-stoichiometric compositions or through doping the pristine materials with appropriate elements. Bädeker was the first to discover the TCO qualities in 1907 by the thermal oxidation of sputtered Cd thin films [103]. Since then, TCOs have been pervasively studied because of their wide variety of technology applications, such as flat panel displays, photovoltaic cells, optoelectronic devices, transparent thin films transistors, gas sensors, low-emissivity windows, and thin-film resistors [104]. Most of the commercially available TCOs are binary or ternary compounds containing one or two metallic elements. For example, thin solid films of ZnO [105], SnO_2 [106], In_2O_3 [107] and CdO [108] are all well-known TCOs. However the controlled doping of some binary oxides can increase the density of charge carriers without degrading the optical transmission, as for the case

of In_2O_3:Sn [99, 109] , SnO_2:F [101], ZnO:Al, SnO_2:Sb [110] which are among the most utilized TCOs in technological applications. An alternative choice is to consider ternary oxides, such as Cd_2SnO_4 [100], $CdSnO_3$, Zn_2SnO_4 [111], $CdIn_2O_4$ and $Zn_2In_2O_5$ [100, 112]. In particular, cadmium stannate Cd_2SnO_4 seems to be the most adaptable solution in a wide variety of applications due to its high transparency, low sheet resistance ($\sim 7.2\ \Omega/\square$), low visible absorption coefficient ($\alpha = 0.02$) and the highest dc-conductivity/visible absorbance coefficient ratio ($\sigma/\alpha = 7\ \Omega^{-1}$) [104]. Although a single phase is essential to reach high electrical conductivity together with low optical absorbance [113], the crystal phase of thin films is not strictly required for TCOs. For example, Nozik [114] prepared amorphous Cd_2SnO_4 thin films with a wide range of conductivities, retaining high visible transmittance, in which oxygen vacancies provided the donor states. Hosono et al. [115] deposited wide-gap Cd-based amorphous oxides, relating the high electron conductivity either to the formation of oxygen vacancies or to ion implantation of excess cations.

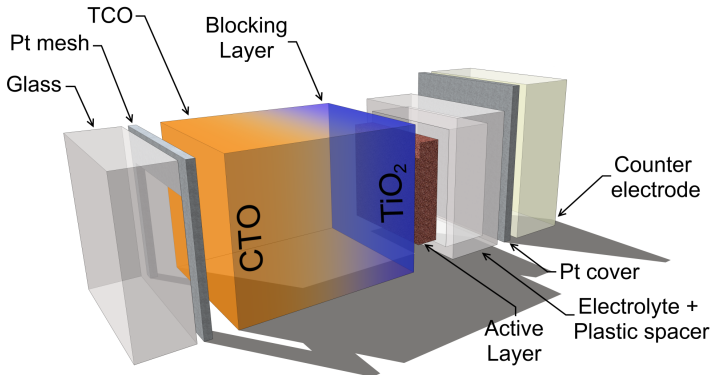

Figure 2.3: *Schematic of the multilayered structure which constitutes the DSSC. Labels point out the different components. Adapted from Ref. [69].*

2.2.2 DSSC fabrication

All the details concerning the fabrication of the DSSCs, in which the aforementioned CTO/TiO_2 heterointerfaces are applied, can be found in Ref. [61]. Here a brief description of the DSSC assembling is presented: starting from

glass substrate, a properly designed Pt mesh was deposited by DC-sputtering before the CTO deposition in order to increase the conductivity of the front contact, thereby avoiding the detrimental effects which can occur at the interface between the glass substrate and the CTO. Then, a 650 nm thick layer of CTO and a thin film (of different thickness) of TiO_2 were grown to complete the front contact multilayer. At a later stage, one layer of TiO_2 nanoparticles (20 nm in size) with an average thickness of 2.5 μm was directly tape-casted on the front contact as the active layer of DSSC. To accomplish the photoanode, the entire structure so far realized was dipped for 20 h into a dye solution. A platinized FTO conducting glass was applied as counter-electrode and sealed by a 25 μm thick plastic spacer. Cells have been finally assembled injecting the I^-/I_3^- redox-couple electrolyte by means of capillary force. A schematic picture for the DSSC fabricated is shown in Figure 2.3.

2.3 XPS results

To evaluate the Cd and Sn stoichiometry in the bulk CTO, normal emission XPS data were collected for each heterostructure in the 400-500 eV binding energy region, where the Cd 3d, Ti 2p and Sn 3d core levels are detectable, as displayed in Figure 2.4 (a). The spectra were properly normalized with respect to the analyser transmission. The core level satellites of the non-monochromatized x-ray source were removed by a deconvolution procedure and an universal-cross section Tougaard background [47] was subtracted from the experimental data. The resulting Sn/Cd stoichiometry ratio values are listed in Table 2.1. As can be observed, the Sn/Cd stoichiometry ratio values decrease with the thickness, ranging from 1.92 ± 0.08 for the bare CTO layer to down to 0.45 ± 0.10 for the CTO-TO60 interface. The stoichiometry variation of the Sn 3d/Cd 3d ratio as a function of the TO deposition time could be explained by referring to two mechanisms: a stoichiometry gradient in the CTO surface and/or a substitution of different cation species across the interface. Both effects can be studied by means of an AR-XPS analysis. The investigation of these mechanisms constitutes the goal of the next sections.

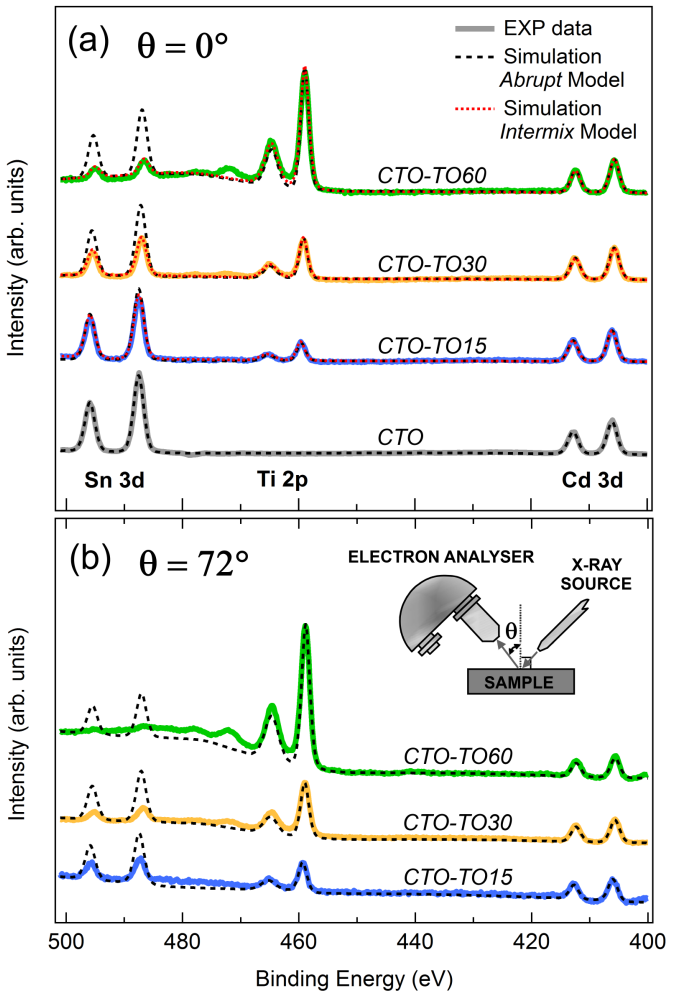

Figure 2.4: *Experimental XPS data (solid lines) for the bare CTO and CTO-TOs collected at the polar angle $\theta = 0^\circ$ (a) and at $\theta = 72^\circ$ (b). Calculated XPS spectra within the abrupt interface model (black-dashed) and the intermix model (red-dotted). All spectra are normalized to the Cd 3d peak area. Inset: Experimental setup geometry, with the polar angle θ.*

Sample	η (%)	Improv.	XPS Sn3d/Cd3d	Abrupt Model Sn3d/Cd3d	Intermix Model Sn3d/Cd3d
CTO	2.28	-	1.98 ± 0.08	1.92	-
CTO-TO15	2.87	+25%	1.69 ± 0.01	1.91 ± 0.27	1.60 ± 0.10
CTO-TO30	3.12	+36%	1.01 ± 0.03	1.84 ± 0.20	1.04 ± 0.05
CTO-TO60	3.05	+33%	0.45 ± 0.10	1.75 ± 0.19	0.44 ± 0.02

Table 2.1: *From the left: DSSC efficiency (η) (taken from Ref. [61]) and efficiency improvements. Quantification analysis of the Sn/Cd ratio from: experimental XPS spectra, calculated XPS spectra within the abrupt model and the intermix model. Experimental and calculated XPS spectra are displayed in Figure 2.4(a).*

2.4 AR-XPS results

2.4.1 CTO

To investigate the Sn/Cd stoichiometry, an AR-XPS analysis was carried out for the bare CTO, as shown in Figure 2.5. The integrated Cd 3d and Sn 3d core level areas were collected in the 0°- 80° polar angle (θ) range (see the inset of Figure 2.4) with steps of 4°. All data were normalized by setting the Cd 3d intensity values equal to 1. Data in Figure 2.5 clearly evidence a pronounced variation of the Sn/Cd ratio with the polar angle in the bare CTO. This indicates the presence of a stoichiometry gradient of the metal cations for the bare CTO close to the surface, i.e. at high θ values, where the surface sensitivity of the XPS probe is known to be enhanced.

In the modelling carried out by using the BriXias code [44] (presented in paragraph 1.6) the fitting algorithm is tuned to reproduce the experimental data (i.e. the peak intensity dependence on the polar angle θ) using as fitting parameters the thickness of each layer above the bulk material. The AR-XPS data fitting shown in Figure 2.5 is based on the model described in the inset of Figure 2.5 which is able to reproduce the same Sn/Cd stoichiometry gradient. This model consists of two effective layers: the CTO bulk layer, which is characterized by a Sn/Cd ratio equal to 1.92 as measured by XPS in normal emission (see Table 2.1), and the CTO top layer, which shows a reduced Sn/Cd stoichiometry equal to 1.27 for an estimated thickness of 3.5 ± 0.1 Å. These sto-

ichiometry and top layer thickness values are those yielding the best fit of the experimental AR-XPS data (points in Figure 2.5) with the model calculations (continuous lines in Figure 2.5).

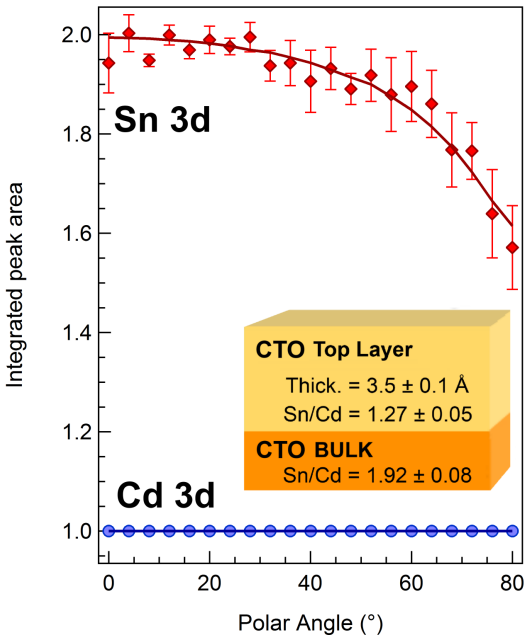

Figure 2.5: *AR-XPS data on the Cd 3d (blue dots) and Sn 3d (red diamonds) core levels for bare CTO. Fitting curves are displayed as solid lines. The integrated peak areas are normalized with respect to the Cd 3d values. Inset: effective two-layer model resulting from the fitting procedure of the AR-XPS.*

2.4.2 The *abrupt* model for the CTO-TOs

Figure 2.6 shows the AR-XPS data collected from the CTO-TOs heterojunctions in the 0°- 52° polar angle range. Here, in addition to the Cd and Sn AR-XPS intensity profile also the Ti 2p intensity profile is shown. To interpret the experimental data, we considered a simple model - hereafter called *abrupt* model, displayed in Figure 2.7 (a) - based on an *abrupt* interface be-

tween a continuous film of TiO_2 (the BL) and the effective two-layer model of Figure 2.5, developed for the CTO. For the present model, the convergence of the fitting procedure is achieved only for the CTO-TO15 sample (Figure 2.6 (a)), whereas a large mismatch occurs for the other samples (Figure 2.6 (b) and (c)) up to the inversion of the Cd 3d and Sn 3d fitting curves in the CTO-TO60 (Figure 2.6 (c)). On the other hand, the fit appears to reproduce the angular (i.e polar angle) dependence of the data, as is evident when the fitting curves are vertically shifted by suitable offset values. Therefore, the *abrupt* model well fits the bare CTO behavior but is inappropriate to model the CTO-TOs heterojunctions because of a clear stoichiometry mismatch (offset) between theory and experiment. These limits can be also retrieved from Figure 2.4 (a) which shows the comparison between the experimental data (solid lines) with the calculated XPS spectra (black-dashed lines). With the exception of the bare CTO, the model overestimates the Sn 4d core line peak intensity, thereby affecting the Sn/Cd ratios as summarized in Table 2.1.

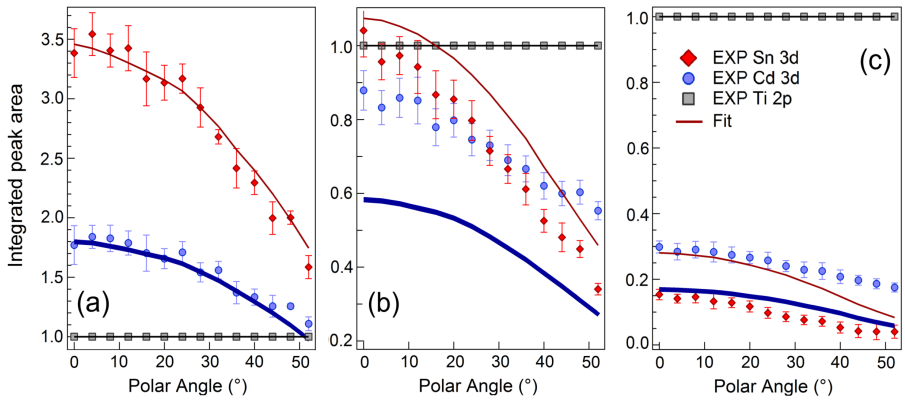

Figure 2.6: *AR-XPS data for (a) CTO-TO15, (b) CTO-TO30 and (c) CTO-TO60. The integrated peak areas for the Cd 3d (blue dots), Sn 3d (red diamonds) and Ti 2p (grey squares) are collected from 0° to 52° of the polar angle θ. All data are normalized setting the Ti 2p values equal to 1. The fitting curves (solid lines) are obtained on the basis of the abrupt interface model (Figure 2.7 (a)); Cd 3d thick blue line, Sn 3d thin-red line.*

2.4.3 The *intermix* model for CTO-TOs

In order to improve the interface modeling, an extra process - i.e. the interdiffusion of metal cations - was considered. Interdiffusion was properly accounted for by a model - hereafter denoted as *intermix* model - where the substitution between different metal cation species can occur at the interface of each CTO-TO heterojunction, while the Sn/Cd stoichiometry gradient presented in Paragraph 2.4.1 is maintained in the bulk material. The cations involved in the interdiffusion process appear to be Ti and Sn; this is consistent with the results of Figure 2.4 (b), which shows the comparison between data collected at $\theta = 72^{\circ}$ polar angle for the CTO-TOs and the XPS spectra calculated on the basis of the *abrupt* model. At such a grazing electron take-off angle both Sn and Cd peak intensities result to be attenuated, as the bulk contribution is reduced in this geometry. However, the Sn 3d attenuation is larger than that measured for Cd 3d, indicating that Sn could be replaced by Ti during the growth of the BL at the topmost layers of CTO. Moreover, the Sn 3d signal tends to disappear in the experimental spectrum of CTO-TO60 (green-solid line) - in contrast with the XPS simulations (black-dashed line) - while the Cd 3d peak is still well detectable, showing the present limits of the *abrupt* model.

The basic idea of the intermix model is that Sn in the bare CTO can be substituted by Ti during the RF-magnetron sputtering deposition, thus changing the bulk composition, while maintaining the stoichiometry gradient very close to the original value at the same time. Modelling is achieved by adding two effective layers (hereafter denoted as L_1 and L_2) sandwiched between the TO (L_0) and CTO (L_3) layers, as shown in Figure 2.7 (b). Starting from the surface, the following layers appear: a continuous film of TiO_2 (L_0), two layers aimed to account for the cation interdiffusion and the stoichiometry gradient (L_1 and L_2) and a bulk layer for CTO (L_3). Considering the XPS stoichiometry evaluations of Table 2.1, L_3 presents a fixed Sn/Cd ratio of 1.92 for all the samples, while L_2 and L_1 are arranged in order to allow for Sn substitution with Ti as:

$$\mathrm{CdSn}_{(1.92-x)}\mathrm{Ti}_x\mathrm{O}_y \qquad (L_2) \tag{2.1}$$

and

$$\mathrm{CdSn}_{[1.92-(x+\alpha)]}\mathrm{Ti}_{(x+\alpha)}\mathrm{O}_y \qquad (L_1) \tag{2.2}$$

where 1.92 is the Sn bulk stoichiometry in CTO and x equals the difference between 1.92 and the Sn/Cd experimental value for each CTO-TO (see Table

2.1). Finally, α is an effective value accounting for further Sn replacement with Ti in the L_1 layer (which is the closest to the growing TO layer during the deposition process). The α value is regarded as a fitting parameter and, for the present experiment, α resulted to be 0.65 ± 0.05.

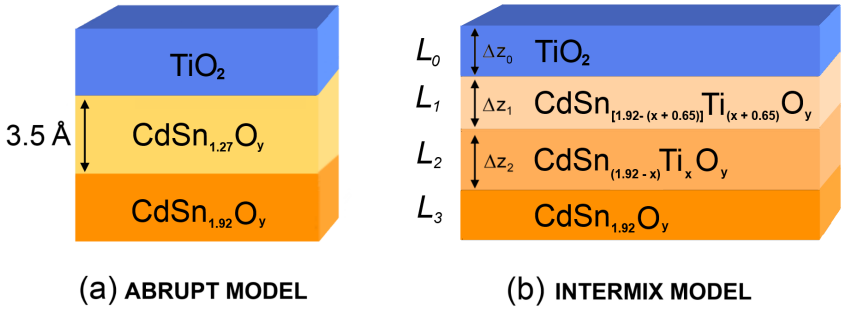

Figure 2.7: *(a) Abrupt model: TiO_2 continuous film and the two-layer model for the CTO (Figure 2.5) which accounts for only the Sn/Cd stoichiometry gradient. (b) Effective four-layer intermix model. From the left: labels for each layer L_i ($i = 0, 1, 2, 3$), labels for each thickness Δz_i , and the chemical formulas for the Ti ↔ Sn interdiffusion process.*

Figure 2.8 (a), (b) and (c) show the fitting results obtained with the *intermix* model for CTO-TOs, having set the thickness of each layer (Δz_i, $i = 0, 1, 2$) as a fitting parameter. The results are summarized in Table 2.2, while the corresponding four-layers effective models are depicted in Figure 2.8 (d), (e) and (f). The resulting effective depth profiles for the metal cations are displayed in Figure 2.8 (g), (h) and (i). The average thickness Δz_{BL} for the TO film has been estimated by setting as upper limit the bare sum of Δz_i and as lower limit the sum of Δz_i with each term weighted by the estimated Ti concentration. Incidentally, it is important to remark that the present Δz_{BL} values are consistent with those (Exp Δz_{XXR}, in Table 2.2) independently obtained from X-Ray Reflectivity (XRR) [61].

The reliability of the AR-XPS analysis can also be evaluated by the comparison between the experimental (solid lines) and the XPS spectra calculated by the intermix model (red-dotted lines), as presented in Figure 2.4 (a). Now, the peak intensities of the calculated spectra well reproduce the experimental data (see Table 2.1).

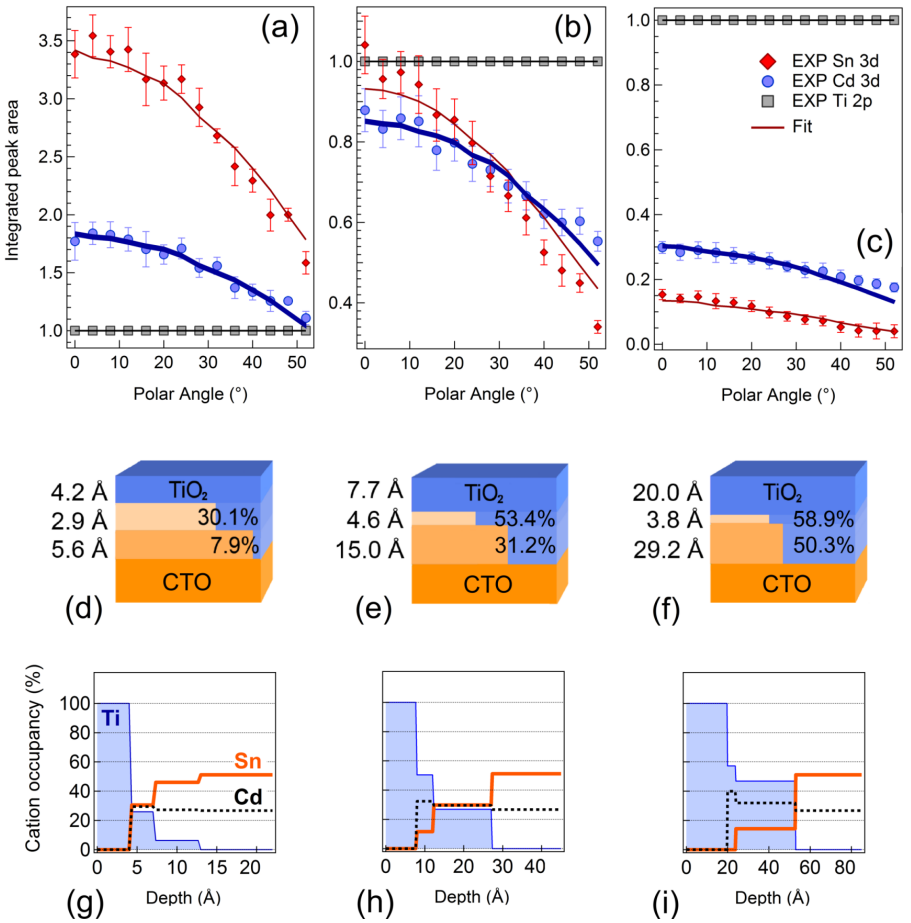

Figure 2.8: *AR-XPS data for (a) CTO-TO15, (b) CTO-TO30 and (c) CTO-TO60. The integrated peak areas for the Cd 3d (blue dots), Sn 3d (red diamonds) and Ti 2p (grey squares) are collected in the 0° to 52° range of the polar angle θ. Fitting curves within the intermix model are displayed as solid lines; thick-blue line for Cd 3d and thin-red line for Sn 3d. All data are normalized by setting the Ti 2p intensity values equal to 1. The four-layer models resulting from the fitting procedure are displayed in (d) for CTO-TO15, (e) for CTO-TO30 and (f) for CTO-TO60; on the left the resulting thicknesses are shown, while inside each layer the Ti percent occupancy is reported. The complete set of the resulting parameters from the fitting analysis is listed in Table 2.2. The effective depth profiling for Ti, Cd and Sn are displayed in panel (g) for CTO-TO15, (b) for CTO-TO30 and (c) for CTO-TO60.*

Intermix Model	CTO-TO15 (Å)	CTO-TO30 (Å)	CTO-TO60 (Å)
Δz_0	4.2	7.7	20.0
Δz_1	2.9	4.6	3.8
Δz_2	5.6	15.0	29.2
Average Δz_{BL}	5.5 - 12.7	16.0 - 27.3	37.4 - 53.0
Exp. Δz_{XRR} [*]	10.9	21.9	46.7

Table 2.2: *Fitting results for the AR-XPS data of Figure 2.8 by using the intermix model of Figure 2.7 (b).* Δz_{0-2} *are the thicknesses for the effective layers* L_{0-2}, Δz_{BL} *is the average thickness for the BL while* Δz_{XRR} *is the experimental measurement of the BL thickness by XRR.* Δz_{0-2} *are defined within* ± 0.1 *Å of uncertainty. [*] from Ref. [61].*

2.5 Interface Band Diagram

The interface band diagram of the present heterojunctions can be drawn by considering the layer thickness study so far carried out and the evaluation of the energy offsets of the interface layers with respect to the parent (CTO and TO) compounds. In order to retrieve the required energy values, an analysis of the valence band (VB) and the conduction band (CB) offset was carried out referring to a recent work of Goldfarb *et al.* [116]. Indeed, by means of the binding energy (BE) of the Ti 3p and Cd 4d shallow core levels, as well as the VB maximum (VBM), the effective band diagram at the interfaces can be reconstructed. Figure 2.9 (a) shows the XPS spectra taken into account, i.e. the two bulk references - the CTO and a 50 nm thick TiO_2/Si(100) - and the three CTO-TOs heterostructures. Since the samples were in ohmic contact with a gold clip during the XPS measurements, all spectra are aligned in BE considering the energy of Au $4f_{7/2}$ equal to 83.98 eV [117, 118]. The BEs for the Cd 4d and Ti 3p core levels are indicated in Figure 2.10 (b) and (c). The VBM is determined by extrapolating the leading edge of the VB spectra to the energy axis in order to account for the instrumental broadening. This procedure is displayed in Figure 2.9 (b) and the VBM values for CTO and TiO_2 are shown in the same graph. The reliability of the VBM evaluation has been verified by considering the study of Chambers *et al.* [119] (see Appendix A.2). The VB

offsets in CTO-TOs are determined as follows:

$$\Delta E_V(\text{CTO-TOs}) = \Delta E_{\text{CL-VBM}}(\text{TiO}_2) - [\Delta E_{\text{CL-VBM}}(\text{CTO}) + \\ + \Delta E_{\text{CL}}(\text{CTO-TOs})] \tag{2.3}$$

where $\Delta E_{\text{CL-VBM}}$ is the difference between the BE of the shallow core level (Ti 3p or Cd 4d, in the present case) and the VBM in the selected bulk material (respectively, TiO_2 or CTO) while ΔE_{CL} is the difference between the BE of the selected shallow core levels in the heterostructures. Thereafter, the CB offset is estimated from ΔE_V by

$$\Delta E_C(\text{CTO-TOs}) = [E_g(\text{TiO}_2) + \Delta E_V(\text{CTO-TOs})] - E_g(\text{CTO}) \tag{2.4}$$

where E_g is the energy gap, which is within the range $2.7-3.1\ eV$ for CTOs [120]. Since the bare CTO is conductive [61, 98, 102], we consider that the energy gap is less than the VBM $= 2.71\ eV$, such that the CB is just below the Fermi level. States at the Fermi edge (EF) are not clearly detected with the present XPS probe, likely due to the low XPS cross-section for oxygen, which is supposed to mainly contribute to filled states in the VB region [121]. However, the CTO VB spectrum shows a tail of states on the low BE side that may eventually yield a non-zero spectral weight at EF. Referring to T. Meng *et al.* [122] that have systematically studied the E_g dependence on the Sn/Cd ratio, we have selected $E_g(\text{CTO}) = 2.66 \pm 0.05\ eV$ (see Appendix A.3 and A.4 for more details). On the other hand, for TiO_2 we assume the energy gap of the anatase phase, i.e. $3.20\ eV$ [123], which is proved to be predominant in the film as reported in Ref. [102] by Glancing Incident X-Ray Diffraction (GIXRD) measurements on samples grown in similar conditions.

The scheme of the energy levels is shown in Figure 2.10 (a) while the resulting ΔE_V and ΔE_C are listed in Table 2.3 (see Appendix A.1 for the uncertainty evaluation). Here the band offset results are referred to the bulk CTO and TiO_2, represented by L_3 and L_0 respectively. The VBM shift in the L_1 and L_2 regions cannot be directly accessed by the present method, and therefore the energy levels of the end members (CTO and TO) have been connected by straight lines as a guide for the eye in Figure 2.11.

The following results are obtained for all the CTO-TOs: *(i)* the heterojunction is of type I (straddling gap) as shown in Figure 2.11 (d), (e), (f);

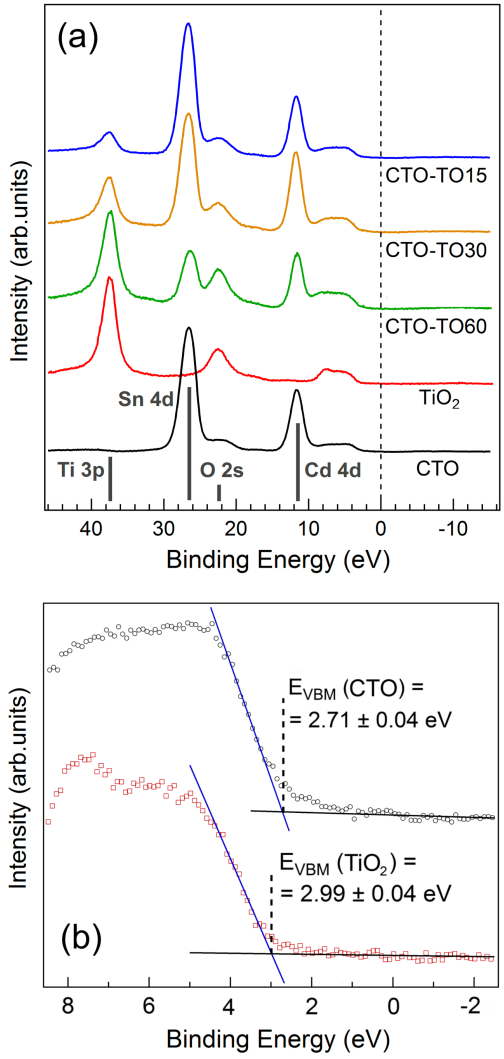

Figure 2.9: *(a) Extended XPS data in the Ti 3p, Sn 4d, Cd 4d and VB binding energy range for the CTO-TOs heterostructures and the parent compounds (CTO and TiO_2). The core level position are marked by grey bars which are proportional to the photoemission cross sections. (b) Enlargement of the VB of CTO (black circles) and TiO_2 (red squares) and extrapolation of the VBM. E_{VBM} values for CTO and TiO_2 are reported in the panel.*

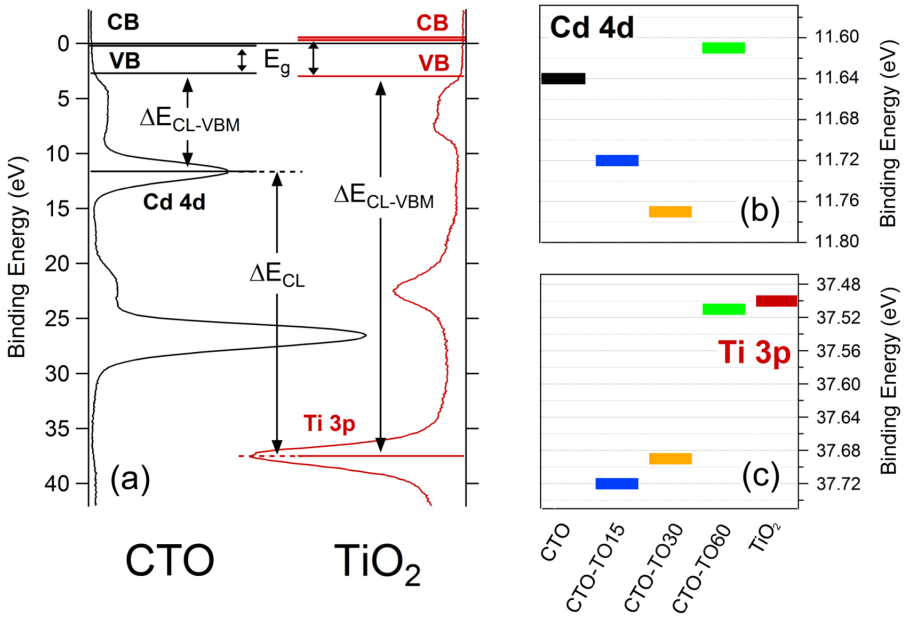

Figure 2.10: *(a) Scheme of the energy levels considered for the band offset analysis. XPS spectra for CTO (left) and TiO_2 (right) are displayed on the panel sides. BE positions of the Cd 4d and Ti 3p core levels for the heterostructures CTO-TOs and the parent compounds are reported in panel (b) and (c) respectively. The line thickness accounts for the uncertainty of the BE position which is less than ± 0.01 eV.*

Sample	$\Delta E_V(eV)$	$\Delta E_C(eV)$	$IB(eV)$
CTO-TO15	-0.42	0.12	-0.01 ± 0.04
CTO-TO30	-0.34	0.20	0.02 ± 0.04
CTO-TO60	-0.32	0.22	0.20 ± 0.04

Table 2.3: *From the left: valence band offsets (ΔE_V), conduction band offsets (ΔE_C) and the insulating barrier (IB) considering the selected bang gap of $E_g(CTO) = 2.66$ eV and $E_g(TiO_2) = 3.20$ eV. The minus sign in the offsets means that the band maximum value of the bulk material in the heterojunction presents a BE lower than the one related to the film. ΔE values are defined within ± 0.1 eV of uncertainty. All these values are displayed in Figure 2.11.*

(ii) the type I character is maintained independently on the BL thickness, and *(iii)* ΔE_C increases with the BL thickness as reported in Table 2.3. Furthermore, from the details of the CB region displayed in Figure 2.11 (a), (b) and (c) it turns out that *(iv)* the insulating barrier (IB), which exceeds the Fermi energy and is generated by the BL in the L_0 layer, increases with the BL thickness. Therefore we can establish that *(v)* the increase of the IB size can make the heterojunction more efficient for an application in a DSSC - at least in terms of minimizing the electron recombination - in view of the correlation of the efficiency gain with the increase of the BL average thickness. This is indeed demonstrated by comparing the IB size (Table 2.3) and the DSSC efficiency (Table 2.1): in the CTO-TO15 the lowest efficiency is combined with an IB $< 0\ eV$ while in CTO-TO30 the best efficiency occurs when IB $> 0\ eV$.

On this basis, the DSSC efficiency is expected to increase with the BL thickness and thereby the CTO-TO60 should exhibit the highest efficiency. This actually does not occur and similar behaviors can be found in several studies [63, 96, 124–126, 128, 129]. In order to rationalize the efficiency reduction beyond a critical thickness of the BL, both the IB and the ΔE_C have to be taken into account. In facts, CTO-TO30 and CTO-TO60 show a similar ΔE_C in contrast with a different IB. This situation is ascribed to the upwards shift of the whole band across the junction which makes the CB of CTO-T60 closer to EF in the L_3 layer (CTO) and well above EF in the L_0 layer (TO). In this way, the IB of CTO-T60 results to be higher in energy and larger in depth. This may yield a reduction of the injection rate, justifying the efficiency reduction which is usually found when the BL is *too* thick.

In conclusion, the blocking layer generates an insulating barrier between the excited dye and the TCO which in the present DSSCs is found to improve the overall efficiency, as long as its size is smaller than the critical values within about 2.2 to 4.7 nm (Δz_{BL} for CTO-TO30 and CTO-TO60, Table 2.2). In this case, the injection rate should prevail over the electron recombination rate. Otherwise, in agreement with Ref. [63] and [128], the evident upward band shift in CTO-TO60 with respect to CTO-TO30 could be an hint to state that the IB can almost inhibit the recombination process but at the expense of an injection rate reduction for a BL thickness larger than the critical value, negatively affecting the cell efficiency. Therefore, the best performances of the CTO-TO30 cell can be ascribed to a subtle balance between the barrier thickness (large

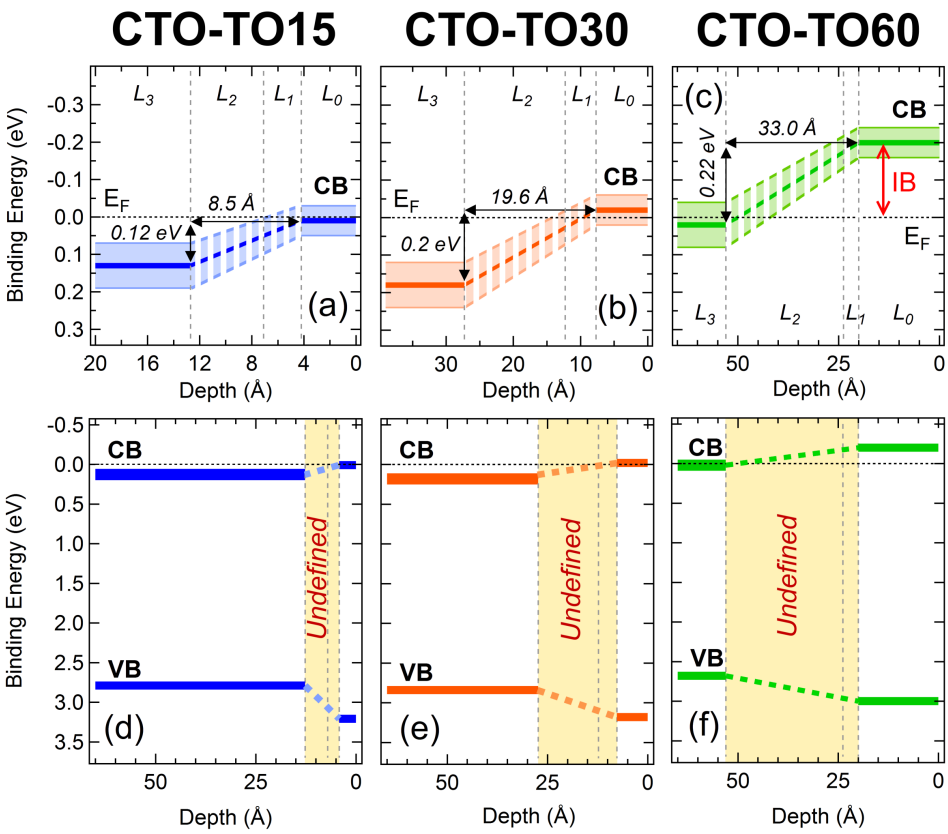

Figure 2.11: *Effective band diagram for the VB and the CB of the heterostructures based on the intermix model results for CTO-TO15 (d), CTO-TO30 (e) and CTO-TO60 (f). In the (a), (b) and (c) panels the enlargements for CB are displayed. The insulating barrier (IB) is evidenced by the red arrow. The shaded regions in panel (a), (b) and (c) and the thickness of the lines in panel (d), (e) and (f) stand for the uncertainty equal to* ± 0.04 *eV except for the CTO CB which is* ± 0.06 *eV.*

enough to prevent electron recombination, that is, tunneling from CTO back to the electrolyte) and the increased CB energy offset (0.2 eV) with respect to the CTO-TO15 case (0.12 eV). On the other hand the CTO-TO60 junction displays the largest offset (0.22 eV), which is favorable to avoid electron recombination, but its BL thickness could be too large to enable an efficient charge (electron) transport from the TiO_2 nanocrystals to CTO.

2.6 Comparison with the literature

Several works have so far presented a study of the DSSC efficiency in relation with the BL thickness, but only some of these have shown an efficiency reduction above a critical thickness of the BL. Other factors affecting the DSSC performance have also been proposed, such as a reduction of the light transmittance due to the BL thickness [124] or an increment of the internal series resistance of the solar cell [125, 126].

In Table 2.4 we have listed the studies where the BLs are based on TiO_2 and prepared by different deposition techniques such as RF-magnetron sputtering, DC-magnetron sputtering, spray pyrolysis, atomic layer deposition (ALD), spin-casting and electrodeposition. In particular we have focused on two parameters to be compared with our results: *(i)* the relative percent enhancement (RPE) of the DSSC efficiency between the cell with the front contact formed by the bare TCO (without BL) and the cell with the TCO/BL heterojunction as front contact which exhibits the highest efficiency and *(ii)* the BL thickness yielding the best efficiency (TBE). We note that CTO-TO30 shows the highest RPE for the RF-magnetron sputtering technique (+36%) and the overall best ratio between RPE and TBE. In fact, CTO-TO30 presents a TBE of 2.2 ± 0.6 nm which is nearly one order of magnitude smaller than the other cases.

This could be explained by the combination of the interdiffusion process of the Ti cations at the interface and the Sn/Cd stoichiometry gradient of the bulk CTO: both effects produce an interfacial layer (L_{1-2}) which might smoothly connect the conduction band offset between the surface L_0 layer and the bulk L_3 (Figure 2.12(a)), thereby favoring the travel of the electrons with respect to the case of a potential barrier formed by a single sharp step (Figure 2.12 (b)), which is distinctive of an abrupt TCO/BL heterojunction. In this way (Figure 2.12 (a)), the electrons injected in the TiO_2 empty states should travel

Deposition Technique	RPE (%)	TBE (nm)	Reference
RF-magnetron sputtering	+36	2.2	CTO-TO30
	+21	16	[63]
	+26	93	[97]
DC-magnetron sputtering	+10	18	[125]
	+42	300	[126]
Spray-pyrolysis	+11	75	[127]
	+87	150	[128]
ALD	+29	25	[129]
Electrodeposition	+59	450	[124]
Spin-casting	+33	160	[87]

Table 2.4: *Comparison among several works in which the front contact is the heterojunction between a TCO and a TiO_2 BL deposited by different techniques. From the left: Relative Percent Enhancement (RPE) for DSSC efficiency between a bare TCO front contact and the TCO/BL front contact which exhibits the best cell efficiency and the BL Thickness for the Best Efficiency (TBE).*

a shorter path at a constant flat band (L_0) - thereby decreasing the electron injection time - and then run down a smooth potential barrier (L_{1-2}), which acts as a buffer layer. In turn, the electrons in the CTO conduction band should pass through a larger potential barrier to undergo recombination. The combination of these effects is expected to yield the better performances observed for CTO-TO30 DSSC.

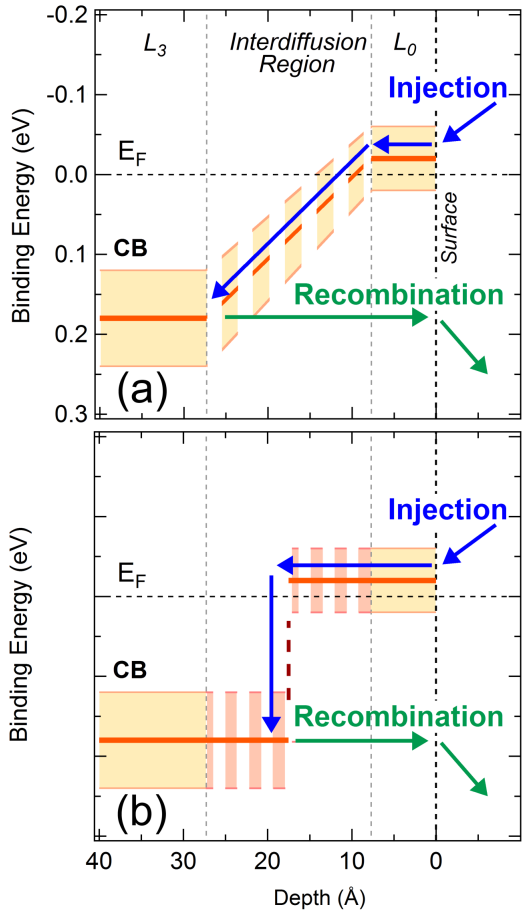

Figure 2.12: *CB enlargements for the CTO-TO30: (a) interpretation of the interfacial layer (L_{1-2}) as a link between the band offset of L_0 and L_3 due to the cation interdiffusion process and (b) representation of the equivalent abrupt band offset.*

2.7 Conclusions

The present chapter was aimed to track possible Ti/Sn interdiffusion processes and Sn/Cd stoichiometry gradients at the nanostructured CTO-TO interface and, on this basis, extract a band alignment at the interface to be eventually related with the measured DSSC efficiency.

In the general frame of the studies on the physical and chemical properties at the origin of DSSC performances, the present work points out the relevance of considering cation substitution and interdiffusion at the interface, along with their effects on the VB and CB energy level profiles across the front contact that have been tracked by modeling of AR-XPS data.

In fact, by means of AR-XPS we have evidenced a Sn/Cd stoichiometry gradient in the amorphous CTO film. Then, a cation interdiffusion between Ti and Sn has been evidenced at the heterointerfaces (CTO-TOs) between the CTO and different thin films of TiO_2 grown via RF-magnetron sputtering, as shown in the data on the basis of a four-effective layer model which included two intermediate layers where Sn was replaced by Ti. In addition, we have evaluated the effective VB and CB band diagram for the CTO-TOs by using suitable energy gap values for CTO and TiO_2. Details of this band diagram qualitatively explain the observed efficiency variations on the basis of a better electron recombination along with an efficient charge injection across the junction.

Chapter 3

The case of $LaAlO_3/SrTiO_3$ heterointerface

In recent years, well-defined interfaces between complex oxide have shown outstanding electronic and magnetic properties with promising potentiality for future devices. Some examples are the onset of superconductivity confined to nanometer-sized interfaces [131,132] or magnetism at the interface between non-magnetic oxides [133] or even the formation of two-dimensional electron gas (2DEG) at the interface between two insulators, such as $SrTiO_3$ and $LaAlO_3$ [5], $LaTiO_3$ [6], $LaVO_3$ [134] or $KTaO_3$ [135]. In this scenario, epitaxially grown perovskite oxides play a key role, displaying at the nanometer scale interface properties which are rarely evidenced from their single building blocks.

In particular, during the last decade, an extraordinary attention has been focused on the $LaAlO_3/SrTiO_3$ heterojunction due to the wide variety of unexpected properties arising at the interface, from the 2DEG to the coexistence of superconductivity and ferromagnetism [136], as well as the electric-field-induced metal-insulator phase transition [137]. So far, a large number of studies have attempted to determine the physical properties of such system, in order to control the interface properties through chemical interactions at the surface, suitable materials combination, or strain engineering [7]. Despite of a long standing fundamental research, many scientific questions yet remain to be answered before the goal can be shifted towards the applications.

In the present chapter, a spectroscopic investigation of insulating and conductive $LaAlO_3/SrTiO_3$ heterointerfaces is carried out by means of different soft x-ray photoemission techniques. The study of the electronic properties can provide fundamental information on the origin of relevant physical phenomena at interface, in particular the profiling of energy-level alignment across the heterointerface. The latter achievement, for instance, could be essential to disclose the basic information for the design, characterization, and tuning of devices based on the intrinsic electric fields arising at the interface, such as application in photovoltaics [8, 9], field-effect transistors [10], and devices based on tunable conductivity and charge writing [11, 12]. For this purpose, special attention is paid to some controversial points, such as the band-offset, the density and distribution of Ti^{3+} states, the band-bending in $LaAlO_3$ film, as well as the photo-induced effects due to the x-ray irradiation. Most of following analysis is based on two already published studies [29, 138].

3.1 Perovskite oxides

Perovskite oxides display an extraordinary diversity of physical properties, from insulating to semiconducting, metallic, magnetic, piezoelectric, ferroelectric, multiferroic and even superconducting behavior, combining a plethora of distinctive crystal structures which vary from cubic to orthorombic, rhombohedral, tetragonal and monoclinic [139].

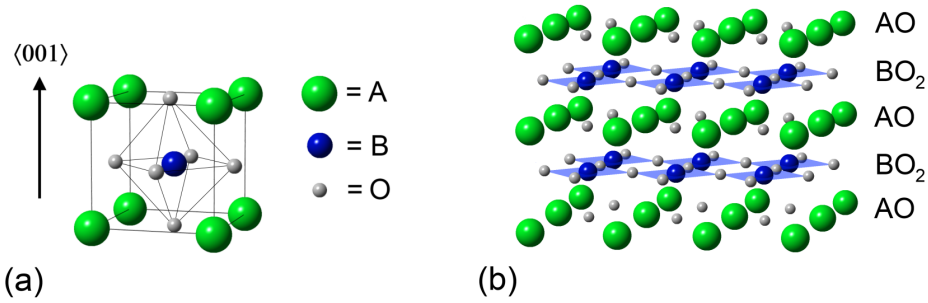

Figure 3.1: *(a) Ideal cubic structure for perovskites, which can be alternatively seen as a stacking of AO and BO_2 atomic planes (b).*

The ideal cubic structure ABO_3 is represented in Figure 3.1 (a) which is a body-centered cubic lattice where the B element at the center, surrounded by an octahedron of six oxygen ions, exhibits a smaller cation radius than the eight A cations at the corners. Alternatively this structure can be viewed as a stacking of AO and BO_2 atomic layers along the (001) direction, as shown n Figure 3.1 (b). Actually, more than 30 elements can be hosted on the A site and over half of the periodic table on the B site, especially transition metal elements. This great chemical variability offers the opportunity to engineer novel functionalities into oxides, thus tailoring thin films with customized electronic, magnetic and optical properties in a unique way [140]. However, the multiple cation interchange in both sites can lead to lattice distortions, due to different cation radii, leading to crystal structures far from the ideal cubic one. To rationalize such a tendency, a tolerance parameter t was introduced by Goldschmidt [141] in relation with the ionic radii (R) as in the formula

$$t = \frac{R_A + R_O}{\sqrt{2}(R_B + R_O)} \tag{3.1}$$

according to which the ideal cubic occurs for $t = 1$, while deviations from this value lead to distorted configuration due to the rotation of the oxygen octahedra, from rhombohedral ($0.93 < t < 1$) to orthorhombic configuration ($t < 0.93$). Anyhow a stable perovskite structure is maintained solely in the range $0.8 \leq t \leq 1$.

In the presence of a transition-metal atom on the B site, the electronic properties of the system are closely related to the lattice structure. In facts, the crystal (or ligand) field effect due to the p orbitals of the neighbouring oxygens lifts the degeneracy of the d orbitals of the transition-metal cation. Then, considering an octahedral structure (O_h), a doublet of higher energy states e_g is generated for the orbitals pointing towards the oxygen sites ($d_{x^2-y^2}$, d_{z^2}), whereas a triplet of states t_{2g} with lower energy is formed for the orbitals pointing between them (d_{xy} , d_{yz} , d_{zx}). Moreover, transition metal ions are generally multivalent and this feature allows them to host additional electrons in the outer shells. Besides, because of the high directionality of the outer orbitals (especially $3d$ and $4d$) - which increase the probability of electron-electron interactions - minimal variations to the A-O and B-O bonding lengths related to the rotation, stretching and tilting of the oxygen octahedra can lead to a further lifting of degeneracy and a potential raising of unexpected transitions which can

substantially change the physical properties of the system [142]. The degree of distortion is set by the trade-off between the gain in energy due to the level splitting and the increase of the elastic energy due to the lattice modification. In other words, the system undergoes spontaneously a distortion if the electronic energy gain is greater than the loss in elastic energy. For instance, in the case of a stretching of the apical position of the oxygens in the octahedra, the breaking of the cubic symmetry involves the increase of the energy of the d orbitals which are closer to the p orbitals (i.e. $d_{x^2-y^2}$ and d_{xy}) and the energy decrease of the others (d_{xz} , d_{yz} and d_{z^2}) because of the larger distance, as shown in Figure 3.2. As the latter involves only the oxygen ions in the neighbourhood of the metal cation, this is a local effect which is generally called Jahn-Teller effect.

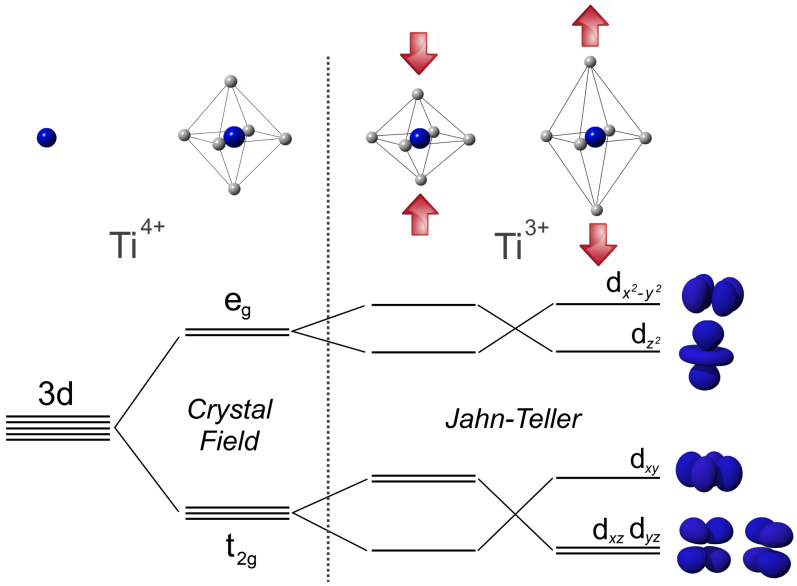

Figure 3.2: *Splitting of the d-orbitals of Ti due to (left) the crystal field in a octahedral structure (O_h) and (right) the Jahn-Teller effects for distorted structures (D_{4h}).*

3.1.1 $LaAlO_3$

Lanthanum aluminate, $LaAlO_3$ (LAO for short), is a closed-shell ($4f^0$) wide band gap insulator ($5.6-6.5\ eV$) [143,144] with a perovskite structure which has been extensively used as a substrate material for the deposition of functional thin films due to its small lattice mismatch with many oxides [145]. In particular, LAO has been studied as a promising candidate for high dielectric constant gate oxide in order to replace SiO_2 in microelectronic devices [143] because of many noteworthy features, such as high dielectric constant ($23 - 25\varepsilon_0$) [147], an atomically flat interface with oxides [148] and large band offsets with Si ($2.52 - 2.86\ eV$) [144].

LAO exhibits a rhombohedral perovskite structure at low temperature (space group $R\bar{3}c$) and undergoes a phase transition approaching the cubic symmetry of the ideal perovskite (space group $Pm\bar{3}m$) above $\sim 800\ K$ [146]. At room temperature, the deviation from the cubic phase consists of a small rotation of the AlO_6 octahedra, with a lattice constant of 3.791 Å with only a 3% of mismatch with the $SrTiO_3$ lattice which then renders LAO suitable for an epitaxial growth onto $SrTiO_3$. An alternative view of the LAO structure is to consider the lattice as a stacking of charged layers, $(Al^{3+}O_2^{2-})^-$ and $(La^{3+}O^{2-})^+$.

3.1.2 $SrTiO_3$

Strontium titanate, $SrTiO_3$ (STO), is intrinsically a band insulator ($3.2 - 3.75\ eV$) [151, 152] with a closed-shell $3d^0$ electronic configuration. STO has a perfect cubic perovskite structure at room temperature (space group $Pm\bar{3}m$) with a lattice constant of 3.905 Å [153] and can be seen as a stack of alternating charge neutral planes of $(Ti^{4+}O_2^{2-})^0$ and $(Sr^{2+}O^{2-})^0$ in the (001) direction. Below $\sim 110\ K$ a structural phase transition occurs towards a tetragonal structure (space group I4/mcm), in which the next neighbouring TiO_6 octahedra undergo a mirrored rotation in such a way to double the unit cell in the three crystallographic directions [154,155]. A further lowering of temperature produces a transition into orthorhombic and triclinic structures [156] and all such structural changes lead to the lifting of the orbital degeneracy of the electronic system, inducing variations in the electronic properties of the material.

Then, it is noteworthy that STO has been investigated for decades as a suitable substrate for epitaxial growth of thin films, such as superconducting cuprates [157] and manganites [158], because of a similar lattice constant with respect to many oxide materials. In addition, STO has also attracted the attention for its catalytic [159, 160], dielectric [161], ferroelectric [162] and paraelectric [163] properties. Even though STO is an insulator with an high resistivity ($> 10^9\ \Omega \cdot cm$), it can turn into metallic by doping of either La on the Sr site [164], Nb on the Ti site [165, 166], or by oxygen vacancies [167] which can be created by annealing above 800°C in low oxygen pressure $\leq 10^{-6}\ mbar$ or by Ar^+ sputtering [168]. In the case of doping with a carrier density above $10^{19}\ cm^{-3}$ a superconducting phase is even evident below $\sim 300\ mK$ [169–171]. Therefore, it is clear that a very rich selection of physical properties coexist in this compound, thereby clarifying the reasons why STO is the subject of intense research efforts looking for potential applications in oxide-based electronic devices [149, 150].

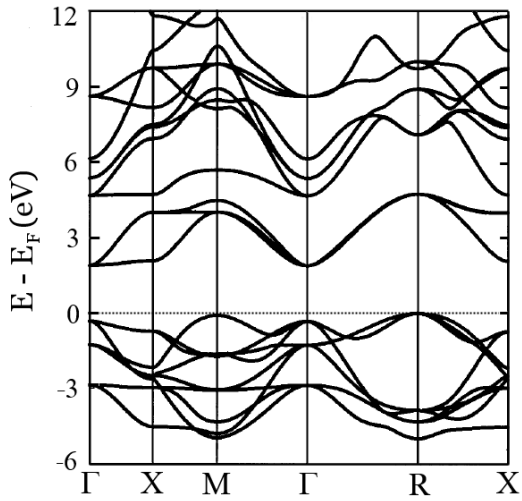

Figure 3.3: *Ab-initio calculation in the local density approximation for the band structure of STO. Adapted from Ref. [151].*

In Figure 3.3 the band structure of STO is adapted from Ref. [151] where the empty $3d$ bands of Ti show minima at Γ and X whereas the full $2p$ bands

of O present maxima at Γ , R and M. As discussed in the previous paragraph, the fivefold degenerate d-orbitals of Ti are splitted by the crystal field of the surrounding oxygen ions into two levels, an higher energy doublet (e_g) and a threefold degenerate state (t_{2g}) at lower energy (see Figure 3.2). The electrons which are localized in the t_{2g} orbitals (d_{xy} , d_{yz} , d_{xz}) are coupled to identical orbitals on neighbouring lattice sites through the p-orbitals of oxygens in the middle, showing an hopping matrix element larger in the plane of the orbital's lobes than in the perpendicular direction [156]. In other words, the hopping between d_{xy} orbitals is stronger along the x and y directions (light effective mass) with respect to the z direction (heavy effective mass), as displayed in Figure 3.4 (a). The Fermi surface corresponding to the d_{xy} , d_{yz} and d_{xz} orbitals is an ellipsoid-shaped volume in the reciprocal space in the k_z , k_x and k_y directions respectively, as shown in Figure 3.4 (b). Then, the resulting band structure is composed of three dispersing three-dimensional bands which are degenerate at the Γ point [173], one weakly dispersing band (heavy-mass) and two degenerate strongly dispersing bands (light-mass), as displayed in Figure 3.4 (c) for the k_y direction.

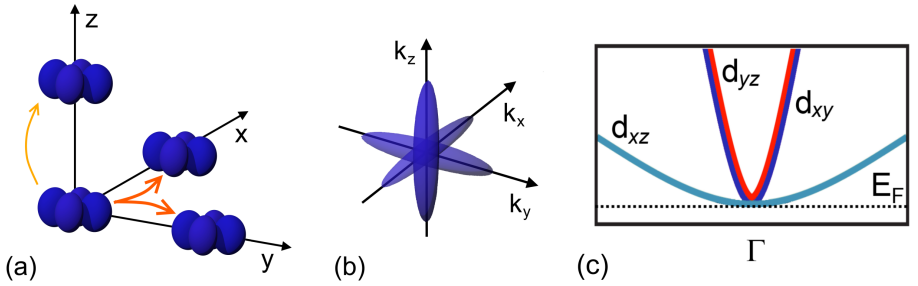

Figure 3.4: *For a bulk STO: (a) d_{xy} orbitals related to neighbouring Ti atoms. In-plane hopping matrix elements (represented by dark-orange arrows) are greater than those in the perpendicular direction (light-orange arrow). (b) Fermi surface corresponding to the threefold degenerate t_{2g} states. (c) Conduction band in STO along k_y, formed by an heavy-mass band (d_{xz}) and two degenerate light-mass bands (d_{xy} , d_{yz}).*

3.1.3 $LaAlO_3/SrTiO_3$ interface

What looked absolutely paradoxical just ten years ago has recently become something usual and obvious, namely that a metallic interface can arise from the junction of two insulating materials. This happened in 2004 when Ohtomo and Hwang reported the first observation of a high-mobility two-dimensional electron gas (2DEG) at the interface between $LaAlO_3$ and $SrTiO_3$ [5]. In fact, when the bulk STO is TiO_2-terminated, the interface can switch to metallic as long as more than three layers of LAO are deposited on top of STO, whereas remains insulating up to the third layer [137]. In this case the heterojunction is defined as n-type - as shown in Figure 3.5 - while, if the bulk STO is SrO-terminated, the interface is identified as p-type which is found to be insulating. Moreover, when the 2DEG is present, the n-type interface exhibits even a variety of unexpected properties, such as superconductivity at low temperatures [131], magnetism [133, 174], electric-field-tuned metal-insulator phase transition [175–177] and nanoscale electronic phase separation [136, 178].

The metallic conductivity has been originally explained on the basis of the picture of the polar catastrophe [139, 179], shown in Figure 3.6. Looking at the (001) planes, STO is a nonpolar solid since both $Sr^{2+}O^{2-}$ and $Ti^{4+}O^{2-}$ planes are charge neutral, while LAO is a polar solid, as it is composed of $La^{3+}O^{2-}$ and $Al^{3+}O^{2-}$ charged layers. Therefore, the stacking of $(LaO)^+$ and $(AlO_2)^-$ layer by layer on top of STO leads to a divergent electrostatic potential (the so-called polar catastrophe) that can be compensated by a charge transfer of 0.5 e^- per unit cell to the interface for the case of LaO deposited on TiO_2. Such a response of the system to the diverging potential created by LAO is thought to be responsible for metallicity at the interface. On the other hand, an extra hole is required to avoid the divergent potential for a p-type interface. However, there are no energetically favorable electronic states to host the extra hole and the compensation occurs through the creation of oxygen vacancies at the interface, yielding to an atomic interface reconstruction [179].

In non-oxide semiconductors, the relaxation of polar discontinuity in heterointerfaces is usually achieved by an atomic reconstruction process, where the interface stoichiometry is altered by interdiffusion, point defect, and dislocation and in general by a structural roughening. In oxides, the possibility of multiple valence ions allows also an electronic reconstruction that, in the LAO/STO case, should move electrons from the surface to the empty Ti d-

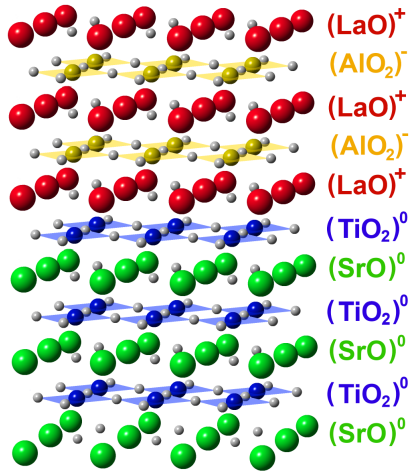

Figure 3.5: *Crystal structure of $LaAlO_3/SrTiO_3$ n-type heterostructure (with $(LaO)^+/(TiO_2)^0$ interface) showing the ionic charge for each layer.*

levels, leading to $3d^1$ electronic states. The signature of this charge transfer is the density distribution of the Ti^{3+} states, recently evidenced by soft x-ray photoemission with photon energy tuned at the Ti 2p-3d threshold [180, 181]. In addition, an indication of Ti^{3+} states was also provided by core-level x-ray photoelectron spectroscopy (XPS) [181,182] and hard x-ray photoelectron spectroscopy (HAXPES) experiments [183,184]. Earlier investigation did not report any Ti^{3+} feature either in Ti 2p core level photoemission [185] or in Ti 3d states by resonant photoemission measurements [186].

The n-type interface is known to become conducting for a LAO thickness above 4 u.c. The thickness dependence of conductivity could be explained by a band-bending effect [187] induced by polarity discontinuity: the density of states (DOS) of the LAO valence band (VB) should be shifted to higher binding energies (BE) until, for a capping equal to or greater than 4 u.c., the LAO VB maximum (VBM) is superimposed to the empty levels of STO. The conduction should now be triggered by a tunneling effect from the surface to the interface electronic states. However, only core-level shifts much smaller than those predicted by the polar catastrophe have so far been observed [182, 184, 188, 189],

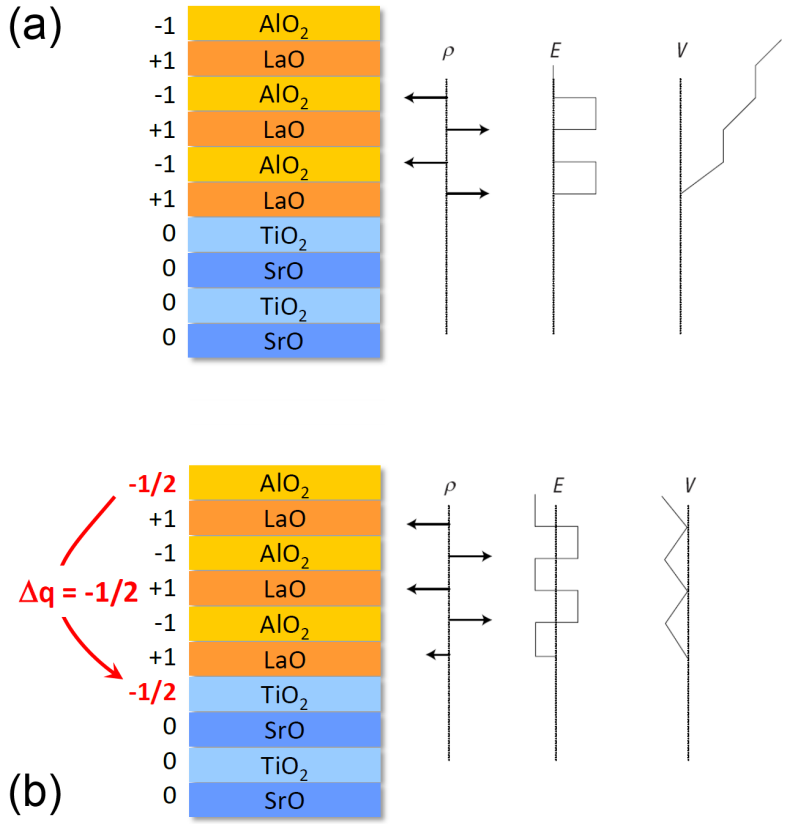

Figure 3.6: *In STO the (001) planes have neutral charge whereas in LAO have an alternating net charge (ρ). If the interface is n-type (LaO/TiO_2), this produces a non-negative electric field (E), leading in turn to an electric potential (V) that diverges with thickness, called polar catastrophe (a). This situation can be avoided if 0.5 e^- per u.c. is added to the first Ti layer at the interface (b). The interface dipole produced makes the electric field oscillate around zero limiting the potential to be finite. Adapted from Ref. [179].*

although a shift of 3.2 eV, which is needed to span the electronic gap in STO, should be easily observed. In principle, however, both atomic and electronic reconstructions could be present in the LAO/STO case. For example, there are different experimental proofs of interdiffusion [185, 190, 191] (with La ions drifting inside STO, a form of atomic reconstruction), but this mechanism alone cannot be solely responsible of the conductivity.

Finally, the sample growth conditions deeply affect the transport properties; an oxygen-poor growth atmosphere can induce oxygen vacancies and thus a 3D conductivity [133, 192, 193, 215] while an excessively rich one can even result in a 3D growth and thus in a different kind of heterostructure [131]. Depending on the O_2 partial pressure during growth, three phases are usually identified [133,194]: one dominated by oxygen vacancies contribution ($P_{O_2} \sim 10^{-6}$ $mbar$), one displaying superconductivity (10^{-5} $mbar$), and one displaying a magnetic behavior (10^{-3} $mbar$). It is quite a challenging task to find a unified description of all these phenomena.

3.2 Materials and Methods

We have investigated three different LAO/STO heterostructures which were grown by pulsed laser deposition (PLD) on TiO_2-terminated STO single crystals at the MESA+ Institute for Nanotechnology, University of Twente: two n-type 3 u.c. and 5 u.c. LAO/STO samples were grown in a $P_{O_2} \sim 10^{-3}$ $mbar$ oxygen partial pressure while an insulating n-type 5 u.c. LAO/STO sample was grown at 10^{-1} $mbar$ O_2 partial pressure. The 3 u.c. sample and the insulating 5 u.c. sample showed a sheet resistance above 1 $G\Omega/\square$, while the conducting 5 u.c. sample exhibited a sheet resistance of 5.5 $k\Omega/\square$ at 300 K. For a 5 u.c. grown under the same conditions, the carrier density and the mobility dependence on temperature are reported in Figure 3.7. For a temperature above 200 K, the carrier density increases up to $1.7 \cdot 10^{14}$ cm^{-2} while the mobility shows an opposite behavior approaching the zero value. According the the systematic study reported in Ref. [222], the P_{O_2} during the growth should rule out the presence of oxygen vacancies in both the 5 u.c. conductive and the 3 u.c. insulating samples. In addition, two reference single crystal LAO and STO samples (MaTeck GmbH) terminated with the (001) surface have also been considered as reference samples.

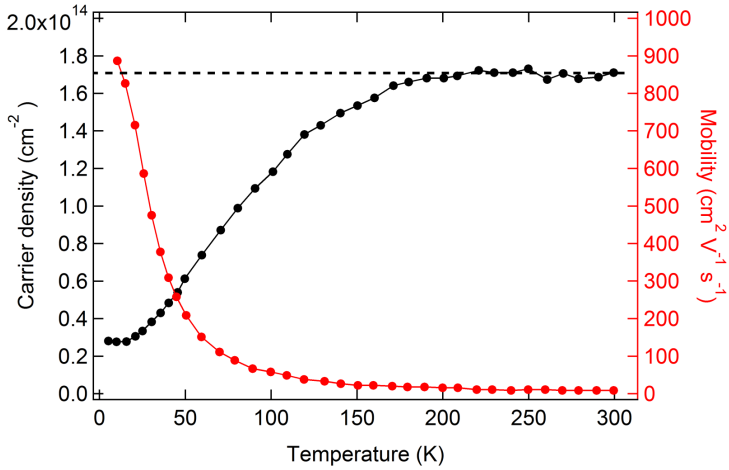

Figure 3.7: *Transport measurements on a LAO/STO 5 u.c. conductive sample. The carrier density (black dots) is referred to the left axis while the mobility (red dots) is related to the right axis.*

3.2.1 Experimental details

The LAO/STO data discussed in this thesis have been collected at three different laboratories:

- Surface Science and Spectroscopy Laboratory of the Università Cattolica (Brescia, Italy). The experimental setup is composed by a non monochromatized dual-anode PsP x-ray source; the Mg K_α line ($h\nu = 1253.6\ eV$) has been used to achieve a better resolution ($\sim 0.7\ eV$), while the Al k_α line ($h\nu = 1486.6\ eV$) has been used when the maximum probing depth was needed. The analyzer for XPS was a SCIENTA R3000, operating in the transmission or angular mode. Data which were obtained here are presented in paragraph 3.3 , 3.4, 3.5.1, 3.5.3 and chapter 4.

- BACH beamline of the Elettra synchrotron light source in Trieste (Italy). Here the resonant photoemission and x-ray absorption experiments have been carried out on solely the 5 u.c. conductive and the 3 u.c. insulating LAO/STO samples. All data have been collected at room temperature with a Scienta R3000 electron spectrometer. The samples have been

grounded by contacting the pads used for transport measurements and aligned in BE using a reference gold clip in contact with the samples. Data which were obtained here are presented in paragraph 3.5.2 and 3.6.

- NANOSPECTROSCOPY beamline of the Elettra synchrotron light source in Trieste (Italy). Here μ-probe photoemission and photoemission electron microscopy experiments were carried out only on the 5 u.c. conductive sample. Data related to this investigation are presented in paragraph 3.7.

3.2.2 Cleaning Method

Generally, clean surfaces exposed to the atmosphere easily adsorb many gaseous organic substances in a short time. For LAO/STO heterostructures it is appropriate to minimize the surface contaminants because they could lead to complications in the treatment of data analysis, especially for the not-linearly damping of the photoemission signal as a function of the acquisition angle (polar angle θ). For oxide materials, however, the surface properties are sensitive to the method used to clean the surface, as demonstrated by annealing treatments [195, 196] or Ar-ion sputtering etching [197, 198] which can introduce oxygen vacancies or defects which can modify the physical properties of the systems under investigation. For these reasons, we resorted to a delicate method to remove the carbon contaminants, based on UV irradiation and ozone exposure [199]. The cleaning mechanism using UV+O_3 consists of a photosensitized oxidation process in which the UV radiation accomplishes a dual work; on one side UV rays are absorbed by the contaminant molecules which undergo dissociation, while on the other side the UV rays are absorbed by the atmospheric oxygen, changing it into ozone and atomic oxygen. Then, the products of the contaminant dissociation react with the atomic oxygen to form CO_2 and H_2O which desorb from the surface.

To carry out the cleaning, we exposed our samples simultaneously under a radiation at 254 nm - generated by a RAYTECH UV lamp - and under a continuous flow of ozone - emitted by an home-made device - in order to improve the atomic oxygen production in the process. For instance, after two consecutive cleaning procedures of about 6 h for each on the LAO/STO 5 u.c. conductive sample, the integrated area of the C 1s core level decreased of about 56% and 85% respectively with respect to the original condition.

3.3 XPS characterization

XPS measurements have been carried out to chemically characterize the samples, measure the core-level electronic structure and evaluate the stoichiometry of the heterostructures. First we have acquired a wide-range spectrum for the bare STO, bare LAO, and the three LAO/STO heterostructures with 5 u.c. conductive, 5 u.c. insulating and 3 u.c. insulating specimens, as displayed in Figure 3.8. All spectra have been converted into binding energy aligning the C 1s peak to 284.8 eV, i.e. the energy generally used for the adventitious hydrocarbon [201].

Afterwards, high resolution XPS measurements were carried out for the main core levels as follows. The Sr 3d , La 4d and Al 2s XPS core levels are shown in Figure 3.9 (a). All spectra are normalized and aligned to the Al 2s peak. As can be observed, for the 5 u.c. conducting and the 3 u.c. insulating samples the La 4d core levels are superposed, with an intensity below that of the LAO reference crystal. In turn, the La 4d XPS core lines of the 5 u.c. insulating sample display the largest intensity. Considering the integrated areas for the two core level peaks normalized by the photoemission cross sections taken from Ref. [24], we have obtained the La/Al stoichiometry ratio of 0.88 ± 0.05 for the 3 u.c. LAO/STO, 0.83 ± 0.05 for the 5 u.c. conductive LAO/STO and 1.42 ± 0.05 for the 5 u.c. insulating LAO/STO (setting equal to 1 the ratio for the bare LAO). These features are qualitatively consistent with the results reported in literature [200] and suggest that the P_{O_2} value has a relevant effect on the cation stoichiometry in the LAO overlayer. This is not unexpected, as the 5 u.c. insulating sample is known to show a 3D growth regime rather than the layer-by-layer regime for the other two heterostructures grown at lower P_{O_2} . It has been observed [200] that among possible defects related to a La excess with respect to Al, the formation of Al vacancies seems to be the most likely scenario. In turn, the low La intensity of the heterostructures grown at low P_{O_2}, as compared to the LAO single crystal, apparently shows a La deficiency that could be related to La diffusion through the interface, La substoichiometry, or both. Furthermore, Warusawithana *et al.* [202] relates the arise of the interfacial conductivity in LAO/STO systems to the *sole* condition that the La/Al ratio is $\leq 0.97 \pm 0.03$, thus in agreement with our data. However, the latter work systematically excludes the possibility that oxygen vacancies stem from (i) the pretreatment of the STO surface, (ii) the

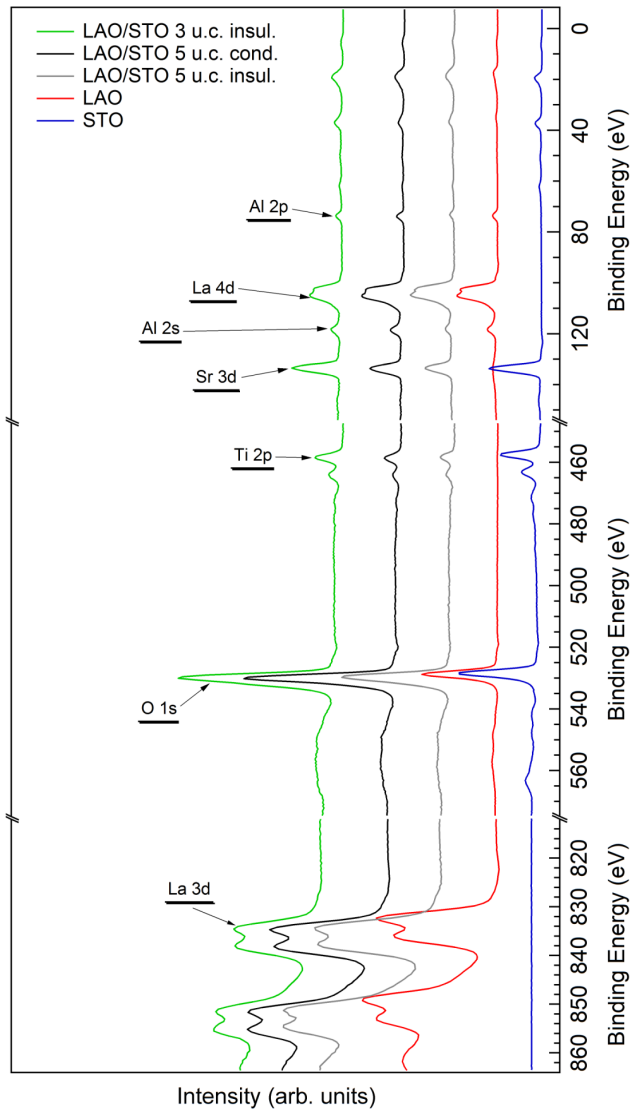

Figure 3.8: *XPS wide range spectra, using Al K_α line, pass energy = 200 eV, for the bare STO and LAO and the three LAO/STO heterostructures: the 5 u.c. conductive, 3 u.c. insulating and 5 u.c. insulating samples. The core levels of main interest are displayed and labeled. The alignment in binding energy was carried out setting the C 1s peak to the 284.8 eV as reference for the adventitious hydrocarbon.*

oxidizing conditions during the growth or (*iii*) the PLD deposition method. In addition, even (*iv*) the cation interdiffusion across the interface is ruled out to have an essential role in the 2DEG activation, thereby making this a hot topic of discussion.

The O 1s spectra from the three heterostructures are shown in Figure 3.9 (b). It is important to note that the three spectra are virtually identical, in spite of the different growth conditions and thicknesses of the LAO overlayer. This assures that in all cases a similar oxygen stoichiometry can be estimated at the surface, ruling out the possibility that changes at the interface could be ascribed to major differences in the oxygen stoichiometry on the surface.

In addition, the Sr 3d core levels of the heterostructures appear to be different from those of STO, as displayed in Figure 3.9(c). As reported in Table 3.1, in spite of the high quality of the STO side of the heterojunction, the Sr peaks are not as sharp as pristine STO. The Sr 3d peak of the conducting 5 u.c. sample (1.24 eV) is larger than that of the corresponding 3 u.c. layer (1.18 eV), both being larger than the peak measured for STO (1.05 eV). The results of the Sr 3d core level fitting with Gaussian line shapes are shown in Figure 3.9 (d-f). A similar behavior can be observed for the Ti 2p core level, displayed in Figure 3.10 (a). For the 5 u.c. conducting sample, the full width at half maximum (FWHM) of the Ti $2p_{3/2}$ peak (1.47 eV) is larger than that of the 5 u.c. (1.41 eV) and the 3 u.c. (1.43 eV) insulating samples. It is important to note that the narrower Ti 2p peak is that of STO (1.36 eV). Therefore, we see an overall decrease of the Ti 2p FWHM from the conducting LAO/STO to the insulating STO single crystal. We exclude broadening effects due to charging, which should be opposite to those observed, and therefore we regard the broadening as due to an intrinsic effect. These trends suggest the presence of either a possible band bending at the junction or a disorder (cationic exchange or oxygen vacancies) around strontium and titanium atoms at the interface, yielding potential fluctuations that ultimately may result in a Sr 3d and Ti 2p peak width broadening. Similar effects have been observed in, e.g., the Ti 2p core lines of Fe-doped rutile single crystals [203].

On the other hand, the Ti 2p XPS core lines of the 3 u.c. and the two 5 u.c. heterointerfaces and the pure STO are almost identical to that expected for a Ti^{4+} ion. However, a small bump is detectable on the low-BE side of the 5 u.c. spectrum, in the position usually associated with Ti^{3+} electronic

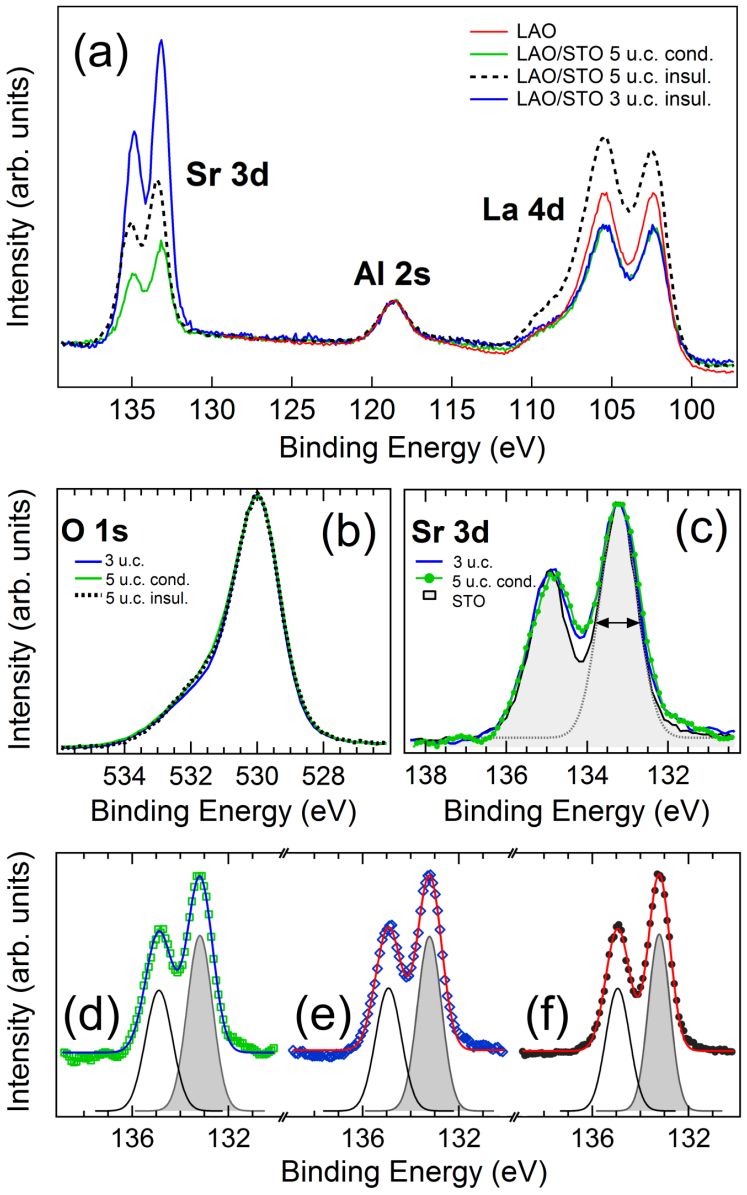

Figure 3.9: *(a) Sr 3d , Al 2s and La 4d XPS spectra collected from LAO and the LAO/STO heterostructures. Spectra have been normalized to the Al 2s peak area. (b) O 1s XPS spectra of the three interfaces and (c) Sr 3d XPS spectra of the STO single crystal and the two LAO/STO grown at low* P_{O_2} *. The bottom panel shows the Sr 3d XPS core-level data fitting of the (d) 5 u.c. conducting, (e) 3 u.c. insulating, and (f) bare STO samples. All spectra are collected using a pass energy of* 50 *eV, by Al* K_α *line for panels (a-b) and Mg* K_α *line for (c-f).*

Sample	P_{O_2} (10^{-3} mbar)	Ti^{3+} / Ti^{4+} XPS ratio	Δ(BE) Ti^{4+} - Ti^{3+} (eV)	Ti 2p FWHM (eV)	Sr 3d FWHM (eV)
5 u.c. cond.	1.0	0.056 ± 0.005	2.03	1.47	1.24
3 u.c. insul.	1.0	0.012 ± 0.005	2.10	1.43	1.18
5 u.c. insul.	100	0.006 ± 0.005	1.78	1.41	–
STO bare	–	0.004 ± 0.005	1.73	1.36	1.05

Table 3.1: *XPS data analysis of Ti 2p and Sr 3d. From the left: Ti^{3+} / Ti^{4+} peak area ratio, energy shift $\Delta(BE)$ between the Ti^{4+} and Ti^{3+} oxidation states and the full width at half maximum (FWHM) for the Ti $2p_{3/2}$ and Sr $3d_{5/2}$ core level peaks.*

states. These states can be detected only through a comparison among different samples and can be easily confused as an additional experimental broadening of the Ti $2p_{3/2}$ peak. For this reason we also show the Ti 2p core line of STO, measured with the same energy resolution (see Figure 3.10 (a)). Considering now the peak area of Ti^{3+} states, which is extrapolated by an accurate fitting procedure of the Ti $2p_{3/2}$ peak as shown in Figure 3.10 (b-e), we can recognize that the conducting compound exhibits a larger contribution than that of the two insulating compounds. The Ti^{3+} /Ti^{4+} ratio sharply decreases from 0.056 (5 u.c.) to 0.012 (3 u.c.) and is nearly negligible for the 5 u.c. insulating sample (0.006) and the STO single crystal (0.004), assuming an uncertainty of ± 0.005 on the peak ratio values. This trend is agreement with other investigations [183, 207] which evidenced an increase of the Ti^{3+} contribution in relation with the number of LAO layers. Furthermore, the Ti^{3+} BE of the samples grown in low P_{O_2} atmosphere is different from that measured for the other samples, the insulating 5 u.c. and the reference STO single crystal. This peak is found about 2 eV below the main line, but this difference is reduced when the 5 u.c. insulating ($1.78\ eV$) and the STO ($1.73\ eV$) samples are considered, suggesting a different origin for these peaks. Indeed, an insulating sample has been reported [181] to show a Ti^{3+} peak closer to the main line with respect to a conducting LAO/STO interface.

The presence of Ti^{3+} states was controversial in early studies on LAO/STO, as not all authors observed these features in spite of the conducting nature of

their samples. As already mentioned, a signature of Ti^{3+} states is the feature appearing on the low-BE side of the Ti $2p_{3/2}$ core line. In addition, this feature should have a counterpart in the valence-band region, detectable either through ResPES at the Ti L edge or through ultraviolet photoemission spectroscopy (UPS) [204]. While Takizawa *et al.* [182] and Yoshimatsu *et al.* [186] discuss the properties of Ti 2p core lines, in Segal *et al.*'s study [188] no mention is made of Ti 2p. Yoshimatsu *et al.* do not report on the Ti^{3+} contribution, but they focus on the BE shift of the Ti $2p_{3/2}$ core line, while Takizawa *et al.* discuss the Ti^{4+} /Ti^{3+} ratio but do not report on the Ti $2p_{3/2}$ BE shift. Furthermore, unlike more recent studies [180, 181], Yoshimatsu *et al.* [186] do not find any evidence of $3d^1$ states in ResPES experiments at the Ti L-edge resonance. For the present samples, evidence of Ti 3d states in the gap are provided in following sections and published on Ref. [29].

Finally, from the Ti^{3+} /Ti^{4+} intensity ratio reported in Table 3.1, an estimation of the sheet charge density (SCD) can also be provided once the Ti^{3+} ion distribution in the layers below the interface is defined. The latter can be obtained by properly considering the attenuation of the Ti signal due to the LAO overlayer, on the basis of the theoretical concepts described in paragraph 1.6. For example, the same ratio can be produced either by a high density of ions close to the interface or by a low density of ions distributed across a larger layer below the interface - as displayed in Figure 3.11 (c-f) - provided that the Ti^{3+} /Ti^{4+} intensity ratio matches the experimental value. Then, the height of the histogram bars in Figure 3.11 (a) for the 5 u.c. conductive represent the Ti^{3+} fraction predicted for a uniform distribution of Ti^{3+} atoms in a layer below the interface as thick as the width of the histogram bar. The thickness of this layer is assumed to be a multiple of the STO unit cell parameter. The corresponding SCD is evaluated for each histogram bar and is shown as a thick red-line related to the right axis. Assuming that all the Ti^{3+} ions are located in the first unit cell below the interface, the resulting SCD is $1.5 \cdot 10^{14}$ cm^{-2}. The wider are the layers of constant density of Ti^{3+} ions, the lower is the density, up to reach the boundary case in which all the atomic layers in the bulk STO present the lowest density as possible for the Ti^{3+} /Ti^{4+} XPS peak area ratio detected, i.e. a fraction of Ti^{3+} ions exactly equal to the Ti^{3+} /Ti^{4+} ratio. The estimated SCD value for the 5 u.c. conducting sample can be compared to the transport measurements carried out on a 5 u.c sample grown under the same conditions

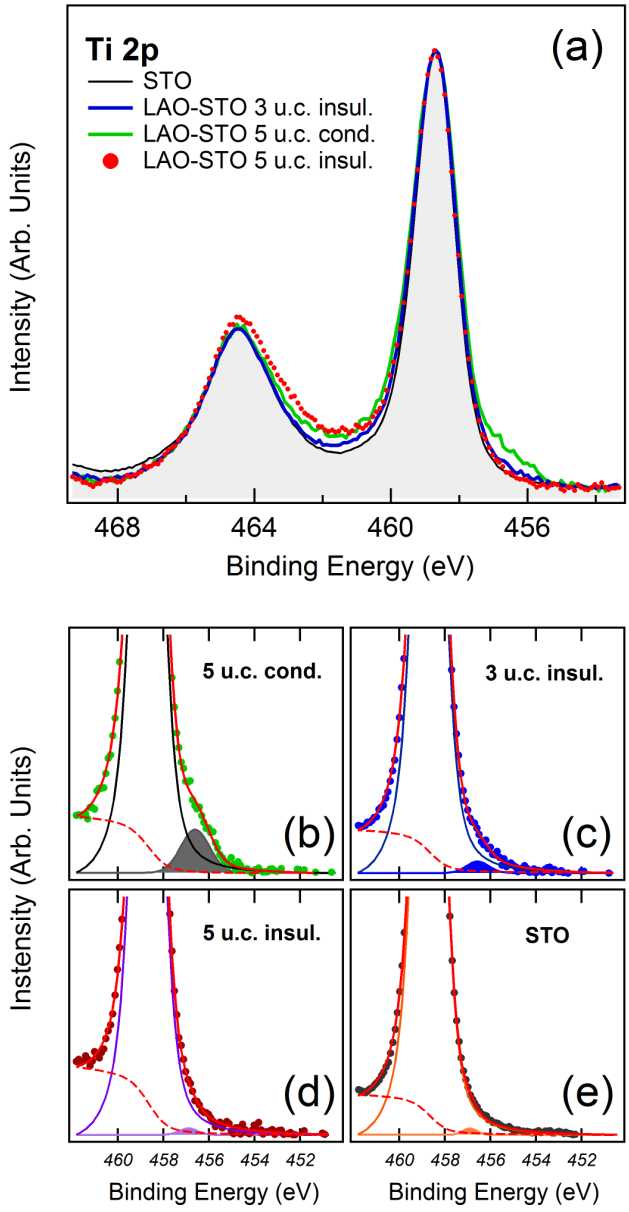

Figure 3.10: *(a) Ti 2p core level spectra collected from the LAO/STO 5 u.c. conductive (thin line), 5 u.c. insulating (dots), 3 u.c. insulating (thick line) and the bare STO (shaded area). Bottom panels (b-e): fitting (thin lines) of the Ti $2p_{3/2}$ core level (dots) with two peaks, accounting for the Ti^{4+} and Ti^{3+} (shaded areas) contributions, and an integral (Shirley type, dashed line) background. All spectra are collected at 50 eV of pass energy by using Al K_α line as x-ray source.*

presented in Figure 3.7. As can be observed, at room temperature the carrier density reaches an asymptotic value of $1.7 \cdot 10^{14}$ cm^{-2} which is displayed in Figure 3.11 (a) as a dashed horizontal line. The intersection between the transport measurements data (black dashed) and the SCD estimation (red solid line) based on XPS data occurs when the SCD is spread down to 2 u.c. below the interface. Therefore, the combination of transport and XPS data analysis provides here a lower limit for the extent of the SCD below the interface. In this way, the present results are in good agreement with those reported by Sing *et al.* on the basis of HAXPES experiments [183].

Differently, a much lower estimation of the sheet charge density is drawn for the insulating 3 u.c. sample, as shown in Figure 3.11 (b). In this case, the lowest limit for the SCD is $3.7 \cdot 10^{13}$ cm^{-2}. In fact, this unexpected non-zero density in the insulating sample seems to point out that only a fraction (about 75%, from the comparison with the 5 u.c. conductive sample) of the Ti^{3+} states detected by XPS can contribute to the conductivity. One explanation for this can be found in Ref. [205], where a distinction between two kinds of charge carriers is provided: low-density, high-mobility carriers for the transport measurements and high-density, low-mobility carriers from optical measurements. Another discrimination about the type of carriers has been proposed starting from density functional calculations [208] between electrons which are localized at the interface and do not participate in the conduction and other delocalized electrons which instead contribute to transport. In addition, a further interpretation takes into account the photogeneration of carriers under UV-ambient light irradiation, which has been observed for both the bare STO [206] - where the effect is ascribed to bulk structural defects, such as Ti, O and Ti-O vacancies - and LAO/STO samples [209, 210] - in which the photoconductivity seems to be due to the bulk compound, because it is independent of the LAO thickness and is activated only when the light energy corresponds to the STO band gap. In any case, the formation of photoinduced charge carriers either by x-ray or ambient light irradiation should be considered, although this issue appears to be far from being assessed [184]. Therefore, in our opinion the presence of Ti^{3+} contribution in the insulating 3 u.c. sample can be regarded as either a localization of a remarkable amount of electrons, which are somehow related to the charge transfer due to the polarity discontinuity but do not take part in the transport until they reach a percolation threshold, or a consequence of

external factors not able however to drive alone the build-up of the 2DEG at the junction.

3.4 Band offset analysis

In this paragraph our attention will be focused on the band offset analysis for the three heterostructures in comparison with their parent compounds - i.e. the bare LAO and STO single crystals. In order to avoid inaccuracies about the energy alignment of core levels, we consider the single wide-range XPS spectra of Figure 3.8 to measure the BE position of different core lines from the bare LAO single crystal (La 4d , Al 2s and Al 2p) and two core lines of the bare STO parent compound (Sr 3d and Ti 3p), as well as the BEs of the core level peaks in the three heterostructures. All the samples exhibit a metal contact at each surface corner which is directly connected with the interface. Using the corners, the specimens were fastened to the sample holders by means of metal clips, thereby avoiding the usual resulting charge accumulation on the surface due to the photoemission process for a general insulating sample. Although no flood gun was used, constant BE positions were verified during the x-ray exposure as well as no distortion of the core level shape was evidenced during the measurements. Thus, the evaluations of the valence band offsets ΔE_V are carried out by the equations from (3.2) to (3.7), adapted from Ref. [185]. In this formulation of ΔE_V, a positive (negative) value means that the VBM of STO is at higher (lower) BE than the VBM of LAO at the junction. The energy levels involved in the calculations for both the reference LAO and STO single crystals and the LAO/STO heterostructures are shown in the diagram of Figure 3.12. The resulting ΔE_V are reported in Table 3.2.

Our results appear to be rather puzzling considering both the scattered values obtained for different core lines in the same sample (within 0.51 eV for the 5 u.c. conductive, 0.23 eV for the 3 u.c. insulating and 0.91 eV for the 5 u.c. insulating) and the variable trend of ΔE_V among the three samples for different choices of the core level pair for the band offset valuation which makes it intricate to achieve a rationalization of the junction in relation with the thickness or the conductivity. Nevertheless the average ΔE_V for each sample is within two valence band offset predictions based on ab-initio calculations, i.e. -0.15 eV [211] and -0.90 eV [212]. Secondly, for the same sample we detect substantial

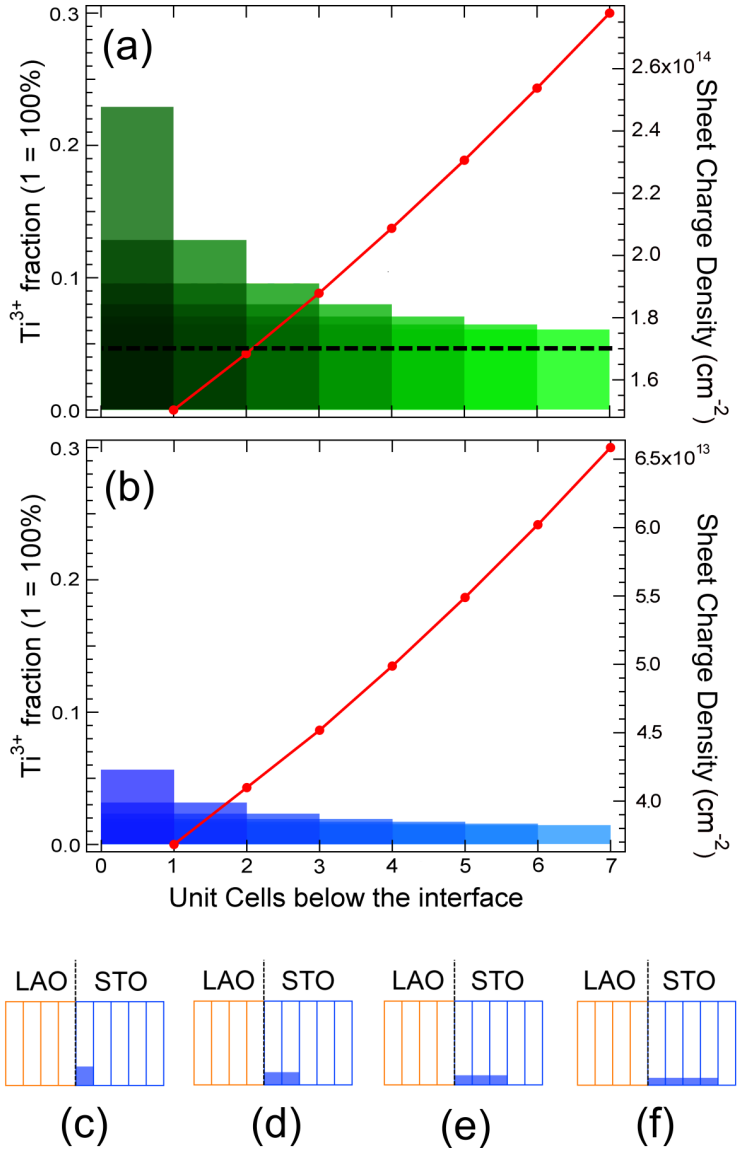

Figure 3.11: *Left axis: distribution of the Ti^{3+} ions as a function of depth below the interface by discrete steps of a unit cell for the (a) LAO/STO 5 u.c. conductive and (b) 3 u.c. insulating. Right axis: sheet carrier density evaluation on the basis of the preceding calculation of the Ti^{3+} ion distribution.*

differences in the ΔE_V on the basis of the selection of the core level peak in the bulk STO. In fact, when Ti is involved as one of the core levels in eq. (3.5), (3.6) and (3.7), larger shifts are usually evidenced with respect to those resulting from eq. (3.2), (3.3) and (3.4). This seems to indicate that in our sample it is possible to observe an element-specific shift.

$$\begin{aligned}\Delta E_V(La4d\text{-}Sr3d) = \Delta E_{La4d-\mathrm{VBM}}(\mathrm{LAO}) - [\Delta E_{Sr3d-\mathrm{VBM}}(\mathrm{STO}) + \\ + \Delta E_{La4d-Sr3d}(\mathrm{LAO/STO})]\end{aligned} \tag{3.2}$$

$$\begin{aligned}\Delta E_V(Al2s\text{-}Sr3d) = \Delta E_{Al2s-\mathrm{VBM}}(\mathrm{LAO}) - [\Delta E_{Sr3d-\mathrm{VBM}}(\mathrm{STO}) + \\ + \Delta E_{Al2s-Sr3d}(\mathrm{LAO/STO})]\end{aligned} \tag{3.3}$$

$$\begin{aligned}\Delta E_V(Al2p\text{-}Sr3d) = \Delta E_{Al2p-\mathrm{VBM}}(\mathrm{LAO}) - [\Delta E_{Sr3d-\mathrm{VBM}}(\mathrm{STO}) + \\ + \Delta E_{Al2p\text{-}Sr3d}(\mathrm{LAO/STO})]\end{aligned} \tag{3.4}$$

$$\begin{aligned}\Delta E_V(La4d\text{-}Ti3p) = \Delta E_{La4d-\mathrm{VBM}}(\mathrm{LAO}) - [\Delta E_{Ti3p-\mathrm{VBM}}(\mathrm{STO}) + \\ + \Delta E_{La4d-Ti3p}(\mathrm{LAO/STO})]\end{aligned} \tag{3.5}$$

$$\begin{aligned}\Delta E_V(Al2s\text{-}Ti3p) = \Delta E_{Al2s-\mathrm{VBM}}(\mathrm{LAO}) - [\Delta E_{Ti3p-\mathrm{VBM}}(\mathrm{STO}) + \\ + \Delta E_{Al2s-Ti3p}(\mathrm{LAO/STO})]\end{aligned} \tag{3.6}$$

$$\begin{aligned}\Delta E_V(Al2p\text{-}Ti3p) = \Delta E_{Al2p-\mathrm{VBM}}(\mathrm{LAO}) - [\Delta E_{Ti3p-\mathrm{VBM}}(\mathrm{STO}) + \\ + \Delta E_{Al2p-Ti3p}(\mathrm{LAO/STO})]\end{aligned} \tag{3.7}$$

The present results have been compared to the reported in several studies, which are focused on the band offset and the core shift analysis. For example, Takizawa *et al.* [182] have focused on the band lineup of p-type and n-type interfaces, both with 1, 3, 4, 5, and 6 LAO u.c. overlayers, grown by PLD in a $1 \cdot 10^{-5}$ $Torr$ oxygen partial pressure. They show that core levels belonging to the same layer of the heterostructure (i.e., La and Al for LAO and Ti and Sr for STO) do not show appreciable shifts (less than 100 meV). In turn, an energy shift is observed for the Al 2p - Sr 3d BE difference which increases with

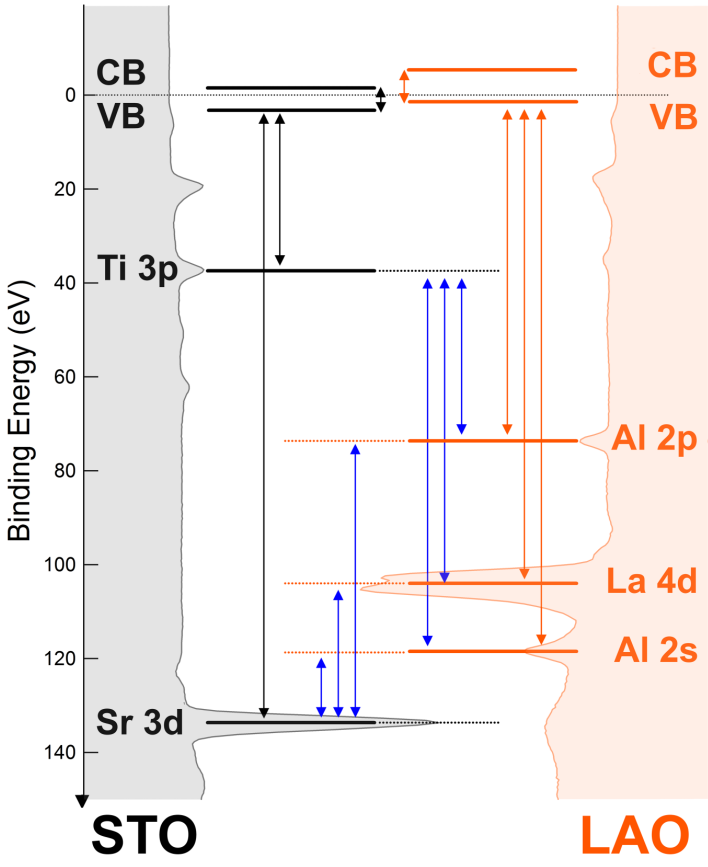

Figure 3.12: *Schematic of energy levels involved in the band-offset analysis. The STO core levels are reported on the left side, while the LAO core levels can be found on the right side. The shaded areas show the XPS data collected from the STO and LAO bulk crystals.*

ΔE_V	**5 u.c. cond.**	**3 u.c. insul.**	**5 u.c. insul.**
$La4d_{5/2}$ - Sr3d	-0.46	-0.56	-0.34
Al2s - Sr3d	-0.54	-0.61	-0.27
Al2p - Sr3d	-0.52	-0.57	-0.10
$La4d_{5/2}$ - Ti3p	-0.89	-0.74	-1.01
Al2s - Ti3p	-0.97	-0.79	-0.94
Al2p - Ti3p	-0.94	-0.75	-0.77
Core Average	-0.72 ± 0.24	-0.67 ± 0.10	-0.57 ± 0.38

Table 3.2: *Valence band offset results calculated according to eq. (3.2)-(3.7). For each sample, the average band offset is estimated from the six values extracted through eq. (3.2)-(3.7). All energies are in eV.*

the number of LAO u.c. for both p- and n-type samples. However, a different result is obtained by Segal *et al.* [188] who consider p-type and n-type interfaces from 2 to 9 LAO u.c. grown by molecular beam epitaxy (MBE) in $3 \cdot 10^{-7}$ $Torr$ oxygen partial pressure. They also evidence a variation of the Sr 3d - La 4d BE difference with the number of LAO layers but with opposite directions for p-type and n-type samples; in facts, the latter BE difference increases for p-type samples whereas it decreases for n-type samples. In addition, the band offset between the LAO and STO compounds is assessed of -0.35 ± 0.18 eV for the 2 u.c. n-type interface by using the La $4d_{5/2}$ and Sr $3d_{5/2}$ core level BE positions, similarly to what carried out in this paragraph. A further hint can be provided by Yoshimatsu *et al.* [186] who investigate the Ti 2p BE shift for both p-type and n-type samples from 0 to 6 LAO u.c. grown by laser MBE at $1 \cdot 10^{-5}$ $Torr$ of oxygen partial pressure. In this case, the Ti 2p BE for the p-type samples is found to be constant, while for the n-type samples the BE decreases with LAO thickness, evaluating a band bending of the STO at the junction equal to -0.25 ± 0.07 eV.

Unlike the papers mentioned so far, Chambers *et al.* [185] did not consider the p-type and n-type set of samples but focused on two 4 u.c. n-type samples grown at rather similar O_2 pressures ($1 \cdot 10^{-5}$ and $8 \cdot 10^{-6}$ $Torr$). Here, the valence band offset is estimated using a set of BE differences, namely, Sr 3d - La 4d, Sr 3d - Al 2p, Ti 2p - La 4d, and Ti 2p - Al 2p. Irrespective of the couple

of atoms selected, similar ΔE_V values are detected in the same sample (at most within 0.16 eV) and an increase of ΔE_V is observed in relation with the surface cleaning, from an average value of -0.06 eV to $+0.34$ eV. Moreover, three 4 u.c. samples of the four ones under investigation exhibit a positive valence band offset, which means that the VBM of STO at the junction has an higher BE than the VBM of LAO, in contrast with our results. However, it is rather interesting to note that in the samples considered in Ref. [185] the Ti^{3+} contribution is not detected on the low BE of the Ti $2p_{3/2}$ XPS peak, whereas in our samples Ti^{3+} states in Ti 2p core lines are evident (Figure 3.10) and related to the $3d^1$ electron emission in the valence-band region probed by resonant photoemission (ResPES), as can be found in Ref. [180] and in the following paragraph. Furthermore, in contrast with the rather uniformly distributed shifts of Ref. [185], our ΔE_V values exhibit a discrepancy depending on the choice of the cation considered (Ti or Sr) - as shown in Table 3.2. However, this may be ascribed to the localization of the Ti^{3+} states at the interface, which may have much larger effects on the local electronic properties than the widespread charge distribution invoked by Chambers *et al.* to justify the lack of a Ti^{3+} low-BE feature in Ti 2p XPS spectra.

A quite similar investigation was carried out by Qiao *et al.* [213] considering a stoichiometric n-type 3 u.c. LAO/STO interface grown via PLD at $1 \cdot 10^{-2}$ $Torr$ oxygen partial pressure. This sample has evidenced an average band offset ΔE_V of $+0.17 \pm 0.08$ eV, involving the La4d-Sr3d, La4d-Ti2p, Al2p-Sr3d and Al2p-Ti2p pairs in the calculation. Once more the resulting ΔE_V is positive, but in this case it is noteworthy that a cation disorder at the junction - i.e. a cation intermixing - has been revealed by an angle-resolved XPS analysis based on the photoelectron attenuation length concept. Here, the comparison with our results is made uncertain because of two additional discrepancies, that is the La:Al stoichiometry ratio - in effect our interfaces are all non-stoichiometric, as shown in Figure 3.9 (a) - and the abruptness of our interfaces which will be discussed in details in paragraph 4. In the end of this brief review of results, a slightly different approach is followed by Berner *at al.* [189] who determined the valence band offset ΔE_V through the combination of results which stem from hard and soft x-ray photoelectron spectroscopies. Considering a set of n-type samples of 4, 5, 6 and 12 u.c. of LAO overlayers grown by PLD at $1 \cdot 10^{-4}$ $mbar$ oxygen partial pressure, they determined ΔE_V within -0.28 eV and -0.39 eV

among all the thicknesses by using solely the BE difference between Al2p-Sr3d.

In conclusion, all the experimental outcomes so far presented are summarized in Table 3.3, which provides us a pronounced scattered scenario whence a clear dependence of the valence band offset on the number of LAO layers or the growth conditions is non-trivial to find. Concerning our results, several parameters should be taken into account for a proper comparison, such as the growth conditions, the presence of Ti^{3+} states, the La:Al stoichiometry ratio, the abruptness of the junction, the surface contamination and the cleaning methods, the core levels involved in the calculation and the x-ray excitation energy used. Since the actual complexity of the matter is evident, it is fair to exploit an independent method to estimate the valence band offset in these compounds, such as the decomposition of the high-energy resolution VB + shallow core levels spectra for each heterostructures into the individual contributions of the bare LAO and STO single crystals, as presented in the next paragraph.

ΔE_V	2 u.c. (eV)	3 u.c. (eV)	4 u.c. (eV)	5 u.c. (eV)	6 u.c. (eV)	12 u.c. (eV)	Growth Technique	P_{O_2} (mbar)	Ref.
Ave.core	-	−0.67	-	−0.72	-	-	PLD	10^{-3}	here
Ave.core	-	-	-	−0.57	-	-	PLD	10^{-1}	here
La4d-Sr3d	−0.35	-	-	-	-	-	MBE	10^{-7}	[188]
Al2p-Sr3d	-	-	−0.34	−0.37	−0.39	-0.28	PLD	10^{-4}	[189]
Ave.core	-	-	−0.06	-	-	-	PLD	10^{-5}	[185]
Ave.core	-	-	+0.14	-	-	-	PLD	10^{-5}	[185]
Ave.core	-	-	+0.20	-	-	-	PLD	10^{-5}	[185]
Ave.core	-	-	+0.34	-	-	-	PLD	10^{-5}	[185]
Ave.core	-	+0.17	-	-	-	-	PLD	10^{-2}	[213]

Table 3.3: *Comparison of valence band offset ΔE_V results from different works. Only n-type LAO/STO interfaces are considered. The oxygen partial pressures during the growth are approximated and converted into* mbar *units for convenience. Soft x-ray photons are used as excitation energy for all the measurements, except for Ref. [189] in which hard x-rays are used.*

3.4.1 Valence band offset by spectra decomposition

As mentioned in the preceding paragraph, it is known [138, 189, 213] that the valence band offset can be also determined directly by means of the linear combination of the VB spectra of the bare LAO and STO compounds with the aim to match the VB spectra of the heterostructures. Although the physical meaning is the same, in order to avoid confusion hereafter we call the valence band offset assessment obtained by the aforementioned method as VBO, whereas we define the valence band offset evaluation obtained by the analysis of the core level shifts presented in the preceding paragraph as ΔE_V.

In Figure 3.13 (a) the valence-band spectra and the closest shallow core levels are displayed, while in Figure 3.13 (b) an enlargement of the VB region is presented. All spectra were collected with the Mg K_α x-ray source. The shallow core levels are labeled as S_I, S_{II} and S_{III}. The O 2s states mostly contribute to the S_I peak, Sr 4p is an unresolved doublet below the S_{II} peak, and La 5p is split in S_{II} and S_{III} peaks (the spin-orbit energy separation is about 2.4 eV, as detected in, e.g., La_2O_3; Ref. [36]).

Generally, the VBO evaluation is achieved by considering only the VB spectra [189, 213]. Then, starting from the bare LAO and STO spectra displayed in Figure 3.13 (b), the valence bands of the three LAO/STO samples $\mathrm{VB_{LAOSTO}}(E_i)$ have been calculated as a linear combination of the bulk precursor spectra $\mathrm{VB_{Bulk}}(E_i)$, as in the following formula

$$\mathrm{VB_{LAO/STO}} = \alpha + \beta \cdot \sum_i \left[\mathrm{VB_{STO}}(E_i + \gamma) + \delta \cdot \mathrm{VB_{LAO}}(E_i + \epsilon)\right] \tag{3.8}$$

where E_i is the binding energy, α and β are set to match the offset and the intensity scaling for the calculated spectrum, respectively, with respect to the experimental reference, γ and ϵ are varied to independently shift the bare LAO and STO experimental spectra while δ is the scaling factor for the bare LAO with respect to the bare STO. γ, δ and ϵ are the free parameters. To find the best linear combination we have used the χ^2 parameter as the formula reported in Ref. [213]

$$\chi^2 = \sum_i \frac{\left[\mathrm{VB_{EXP}}(E_i) - \mathrm{VB_{LAO/STO}}(E_i)\right]^2}{\mathrm{VB_{EXP}}(E_i)} \tag{3.9}$$

where $\mathrm{VB_{EXP}}(E_i)$ is the experimental spectrum related to a LAO/STO heterostructure. The results of this procedure are shown in Figure 3.14 for the

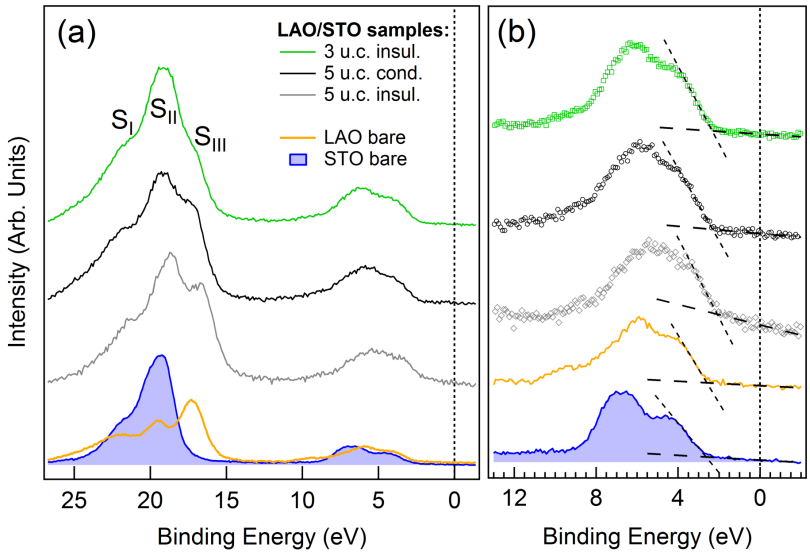

Figure 3.13: *(a) Valence band and shallow core levels for the bare STO and LAO parent compounds and the three LAO/STO heterostructures. (b) Enlargements for the valence band region. All spectra are collected with Mg K_α line (1253.6 eV).*

LAO/STO 3 u.c. insulating, Figure 3.15 for the 5 u.c. conductive and Figure 3.16 for the 5 u.c. insulating, as well as are reported in Table 3.4. We have obtained three VBO values quite different from those (ΔE_V) estimated by the shift analysis of the previous paragraph. However, the present results are affected by a significant indeterminacy. This is proved by the shape of the χ^2 curves as a function of the VBO (in Figure 3.14 (b), 3.15 (b) and 3.16 (b)), which do not exhibit a clear single minimum, meaning that a wide range of VBO values can reproduce the features of the reference spectrum by means of the linear combination of the parent compound spectra. This case is clear especially for the 5 u.c. samples where the relative intensity of the LAO compound than the STO is lower with respect to the 3 u.c. case.

To overcome this experimental deficiency, we have carried out the same analysis but considering this time a larger energy range for the XPS spectra, including both the valence band and the shallow core levels in the calculations.

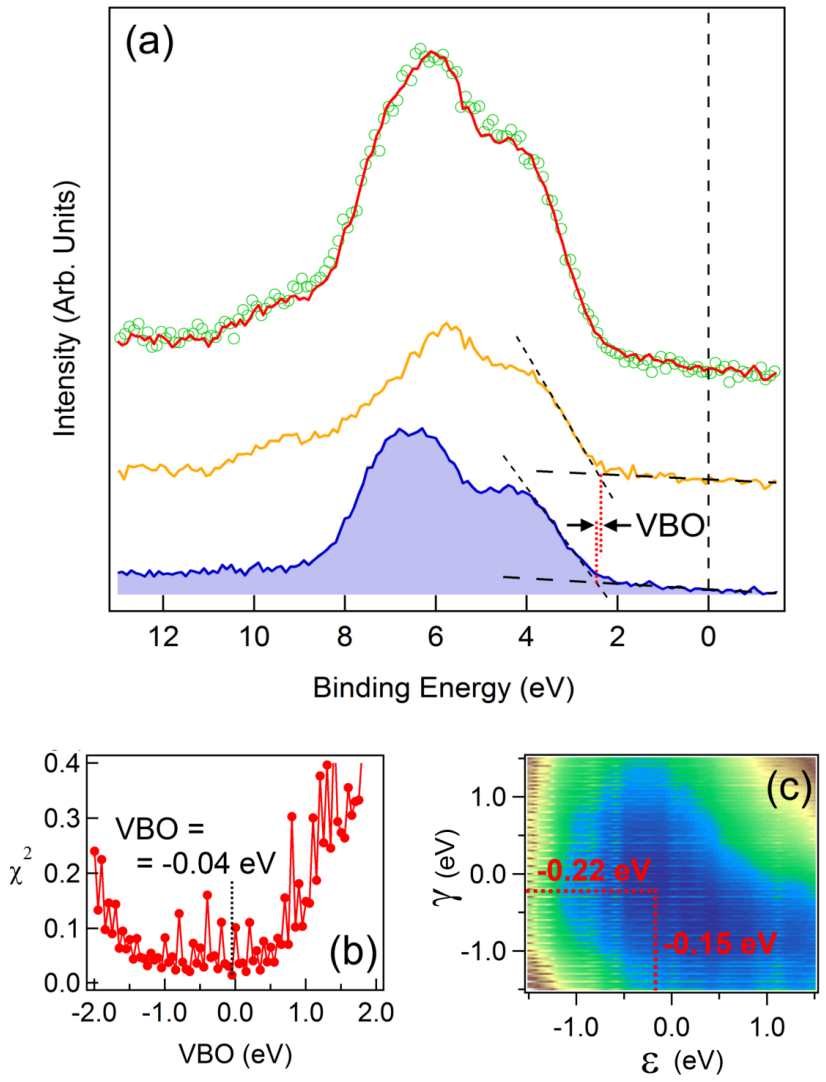

Figure 3.14: *LAO/STO 3 u.c. insulating: (a) XPS for the VB and the resulting calculated spectrum from the linear combination of the bare LAO and STO. VBO is indicated between the VBM extrapolation of the bare LAO and STO spectra. (b) χ^2 parameter as a function of the VBO. (c) χ^2 as a function of γ and ϵ - respectively, STO and LAO shift parameters as in formula (3.8). Red dotted lines point out the minimum of χ^2.*

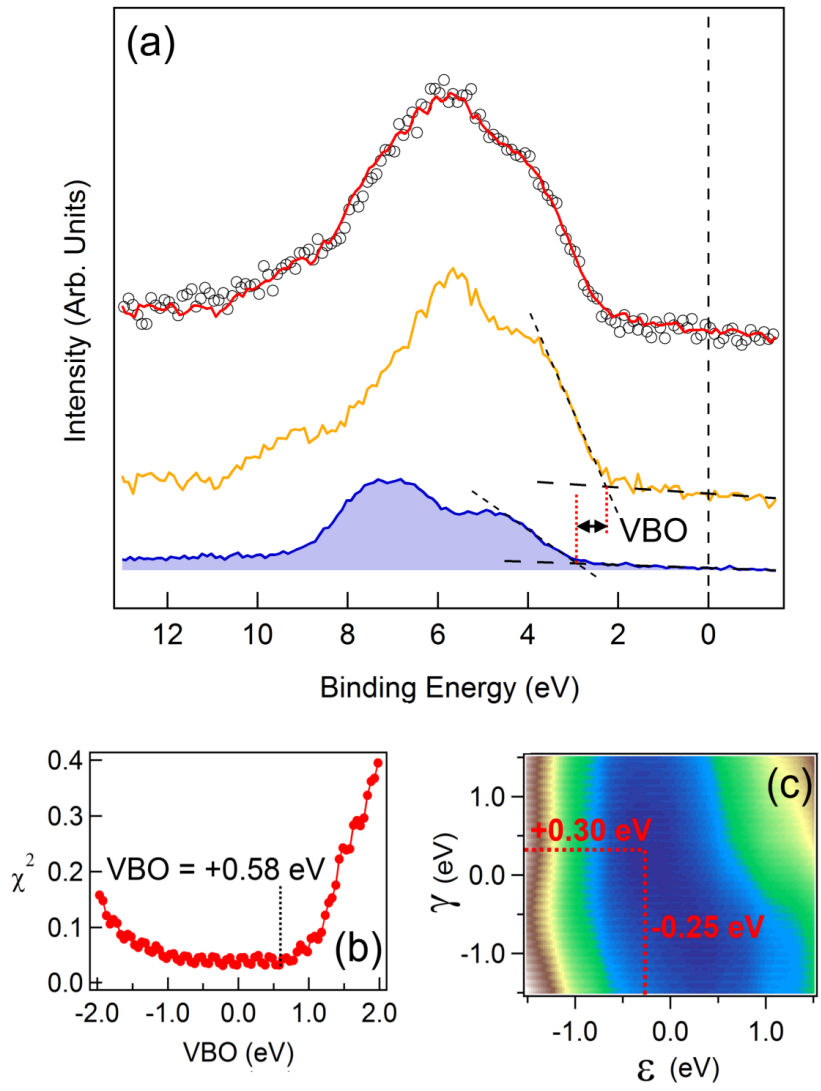

Figure 3.15: *LAO/STO 5 u.c. conductive:(a) XPS for the VB and the resulting calculated spectrum from the linear combination of the bare LAO and STO. VBO is indicated between the VBM extrapolation of the bare LAO and STO spectra. (b) χ^2 parameter as a function of the VBO. (c) χ^2 as a function of γ and ϵ - respectively, STO and LAO shift parameters as in formula (3.8). Red dotted lines point out the minimum of χ^2.*

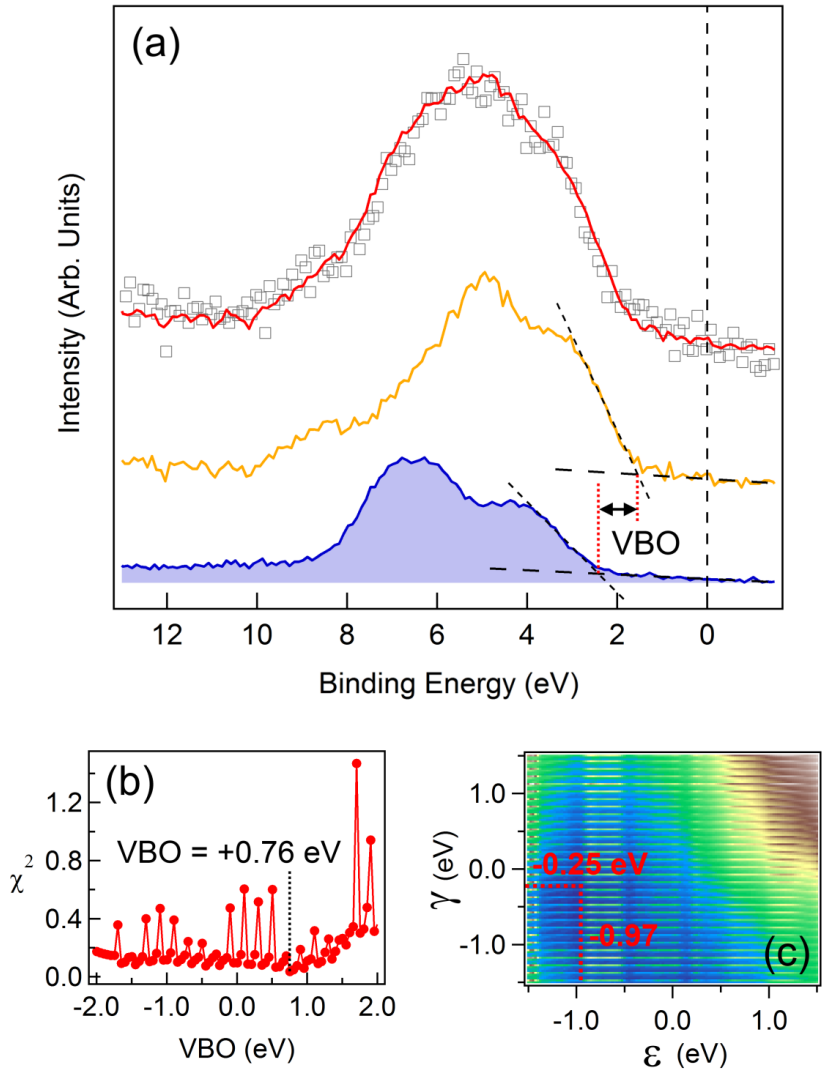

Figure 3.16: *LAO/STO 5 u.c. insulating: (a) XPS for the VB and the resulting calculated spectrum from the linear combination of the bare LAO and STO. VBO is indicated between the VBM extrapolation of the bare LAO and STO spectra. (b) χ^2 parameter as a function of the VBO. (c) χ^2 as a function of γ and ϵ - respectively, STO and LAO shift parameters as in formula (3.8). Red dotted lines point out the minimum of χ^2.*

Methods	5 u.c. cond.	3 u.c. insul.	5 u.c. insul.
Ave. ΔE_V	-0.72 ± 0.24	-0.67 ± 0.10	-0.57 ± 0.38
VBO_{VB}	-0.04	$+0.58$	$+0.76$
VBO_{VB+SCL}	-0.20	-0.10	-0.11

Table 3.4: *Valence band offsets for the LAO/STO interfaces. ΔE_V from the average analysis presented in paragraph 3.4 using the eq. (3.2)-(3.7); VBO_{VB} from the linear combination of the valence band spectra of LAO and STO; and VBO_{VB+SCL} from the linear combination of the spectra of LAO and STO including the valence band and the shallow core levels. All energies are in eV.*

In this way, the shape of the reference spectra for the three heterostructures become more structured - as shown in Figures 3.17 (a), 3.18 (a) and 3.19 (a) - and χ^2 as a function of the VBO exhibits more evident minima, as displayed in Figures 3.17 (b), 3.18 (b) and 3.19 (b). An analogous trend appears for the χ^2 in relation to the energy shift of LAO (ϵ) and STO (γ) spectra, as presented in Figures 3.17 (c), 3.18 (c) and 3.19 (c).

At first glance, the calculated spectra from the linear combination may not exhibit a good matching with the experimental references, as indicated in Figure 3.17 (a), 3.18 (a) and 3.19 (a) by means of the black arrows. However, these discrepancies are due to the non stoichiometric La:Al ratio of the LAO/STO interfaces under investigation (as discussed in paragraph 3.3 and evidenced in Figure 3.9 (a)). In facts, a variation in the La:Al stoichiometry ratio leads to change the relative intensities of both the S_{II} and S_{III} peaks (Figure 3.13 (a)) due to the La 5p core level contribution. Nevertheless, the edges of both the whole shallow core levels peak and the valence band shape are well fit, allowing to find exactly what we are looking for, i.e. the band offset.

In addition, as can be observed from Table 3.4, all differences among the VBO_{BV+SCL} results are within 0.09 eV, similarly to the ΔE_V values which are within 0.15 eV. The latter observation seems to validate the agreement between the different methods for the valence band offset estimation, even though in the VBO approach the higher kinetic energies ($\approx 1228-1253.6\ eV$; Mg K_α) involved in the spectra provide us information which come from a greater depth from the surface due to higher IMFP values. Therefore, we will consider the VBO_{VB+SCL} as our final results for the band offset analysis so far discussed.

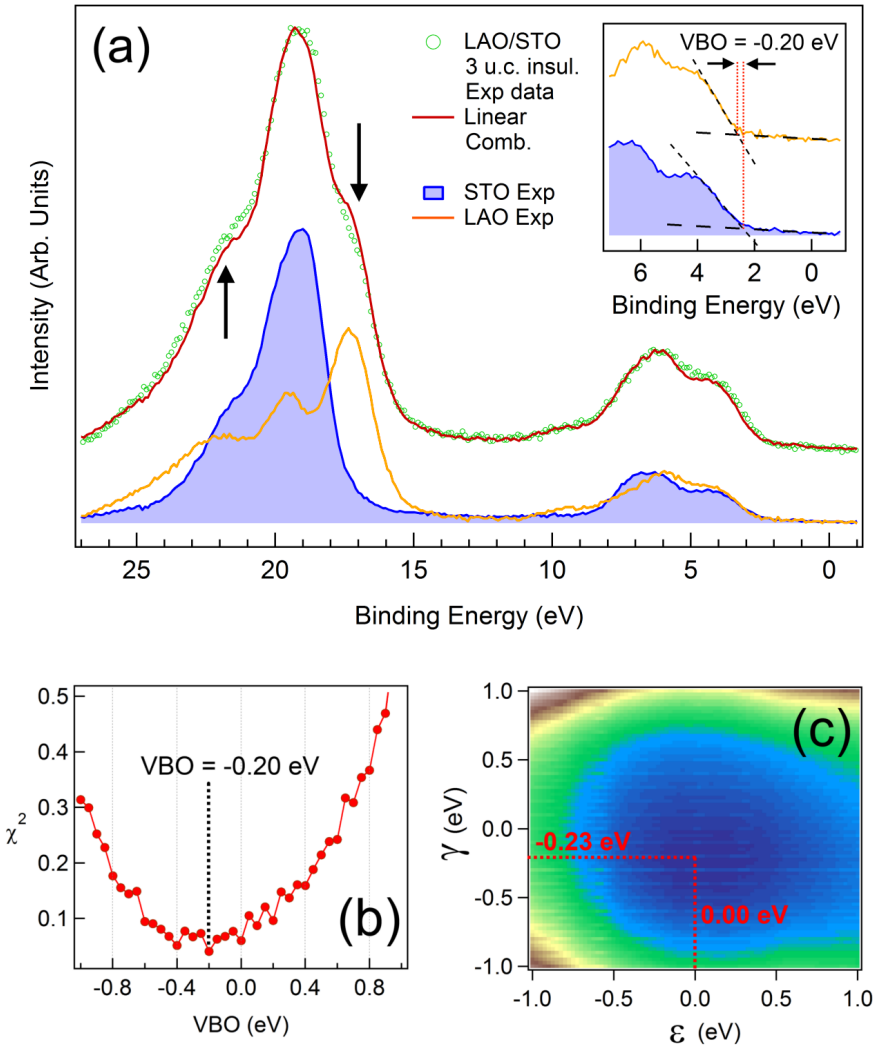

Figure 3.17: *LAO/STO 3 u.c. insulating: (a) XPS for the VB and the shallow core levels and the resulting calculated spectrum from the linear combination of the bare LAO and STO. Inset: enlargement of the VBO estimation. (b) χ^2 parameter as a function of the VBO. (c) χ^2 as a function of γ and ϵ - respectively, STO and LAO shift parameters as in formula (3.8). Red dotted lines point out the minimum of χ^2.*

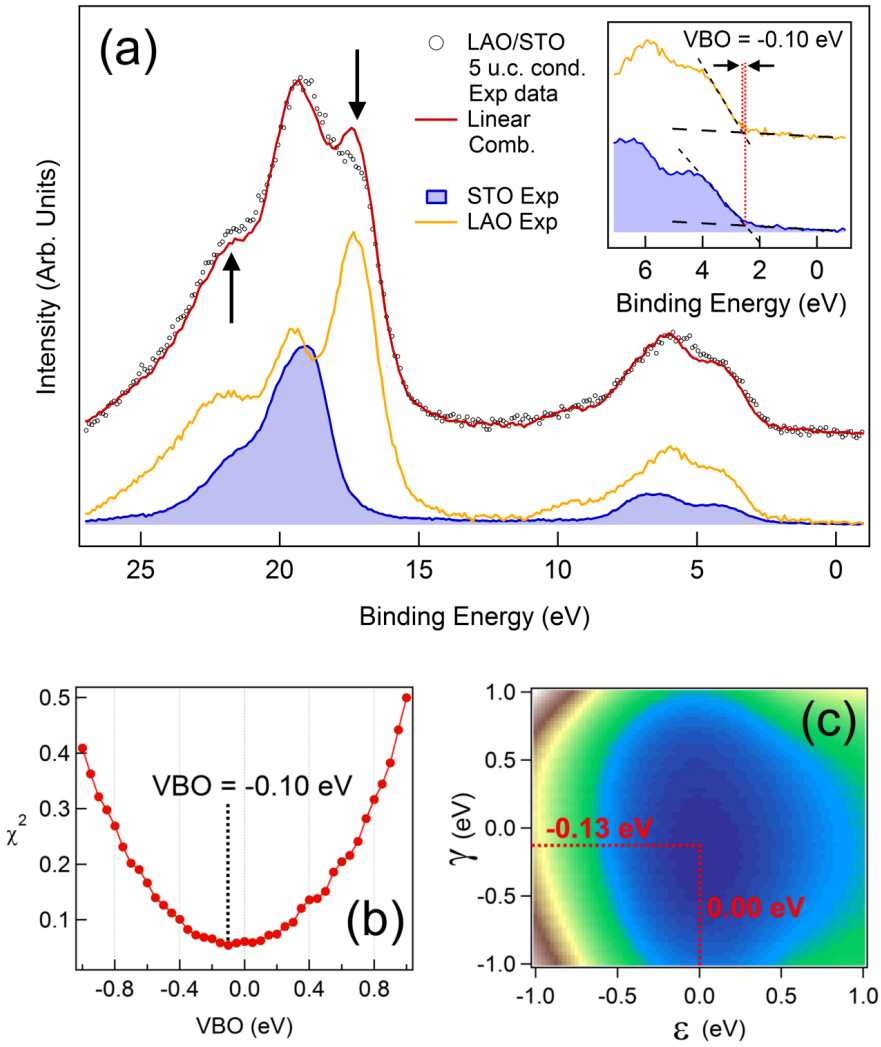

Figure 3.18: *LAO/STO 5 u.c. conductive:(a) XPS for the VB and the shallow core levels and the resulting calculated spectrum from the linear combination of the bare LAO and STO. Inset: enlargement of the VBO estimation. (b) χ^2 parameter as a function of the VBO. (c) χ^2 as a function of γ and ϵ - respectively, STO and LAO shift parameters as in formula (3.8). Red dotted lines point out the minimum of χ^2.*

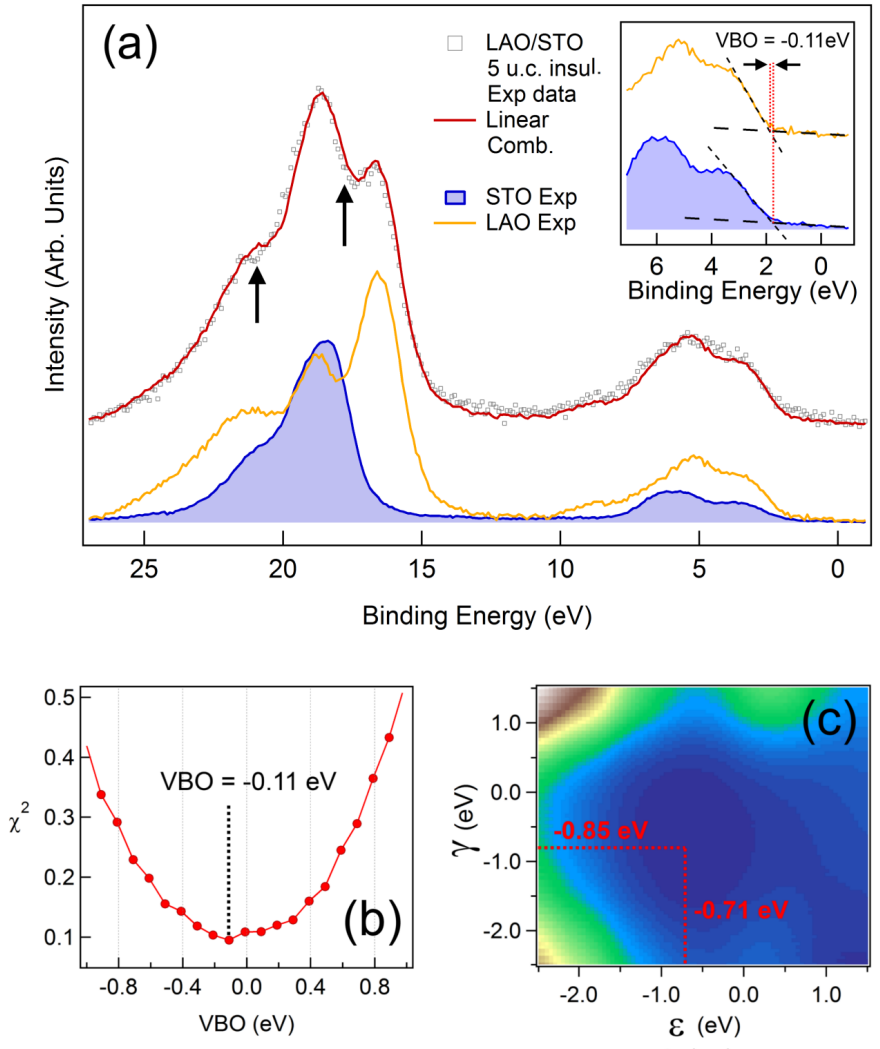

Figure 3.19: *LAO/STO 5 u.c. insulating: (a) XPS for the VB and the shallow core levels and the resulting calculated spectrum from the linear combination of the bare LAO and STO. Inset: enlargement of the VBO estimation. (b) χ^2 parameter as a function of the VBO. (c) χ^2 as a function of γ and ϵ - respectively, STO and LAO shift parameters as in formula (3.8). Red dotted lines point out the minimum of χ^2.*

3.5 Band Profiling

In this paragraph the band diagrams for the 5 u.c. conductive and the 3 u.c. insulating LAO/STO interfaces are reconstructed on the basis of element-specific resonant electronic spectroscopies. By this way, we can provide an unambiguous characterization of the chemical bonds contributing to the density of states in the Fermi level region that can be used to track a profile of the electronic levels across the heterojunction. In fact, exploiting a resonant photoemission experiment at the Ti $L_{2,3}$ and the La $M_{4,5}$ edges, the spectral weight of both Ti 3d and La 4f states in the valence band region can be probed. This allows (*i*) to determine the energy of the valence band maximum on both sides of the junction and (*ii*) to probe the interface states at the Fermi level, which evidence a dominant Ti 3d character and whose origin can be ascribed to several phenomena, such as the generation of oxygen vacancies [192,214,215] and cation intermixing effects [185,190,191] occurring at the interface, which are still under keen debate today. Unlike previous studies based on hard x-ray photoemission [189], that are more sensitive to the bulk of the samples and therefore can probe the electronic properties well below the interface, the present results, obtained with soft x rays, allowed us to probe the extent of band bending of STO at the interface, filling the gap in the experimental tracking of band offsets in the LAO/STO system. Moreover, these results can be combined with the analysis for the bare LAO and STO parent compounds carried out in the previous paragraph by a conventional Al K_α X-ray source, which provides information on the band offset deeper into the bulk than the resonant photoemission. On this basis a scheme of the band diagram at the heterojunction can be drawn. Thus, the band alignment profiling reveals a similar type I (straddling gap) junction for both the 5 u.c. conductive and the 3 u.c. insulating sample, although a large notch in the energy levels at the interface is present only for the conductive sample.

3.5.1 The LAO band: flat or bent?

Before investigating in details the interface, it is necessary to establish the profile of the LAO band. According to the electronic reconstruction scenario, the polar catastrophe can be avoided by a potential gradient in the LAO film, in which the O 2p states are shifted towards the Fermi energy (E_F) with increasing

LAO thickness. At the critical thickness of 4 u.c. these states should cross the E_F and activate an electron transfer to the Ti empty states, leading to the interfacial conductivity. This picture has been confirmed by several DFT studies which predict slightly different values for the O 2p band shift, from approximately 0.4 eV/u.c. [187, 216, 217] to 0.6 eV/u.c. [218]. Even though such a band bending is smaller than the actual one (0.9 eV/u.c.) due to the typical underestimation of band gaps in DFT calculations, it should be easily detectable in XPS both in the shift and the broadening of all the core levels related to the LAO film, because they are affected by the energy change of the valence band maximum. Nevertheless, no experimental evidence has proved this effect so far [182, 184, 188, 189].

A similar conclusion is achieved for our LAO/STO interfaces on the basis of two considerations. First, as shown in Figure 3.20 (a), the shape of the La 4d core level does not change within the set of the LAO single crystal, the 5 u.c. (conductive) and the 3 u.c. (insulating) samples. Secondly, Figure 3.20 (b), (c) and (d) display the comparison between the experimental La 4d peak for the bare LAO (orange dotted lines) and the calculated one for a 5 u.c. LAO/STO interface (red solid lines), considering a band shift of 0.4 eV, 0.6 eV and 0.9 eV per u.c., respectively. In the calculations the relative spectral weight for the different LAO layers is based on Monte Carlo simulations of the DDF of the multilayer structure - by using the BriXias code presented in paragraph 1.6 - while the shape of the La 4d peaks of each layer is that of the bare LAO, taken as reference. The discrepancy between the experimental and the calculated spectra is evident for all the band shift values used.

3.5.2 Resonant photoemission spectroscopy data

So far, only one study based on cross-sectional scanning tunneling microscopy [219] has reported a direct evidence of the potential profile in a LAO/STO heterojunction, grown at 850°C in a $2 \cdot 10^{-5}$ $Torr$ of P_{O_2}. To achieve a similar result by photoemission spectroscopies we have compulsorily to investigate the electronic states close to, or at, the Fermi level in the conducting LAO/STO heterojunctions. These states have been already observed by ultra-violet photoemission spectroscopy by Siemons *et al.* [204], but further investigations were basically hindered by the low intensity of the photoemission process from a

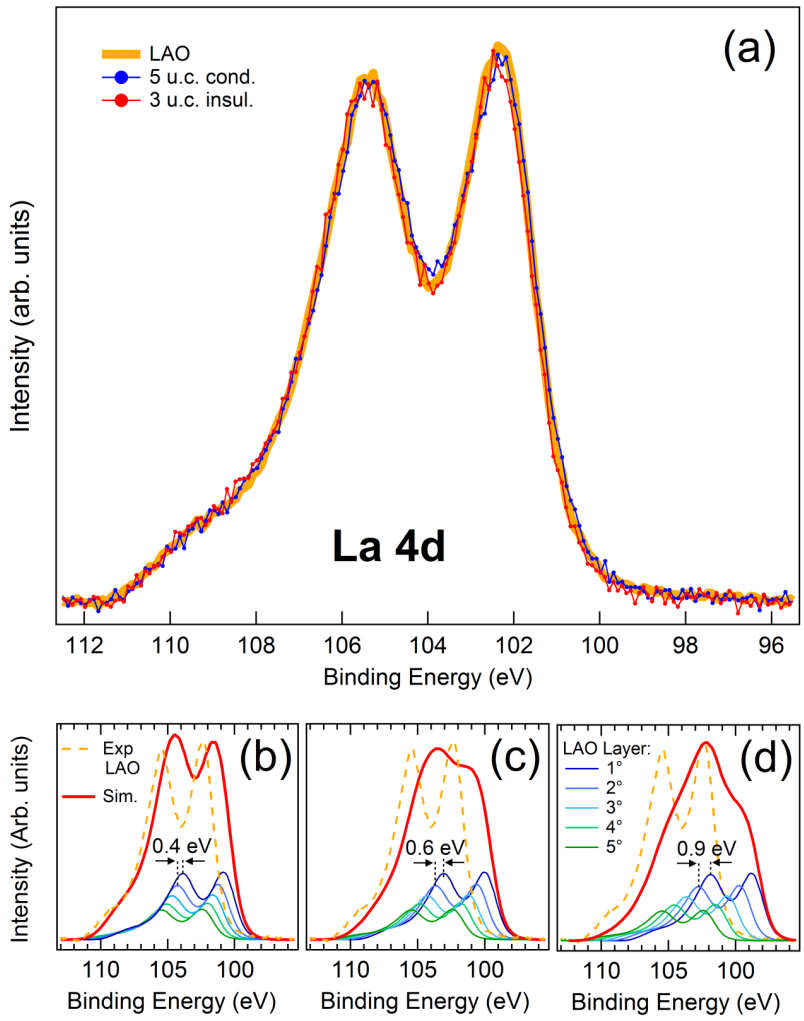

Figure 3.20: *La 4d core level: (a) experimental XPS spectra for the bare LAO single crystal, as well as the LAO/STO 5 u.c. conductive and 3 u.c. insulating sample. The integrated area is normalized for all the spectra. Comparison between the experimental LAO bare (orange dotted) and the 5 u.c. LAO/STO calculated spectrum (red solid line) according to the polar catastrophe model with a band shift of LAO layers of about (b)* 0.4 *eV per unit cell, (c)* 0.6 *eV per unit cell and (d)* 0.9 *eV per unit cell. The contribution from each layer is also displayed.*

buried interface. For this reason, these states have been searched for by resonant photoemission spectroscopy (ResPES) and have been evidenced for the first time by Drera *et al.* [180] in both insulating and conducting samples. As the resonant enhancement was observed at the Ti 2p-3d absorption threshold, the element-specific ResPES technique indicates that the in-gap states have a Ti character and are ascribed to a $3d^1$ configuration of a formally Ti^{3+} ion. Soon after, these states were also evidenced by Koitzsch *et al.* [181] in an attempt to relate their line shape and energy to the oxygen stoichiometry. Recently, Cancellieri *et al.* [220], in contrast with with Refs. [180] and [181], have shown that the $3d^1$ states are absent in insulating systems, while they are clearly detected by ResPES in conducting samples. Finally, in a recent k-resolved ResPES experiment, two distinct features (one in-gap and the other at E_F) have been singled out in a conducting LAO/STO heterojunction [221]. All these results are still providing a rather scattered scenario which seems strongly dependent on details of the STO surface preparation, sample growth, and postgrowth treatment, in spite of common features that would render the samples nominally identical, such as the TiO_2-terminated surface preparation for the STO substrate and the number of LAO unit cells grown above the substrate. Contrasting results also appeared on band alignment profiling based on x-ray photoemission spectra [188, 189, 213], resulting in different junctions (type I or type II).

The present investigation is based on resonant photoemission spectra of only the 5 u.c. conductive and the 3 u.c. insulating sample. The BE alignment has been carried out by referring to a gold clip in contact with the sample. However, the 3 u.c. sample showed a slow charging effect, as compared to the time required for a scan, upon measurement. To obtain a good signal-to-noise ratio, we collected single fast scans of the valence-band region and then we summed up these spectra after alignment to the maximum of the Ti^{4+} resonance at a binding energy BE = 7.5 eV. This spectrum was then aligned to the 5 u.c. sample by referring to the centroid of the resonant emission of Ti^{4+} states in the $6.5 - 9.5$ eV BE range.

Ti $L_{2,3}$ edge

In the resonant photoemission spectroscopy experiments we have collected the valence-band region by changing the photon energy across the Ti $L_{2,3}$ absorption edge, thereby allowing an increase of the titanium-related electronic

states in the valence-band region up to E_F that would be otherwise missed by an off-resonance tuning of the photon energy. In the resonance condition, for a 3d transition metal, the direct photoemission channel ($3d^n \rightarrow 3d^{n-1} + e^-$) can interfere with the autoionization channel triggered by the creation of a core hole ($2p^5 3d^{n+1} \rightarrow 2p^6 3d^{n-1} + e^-$), whereas the autoionization process ultimately turns into the normal Auger emission and the interference effects are lost when the photon energy is increased above the absorption threshold.

Figure 3.21 (a) shows three selected spectra of the valence band region for both the 5 u.c. and the 3 u.c. LAO/STO[1], which are collected on-resonance ($h\nu = 458.2\ eV$) and off-resonance ($h\nu = 450.0\ eV$) for a Ti^{4+} configuration, as well as the spectrum at the photon energy which maximizes the spectral weight for the states which raise at the Fermi energy, hereafter called interface states (IS). For both samples, the overall photoemission intensity in the VB region follows the shape of the XAS spectrum, as shown in detail in Figure 3.21 (c) for selected peaks. In particular, in the $5 - 10\ eV$ BE energy range, resonating features related to bulk STO Ti^{4+} energy levels can be detected, while a careful inspection of the $0.0 - 1.5\ eV$ BE range reveals the presence of the additional interface states. The maximum intensity of the IS, i.e. peak F in Figure 3.21 (a) and (b), is obtained for a photon energy ($h\nu = 459.6\ eV$) different from the energy where the maximum resonance of the main VB Ti^{4+} shape are detected, i.e. peaks D and E, maximum at $h\nu = 458.2\ eV$.

The shallow core levels ($\mathbf{A}_1$, $\mathbf{A}_2$, $\mathbf{A}_3$) do not display resonant enhancement at the Ti L edge, as they are related to photoemission from O 2p, Sr 4p, and La 5p core levels. Peak **B** is the Ti LVV Auger emission, while the shoulder **C** can be ascribed to the VB electronic structure distinctive of $LaAlO_3$, which in fact is more evident in the 5 u.c. sample. Consistently with a previous study on similar samples [180], interface states - shown in details in Figure 3.21 (b) - are detectable also in the 3 u.c. sample, in the same energy region. The difference spectra between the off-resonant ($h\nu = 450.0\ eV$) and the on-resonant for Ti^{3+} ($h\nu = 459.6\ eV$), which are displayed in Figure 3.21 (a) as gray area and dotted red line and hereafter denoted as resonant spectral weight (RSW), provide a direct probe of Ti 3d states of the uppermost STO layers and displays a maximum intensity at BE = $7.5\ eV$ in both samples (peak **G**), while a shift

[1]The complete sets of VB spectra changing the photon energy across the Ti $L_{2,3}$ absorption edge are reported in Ref. [29].

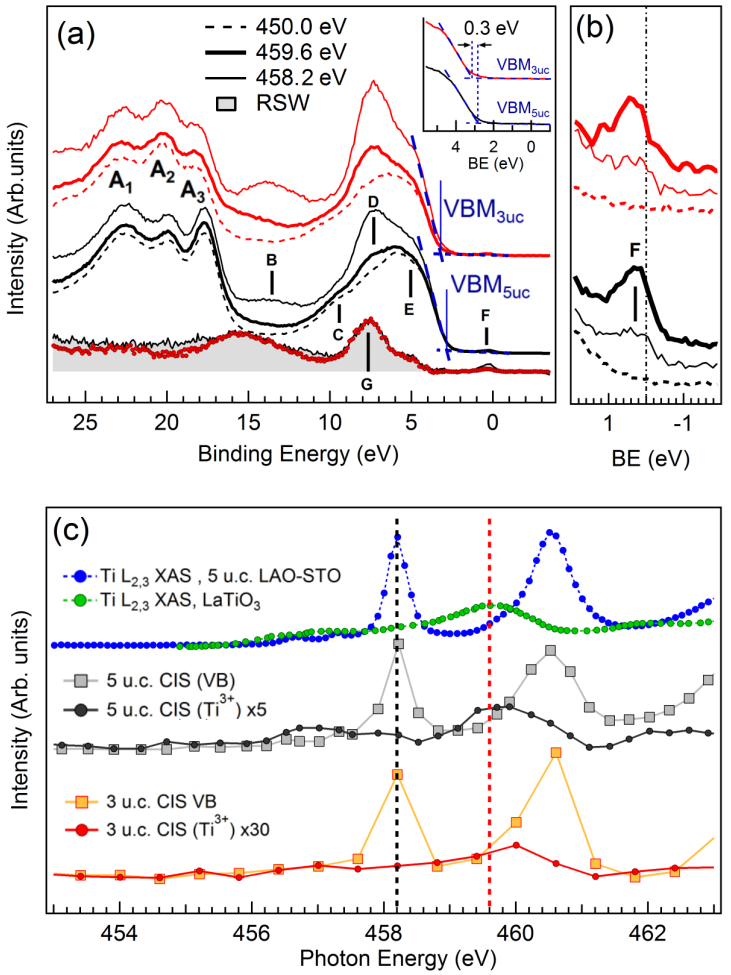

Figure 3.21: *(a) Resonant photoemission spectra of insulating 3 u.c. (upper curves, red lines) and conductive 5 u.c. (lower curves, black lines) LAO/STO heterostructures, measured off-resonance (dashed line, $h\nu = 450$ eV), at Ti^{4+} resonance maximum (thin line, $h\nu = 458.2$ eV), and at the Ti^{3+} resonance maximum (thick line, $h\nu = 459.6$ eV). The blue vertical lines mark the position of valence-band maxima (VBM-3 and VBM-5), which is enlarged in the inset. Normalized resonant spectral weight (RSW) (off-resonance: $h\nu = 450$ eV; Ti^{3+} resonance: $h\nu = 459.6$ eV) of the 5 u.c. sample (shaded gray area) and of the 3 u.c. sample (dotted line). (b) Enlargement of the interface states. Labels as in panel (a). For the two samples, the intensities have been normalized to the maxima of the peaks measured at $h\nu = 459.6$ eV. (C) Constant initial state (CIS) spectra on Ti^{3+} (filled circles, BE $= 1.0 \pm 1.0$ eV) and Ti^{4+} features (filled squares, BE $= 7.5 \pm 1.0$ eV); XAS spectra of the 5 u.c. sample (blue circles) and of a reference $LaTiO_3$ sample (green circles). The vertical dashed lines mark the photon energies (458.2 and 459.6 eV) of the resonant spectra shown in panels (a) and (b).*

of 0.3 eV can be detected between the VB edges, i.e. VBM_{3uc} and VBM_{5uc} in Fig. 2(a), as well as in the La shallow core levels ($\mathbf{A}_2$ and $\mathbf{A}_3$) of the resonant spectra.

The unambiguous proof that Ti^{3+} ($3d^1$) states contribute to the spectral weight in the region below E_F is provided by the constant initial state (CIS) spectra, shown in Figure 3.21 (c), which follow the Ti $L_{2,3}$ XAS[2] (due to bulk Ti^{4+} STO) in the main VB resonances (squares) whereas for the interface states the CIS data (filled circles) closely resemble the XAS profile of $LaTiO_3$ (a bulk Ti^{3+} compound [223]). As a last comment on Figure 3.21 (b), it is noteworthy that peak **F** resonates when the photon energy is tuned not only at one of the Ti^{3+} XAS peaks ($h\nu = 459.6\ eV$), but also at the Ti^{4+} XAS peak ($h\nu = 458.2\ eV$), although to a lower extent. This can be explained by the fact that at 458.2 eV the intensity of the Ti^{3+} XAS profile (Figure 3.21 (c)) is not completely quenched and therefore a weak Ti^{3+} resonance can be expected also at this photon energy.

Although the photoemission spectra of the Ti^{3+} structures seem to be similar in the insulating and the conductive LAO/STO, their intensities are quite different, as shown by the different scaling factor of the CIS spectra in Figure 3.21 (c). By normalizing the RSW spectra at the 7.5 eV peak, as shown in Figure 3.22 (a), the relative ratio of 5 u.c. over 3 u.c. interface states becomes 5:1, in good agreement with the value (0.056 : 0.012) extracted from the Ti 2p core line analysis on the same compounds (see Table 3.1). In addition, the high-resolution spectra on the Ti^{3+} peaks reveal an asymmetric line shape, as displayed in Figure 3.22 (b). Both in the insulating and in the conducting samples, these states cross the Fermi edge, as can be seen by a comparison with the reference spectra collected from the gold film deposited on the sample holder. Then, the Ti^{3+} band of the 3 u.c. sample also displays a smaller width at half-maximum (0.9 eV) with respect to the 5 u.c. case (1.0 eV). This effect recalls the results of the Ti 2p and Sr 3d core levels obtained by XPS and discussed in paragraph 3.3 which could tentatively ascribed to different band bending effects.

Consistently, the RSW of Figure 3.22 (a) represents the Ti 3d spectral weight in the VB region, as well as in the gap of STO. In fact, most of the features of the VB occupied states can be described with DFT calculations of bulk STO.

[2]The XAS spectrum of the 3 u.c. insulating sample is not reported in Figure 3.21 because is indistinguishable from the XAS of the 5 u.c. conductive LAO/STO.

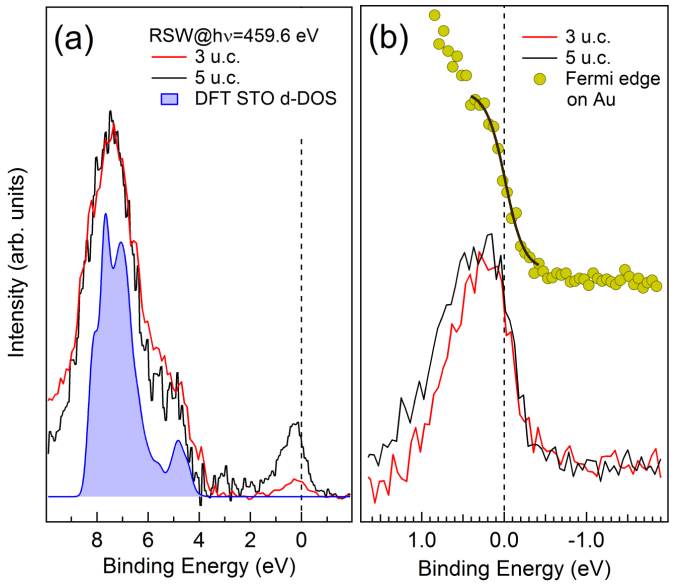

Figure 3.22: *(a) RSW spectra ($h\nu = 459.6 - 450.0\ eV$) for the 3 u.c. insulating and 5 u.c. conductive LAO/STO samples, compared to DFT + U ($U = 8\ eV$) d-projected DOS calculations of a STO bulk crystal taken from [29]. (b) High-resolution interface states spectra. The intensities are normalized to the peak maxima.*

However, the minimum energy separation (about 2.2 eV) between the Ti^{3+} states and the top of the valence band is smaller than the value of the bulk STO band gap (3.2 eV). Therefore the in-gap states should not be related to a simple filling of bulk-like Ti 3d empty states of STO, but to a filling of Ti $3d^1$ states, pinned below E_F by band bending at the interface. Furthermore, if the DOS of the whole heterojunction is considered, plane projected DOS calculations (see, e.g., Ref. [225]), also indicate that about 2 eV above the top of the valence band, STO-related states can be found to be filled by electrons originating from the topmost LAO layers.

As for the soft x-ray analysis of paragraph 3.3, the formation of photoinduced charge carriers either by x-ray or ambient light irradiation could be considered at the origin of the observed IS in the 3 u.c. sample, where they are not expected as the sample is insulating. However, in order to proceed with our study, at

the present stage we regard the IS observed in the 3 u.c. sample as due to an extrinsic effect, while the higher intensity of the resonant IS emission for the 5 u.c. sample is considered as a signature of an extra emission related to the presence of the 2DEG. A further discussion is presented in paragraph 3.6.

La $M_{4,5}$ edge

The ResPES chemical selectivity has also been exploited collecting photoemission data by scanning the photon energy at the La $M_{4,5}$ edge. This opportunity provides us to resonantly enhance the contribution of lanthanum-related electronic f states in the valence band, in the gap, and at E_F. The results are shown in Figure 3.23 (a) for selected photon energies: off-resonance ($h\nu = 820.0\ eV$) and on-resonance ($h\nu = 836\ eV$). In a simple single configuration atomic view, the XAS transition at the La $M_{4,5}$ edge drives the system from the $3d^{10}4f^0$ initial state to the $3d^9 4f^1$ final state that is split into two peaks ($3d_{5/2}$ and $3d_{3/2}$) by the dominant spin-orbit interaction of the 3d electrons, as shown in Figure 3.23 (c). The CIS profile for states around BE $= 5.5 \pm 1.0\ eV$ exhibits a resonant enhancement through the La edge, as expected from La-related states contributing to the valence band, labelled as **C** in Figure 3.23 (a). On the contrary, the CIS profile for states at BE $= 0.5 \pm 1.0\ eV$ does not show any resonant enhancement and the intensity variations appear to be comparable to the noise level. Here $\pm 1.0\ eV$ represents the width of the region, centered either at BE $= 5.5\ eV$ or at BE $= 0.5\ eV$, considered to extract the CIS profile. In the event of $LaTiO_3$ segregations due to interdiffusion at the interface, the lack of La-related spectral weight at E_F is expected. In fact, La 4f states are predicted to be nearly 4 eV above the conduction-band minimum (see, e.g., Figure 7 (a) in Ref. [224]). This virtually leaves the spectral weight at E_F to Ti-derived states of STO.

As in the case of the 3d states in Ti $L_{2,3}$ ResPES, the RSW at the La $M_{4,5}$ edge of Figure 3.23 (a) can be fairly described with f-DOS DFT calculations. Therefore the resonating contribution of 4f electronic levels, along with that of Ti 3d, can be used to pinpoint the energy position of the LAO valence band edge with respect to the STO VB edge ($\Delta_{\mathrm{VBM}} = -0.7\ eV$), as shown in Figure 3.23 (b). This is valid assuming the absence of band bending in the LAO overlayer, as proved by the lack of broadening of La core level states observed by x-ray photoemission in paragraph 3.5.1. This is also consistent with the lack of La-O

spectral weight at E_F, because the presence of a potential gradient in the LAO overlayer should push the valence band states towards the Fermi level and thus a spectral weight should be observed at or near the Fermi energy due to the occupied electronic states in the LAO surface layer [189].

3.5.3 Band alignment at the interface

The results discussed so far can be rationalized in the electronic band energy diagram shown in Figure 3.24 (a) and (b) for the 5 u.c. conductive and 3 u.c. insulating LAO/STO sample, respectively. A relevant bending of the conduction band (hereafter called *notch*) is needed at the interface in order to account for the 2DEG spectroscopic signature, as well as a smaller bending related to the valence band at the junction appears essential to connect the results with those obtained by Mg K_α presented in the previous paragraphs.

First, we start considering the interface state in the 5 u.c. sample. The extent of the notch depends on several factors that need to be accounted for. If the width of the interface state contribution is regarded - as shown in Figure 3.22 (b) - the bending becomes $1.0 \pm 0.1\ eV$. We consider this value as an upper limit for the bending, as the band diagram should be drawn by accounting for the experimental linewidth ($0.40\ eV$, as can be extracted from the gold Fermi edge measured in the same conditions). This reduces the width of the IS peak to about $0.92\ eV$. Furthermore, we can regard the IS peak as a superposition of several peaks, each one shifted by the internal field found at a specific depth. For instance, if we consider an extent of 3 u.c. for the bending, the superposition of three peaks (FWHM $= 0.4\ eV$ each) distributed over a $0.6\ eV$ energy range yields an overall width of $0.90\ eV$ [29], in agreement with our experimental finding of $0.92\ eV$. On this basis, we can estimate a depth of $0.6\ eV$ for the notch. The comparison with recent experimental results and theoretical calculations is also helpful to discuss the present results. Cancellieri *et al.* [226] have found IS with a width of about $0.1\ eV$ measured at $T = 11\ K$ in samples displaying $n_s = 6.5 \cdot 10^{13}\ cm^{-2}$, in agreement with calculations based on a charge transfer $Q = 0.1$ electrons/u.c. Even deeper bands (down to $0.4\ eV$ below E_F at the Γ point) are expected [227] for charge densities of about $10^{14}\ cm^{-2}$. This prediction is therefore consistent with our results on the 5 u.c. conductive sample ($0.6\ eV$) that features a measured charge density of $1.4 \cdot 10^{14}\ cm^{-2}$.

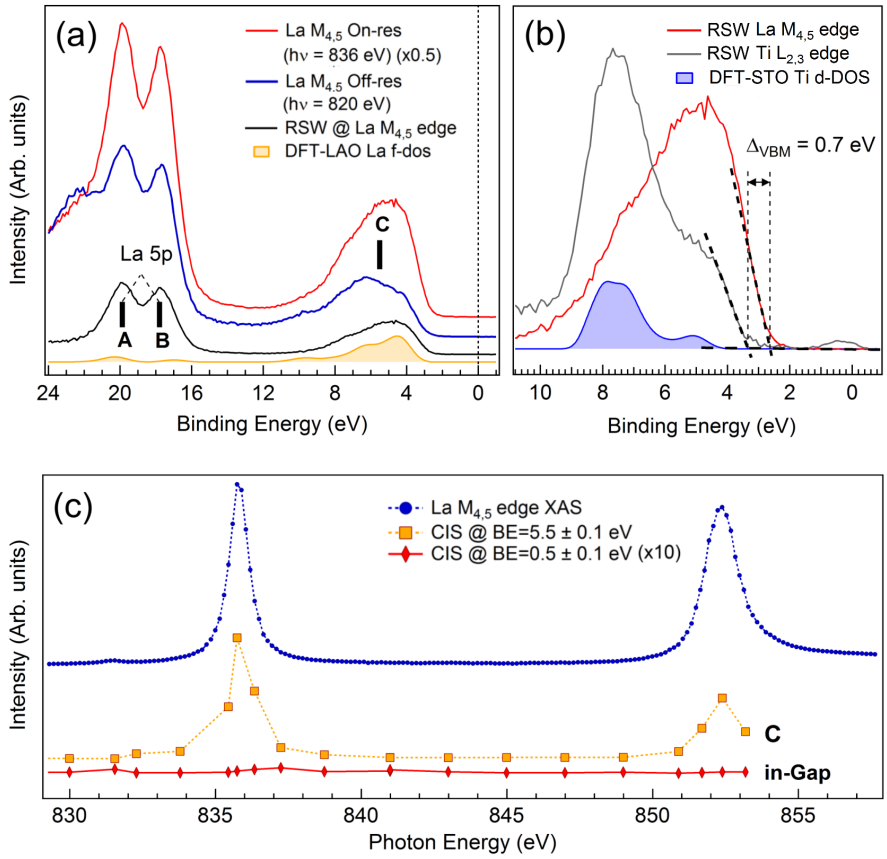

Figure 3.23: *LAO/STO 5 u.c. conductive heterostructure: (a) photoemission spectra at the La $M_{4,5}$ edge, collected out-of-resonance (blue, $h\nu = 820$ eV) and on-resonance (red, $h\nu = 836$ eV, scaled by a factor of 0.5) conditions. Spectral difference RSW (black line) and f-DOS DFT calculations on a LAO bulk crystal (filled orange). (b) Comparison of La 4f and Ti 3d resonating contribution with d-DOS DFT calculations on a STO bulk crystal (filled blue). DFT calculations are taken from Ref. [29]. (c) XAS spectrum and CIS curves collected at the La $M_{4,5}$. The CIS curves have been tracked for the C band (panel a) at BE $= 5.5 \pm 0.1$ eV and for the in-gap states at BE $= 0.5 \pm 0.1$ eV.*

From Figure 3.23 (b) we can measure both the VB shift between the STO VBM and the LAO VBM at the interface ($\Delta^{int}_{\mathrm{VBM}} = +0.7\ eV$) and the absolute position of the LAO VBM. Otherwise, according to the fitting of shallow core level and VB spectra ($\mathrm{VBO_{SCL+VB}}$) presented in paragraph 3.4.1, below the interface the STO VBM is found above the LAO VBM, resulting in $\Delta^{bulk}_{\mathrm{VBM}} = -0.1\ eV$. Therefore, we are able to reconstruct the extent of the VB bending equal to $0.8\ eV$.

Assuming an energy gap of $3.2\ eV$ for bulk STO, the conduction band minimum (CBm) is found at $0.5\ eV$ above E_F, yielding a remarkably notched energy level profile at the interface. This value is higher with respect to the one ($0.28\ eV$) measured by cross-sectional scanning tunneling microscopy [219], but in the light of experimental indeterminacy the two results can be regarded as consistent with each other. Then, considering the energy gap of LAO as $5.6\ eV$, we have completed the band diagram for the 5 u.c. conductive LAO/STO sample, as shown in Figure 3.24 (a). Finally, we can observe a straddling gap (i.e., type I) heterojunction, which is in agreement with the experimental evidence provided in Refs. [219] and [188], but at odds with other studies based on XPS data [189,213]. In particular, the difference with respect to the results presented in Ref. [189] for a 5 u.c. sample grown at $\mathrm{P}_{O_2} = 1 \cdot 10^{-4}\ mbar$ are due to the different alignment of VBM of STO with respect to LAO ($\Delta^{bulk}_{\mathrm{VBM}} = +0.35\ eV$), resulting in a straddling gap (type II) heterojunction.

Concerning the 3 u.c. case, the inset of Figure 3.21 (a) evidences a BE shift ($\approx +0.3\ eV$) of the STO VBM to higher BE with respect to the 5 u.c. sample (VBM_{3uc} vs VBM_{5uc}). Since all the 3 u.c. spectra are aligned to the 5 u.c. spectra by referring to the centroid of the resonant emission of Ti^{4+} states in the $6.5-9.5\ eV$ BE range, the relative shift between VBM_{3uc} and VBM_{5uc} must be related only to the displacement of the LAO band (which, in facts, exhibits the VBM at lower BE than the STO VBM, see Figure 3.23 (b)). In other words, by the shift of $\approx +0.3\ eV$ of the VBM_{3uc} we obtain both the absolute BE position of the LAO band and the VB offset between STO and LAO at the interface, which is $\Delta^{int}_{\mathrm{VBM}} = +0.4\ eV$. As $\Delta^{bulk}_{\mathrm{VBM}}$ was estimated to be $-0.2\ eV$ from XPS data ($\mathrm{VBO_{SCL+VB}}$, paragraph 3.4.1), we can assess the extent of the VB bending which is equal to $0.6\ eV$.

Considering the aforementioned energy gaps for STO and LAO, we manage to complete the band diagram which again displays an heterojunction of type

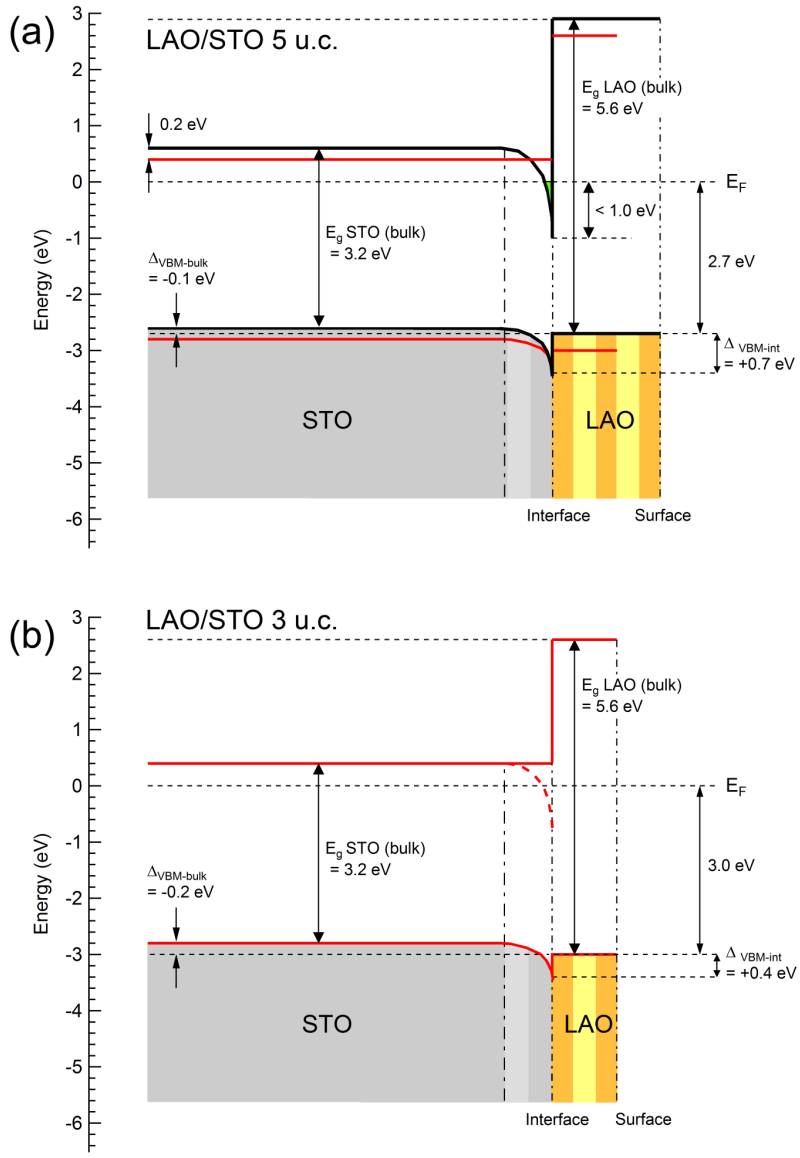

Figure 3.24: *(a) Band diagram for the LAO/STO 5 u.c. conductive heterojunction. The horizontal red lines represent the energy shift for the 3 u.c. insulating sample. (b) Band diagram for the LAO/STO 3 u.c. insulating heterojunction. All energies are defined within* $\pm 0.1\ eV$*, with the exception of* Δ^{int}_{VBM} *values* ($\pm 0.2\ eV$).

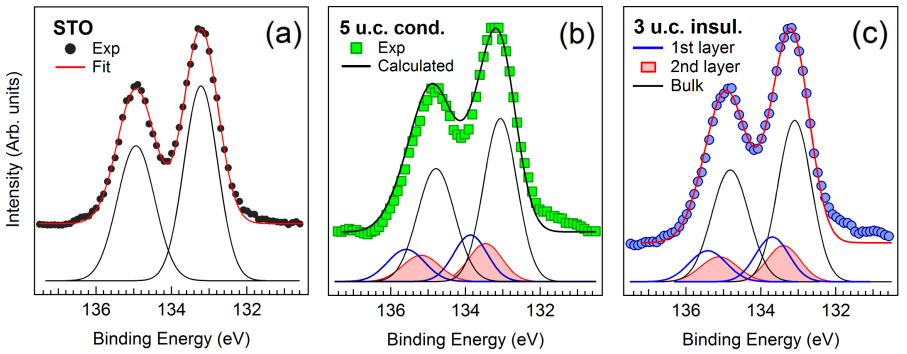

Figure 3.25: *Sr 3d core level of (a) STO, (b) 5 u.c. conductive and (c) 3 u.c. insulating LAO/STO sample by XPS K_α line. In panel (a) the gaussian fitting curves of experimental data are presented. Panel (b) and (c) display the calculated spectra on the basis of the VB offset at the interface of 0.8 eV and 0.6 eV, considered in the band diagrams of Figure 3.24, for the 5 u.c. and the 3 u.c. sample, respectively. The core level shapes used for the calculations are the fitting curves of panel (a).*

I (straddling gap), as shown in Figure 3.24 (b). It is worth observing that when a relatively small value for Δ_{VBM}^{bulk} is retrieved from the fitting of the valence-band photoemission data, the discrimination between a type-I and a type-II junction can be affected by some degree of uncertainty, here estimated as ± 0.2 eV for both the samples. As we regarded the IS observed in the 3 u.c. sample of extrinsic origin, the notch in the conduction band profile is marked with a dashed line to underscore the difference with respect to the 5 u.c. case, as represented in Figure 3.24 (b).

As a confirmation of the analysis so far obtained, we consider the increasing broadening for the Ti 2p and the Sr 3d core levels from the bare STO compound to the 3 u.c. and 5 u.c. LAO/STO heterostructures, reported in Table 3.1. Among all the possibilities discussed in paragraph 3.3 for justifying such a broadening, we have invoked an intrinsic origin like a band bending. On the basis of the STO VB bending at the interface (i.e. 0.8 eV and 0.6 eV for the 5 u.c. and the 3 u.c. sample, respectively) and evaluating in first approximation the extent of this band bending of about 2 u.c. below the heterojunction (from the depth assessment of the 2DEG deduced from Figure 3.11 (a)) we have calculated the Sr 3d core level by the BriXias code, as shown in Figure

3.25. Considering the gaussian fitting curves for the bare STO[3] in Figure 3.25 (a) as the representative shape for a lack of band bending, we have calculated the relative intensities of the Sr 3d peak for the first two STO layers below the interface, as well as the STO bulk contribution, thereby obtaining the total shape by summation. As shown in Figure 3.25 (b), the calculated spectrum for the 5 u.c. sample appears to be slightly more broadened than the experimental data, whereas a good match is presented for the 3 u.c. case, displayed in Figure 3.25 (c). Remarking that the resulting calculated spectra are not fitting curves, we can conclude that the measured VB bending, along with the approximated extent of 2 u.c. for bending, well explain the increasing of broadening in the two LAO/STO samples, even if a more accurate shape in the simulations (e.g., the Voigt function) would be necessary to reach a more precise result.

3.6 About the origin of the interface states

In the following paragraphs we will discuss the origin of the interface states, with a special attention to the photo-induced effects due to the x-ray exposure. Indeed, the sensitivity of LAO/STO samples both to UV (380 nm, corresponding to the STO gap, 3.2 eV) [209] and ambient light[4] (395 nm, slightly below the STO gap, 3.1 eV) [229] is well known[5], to such an extent that transport measurements [209] - and sometimes also x-ray photoemission experiments [189,221] - are carried out on samples stored in the dark for a long time. However, other perovskitic heterostructures [228] have also displayed a similar behavior, revealing for high resistance samples an enduring character even for subgap photons, which can be ascribed mainly to the polar discontinuity at the interface rather than the materials involved; in this context, the persistence of photodoping effect is explained as the spatial separation between the excited electrons and holes in the presence of a strong electric field at the junction [229].

A similar explanation has been recently invoked by Berner *et al.* [189] due to x-ray exposure. Even high-energy photon may create electron-hole pairs which

[3]Sr 3d core level of bare STO exhibits the narrowest FWHM with respect to the LAO/STO heterostructures, as reported in Table 3.1.

[4]This case is proved only for LAO/STO samples fully oxidized by a post-annealing treatment in O_2 at 573 K for 12 h. Such a procedure allows to increase the resistance of the heterostructures by a factor of 50 than the value measured for the as-grown samples.

[5]The same issue was preliminary introduced in paragraph 3.3.

undergo a spatial separation caused by the polar field, accumulating electrons at the interface and holes at the surface. Thereby, the resulting charge separation could lead to a compensation of the potential gradient in the LAO film, making the band flat for an x-ray photoemission investigation. Nevertheless, taking into account these considerations, Slooten *et al.* have evidenced that is not possible to clearly determine any modification in the core level shape or BE position in the time scale needed to carry out a soft x-ray experiment, even reducing the photon flux [184]. However, an alternative point of view can be provided by the study of Plumb *et al.* [230], which have shown an enhancement of the interfacial metallicity due to the x-ray irradiation but ascribed to induced-structural distortions of the surface/interface region of STO such as to accommodate electrons at the interface. Exploiting a beam flux above 10^{14} photons/sec (more than one order of magnitude higher with respect to the Berner's study), the latter interpretation has been supported by an evident modification of the Ti $L_{2,3}$-edge XAS spectrum from a typical Ti^{4+} shape to a Ti^{3+} configuration after 3 h of irradiation, as well as a spectral weight transfer from Ti^{4+} to Ti^{3+} in the Ti 2p core level (see Fig. 2 (a) and (b) of Ref. [230]).

The resonant data presented in section 3.5.2 were collected at BACH beamline, Sincrotrone ELETTRA (Trieste), whose typical spot size in the energy range used for the experiments is around 250x20 μm^2 with a flux of about 10^{11} photons/s, much lower with respect to the aforementioned studies [189, 230]. In facts, we can easily rule out the x-ray induced-metallicity case suggested by Plumb *et al.* [230] considering the XAS spectra at the Ti $L_{2,3}$ edge of Figure 3.26, in which different exposure times of the x-ray beam are taken into account and no clear change is detectable, except for slight variations in the XAS shape which are mainly ascribed to the procedure for the background subtraction.

Alternatively, for these data we may take into account the interpretation of Berner *et al.* [189], even though we have never observed any change in the IS intensity upon exposure to synchrotron radiation for several days. This should rule out that the x-ray irradiation is the driving mechanism for the 2DEG origin, unless the effect occurs immediately upon irradiation, reaches the saturation in a time frame faster than the acquisition time for a photoemission spectrum and remains constant over several days. Nevertheless, as these effects should occur on the STO side of the junction to yield Ti^{3+} electronic states, it is still difficult to justify the lower intensity observed for the 3 u.c. sample with respect

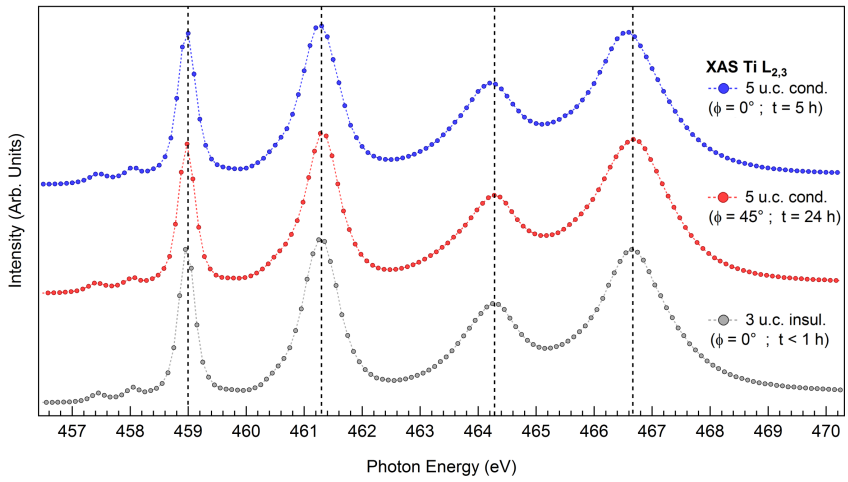

Figure 3.26: *XAS spectra collected at the Ti $L_{2,3}$ edge for the 5 u.c. conductive (blue and red) and the 3 u.c. insulating (grey) LAO/STO sample after different x-ray exposure times and different orientations with respect to the beam incident direction.*

to the 5 u.c. sample, as shown in Figure 3.22 (a). In fact, irradiation effects are supposed to be larger in the 3 u.c. than in the 5 u.c. sample, due to the thinner LAO overlayer on top of the STO substrate, suggesting that the 5 u.c. sample displays an extra intensity with a different origin that adds up to the weak spectral weight observed in the 3 u.c. sample. Therefore, as mentioned in the previous paragraphs, we regard the Ti^{3+} spectral weight evidenced for the 3 u.c. insulating sample as due to an extrinsic origin, whereas the extra contribution shown for the 5 u.c. conductive LAO/STO is considered as related to the presence of the 2DEG.

On the other hand, it is rather interesting to observe that interface states are different from those expected for several other compounds, as shown in Figure 3.27. For instance, a conducting Nb-doped $SrTiO_3$ layer (adapted from Ref. [234]) exhibits a spectral weight constituted by an incoherent emission (defect states at high BE) and a coherent emission at E_F. This indicates that the states we observed at E_F in the LAO/STO interface are distinctive of the heterojunction rather than being related to the surface of an isolated STO substrate. Furthermore, it is known that defects in $SrTiO_{3-x}$ (adapted from Ref. [232]) or

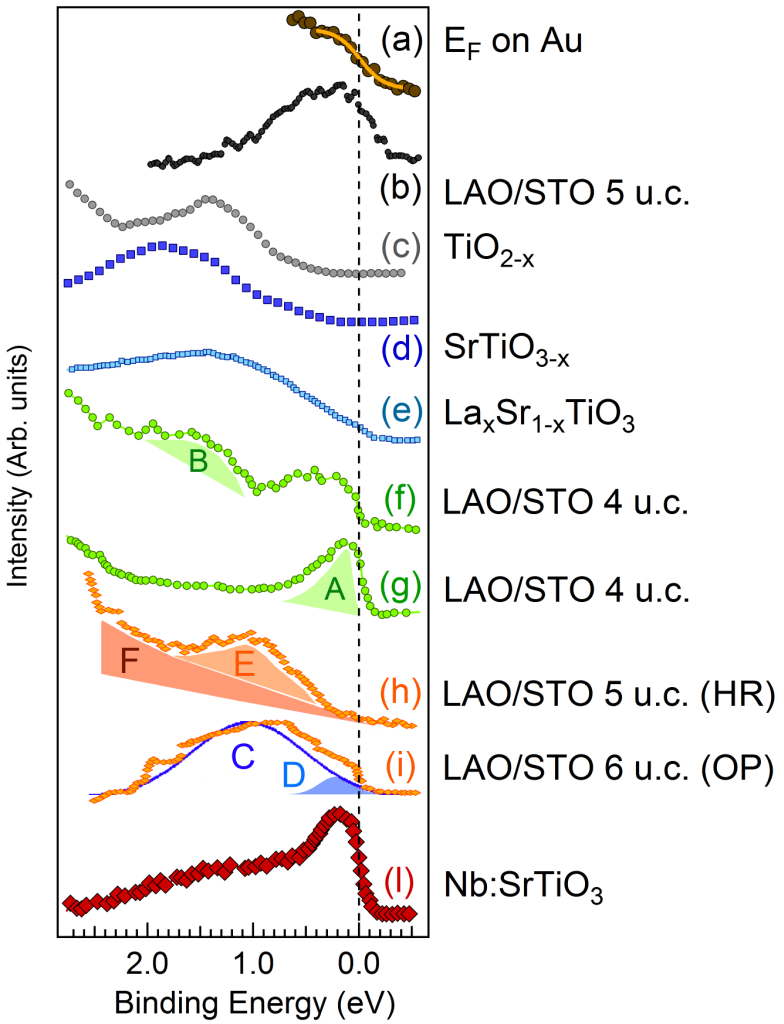

Figure 3.27: *(a) Fermi edge of the gold film deposited on the clip in contact with the specimen. (b) Interface states for the 5 u.c. conductive LAO/STO. Resonant high-resolution spectra of several in-gap states taken from literature: (c) TiO_{2-x} (adapted from Ref. [231]), (d) $SrTiO_{3-x}$ (unpublished data [232]), (e) $La_xSr_{1-x}TiO_3$ (adapted from Ref. [233]), (f) 4 u.c. LAO/STO taken on Ti^{3+} resonance, $h\nu = 459$ eV at 20 K (adapted from Ref. [221]), (g) 4 u.c. LAO/STO taken on Ti^{4+} resonance, $h\nu = 460.2$ eV at 20 K (adapted from Ref. [221]), (h) 5 u.c. LAO/STO grown in $p_{O_2} = 5 \cdot 10^{-3}$ mbar which exhibits high resistance (HR) ($> 10^6$ Ω) at $h\nu = 458.3$ eV (adapted from Ref. [181]), (i) 6 u.c. LAO/STO grown in the oxygen poor (OP) pressure of $4.5 \cdot 10^{-6}$ mbar at $h\nu = 458.3$ eV (taken from Ref. [181]), (l) Nb:SrTiO$_3$ (adapted from Ref. [234]).*

TiO_2 (adapted from Ref. [231]) single crystals (which can be taken as a reference system for the TiO_2-terminated surface of the STO substrate) may contribute to in-gap states far from E_F, even in slightly sub-stoichiometric rutile samples [231] or single crystals where defects are created by several annealing and Ar^+ ion sputtering cycles[6], at an energy distinctively different from the $3d^1$ states probed in the present experiment.

However, a difference appears between our 5 u.c. sample measured at room temperature and the data presented by Berner *et al.* (adapted from Ref. [221]) on a conducting 4 u.c. LAO/STO sample measured at 20 K, where two distinct emissions at E_F (A) and about 1.5 eV below E_F (B) were observed. These contributions are related to delocalized (A) and localized (B) states, where the A states are identified to form the 2DEG at the interface while the B states are ascribed to trapped states due to oxygen vacancies around the Ti sites. A discrepancy is evident also for the data presented by Koitzsck *et al.*. In particular, the 6 u.c. LAO/STO (adapted from Ref. [181]) grown in oxygen poor (OP) atmosphere ($< 10^{-6}$ $mbar$) exhibits another different shape on Ti^{4+} resonance ($h\nu = 458.3$ eV), which is spread out within 2 eV from the Fermi level and was ascribed to a component (C) due to lattice defects and oxygen vacancies formed during the oxygen-poor deposition and to a contribution (D) distinctive of the metallic nature of the interface states. In facts, it is known that oxygen vacancies can provide excess charge that eventually fills the STO states at the interface [235]. Differently, despite of a growth in high oxygen pressure ($5 \cdot 10^{-3}$ $mbar$), the 5 u.c. LAO/STO sample (adapted from Ref. [181]) exhibits an high sheet resistance ($> 10^6$ Ω) and shows on Ti^{4+} resonance ($h\nu = 458.3$ eV) only in-gap states (E) 1 eV far from E_F. The latter is however overlapped to a foot structure (F) present even for off-resonance measurements, which was tentatively ascribed to disorder during the growth and related to the O 2p band. Nevertheless, our 5 u.c. LAO/STO samples shows a low sheet resistance (5.5 $k\Omega$) with respect to the previous case, even though is grown in an oxygen-rich atmosphere ($P_{O_2} \sim 10^{-3}$ $mbar$) which places it quite far from the conditions ($P_{O_2} \sim 10^{-6}$ $mbar$) where a relevant effect of the oxygen vacancies is expected

[6]The reference spectrum for $SrTiO_{3-x}$ taken on Ti^{3+} resonance at $h\nu = 459.6$ eV is an unpublished data collected at the ALOISA beamline, Sincrotrone ELETTRA (Trieste). The experiment was carried out on a single crystal STO (10x10x0.5 mm) obtained from MaTecK GmbH, which was annealed at 600°C for 33 min, sputtered by Ar^+ ions at 1 keV for 15 min and then annealed above 600°C in oxygen pressure of $2 \cdot 10^{-7}$ $mbar$ [232]

[222]. Therefore, for the present sample oxygen vacancies are not expected to be the major source of doping, as also evidenced by a different shape and BE position of the interface states.

Finally, it is worth observing that a model compound for the LAO/STO interface can also be the $La_xSr_{1-x}TiO_3$ system, as interdiffusion of La into the STO lattice observed in LAO/STO (see, e.g., Refs. [185, 190, 191]) may lead to the formation of mixed La-Sr-Ti oxide phases. For the $La_xSr_{1-x}TiO_3$ system, both an emission at E_F and a broad band peaked at about BE = 1.5 eV are observed (adapted from Ref. [233]), the latter also being present in undoped $LaTiO_3$ single crystals [236]. The common understanding is that La substitution introduces electrons into the conduction band of STO, a spectral weight at E_F appears, and $La_xSr_{1-x}TiO_3$ becomes metallic for x as small as 0.1 [233]. In this case, cation substitution would act as a doping mechanism, similar to what happens in, e.g., La-Sr-Cu-O superconducting cuprates. However, no similarity is found between our sample and the case of $La_xSr_{1-x}TiO_3$, suggesting that the observed states cannot be related to interdiffusion in a straightforward way. In fact, we observe states at E_F as if charges are injected into STO by Sr substitution with La, but we do not observe the band peaked at BE = 1.5 eV, characteristic also of undoped $LaTiO_3$ [236].

3.7 High photon flux photoemission electron microscopy and micro-spectroscopy

In this paragraph we will present both x-ray spectroscopy and microscopy data, such as XPEEM (X-ray Photoemission Electron Microscopy), XAS-PEEM, μ-XPS and MEM (Mirror Electron Microscopy). These experiments were collected at NANOSPECTROSCOPY beamline, Sincrotrone ELETTRA (Trieste), whose typical spot size in the energy range used for the experiments is around 7x2 μm^2 with a flux of about 10^{11} photons/s, which means a photon flux per μm^2 above 2 orders of magnitude higher with respect to data acquired at BACH beamline so far presented. The latter allows us to emphasize the photodoping effect - if present - and possibly recognize its role in the arise of conductivity at the interface. In addition, by means of these techniques we are able to laterally investigate the chemical homogeneity in a nanometer scale and monitor the

evolution of the electronic properties of the sample under the x-ray irradiation as a function of time of exposure. While a reduction of Ti from 4+ to 3+ is evident due to the x-ray irradiation, we have also observed a regeneration of Ti under the exposition of the sample to low oxygen pressures ($10^7 - 10^{-8}$ $mbar$) at room temperature during the measurements. In this section we will focus only on the LAO/STO 5 u.c. conductive sample.

3.7.1 Photoemission electron microscopy data

Figure 3.28 (a) shows a MEM image for a μm-sized area of the surface. Despite of a preliminary UV+O_3 cleaning procedure, intensity variations of the reflected electrons on the sample surface are clearly detectable and tentatively ascribed to carbon islands (dark regions). This interpretation can be confirmed by XPEEM of Figure 3.28 (b-c) and 3.29 (a-c). Considering the same detection region for the MEM image, Figure 3.28 (b) displays an XPEEM image (at the energy corresponding to the Al 2s core level) with a non homogeneous intensity which traces the island structures of Figure 3.28 (a), as labeled by numbers 1-5. Taking into account different flat regions (red squares) and different island structures (green shapes), we have obtained the average XPS spectra for these areas, as displayed in Figure 3.28 (c). Normalizing the intensity of the Al 2p core level, no variations in the integrated areas are detected for the Sr 3d and Al 2s peaks. Differently, a discrepancy of about 5% is present for La 4d core level, which seems to exhibit a transfer of the spectral weight at BE = 98 eV. Since the change is evident only for the flat areas, we rule out the possibility that such a contribution is an Auger peak, because it should be detectable also for the island regions without modifying the relative integrated areas for all the core levels.

Moreover, Figure 3.29 (a) shows an XPEEM image (at the BE corresponding of C 1s core level) for another region of the sample surface. Also in this case, flat zones (in grey color) and islands (in white) are evident, despite of a reduced irradiated area of the sample surface. Figure 3.29 (b) and (c) display the C 1s and La 5p core levels for the different areas, i.e. the red square for the flat zone and the blue circle for the island. By normalizing the integrated area of the La 5p peaks (Figure 3.29 (c)), the intensity of C 1s is higher for the island region with respect to the flat zone (blue-dotted line, Figure 3.29 (b)). This

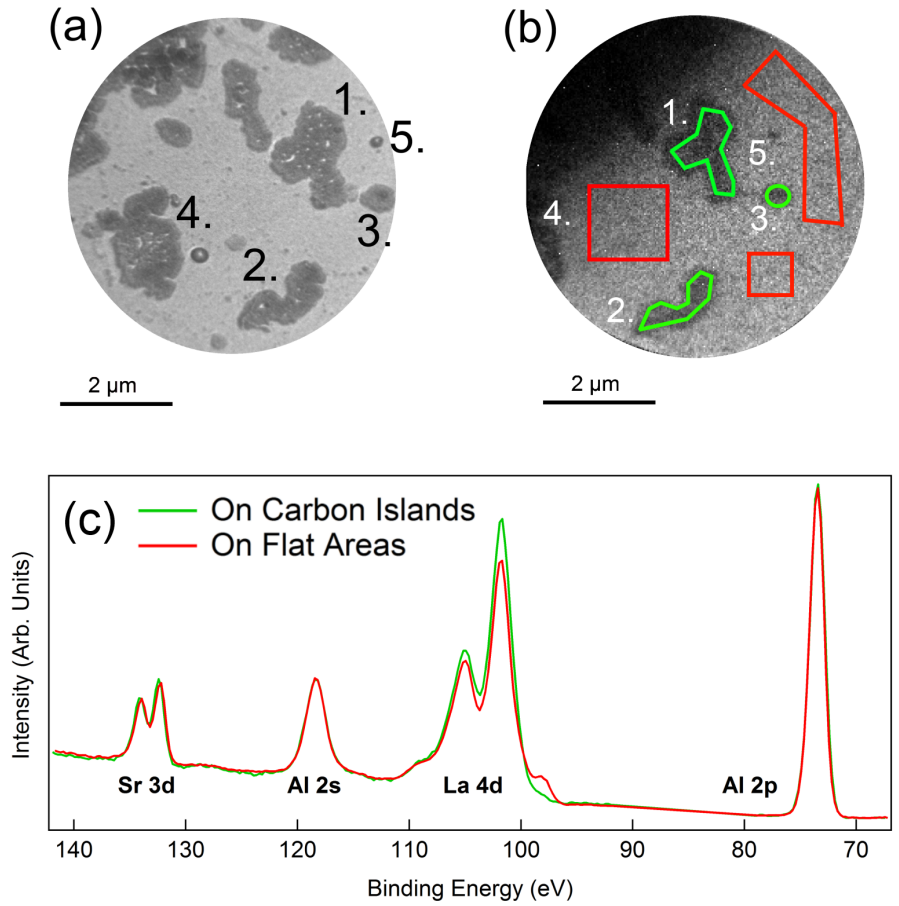

Figure 3.28: *LAO/STO 5 u.c. conductive sample: (a) MEM image for the surface region under investigation; carbon islands are evident in dark color. (b) XPEEM image (at the Al 2s core level) for the same region of panel (a) at* $h\nu = 420$ *eV. Numbers from 1 to 5 point out the island structures shown in panels (a) and (b). Flat areas (red squares) and carbon islands (green shapes) are selected to obtain (c) average XPS spectra for the BE range of the Sr 3d, Al 2s, La 4d and Al 2p core levels.*

evidence allows to achieve two conclusions: first, the flat zones also exhibit a carbon contamination - as expected without an in-situ cleaning procedure before the experiments - and, secondly, we can definitely recognize the chemical composition of the islands as compact carbon regions - probably graphite islands originating from the hydrocarbon contamination of the surface under the high-brilliance synchrotron beam, in a similar way to what generally happens for the surface of beamline mirrors exposed to synchrotron radiation [237].

On this basis, we tentatively explain the shape modification of La 4d peak of Figure 3.28 (c). Since this effect seems to be related only to the lack of the compact carbon islands, we may speculate that otherwise the presence of carbon island can somehow shield the LAO surface from defects, structural changes or charging effects due to the direct x-ray beam exposure, as we probably expected from the increase in photon flux per μm^2.

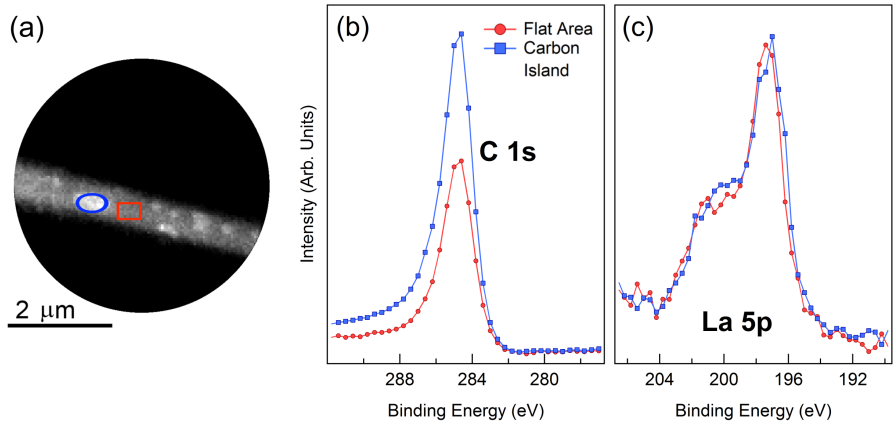

Figure 3.29: *LAO/STO 5 u.c. conductive sample: (a) XPEEM for the C 1s core level. A carbon island (blue circle) and a flat area (red rectangle) are selected for the average XPS of the (b) C 1s and (c) La 5p core levels.*

For a different surface area of the sample, Figure 3.30 (a) shows a XAS-PEEM image in partial yield at the Ti $L_{2,3}$-edge which can also detect an intensity modulation ascribed to carbon islands. In fact, considering three different regions - i.e. a flat zone in the red circle, a carbon island in the green rectangle and an average region in the black circle - we can obtain two information:

as shown in Figure 3.30 (b), the XAS profiles appear (*i*) very similar to one another(dotted lines) and (*ii*) comparable to the XAS spectrum collected with low-flux (at BACH beamline, as already presented in Figure 3.21 (a)). These evidences allow us to assert that our experimental condition is different than that reported by Plumb *et al.* [230], which exhibits a clear shape modification towards a $LaTiO_3$ structure. This can be justified by the fact that we are in a intermediate photon flux per μm^2 ($\approx 10^{13}$ photons/s) with respect to Ref. [230] (10^{14} photons/s) and our previous data with low-flux (10^{11} photons/s).

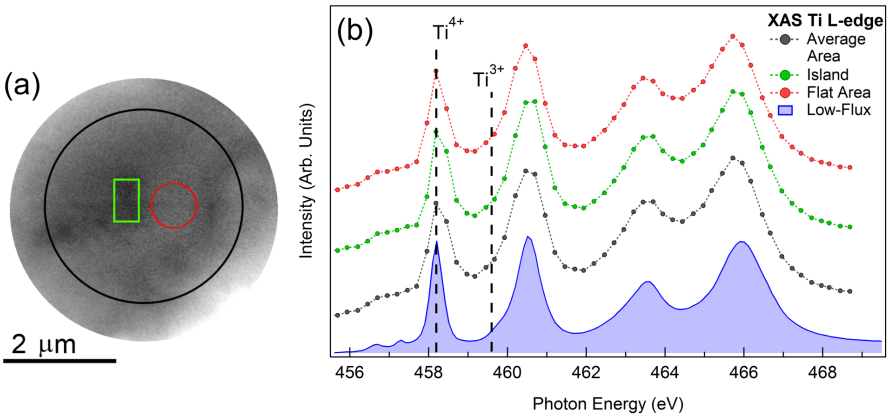

Figure 3.30: *LAO/STO 5 u.c. conductive sample: (a) XAS-PEEM of a micro-sized region for $h\nu = 457$ eV. A flat region (red circle), a carbon island (green rectangle) and an average region (black circle) are selected for (b) average XAS spectra. The XAS in blue-shaded is taken from Figure 3.21 (c) as reference for an experiment obtained by a low-flux x-ray beam.*

3.7.2 μ-XPS data as a function of the x-ray exposure time

In this section we are interested to monitor the possible evolution of the electronic states in relation with the time of exposure to the x-ray high-flux beam. For this purpose we exploit μ-XPS experiments for the Sr 3d, La 4d, Al 2s, as well as Ti 2p in order to enhance, if existing, the relation between the x-ray exposure and the electronic states related to Ti^{3+} oxidation states.

Figure 3.31 (a) displays the rough data for the Sr 3d core level as a function of the irradiation time. The experiment started from a surface area exposed

to the beam for a long time. At about $t = 200$ *sec*, a black arrow points out the time when the sample was laterally shifted of ~ 60 μm to detect a not-yet-irradiated μm-surface region. Exactly at that time, a rigid BE shift of the core level peaks ascribed to charging effects is detected. Figure 3.31 (b) shows the present data aligned in BE for the analysis. The labels (A-E) on the right of Figure 3.31 (b) indicate the time intervals in which the average μ-XPS profiles for the Sr 3d core level are measured. The latter spectra are displayed in Figure 3.31 (c), where no significant changes of the lineshape can be noted.

In a similar way, Figure 3.32 (a) shows the evolution of the La 4d core level from a long-time irradiated surface area to a region not yet exposed to synchrotron light. This change is marked by the black arrow on the left axis. As before, a BE shift of La 4d peaks is present. Figure 3.32 (b) represents the previous panel aligning the spectra at La $4d_{5/2}$ peak and the labels (A-F) on the right axis select the time intervals considered for the analysis. Unlike the Sr 3d case, here a change in the lineshape of La $4d_{5/2}$ is observed, as well as a clear decrease of 0.3 eV in the peak maxima separation of the two spin-orbit slit components, displayed in Figure 3.32 (c). Panel (d) shows the average μ-XPS profiles for the intervals A-F of panel (b). All spectra are normalized by the integrated area. As indicated by Figure 3.32 (c) and spectra in Figure 3.32 (d), La 4d core level tends to recover the long-irradiated shape (label A, red solid line) but on a time scale which exceeds that monitored for this experiment.

The μ-XPS experiment for the Al 2s core level is resembling the La 4d case. Figure 3.33 (a) displays a pronounced charging effect after the change to the unexposed region, which is marked by the black arrow on the left axis. The BE alignment shown in Figure 3.33 (b) allowed us to evaluate the FWHM variation of FWHM, as fully described by Figure 3.33 (c). In addition, Figure 3.33 (d) shows the μ-XPS profiles normalized by the integrated area for the time intervals labeled as A to E on the right of Figure 3.33 (b). Moreover, it is interesting to note in Figure 3.33 (c) a faster recovering to the starting condition with respect to the La 4d case.

The data so far presented appear to be strongly layer-dependent. In fact, it is noteworthy that the most evident discrepancy occurs between the Sr 3d and the cation core levels of the LAO film (i.e. La 4d and Al 2s); the former is totally unchanged under the x-ray exposure, whereas the latter pair exhibits lineshape modifications as a function of the irradiation time but with different

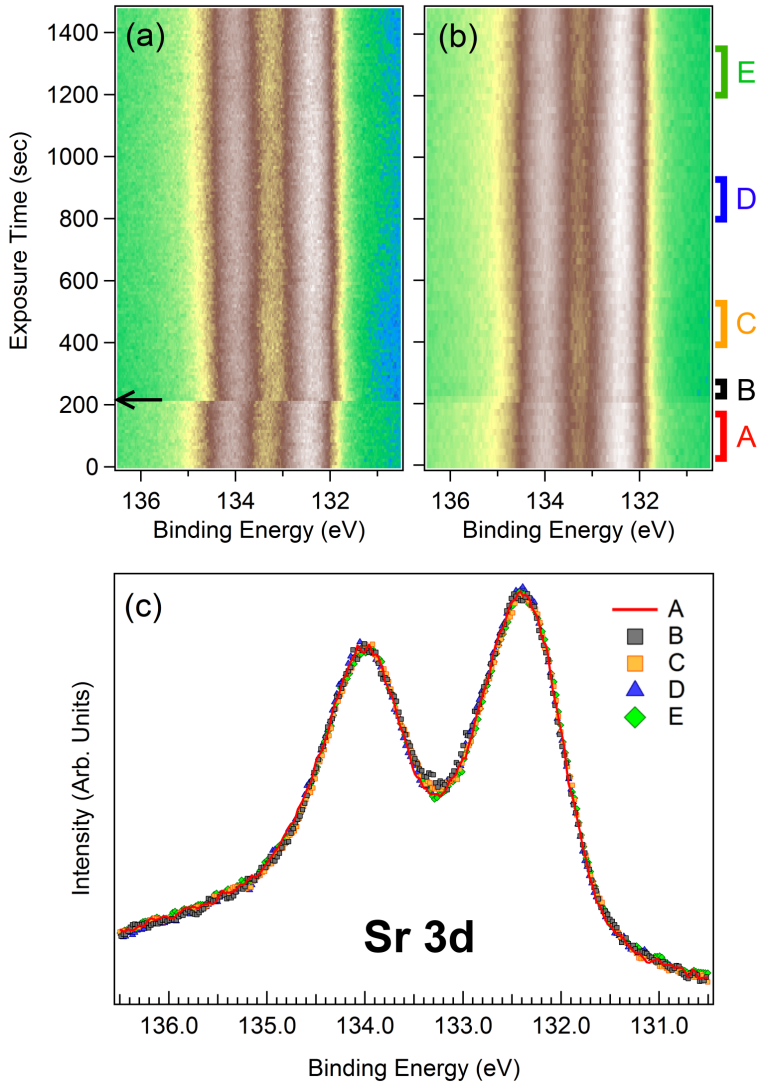

Figure 3.31: *LAO/STO 5 u.c. conductive sample: (a) μ-XPS of Sr 3d core level as a function of the x-ray exposure time, using $h\nu = 459.6\ eV$. The black arrow points out the time of shift from a long-irradiated surface area to a not-irradiated region. (b) Data of panel (a) aligned in BE to correct the BE shift due to charging effects. Labels on the right (A-E) indicate the time intervals in which the average μ-XPS profiles of panel (c) are obtained. (d) All spectra are normalized by the integrated area.*

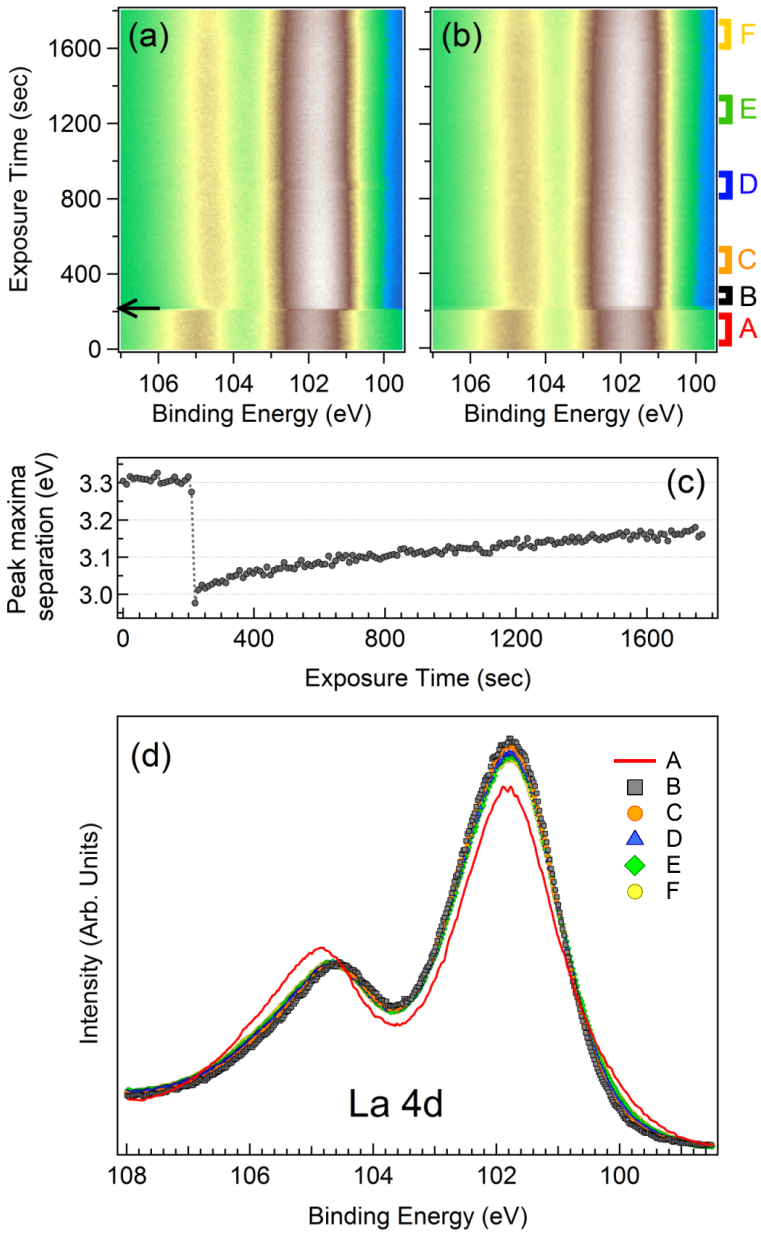

Figure 3.32: *LAO/STO 5 u.c. conductive sample: (a) μ-XPS of La 4d core level as a function of the x-ray exposure time, using $h\nu = 459.6\ eV$. The black arrow points out the time of shift from a long-irradiated surface area to a not-irradiated region. (b) Data of panel (a) BE-aligned at La $4d_{5/2}$ peak to correct the BE shift due to charging effects. Labels on the right (A-F) indicate the time intervals in which the average μ-XPS profiles of panel (d) are obtained. (c) Energy separation between the peak maxima of La $4d_{3/2}$ and La $4d_{5/2}$ as a function of the x-ray exposure time. (d) All spectra are normalized by the integrated area.*

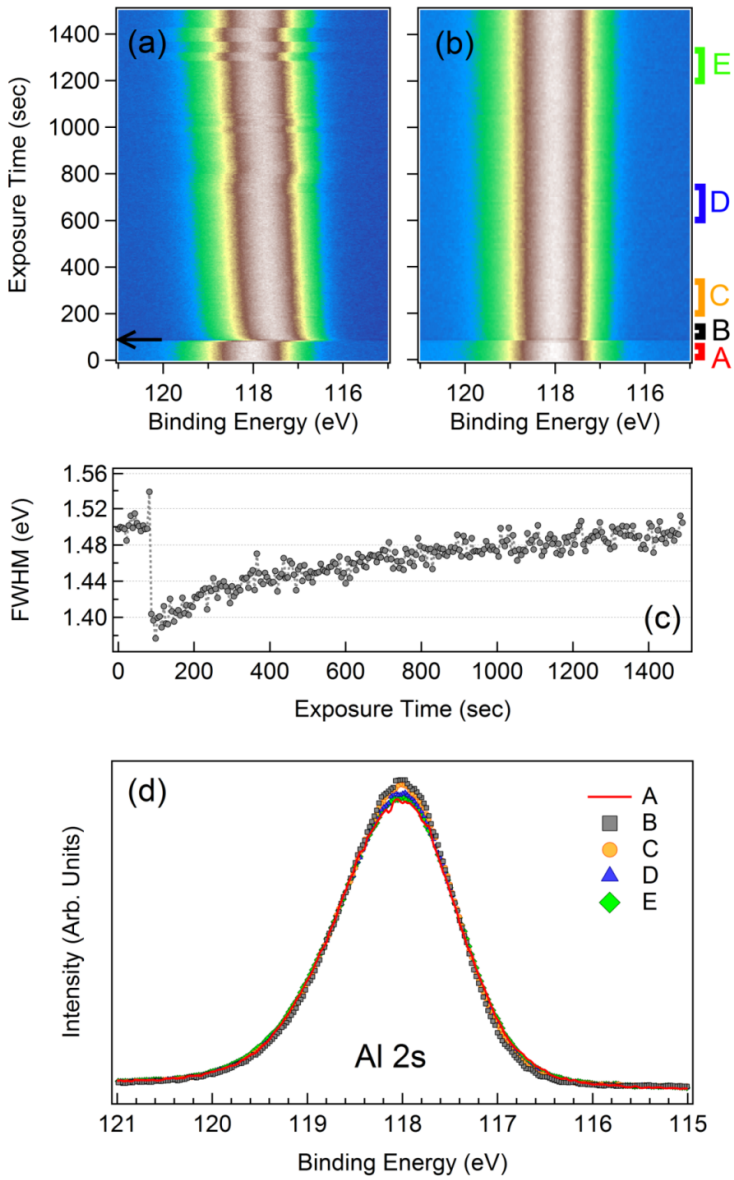

Figure 3.33: *LAO/STO 5 u.c. conductive sample: (a) μ-XPS of Al 2s core level as a function of the x-ray exposure time, using $h\nu = 459.6$ eV. The black arrow points out the time of shift from a long-irradiated surface area to a not-irradiated region. (b) Data of panel (a) aligned in BE to correct the BE shift due to charging effects. Labels on the right (A-E) indicate the time intervals in which the average μ-XPS profiles of panel (d) are obtained. (c) Full width at half maximum (FWHM) for the Al 2s peak as a function of the x-ray exposure time. (d) All spectra are normalized by the integrated area.*

recovering dynamics. The origin for these phenomena may be tentatively ascribed to charging of the insulating LAO layers and/or beam-induced damages at the topmost layers.

Nevertheless, the most interesting case appears to be the Ti 2p core level described below. Figure 3.34 (a) shows the μ-XPS spectra as a function of the exposure time, while Figure 3.34 (b) shows the stack of BE-aligned spectra. As the previous cases, the black arrow points out the moment of change from a long-exposed surface region to a non-irradiated area. Different time intervals, which are labeled on the right of Figure 3.34 (b), are averaged to display the μ-XPS profiles of Figure 3.34 (c), normalized by the integrated area. As expected by the results of Plumb *et al.* [230], Ti $2p_{3/2}$ shows a reduction from Ti^{4+} to Ti^{3+}, which increases with time reaching the starting condition about within 4000 *sec.* Figure 3.35 (a-f) display the fitting curves for the time intervals selected (A-F), using a double-Voigt function for the fits. The results for the Ti^{3+}/Ti^{4+} area ratios and the BE difference ($\Delta(BE)$) between the two contributions are reported in Table 3.6. Considering the area ratios, we obtain higher values with respect to the 0.056 reported in Table 3.1. Here, we can note that the Ti^{3+}/Ti^{4+} ratio varies by a factor 4 from the long- to the not-yet irradiated condition. Concerning the $\Delta(BE)$ between Ti^{4+} and Ti^{3+}, we measure a small shift within 0.18 eV (close to the energy resolution of the experiment of 0.15 eV); the largest BE difference (1.82 eV) is observed for the lowest ratio (0.15, B) whereas the smallest $\Delta(BE) = 1.76 - 1.77$ are present for the highest reduction cases ($0.68 - 0.66$, A and F, respectively).

Ceasing the analysis at this point would not allow us to assert anything decisive for the physics of the system, because the Ti^{3+} contribution may be ascribed to several origins, such as the formation of oxygen vacancies in the STO side [204, 215], disorder-induced defects [181], structural distortions induced by the beam exposure [230] or oxygen vacancies on the LAO surface which induce a charge confinement at the interface [184, 216]. However, an additional feature can be provided exposing the sample to low oxygen pressure at room temperature during the experiment. As shown in Figure 3.36 (a) and (b), starting from a long-irradiated area (A, red-dotted line) with a base pressure of $4.7 \cdot 10^{-10}$ *mbar* we can detect an highly-reduced Ti 2p shape as in the previous analysis, but if we insert oxygen during the measurement reaching a pressure of $3.0 \cdot 10^{-8}$ *mbar* (B, green-dotted line) we can note a reduction of the Ti^{3+}

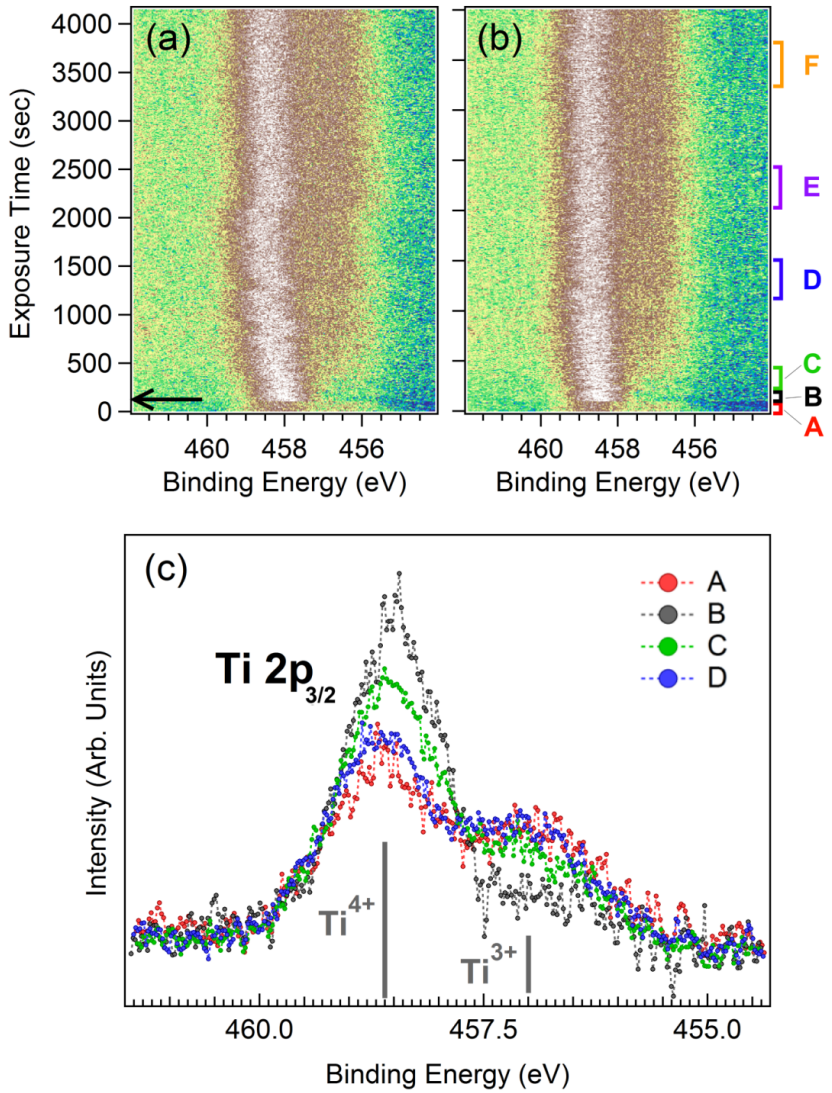

Figure 3.34: *LAO/STO 5 u.c. conductive sample: (a) μ-XPS of Ti 2p core level as a function of the x-ray exposure time, using hν = 760 eV. The black arrow points out the time of shift from a long-irradiated surface area to a not-irradiated region. (b) Data of panel (a) aligned in BE to correct the BE shift due to charging effects. Labels on the right (A-F) indicate the time intervals in which the average μ-XPS profiles of panel (c) are obtained. All spectra are normalized by the integrated area.*

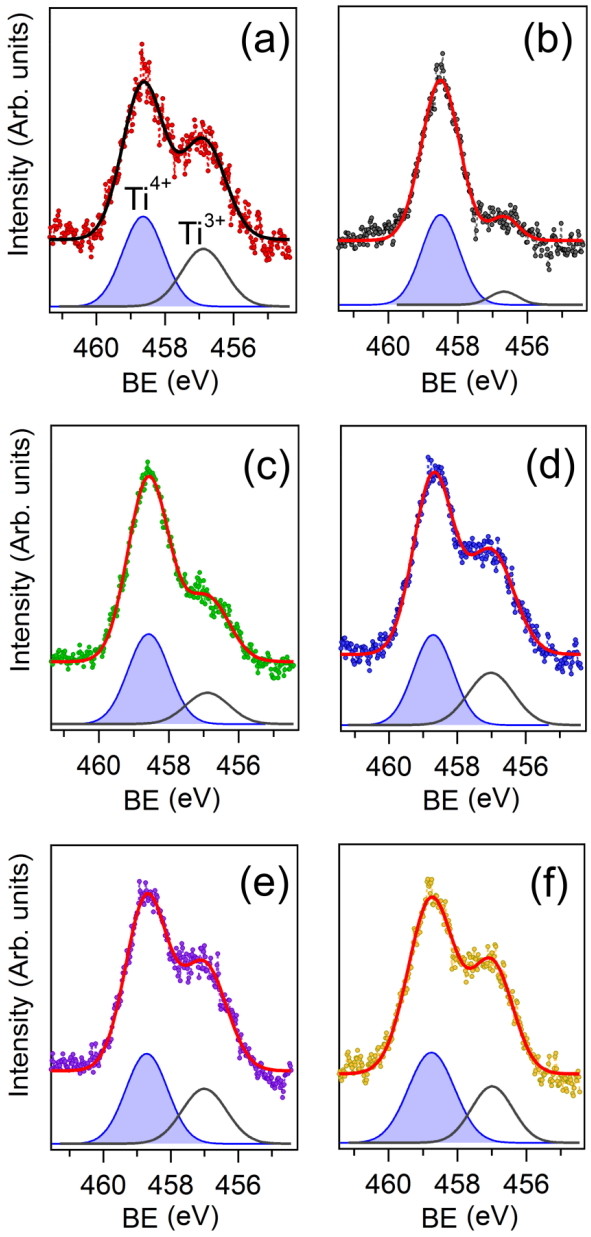

Figure 3.35: *LAO/STO 5 u.c. conductive sample: fitting curves for the Ti $2p_{3/2}$ core level μ-XPS spectra of Figure 3.34 (c). A double Voigt function is used for the fitting procedure. Time interval A (a), B (b), C (c), D (d), E (e) and F (f) are displayed. The fitting results are summarized in Table 3.5.*

spectral weight. In addition, increasing the oxygen pressure by one order of magnitude up to $2.3 \cdot 10^{-7}$ *mbar*, a further decrease od the Ti^{3+} contribution occurs (C, grey-dotted line). Then, once terminated the oxygen exposure and almost recovering the base pressure, $5.6 \cdot 10^{-10}$ *mbar* (D, blue-dotted line), the Ti 2p core level appears to reduce again. Indeed, the Ti^{3+} contribution in the latter condition (D) does not exhibit a complete reduction as in the starting point (A), however, we have to consider that the x-ray flux was changed (i.e., decreased) with respect to the preceding experiment of Figure 3.34 and then the starting position (A) could be taken advantage of both a longer and more intense photon flux.

In comparison with the μ-XPS experiment without the oxygen exposure, here the lower noise-to-signal ratio allows a more careful fitting analysis considering two different Ti^{3+} peaks, as shown in Figure 3.36 (b) (labeled A and B). This choice takes into account the possibility that the interface states originating the 2DEG can be related only to one of them, whereas the remaining peak may be ascribed to structural defects as presented by Koitzsch *et al.* [181]. The fitting results are displayed in Figure 3.36 (c) for the A interval, (d) for B, (e) for C and (f) for D, while the area ratios and the difference in the BE positions among the Ti^{4+}, Ti^{3+}_A and Ti^{3+}_B contributions are reported in Table 3.6. With the intent to find out a rationale among the area ratios, we can note that the scale factors among the time intervals A-D are nearly the same for Ti^{3+}_A/Ti^{4+} and Ti^{3+}_B/Ti^{4+}, which tends to rule out that Ti^{3+}_A and Ti^{3+}_B are related to a different origin. In addition, the BE differences do not appear connected to the oxygen exposure, showing a decrease for both $\Delta(BE)$ values from A to D time window, which should represent nearly the same condition (in terms of Ti reduction). Concerning instead the Ti^{3+}_{tot}/Ti^{4+}, in this case we are allowed to make a direct comparison with the results of Table 3.5. Despite of a marked decrease between the pair of A and D ratios of Table 3.6 (0.44 and 0.41, respectively) and that of A and F cases of Table 3.5 (0.68 and 0.66, respectively), which can be attributed to different photon fluxes[7], it is noteworthy that the relative scale factor between the highest Ti reduction cases (A and F, Table 3.5; A and D, Table 3.6) and the lowest Ti reduction condition (B, Table 3.5; C, Table 3.6) are almost the same[8] (4.46 for Table 3.5 and 4.72 for Table 3.6). Since the photon fluxes are indeed

[7]Spectra are not normalized to the photon flux.

[8]The scale factor between the highest and the lowest Ti reduction cases for results in Table

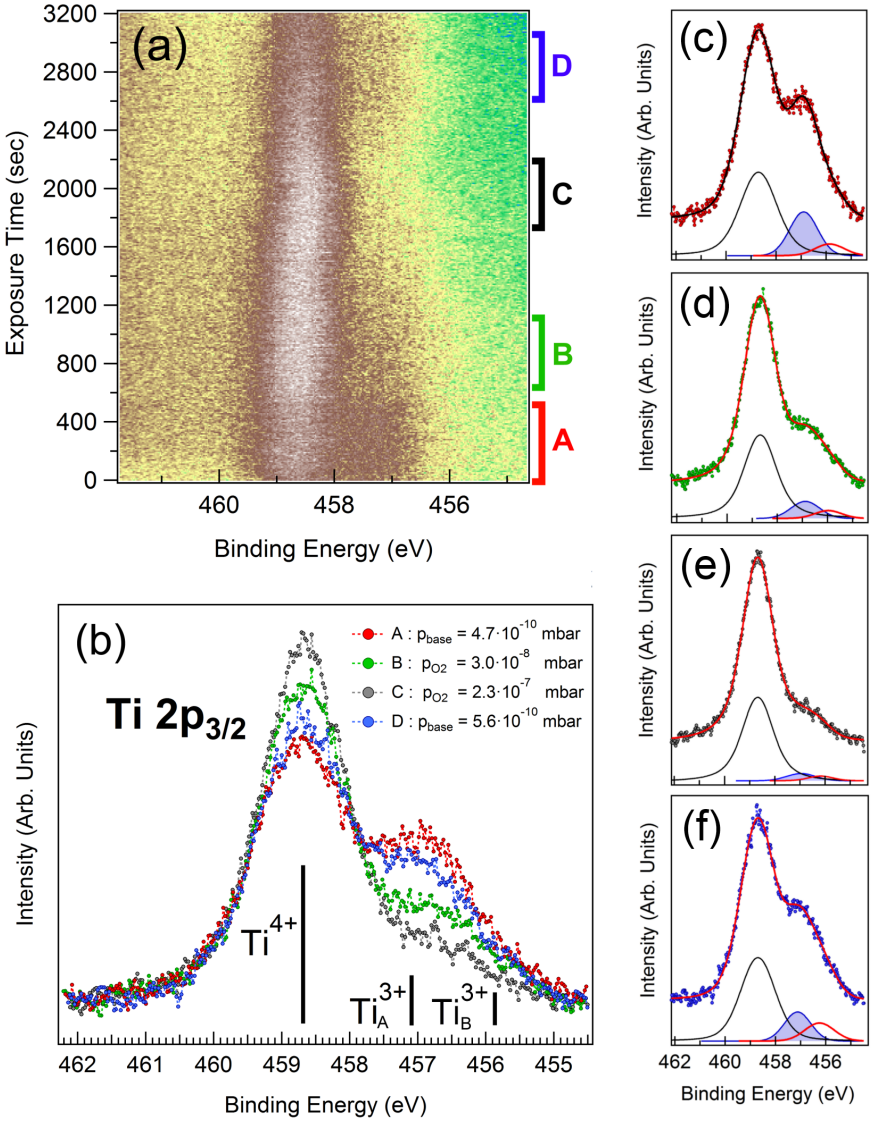

Figure 3.36: *LAO/STO 5 u.c. conductive sample: (a) μ-XPS of Ti $2p_{3/2}$ core level as a function of the beam irradiation time in exposure of different oxygen pressures, using $h\nu = 760$ eV. Labels on the right (A-D) indicate the time intervals in which the average μ-XPS profiles of panel (b) are obtained. The right panels (c-f) show the fitting curves of the Ti $2p_{3/2}$ core level for the time interval A (c), B (d), C (e) and D (f). The fitting results are summarized in Table 3.6.*

different, this coincidence of factors may be a sign that under oxygen exposure of the sample at room temperature is possible to probe the same Ti^{3+} spectral weight with respect to a not-yet irradiated region. In these terms, the oxygen exposure may *regenerate* the intrinsic oxidation of Ti, which is unavoidably modified by the lengthened exposure to the x-ray beam, as long as the oxygen pressure is enough to balance the reduction process (at least 10^{-7} $mbar$).

Data Fig. 3.35	**Time interval**	**Ti^{3+}/Ti^{4+} Area ratio**	**Δ(BE) Ti^{3+}-Ti^{4+} (eV)**
a	A	0.68	1.76
b	B	0.15	1.82
c	C	0.36	1.68
d	D	0.66	1.69
e	E	0.65	1.71
f	F	0.66	1.77

Table 3.5: *Results from the fitting analysis of Figure 3.35 (a-f). The area ratios and the binding energy differences between Ti^{3+} and Ti^{4+} contributions are reported.*

At this point it is crucial to understand the origin of the Ti^{3+} states among the aforementioned options - i.e. oxygen vacancies at the interface, interfacial defects, structural distortions and surface oxygen vacancies. For this purpose, other experiments are needed to clarify the intricate scenario, for instance, a possibility could be to investigate the valence band and the gap region both in Ti^{3+} and Ti^{4+} resonance condition in order to determine (*i*) which kind of in-gap states are generated by the high-flux beam exposure (e.g., interface states or in-gap states or both), (*ii*) if it is possible to recognize a connection between the latter states and the Ti^{3+} contributions evidenced for the Ti 2p core level, (*iii*) if they exhibit a response to the oxygen exposure and (*iv*) if this effect can be

3.5 is given by:

$$\frac{(A+F)/2}{B} = \frac{(0.68+0.66)/2}{0.15} = 4.46$$

For results in Table 3.5 the following formula is used:

$$\frac{(A+D)/2}{C} = \frac{(0.44+0.41)/2}{0.09} = 4.72$$

.

compared with the regeneration process so far discussed. Moreover, in the case that there is a connection between the interface states probed with low-flux and the additional states induced by the x-ray exposure, we should also answer (v) if the origin of the additional states follows the same mechanism of the states at the origin of the 2DEG. Otherwise, supposing that the interface states are different from those induced by x-ray irradiation exposure, (vi) a comparison with the spectra reported in Figure 3.27 could be useful to obtain further hints about the effect of the x-ray beam on the LAO/STO system.

Data Fig. 3.36	**Time range**	$\mathbf{Ti^{3+}_{tot}/Ti^{4+}}$ **ratio**	$\mathbf{Ti^{3+}_{A}/Ti^{4+}}$ **ratio**	$\mathbf{Ti^{3+}_{B}/Ti^{4+}}$ **ratio**	**Δ(BE)** $\mathbf{Ti^{3+}_{A}}$**-**$\mathbf{Ti^{4+}}$	**Δ(BE)** $\mathbf{Ti^{3+}_{B}}$**-**$\mathbf{Ti^{4+}}$
c	A	0.44	0.35	0.10	1.80 eV	2.84 eV
d	B	0.21	0.15	0.06	1.80 eV	2.71 eV
e	C	0.09	0.06	0.03	1.74 eV	2.50 eV
f	D	0.41	0.24	0.16	1.58 eV	2.46 eV

Table 3.6: *Results from the fitting analysis of Figure 3.36 (c-f). The area ratios and the binding energy differences among Ti^{3+}_{A}, Ti^{3+}_{B} and Ti^{4+} contributions are reported.*

3.8 Conclusions

In this chapter, we have studied three LAO/STO heterostructures - i.e. the 5 u.c. conductive, 3 u.c. insulating, and 5 u.c. insulating sample - by means of various soft x-ray photoemission spectroscopy techniques. The main results can be summarized as follows. In Figure 3.9 we have detected a La/Al stoichiometry discrepancy among the samples in relation with the oxygen partial pressure during the growth, whereas Figure 3.10 has shown the presence of a Ti^{3+} contribution related to the Ti 2p core level. The resulting Ti^{3+}/Ti^{4+} ratios - reported in Table 3.1 - have been interpreted in terms of sheet carrier density at the interface - as shown in Figure 3.11 - obtaining an evaluation of the depth distribution of the Ti^{3+} ions below the junction. Furthermore, the band offset analysis has been carried out by two different approaches, i.e the

Kraut's method and the linear combination of the VB spectra of the parent compounds (bare STO and LAO) to match the VB profile for the heterostructures. On the basis of the obtained results and resonant photoemission measurements, the band diagrams for the 5 u.c. conductive and the 3 u.c. insulating samples have been reconstructed in Figure 3.24 and the interface states related to the 2DEG have been evidenced and compared with other in-gap states of different compounds, as shown in Figure 3.27.

Besides, exploiting an high-flux μ-sized focused x-ray beam, the chemical homogeneity on the nm-scale has been proved by an XPEEM analysis (Figure 3.28 and 3.29), which ascribes the modulation of the photoemission intensity only to different carbon contaminations (i.e. common adventitious hydrocarbon in the flat regions or compact islands). Indeed, the chemical homogeneity is further remarked by the results from the XAS-PEEM (Figure 3.30), which evidence an nm-scale homogeneous XAS Ti L-edge referred to a Ti^{4+} oxidation state, without signatures of Ti^{3+} configuration despite of a 2 h long acquisition time. This fact excludes - at least for the sample under investigation and for the photon flux used for the experiment - the case of structural distortions, such as Ti-O buckling invoked by Plumb *et al.* [230]. Another hint, which suggests that the x-ray irradiation may not influence the crystal structure in the bulk, stems from the unexpected lack of shape deformations of Sr 3d in μ-XPS measurements as a function of the exposure time (Figure 3.31). The latter has a significant importance in comparison with the other μ-XPS results of La 4d and Al 2s (Figure 3.32 and 3.33, respectively), which differently show evident changes in the core level lineshape. Furthermore, Al 2s exhibits a different relaxation time with respect to the La 4d case (Figure 3.32 (c) and Figure 3.33 (c), respectively), recovering the long-irradiated condition apparently in half the time. These facts not only evidence a diversity between the bulk elements (Ti and Sr) and the film elements (Al and La), but even show a different behavior between the elements belonging to the same compound (between Al and La), as if the effects of x-ray exposure have different consequences on different elements. Finally, concerning the Ti 2p μ-XPS data of Figure 3.34 and 3.36, we have detected an increase of the Ti^{3+} contribution as a function of the x-ray irradiation and a regeneration of the original condition after the exposure of the sample in low oxygen pressure at room temperature. Thus, considering that (i) the Ti^{3+} states are located at the interface and (ii) it is reasonable to believe that the molecular oxygen

reacts with the sample surface, we are encouraged to suggest that the origin of the Ti^{3+} states is more likely connected to the surface rather than the interface.

Therefore, on the basis of the comparison among different in-gap states of paragraph 3.6, we may rule out both the oxygen vacancies and the defects, which can be located at the interface, as the origin of both the Ti^{3+} states and the interface states. In this way, we may exclude even the photogeneration of electron-hole pairs directly due to the x-ray irradiation, at odds with the observations of Berner *et al.* [189, 221], suggesting instead that the surface oxygen vacancies, along with the induced structural deformations in the film, are indeed caused by the x-ray beam and, in turn, they may be responsible for the interfacial conductivity. In fact, the origin of the 2DEG can be justified by the presence of surface oxygen vacancies, acting as a charge reservoir whence most of the electrons in excess are confined at the interface [216]. In this case, the oxygen vacancies may induce localized in-gap states thanks to the disordered arrangement on the surface, whereas the two extra-electrons per vacancy released can be transferred into the empty band of the interfacial Ti via the polar field of LAO, thereby resulting both in a reduction of the internal field and the flattening of the LAO band which thus should not exhibit core level shifts or broadening in relation with the film thickness, as shown in Figure 3.20. Indeed, several DFT calculations [216, 238–240] predict a similar result in which the formation of oxygen vacancies on the LAO surface is energetically favorable with respect to the STO substrate. In conclusion, a final hint which may support this interpretation can be provided by the calculated band diagrams presented in Figure 8 (b) and (c) of Ref. [216] for an amount $\geq 25\%$ of oxygen vacancies on the LAO film, which are in agreement with our band profiles of Figure 3.24 reconstructed on the basis of direct photoemission measurements.

Chapter 4

AR-XPS study on $LaAlO_3/SrTiO_3$

Another controversial issue at the center of a keen debate is the presence of the cation interdiffusion across the LAO/STO interface[1]. So far, several studies have evidenced a cation disorder at the junction using different techniques, such as angular dark field (ADF) imaging in scanning transmission electron microscopy (STEM) [179, 209, 241], surface x-ray diffraction (SXRD) [190, 191], angle-resolved XPS (AR-XPS) [185, 213], crystal truncation rod (CTR) [190], Rutherford backscattering (RBS) [185], cross-sectional STEM with electron energy loss spectroscopy (STEM-EELS) [185, 202], x-ray reflectivity (XRR) [190], medium-energy ion spectroscopy (MEIS) [185,241,242], time-of-flight secondary ion mass spectrometry (ToF-SIMS) [185] and Kelvin probe force microscopy (KPFM) [242]. Cation interdiffusion is found to be present also when different deposition techniques are used (generally, PLD and MBE) and even though the surface quality of the LAO film during the growth is monitored by reflection high-energy electron diffraction (RHEED) to verify the two-dimensional layer-by-layer growth of the film. Usually, the low surface roughness is further confirmed by atomic force microscopy (AFM), showing smooth terraces with clear unit cell steps which follow the surface morphology of the TiO_2-terminated STO

[1] Hereafter, only the n-type LAO/STO interface is considered.

substrates [222]. However, it is noteworthy that the growth conditions - especially the annealing procedure and the oxygen pressure during/after the film deposition - can significantly affect the two-dimensional layer-by-layer growth of the film [222], in terms of full stoichiometry and/or surface roughness. Nevertheless, in the $10^{-5} - 10^{-3}$ *mbar* range of oxygen partial pressures and for growth temperatures between 750°C and 850°C, a LAO film can be grown with an interface of high quality, as demonstrated by different groups [131, 209].

In this complex scenario, we can retrieve several hints about the distribution and the role of cation disorder at the LAO/STO interface, equally supported by ab-initio DFT calculations. For instance, Willmott *et al.* [191] have revealed the layer-by-layer constituent concentration by SXRD for a 5 u.c. LAO/STO heterostructure[2], showing a not-abrupt junction where the cation interdiffusion occurs at different depths for two cation pairs, i.e. Sr-La and Ti-Al. From the resulting intermix, a layer of about 1-2 u.c. of $La_{1-x}Sr_xTiO_3$ is recognized at the interface, leading to a lattice expansion due to presence of Ti^{3+} ions which may induce the interfacial conductivity. A similar cation distribution has been obtained by Chambers *et al.* [185, 213], who are the only ones to have taken advantage so far of the AR-XPS technique to study the abruptness of the LAO/STO interface[3]. Although an analytical approximation of the core-level photoemission intensity has been used to model the signal attenuation as a function of the take-off angle of detection, an evaluation the elemental profiles as a function of the depth has been achieved, suggesting the outdiffusion of Sr and Ti cations into the LAO film and the indiffusion of La and Al cations into the bulk. Subsequently, Vonk *et al.* [190] have evaluated a La-interdiffusion depth of 2 u.c. by XRR on a LAO/STO 5 u.c. sample[4]. This result is corroborated by a CTR investigation [190], which detects a significant amount of La-vacancies in the film - especially in the overlayer - up from the deposition of the first LAO layer; the latter outcome is interpreted as a La-Sr exchange even during the deposition in both the STO bulk and the topmost layer of the LAO film,

[2]LAO/STO 5 u.c. grown by PLD at 770°C in $p_{O_2} = 5 \cdot 10^{-6}$ *mbar*. The deposition was monitored by RHEED [191].

[3]LAO/STO 4 u.c. grown by PLD at 770°C in $p_{O_2} = 1 \cdot 10^{-5}$ and $8 \cdot 10^{-6}$ *mbar*. The deposition was monitored by RHEED and the terrace-step surface morphology was verified by AFM [185, 213]

[4]LAO/STO 1-5 u.c. grown by PLD at 770°C in $p_{O_2} = 3 \cdot 10^{-5}$ *mbar*. The deposition was monitored by RHEED and the terrace-step surface morphology was verified by AFM [190].

thereby forming charge-neutral $La_xSr_{1-1.5x}O$ layers. As a consequence, Ti-Al intermixed layers or Ti-vacancies at the interface are suggested to structurally compensate the diverging electrostatic energy build-up.

Recently, a study of Warusawithana *et al.* [202] have instead connected the arise of the interfacial conductivity to the La/Al stoichiometry of the film. In facts, on the basis of STEM-EELS measurements on LAO/STO 8 u.c. samples[5], both insulating and conductive samples have evidenced cation interdiffusion across the junction, but no correlation between conductivity and a specific exchange of cation pairs has been observed. On the other hand, the insulator-to-metal transition has been obtained only for La/Al $\leqslant 0.97 \pm 0.03$, having ruled out the extrinsic origin of defects during the growth. Furthermore, this interpretation has been found consistent with the polar catastrophe model; actually, combining the DFT calculations and the results by STEM-EELS, for the La/Al>0.97 case the formation of Al_2O_3-vacancy-complexes at the interface has been revealed, removing the divergent potential without the transfer of electronic charge, whereas for the La/Al$\leqslant$ 0.97 case the Al-La substitution should inhibit the cation migration to form interfacial vacancies, suggesting an electronic charge transfer along with a surface reconstruction as the reason for the 2DEG origin.

In this chapter, an AR-XPS study is presented for the 5 u.c. conductive, 3 u.c. insulating and 5 u.c. insulating LAO/STO interfaces. The goal of the present analysis is (*i*) to improve the model so far taken into account for the AR-XPS analysis on the basis of the BriXias code[6] and (*ii*) to verify its effectiveness for an interface characterization aimed at achieving the cation profiles across the heterojunction, (*iii*) to obtain information about the abruptness of the interface, (*iv*) the film thickness, (*v*) the La/Al film stoichiometry ratio or (*vi*) to investigate possible effects of interfacial cation disorder (i.e. interdiffusion, substitution, vacancy).

[5]LAO/STO 8 u.c. grown by MBE at 680°C in $p_{O_2} = 1.3 \cdot 10^{-6}$ *mbar*. The deposition was monitored by RHEED [202].

[6]See paragraph 1.6 for a detailed description about the modeling of the XPS peak angular dependence.

4.1 Method and Model

Angle-resolved XPS experiments consist of collecting the core-level photoemission peak intensity as a function of the polar angle θ, which is defined by the normal of the surface and the direction of the photoelectron detection, as displayed in Figure 4.2 (a). This method is widely used to probe non-destructively the chemical composition as a function of depth and evaluate the thickness of thin films in multilayers. The physical origin of the angular dependence attenuation of the core-level photoemission intensity stems from the inelastic and elastic scattering processes, which the photoelectrons undergo during the propagation from the emitter to the surface. Considering in first approximation only the inelastic scattering processes, this phenomenon can be treated as an isotropic damping in relation with the distance crossed by the photoelectrons inside the matter, i.e. the inelastic mean free path (IMFP), λ_i. Thus, the *effective escape depth* is usually approximated as $\sim 3\lambda_i \sin\theta$ - that is the depth within which the $\sim 95\%$ of signal is generated - where λ_i can be analytically calculated by the well-known TPP-2M formula [19] as a function of the kinetic energy of the photoelectrons and several properties of the material which slows down the electron motion (i.e., density, atomic weight, band-gap, free-electron plasmon energy and the number of valence electrons per atom). Since a comparison of the angular peak intensities between the film and substrate is strictly needed for an AR-XPS analysis, the *effective escape depth* restricts the depth range of the method to thin films below ~ 5 *nm* for soft x-ray investigation, whereas hard x-ray experiments provides the possibility to probe multilayers in which the heterojunction is more in depth.

If also the elastic scattering processes are taken into account, the effective modeling of the XPS intensity becomes more complex. For the present analysis, we have considered both inelastic and elastic electronic scattering processes as already presented in paragraph 1.6. Starting from the multilayer model shown in Figure 4.1 - which reproduces the layered structure of $SrO\text{-}TiO_2$ in the STO substrate and $LaO\text{-}AlO_2$ in the LAO film - we have calculated by Monte Carlo (MC) computations[7] the depth distribution function (DDF) of the LAO/STO interface. Thus, on the basis of eq. 1.45 in paragraph 1.6, we can obtain

[7]The MC calculations are based on the algorithm described by Werner in Ref. [48] and were carried out within the BriXias code [44] for the present study.

the photoemission intensity[8] related to a core-level peak as the sum of the contributions of each layer:

$$I_{Al}(E_k,\theta) = K \cdot \sum_{n=0}^{N} \left[C_{2n}^{Al} \cdot \int_{2n}^{2n+1} \phi(E_k,\theta,z)dz \right] \tag{4.1}$$

$$I_{La}(E_k,\theta) = K \cdot \sum_{n=0}^{N} \left[C_{2n+1}^{La} \cdot \int_{2n+1}^{2n+2} \phi(E_k,\theta,z)dz \right] \tag{4.2}$$

$$I_{Ti}(E_k,\theta) = K \cdot \sum_{n=N}^{100} \left[C_{2n}^{Ti} \cdot \int_{2n}^{2n+1} \phi(E_k,\theta,z)dz \right] \tag{4.3}$$

$$I_{Sr}(E_k,\theta) = K \cdot \sum_{n=N}^{100} \left[C_{2n+1}^{Sr} \cdot \int_{2n+1}^{2n+2} \phi(E_k,\theta,z)dz \right] \tag{4.4}$$

where K is the normalization constant which includes the photoionization cross section [24], the atomic density of the species and analyzer-dependent parameters, n is the label for the atomic layer, N is the number of unit cell of the LAO film, C_n^j is the occupation factor of the cation j in the atomic layer n, and $\phi(E_k,\theta,z)$ is the DDF of an electron generated at a depth z with a kinetic energy E_k at the polar angle θ for the LAO/STO multilayer model. In this way, it is possible to simulate the effective angular photoemission intensity of selected core level peaks by changing only the cation occupation in the atomic layers of the model of Figure 4.1.

Nevertheless, in periodic lattices marked variations of the photoemission intensity occur in relation with polar θ and azimuthal ϕ angles (see Figure 4.2) due to the photoelectron diffraction (XPD). This effect adds uncertainty to the modeling and should be considered in the data treatment and analysis. On the other hand, a fully quantitative analysis of the elastic scattering effects, based on a mechanical multiple scattering formalism [243], allows to obtain structural local information around each photoemitter atomic species in the crystal. However, the specific case of the LAO/STO interface - which may

[8] A common scaling factor is consider for eq. (4.1)-(4.4) in order to tune the calculations with respect to the experimental intensity. In addition, an extra layer on the LAO surface is added in the multilayer model of Figure 4.1 to account for the adventitious carbon contamination of the samples. The effective thickness of this layer is adjusted by fitting procedure to match the slope of the overall experimental AR-XPS profiles.

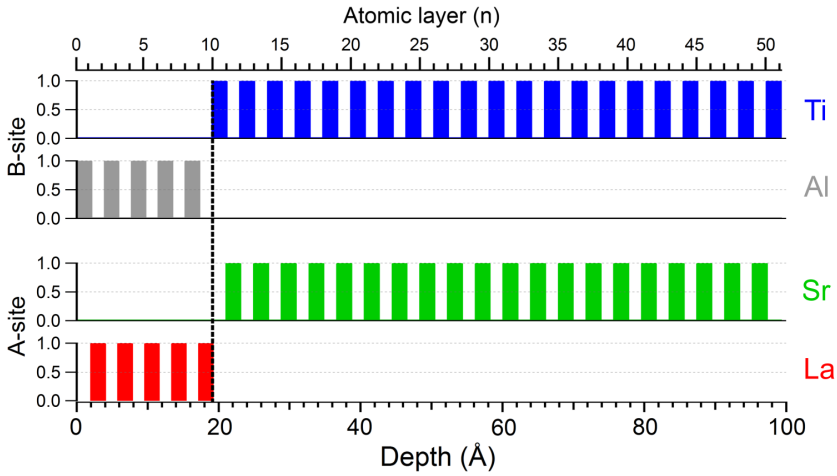

Figure 4.1: *Layered structure model for the 5 u.c. LAO/STO interface used for the DDF calculations. The intensity of the bars stands for the cation occupation of the layer.*

exhibit cation substitutions, dislocations, as well as vacancies across the junction - makes these calculations extremely complex and CPU time-expensive because of the high number of atomic arrangements which should be taken into account.

For this reason, the effective approach described by eq. (4.1)-(4.4) has been used to interpret the experimental results, trying to reduce the polar photodiffractive modulation by means of an average on the azimuth ϕ angles. Thus, selecting[9] the Sr 3d, Al 2s and La 4d core level peaks shown in Figure 3.9 (a), we have collected the XPS integrated peak area[10] in the 0°-65° range of the polar angle θ and 0°-45° for the azimuthal angle ϕ, obtaining the XPD pattern for each core level, as displayed in Figure 4.2 (b) for the Sr 3d peak. Then, we have averaged each polar scan on the azimuthal angle ϕ, thereby averaging out the sharp XPD modulations[11] and obtaining the averaged AR-XPS profiles, as

[9] Because of a similar binding energy allowing to collect single spectra for all the peaks.

[10] After the removal of the satellite lines and the subtraction of a Shirley background.

[11] Except for the peak at $\theta = 0°$due to the forward-focusing effect. This intensity enhancement is generated via the small-angle elastic scattering by atoms in the outgoing path immediately adjacent to the emitter. This effect is more evident for the photoelectrons of the film (La and Al), since the electrons emitted from the substrate (Ti and Sr) are de-focused by the atoms in the LAO film along the photoemission direction, in relation with the film

shown in Figure 4.2 (c).

Since the photoemission intensity of the Ti 2p core level is weaker than those of Sr 3d and La 4d, the photodiffraction modulations related to Ti 2p become negligible[12]. Therefore, we have collected the AR-XPS profile for Ti 2p within the range of 0°-65°polar angle θ at *only* $\phi = 0°$. In this case, we have used the *transmission-mode* of the electron analyzer in order to maximize the count ratio and speed up the acquisition time; however, this procedure reduces the polar angular resolution with respect to the *angular-mode* case, which was instead used for the acquisition of other core levels.

4.2 Abrupt interface model: stoichiometric case

Considering the Sr 3d, Al 2s and La 4d core levels, we have calculated the AR-XPS profiles for a layered structure model including an abrupt interface, a nominal thickness for the different films (5 u.c. or 3 u.c.) and the nominal 1:1 stoichiometric ratios for both the film ($La/Al = 1$) and bulk ($Ti/Sr = 1$) components. The results are shown in Figure 4.3 (a) for the 5 u.c. conductive, (b) for 5 u.c. insulating and (c) for 3 u.c. insulating LAO/STO sample. Even though a quite good matching between the experimental and calculated profiles can be observed for the 3 u.c. sample in panel (c), in the 5 u.c. samples an evident discrepancy is present for the Sr 3d peak. In addition, a slight difference can also be noted for the Al 2s core level in (a) 5 u.c. conductive and (c) 3 u.c. insulating samples. In the former case, we may explain the discrepancy between experiment and the modeling either with a film thickness variation (island formation) or a cation interdiffusion across the interface, whereas the latter may be a signature of a modified La/Al stoichiometry ratio in LAO film.

4.2.1 Terrace roughness model

To correct the Sr 3d discrepancy shown in Figure 4.3 (a) and (b), we have taken into account the possibility of island formation during the film deposition

thickness.

[12] A demonstration is given by the Al 2s core level displayed in Figure 4.2 (c), which shows a slight attenuation of the XPD modulation from the polar scan taken at $\phi = 0°$(grey circles) and the ϕ-averaged profile (black solid line). Because Ti 2p exhibits a similar photoemission intensity to Al 2s peak, the same reasoning is valid.)

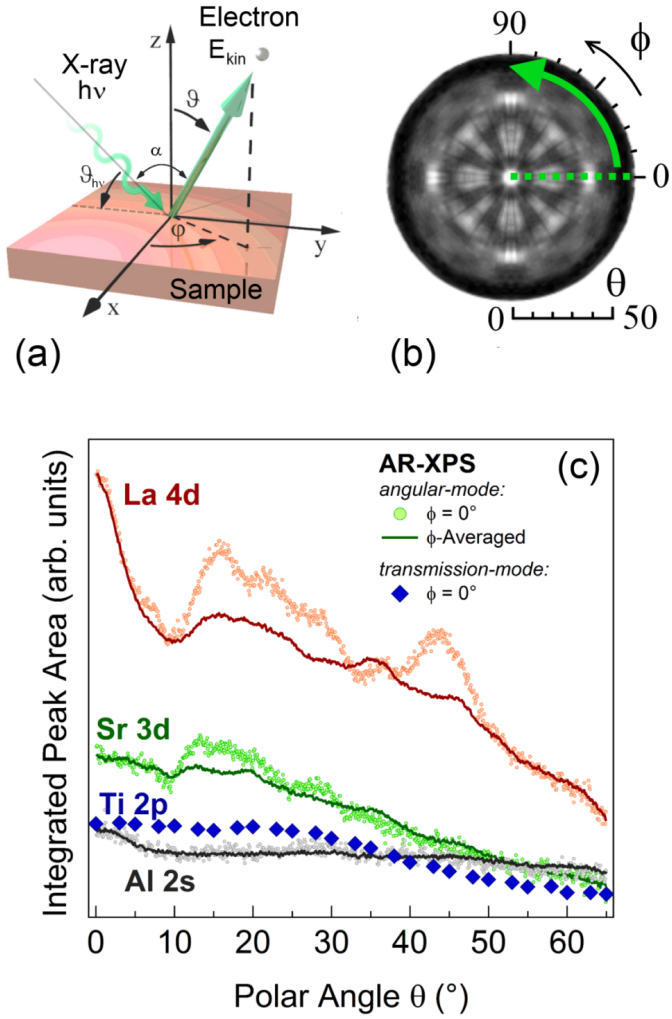

Figure 4.2: *(a) Schematic of the experimental geometry: polar angle θ, azimuthal angle ϕ. The α angle between the x-ray source and the electron analyzer is fixed at 54.5°, eliminating the asymmetry correction. (b) XPD pattern for the La 4d core level in the LAO/STO 3 u.c. insulating. The green dotted line points out the polar scan at $\phi = 0$°, while the green arrow indicates the angular ϕ-range used for the average. (c) Angular-mode ϕ-averaged AR-XPS profiles for the La 4d (red solid line), Sr 3d (green solid line) and Al 2s (grey solid line) peaks. Angular-mode AR-XPS profiles at $\phi = 0$°are displayed for comparison (filled circles). Transmission-mode AR-XPS of Ti 2p (blue diamonds) is taken for $\phi = 0$°and normalized with respect to the other profiles.*

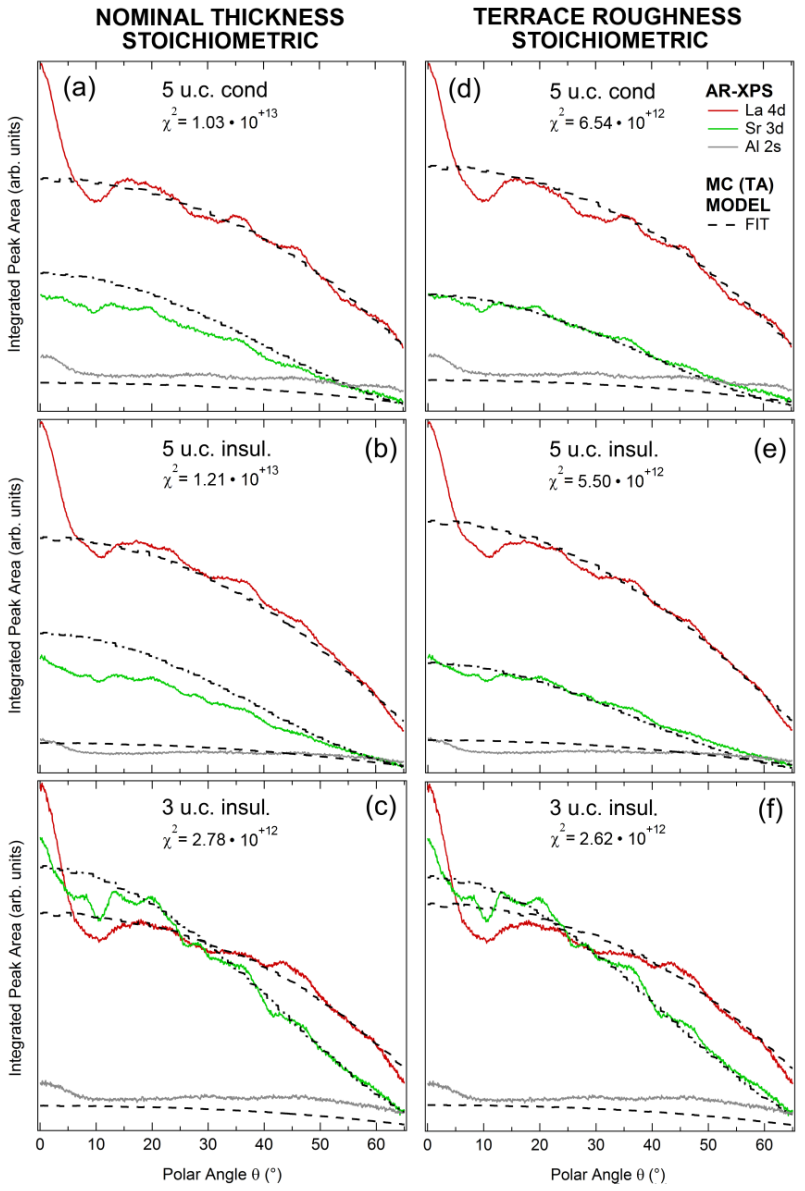

Figure 4.3: *ϕ-averaged AR-XPS data of the LAO/STO samples for La 4d (red line), Sr 3d (green line) and Al 2s (grey line) core levels. Left panels (a-c): calculated curves (black dotted lines) for a model based on (*i*) the abrupt interface, (*ii*) the exact stoichiometry of the film and bulk compounds and (*iii*) the nominal film thickness. Right panels (d-f): fitting curves (black dotted lines) for the results of the terrace roughness model reported in Figure 4.4. Points (i) and (ii) are considered.*

due to not-optimal growth conditions [222]. In this model two extra variables are added with respect to the previous case, that is (*i*) the island thickness above the surface level and (*ii*) the island surface occupation (for instance, 0% occupation means that no islands are present, whereas 100% occupation stands for a flat film surface with a film thickness which is increased of the island thickness). Moreover, we have considered the former (*i*) as a discrete variable, while the latter (*ii*) as a fitting variable. Figure 4.4 shows the resulting configurations for the 5 u.c. conductive (green), 5 u.c. insulating (red) and 3 u.c. insulating sample (blue), considering the best island surface occupations in relation with selected island thicknesses (n u.c.); a schematic of the terrace roughness model is displayed as an inset.

By spanning different terrace heights (*i*) and widths (*ii*), the points of each curve in Figure 4.4 yield virtually the same χ^2 value. As samples with a large island thickness (*i*) are less likely to be grown, we focus on the results obtained for the simplest case, i.e. the terrace with 1 u.c. above the nominal thickness. Thus, considering $n = 4$ for blue and $n = 6$ for red and green curves of Figure 4.4, the resulting AR-XPS profiles from the fitting procedure are displayed in Figure 4.3 (d) for the 5 u.c. conductive, (e) for 5 u.c. insulating and (f) for 3 u.c. insulating LAO/STO sample. In each sample, we observe that the fitting of the Sr 3d profile is clearly improved. Therefore, the convergence of the fitting procedures appears

- for the 3 u.c. insulating sample with an almost ideal configuration, in which the film shows small islands of about 20% of occupation;
- for the 5 u.c. conductive sample with a film thickness increased of 1 u.c. for almost the whole surface area (about 80%);
- for the 5 u.c. insulating sample with a film thickness increased of 1 u.c. for the whole surface (100%).

In such a way, the average AR-XPS data can be modeled using an abrupt interface by ascribing to surface roughness the mismatch between the calculations for a nominal thickness of the LAO film and the experimental bulk profile (i.e., Sr 3d peak). Nevertheless, the discrepancy between experiment and theory concerning the Al 2s profiles for the 5 u.c. conductive and 3 u.c. insulating LAO/STO remains unchanged.

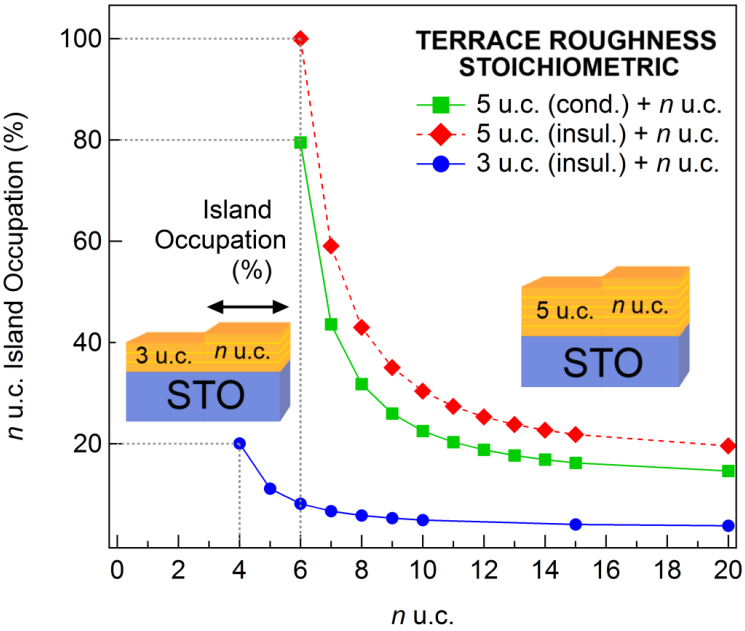

Figure 4.4: *Fitting results of the n u.c. island occupation vs the n u.c. within the terrace roughness model for the LAO/STO samples. The AR-XPS results are equivalent in χ^2 value for each point of the same sample, as shown in Figure 4.3 (d) for 5 u.c. conductive, (e) for 5 u.c. insulating and (f) for 3 u.c. insulating sample.*

4.2.2 Surface cation vacancies

In this section, an improvement of the previous model is carried out in order to account for the Al 2s profile discrepancy between the experiment and theory so far shown in Figure 4.3 (a), (c), (d) and (f). Instead of island formation on the surface, here we have considered the possibility to add at most two overlayers of LAO, which can host both La and Al cation vacancies, on the surface of the LAO film characterized by a nominal thickness (i.e., 5 u.c. or 3 u.c.). The fitting results and the schematics of the layered structure model are shown respectively in Figure 4.5 (a) and (d) for the 5 u.c. conductive, (b) and (e) for 5 u.c. insulating, (c) and (f) for 3 u.c. insulating LAO/STO. Considering the AR-XPS profiles (a-c), in every sample a good match has been achieved,

whereas from the layered models (d-f) we can note that:

I. the conductive LAO/STO (a,d) exhibits an overall extra effective thickness of $\sim$ 1.25 u.c. (i.e. the total amount of AlO_2 + LaO extra layers) with respect to $\sim$ 0.75 u.c. for the insulating samples;

II. the 5 u.c. conductive and 3 u.c. insulating samples, which were grown in the same p_{O_2} conditions, show a greater extra-layer occupation of AlO_2 with respect to LaO, in comparison with the 5 u.c. insulating LAO/STO.

At this stage, the first result (I.) may be a distinctive structural feature related to the interfacial conductivity - in comparison with both the insulating samples - while the second result (II.) appears as a clear indication of a modified La/Al stoichiometry ratio of the LAO film in relation with the growth conditions, as already evidenced in Figure 3.9 (a).

4.3 Abrupt interface model: La/Al stoichiometry correction

At the light of the results so far obtained about the modified La/Al stoichiometry for the LAO/STO samples, the goal of the present section is to estimate the average La/Al stoichiometry ratio for each heterojunction in the limit of an abrupt interface.

Assuming that the La/Al ratio is not dependent on the LAO thickness, we have considered the nominal film thicknesses (i.e., 5 u.c. and 3 u.c.) in the layered structure model, using the overall cation concentration of La and Al as fitting variables. Moreover, taking into account the conclusions[13] of Warusawithana *et al.* [202] and the La/Al ratios measured by XPS in paragraph 3.3, we have improved the model in order to change the La/Al stoichiometry by:

- AlO_2-complexes vacancies for the 5 u.c. insulating sample, since it shows an insulating character[14] and exhibits a La/Al ratio > 1;

[13] Go to the introduction of this chapter for a brief review.

[14] Due to the growth condition $p_{o_2} = 10^{-1}$ *mbar* and despite of the LAO thickness exceeds the critical thickness of 4 u.c. for the arise of conductivity.

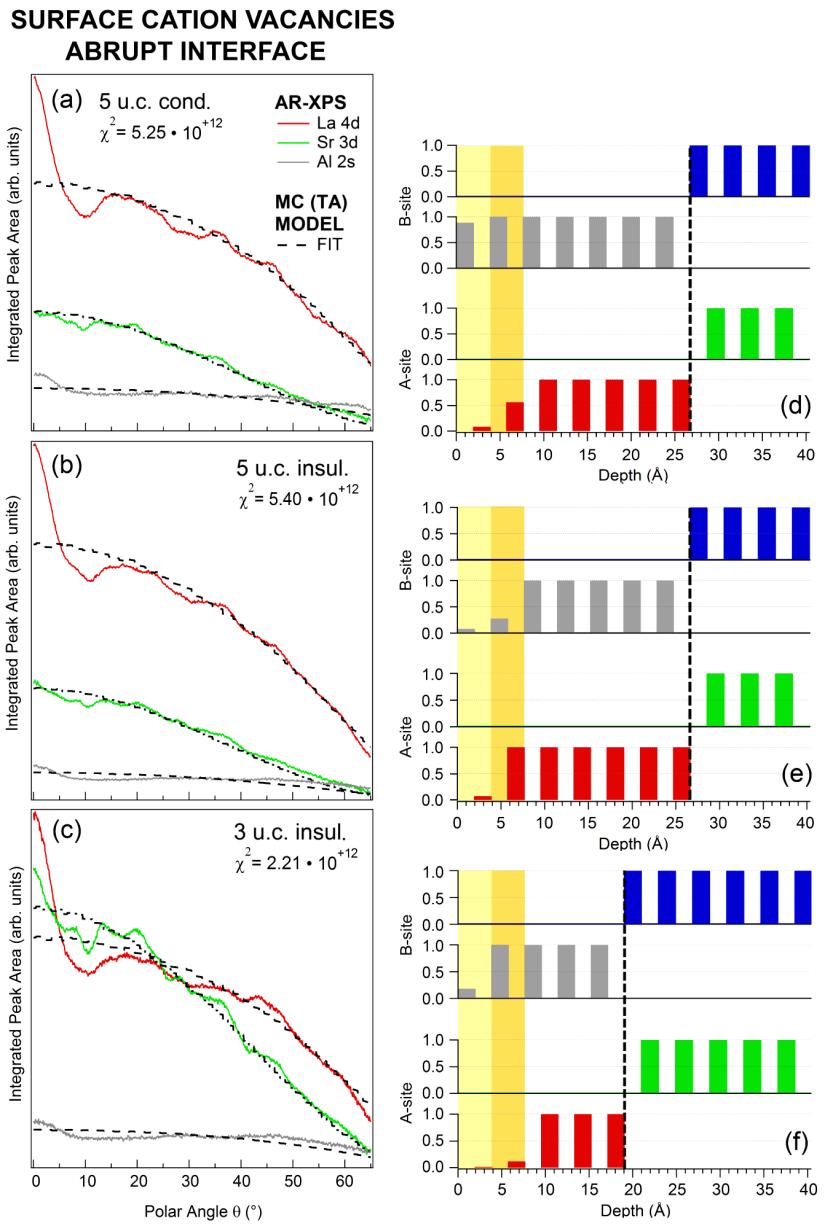

Figure 4.5: *Left panels (a-c): ϕ-averaged AR-XPS data of the LAO/STO samples for La 4d (red line), Sr 3d (green line) and Al 2s (grey line) core levels and calculated curves (black dotted lines) for a model based on* (i) *the abrupt interface,* (ii) *the exact stoichiometry of the nominal film thickness and bulk compounds and* (iii) *the surface La- and Al-cation vacancies. Right panels (d-f) display the stack of layers (blue, TiO_2; grey, AlO_2; green, SrO; red, LaO) in which the intensity (0-1) means the percent effective occupation. Orange-shaded regions highlight the two extra layers which are added at the surface as extension of the nominal thickness for the LAO film.*

- La-Al substitutions for the other samples[15], because they exhibit interfacial conductivity above the LAO critical thickness (i.e., 4 u.c.) and show a La/Al ratio < 1.

Thus, Figure 4.6 (a-c) display the fitting results for the La 4d and Al 2s ϕ-averaged AR-XPS profiles, resulting in a La/Al stoichiometry ratio of 0.71 for the 5 u.c. conductive (a), 1.26 for 5 u.c. insulating (b) and 0.68 for 3 u.c. insulating (c) samples. These estimations appear to be quite confident with those based on the direct measurement of the XPS peak area (0.83 for 5 u.c. cond.; 1.42 for 5 u.c. insul.; 0.88 for 3 u.c.). Nevertheless, the small discrepancy (within 0.2) can be ascribed to the various restrictions applied in the present model (e.g., abrupt interface, nominal thickness, ...). The schematics for the resulting fitting analysis are shown in Figure 4.8 (d-f).

Then, by setting the layered structure model with the La and Al cation occupancies just found, we have calculated again the AR-XPS profiles considering also the substrate Sr cation, i.e. Sr 3d core level. The fitting results are displayed in Figure 4.6 (d-f). As expected, we can observe a pronounced overestimation of the Sr profile by the model, enhanced by La/Al correction especially for the 3 u.c. sample.

[15]Grown at $p_{O_2} = 10^{-3}$ *mbar*, within the optimal range of deposition.

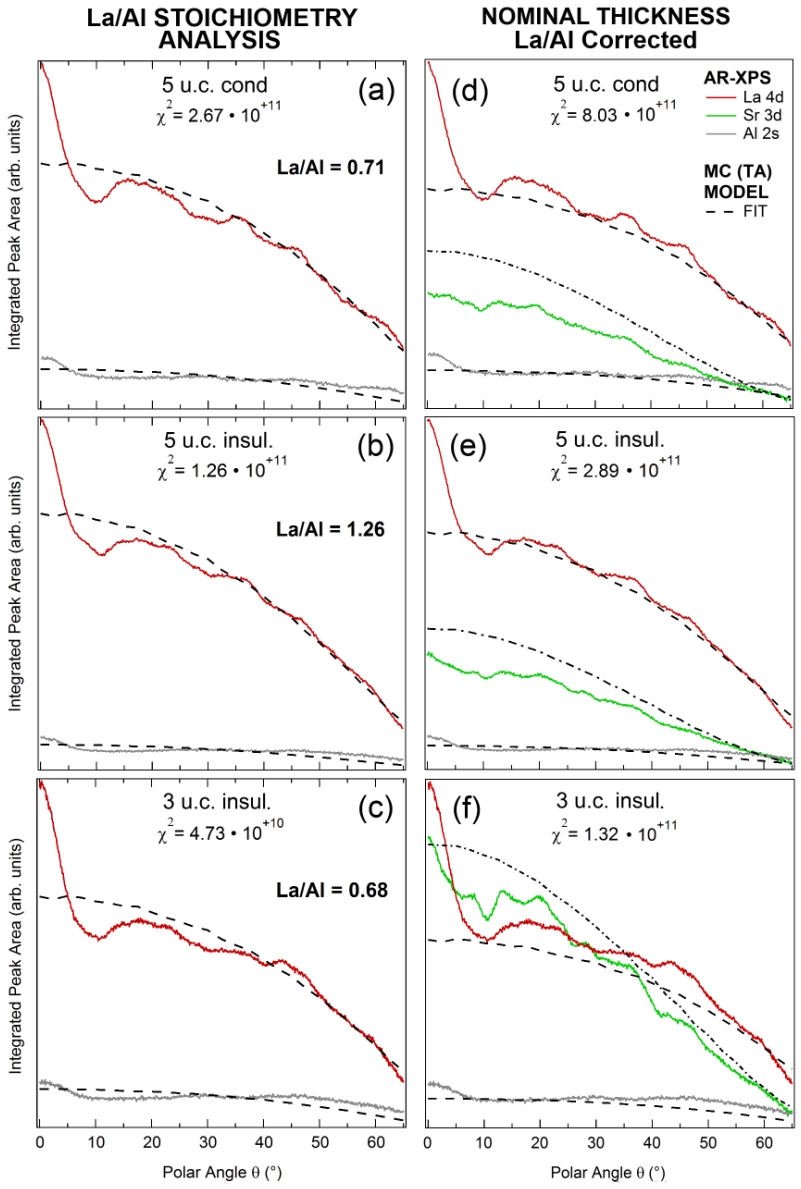

Figure 4.6: *Left panels (a-c): ϕ-averaged AR-XPS data of the LAO/STO samples for La 4d (red line) and Al 2s (grey line) core levels for a stoichiometry evaluation of the film compounds. Calculated curves (black dotted lines) for a model based on (*i*) the abrupt interface, (*ii*) the exact stoichiometry of the bulk compounds and (*iii*) the nominal thickness of the LAO film. La/Al resulting ratios are reported for each sample. Right panels (d-f) display the comparison between the experimental AR-XPS for La 4d, Sr 3d (green line) and Al 2s and the calculated profiles (black dotted lines) on the basis of the points (i), (ii) and (iii) and the resulting correction of the La/Al stoichiometry.*

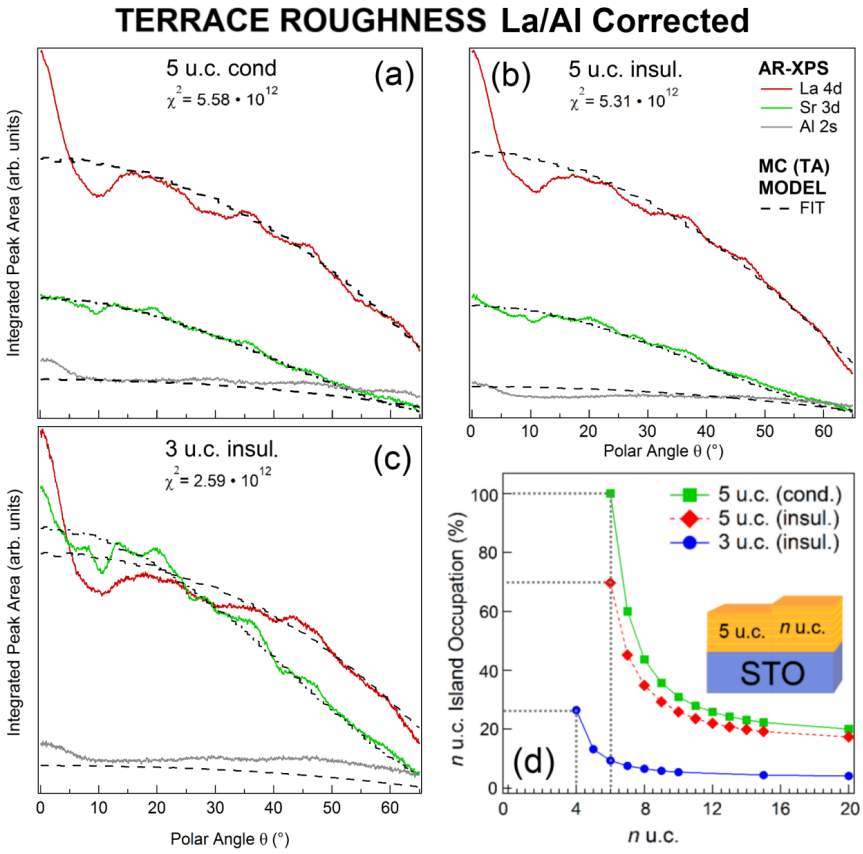

Figure 4.7: *Panels (a-c): ϕ-averaged AR-XPS for La 4d (red line), Sr 3d (green line) and Al 2s (grey line) and the fitting curves (black dotted lines) for the results of the terrace roughness model reported in panel (d). The (i) abrupt interface, (ii) stoichiometric bulk and (iii) the La/Al stoichiometry correction are taken into account. (d) Fitting results of the n u.c. island occupation vs the n u.c. within the terrace roughness model with the La/Al stoichiometry correction. The AR-XPS results are equivalent in χ^2 value for each point of the same curve.*

4.3.1 Terrace roughness model with La/Al correction

In addition, similarly as in paragraph 4.2.1, we have applied the terrace roughness model to adjust the convergence of the fitting procedure, but using this time the La/Al stoichiometry correction. The resulting profiles are shown in Figure 4.7 (a-c), while panel (d) displays the width (% occupation) vs thickness (n u.c.) relationship for terraces on the three samples. Comparing the present results with those of Figure 4.4 for the stoichiometric terrace roughness model, we can observe a slight deviation for the 3 u.c. sample and the inversion of results for the 5 u.c. samples, where the conductive LAO/STO (100% occupation) is this time more covered than the insulating one ($\sim$ 70%). Considering instead the resulting AR-XPS fitting profiles of Figure 4.7 (a-c) with respect to those displayed in Figure 4.3 (d-f), we can appreciate the improvement of the present model by a slight decrease of the χ^2 values.

Therefore, we can conclude that the present results are similar to those obtained in paragraph 4.2.2, but using a different modeling. In facts, the La/Al stoichiometry correction (and evaluation) has been carried out - for the latter (par. 4.2.2) - by means of additional LAO layers on the surface, which can host selective cation vacancies (Al or La), or by a terrace roughness model in which all the layers have been previously corrected in the overall La/Al stoichiometry ratio - as in the present paragraph.

4.3.2 Remarks about the abrupt interface model

So far we have considered in the AR-XPS analysis only a single core level from the bulk substrate, i.e. the Sr 3d peak. The reason of this choice stems from the narrow binding energy range which include Sr 3d, Al 2s and La 4d, which allowed us to take all the core levels in single spectra, thereby exploiting a longer acquisition time with the electron analyzer in the optimal condition (angular-mode) to reach the highest θ-angular resolution. However, the information of the Ti 2p core level are essential to understand if the restriction of the abrupt interface is suitable or a cation disorder must be taken into account. In such a way, adding the Ti profile for each sample[16], we have carried out the calculations

[16] As already described in paragraph 4.1, the AR-XPS for Ti 2p was collected with discrete steps in polar angle θ due to a different acquisition mode of the electron analyzer, i.e. transmission-mode, to speed up the experiments because of a reduced photoemission intensity

assuming

- an abrupt interface,
- a nominal film thickness,
- a La/Al stoichiometry ratio correction.

The results are shown in Figure 4.8 (a-c) for the AR-XPS profiles and in panels (d-f) for the schematics of the resulting layered structure models. In every sample (a-c), we can observe a quite good match for the Ti 2p profiles, despite of slight discrepancies in the slopes, whereas the overestimation of the experimental Sr 3d profiles is still rather pronounced. This overall evidence suggests that AR-XPS data may not be modeled using an abrupt interface, since any additional layer on the surface (homogeneous or islands) decreases both the Sr and Ti AR-XPS profile intensity. In other words, within the restriction of the abrupt interface is not possible to correct the Sr 3d profile leaving the intensity of the Ti 2p unchanged. Therefore, we have achieved the following hints:

I. the experimental AR-XPS data cannot be modeled in the abrupt interface approximation if only the film thickness or the surface roughness are changed;

II. other structural modifications may be present either at the interface (e.g., cation substitution, vacancies, interdiffusion) or in the bulk substrate (i.e., a modified Ti/Sr stoichiometry ratio).

compared with the other core levels.

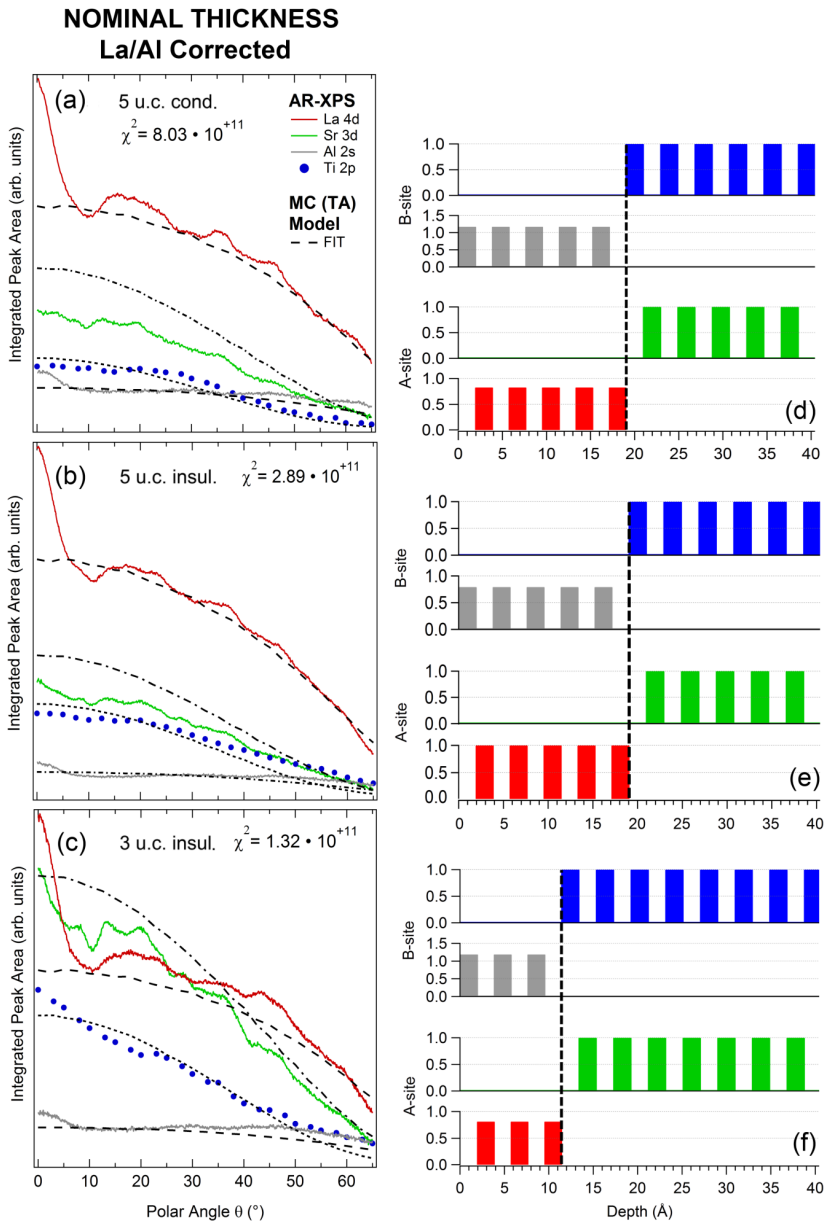

Figure 4.8: *Left panels (a-c): ϕ-averaged AR-XPS data of the LAO/STO samples for La 4d (red line), Al 2s (grey line), Sr 3d (green line) and Ti 2p (blue dots) core levels. The calculated profiles (black dotted lines) are obtained on the basis of (i) the abrupt interface, (ii) the nominal thickness of the LAO film, (iii) the exact stoichiometry for the bulk compounds and (iv) the correction of the La/Al stoichiometry of the film. Right panels (d-f) display the stack of layers (blue, TiO_2; grey, AlO_2; green, SrO; red, LaO) related to (a-c) panels respectively. The intensity of the bars (0-1) means the percent effective occupation.*

4.4 Interdiffusion model

As mentioned in the previous paragraph, the LAO/STO interface may be non-abrupt. As reported in several studies, multiple structural modifications can occur at the heterojunction, for instance the La-diffusion into the bulk as $La_xSr_{1-1.5x}O$ [190], La- and/or Al-vacancies at the interface layer [190,202], Al-Ti substitutions [185,191], Sr- and Ti-migration into the film [185,190,191,202], La- and/or Al-deficiency on the surface [190] and La-Al substitutions [202]. Considering the layered structure models of Figure 4.8 (d-f), which provide the La/Al stoichiometry evaluations for the samples, we have developed a fitting procedure which takes into account all the aforementioned processes, keeping the starting La/Al stoichiometry ratios unchanged and obtaining the layered structure model by which we can effectively reproduce the experimental AR-XPS profiles in the calculations. The fitting results are shown in Figure 4.9.

Generally, we can note that a good match is achieved for each sample, even if both the Al 2s and Ti 2p experimental profiles exhibit a slight slope-discrepancy, especially for the high θ-angles. However, it is noteworthy that both the Al 2s and Ti 2p are the profiles with the lowest intensity, for which the experimental uncertainty may affect more than in the other core levels. In addition, Ti 2p was collected with a low-angular resolution without the average procedure on ϕ-angles which could further reduce XPD modulations, particularly in the 3 u.c. sample where the forward-focusing at $\theta = 0^\circ$ is more pronounced. For these reasons, the accuracy about the Al and Ti cation occupation in the resulting layered models should be considered more qualitatively.

The 5 u.c. conductive sample shows (Figure 4.9 (d)) the greatest interdiffusion between the La and Sr cations, which is negligible after the fourth STO layer below the nominal interface (black dotted line) and is mostly limited at 2-3 u.c. at the junction, in agreement with other studies [185, 190, 191]. Moreover, the La-Al substitutions or La- and Al-vacancies slightly affect the final result. A similar cation interdiffusion is obtained for Ti and Al, with a small outdiffusion of Ti in the film.

Differently, the 5 u.c. insulating sample displays (Figure 4.9 (e)) a reduced La-Sr exchange depth across the nominal interface with respect to the previous case, mainly limited to the first layer below the junction. Here, an increased cation disorder can be observed concerning both the Al-Ti and Al-La substitu-

tions, Ti migration into the film, as well as La- and Al-vacancies.

However, it is noteworthy that the 3 u.c. sample exhibits (Figure 4.9 (f)) the lowest cation interdiffusion. In facts, the La-Sr substitution is mainly restricted to the first layer below the nominal interface and a similar result appears for the Al-Ti exchange.

In conclusion, starting with the results of Figure 4.8, which are based on:

- the abrupt interface,
- the nominal film thickness,
- and the stoichiometry correction of the LAO film in relation with the La/Al stoichiometry ratio[17], as suggested by Ref. [202],

and considering within the effective model all the structural modifications (in terms of cation occupancy of each laer) presented at the beginning of this paragraph, the following results are achieved:

- for $p_{O_2} = 10^{-3}$ *mbar* during the growth (5 u.c. cond. and 3 u.c.), an interdiffusion of the La-Sr and Al-Ti cation pairs is observed across the nominal interface within 3-4 unit cells, in agreement with other studies [185, 190, 191];
- for $p_{O_2} = 10^{-1}$ *mbar* during the film deposition (5 u.c. insul.), a cation interdiffusion of the La-Sr and Al-Ti pairs is evidenced across the nominal interface. However, at odds with the other samples, the La-Sr exchange appears to be rather reduced in depth, the Al-Ti substitution is more broadened and the overall layered structure shows a more pronounced disorder.
- Generally, the La-Sr exchange appears at larger depth with respect to the Al-Ti interdiffusion profile, in contrast with Ref. [191];
- and a Sr-deficiency is present for all the samples, with a low Sr-occupation in the first layer below the nominal interface.

[17] For La/Al$>$ 1, Al-vacancies; for La/Al$\leq$ 1, La-Al exchange.

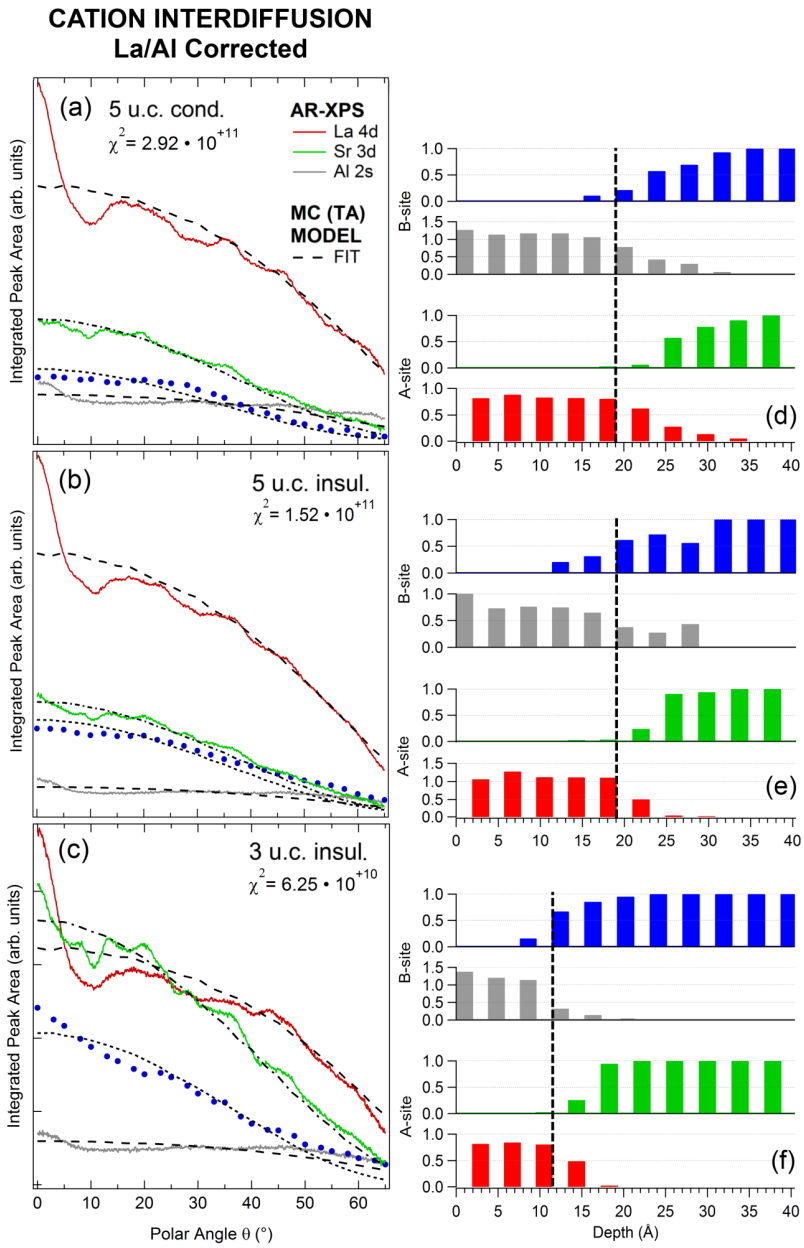

Figure 4.9: *Left panels (a-c): ϕ-averaged AR-XPS data of the LAO/STO samples for La 4d (red line), Al 2s (grey line), Sr 3d (green line) and Ti 2p (blue dots) core levels. The calculated profiles (black dotted lines) are obtained on the basis of (i) the cation interdiffusion model and (ii) the correction of the La/Al stoichiometry of the film. Right panels (d-f) display the stack of layers (blue, TiO_2; grey, AlO_2; green, SrO; red, LaO) related to (a-c) panels respectively. The intensity of the bars (0-1) means the percent effective occupation.*

4.5 Abrupt interface model: La/Al and Ti/Sr stoichiometry correction

The conclusions presented in paragraph 4.3.2 suggest that the condition of an abrupt interface cannot simultaneously provide the modeling of the experimental Sr 3d and Ti 2p AR-XPS profiles. Indeed, the latter remark is valid only in the event that the STO substrate is perfectly stoichiometric.

Considering the PLD technique, it is well-known that the stoichiometry of STO can be tuned by varying the laser fluence [244], whereas a stoichiometry control less than 1% can be performed by MBE [245]. Nevertheless, a recent study of Keeble *et al.* [246] has shown that the stoichiometry tunability of STO thin films deposited on STO substrates (001) by PLD and MBE is driven by the formation of both Ti- and Sr-vacancies. However, a previous work of Keeble *et al.* [248] appears to be more relevant for our case study. Considering a STO thin film ($\sim$ 600 nm) grown by PLD on a STO substrate (001), they have evidenced the presence of a uniform distribution of Sr-vacancies throughout the film by means of positron lifetime measurements, which exhibit a sub-ppm sensitivity for vacancy defects [247]. In addition, a surface region of depth $\sim$ 50 nm has been detected to be characterized by extended vacancy clusters, which should be larger than Sr-3O-Ti divacancies with three nearest-neighbor oxygen vacancies, according to DFT calculations. Moreover, a further hint can be provided by a study of Tarun *et al.* [249], which has shown hydrogen-related defects in as-grown STO substrates annealed in hydrogen by infrared (IR) absorption measurements. This analysis has also revealed that the latter defects can be attributed to Sr-vacancies passivated by two hydrogen atoms, as recently confirmed by Thienprasert *et al.* by DFT calculations [250].

On this basis, we have improved the layered structure models of Figure 4.8 (d-f) by adding the possibility to host Sr-vacancies near the interface. However, since (*i*) our modeling can only *effectively* reproduce the AR-XPS profiles and (*ii*) the fitting variable of Sr-vacancies cannot be related to a stoichiometry constraint[18], the exact evaluation of both the slope and depth profile for the Sr-vacancies cannot be achieved. For this reason, we have selected only the first

[18]For instance, in the interdiffusion model the Sr occupancy profile is linked to the La occupancy by $La_xSr_{1-1.5x}O$.

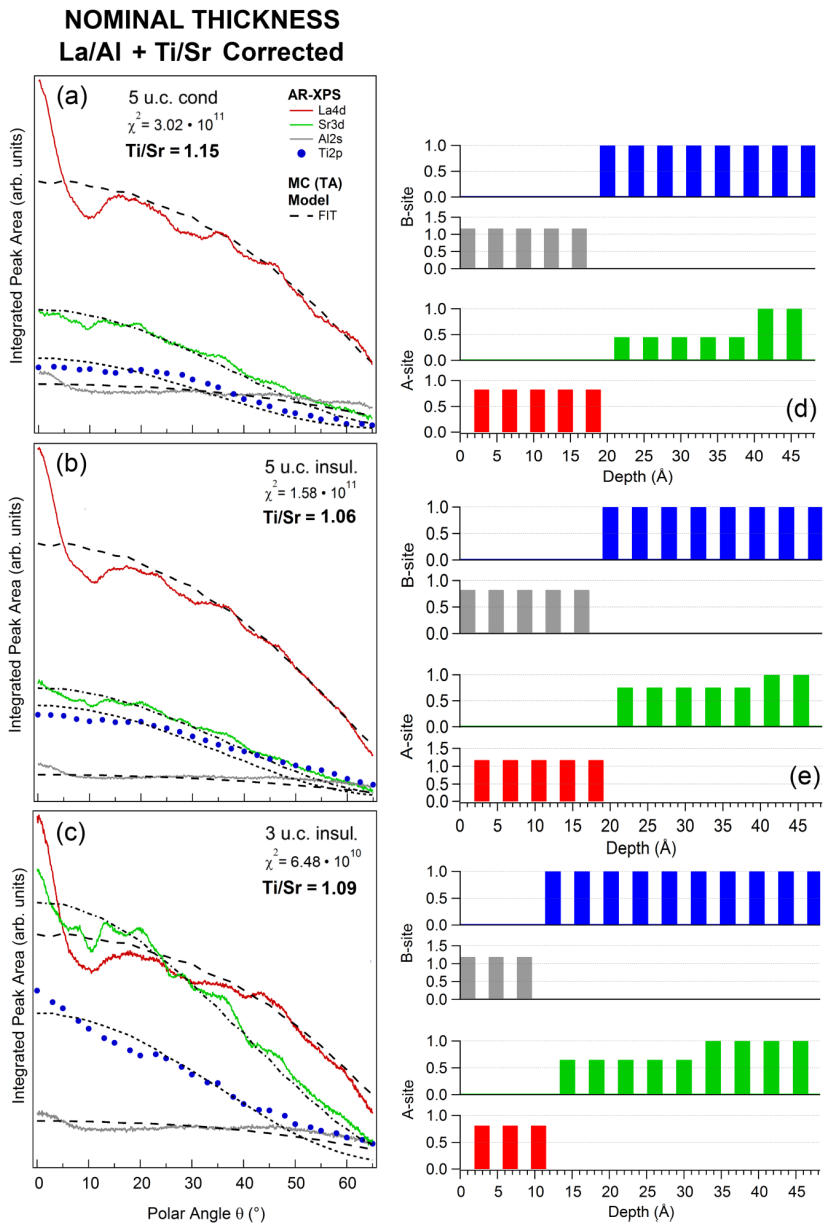

Figure 4.10: *Left panels (a-c): ϕ-averaged AR-XPS data of the LAO/STO samples for La 4d (red line), Al 2s (grey line), Sr 3d (green line) and Ti 2p (blue dots) core levels. The calculated profiles (black dotted lines) are obtained on the basis of (i) the abrupt interface, (ii) the nominal thickness of the LAO film, (iii) the correction of the La/Al stoichiometry of the film and (iv) the correction of the Ti/Sr stoichiometry of the bulk. Right panels (d-f) display the stack of layers (blue, TiO_2; grey, AlO_2; green, SrO; red, LaO) related to (a-c) panels respectively. The intensity of the bars (0-1) means the percent effective occupation.*

five unit cells below the nominal interface in such a way to host a Sr-deficiency[19]. The results of the fitting procedure are shown in Figure 4.10 (a-c), while the schematic of the layered models are displayed in panel (d-f). Therefore, considering:

- the abrupt interface,
- the nominal film thickness,
- the La/Al stoichiometry correction,
- and the possibility to host Sr-vacancy in the first 5 u.c. below the junction,

we have obtained a match of the AR-XPS profiles between the experiment and theory nearly as good as in the interdiffusion model, whereas the amount of Sr-vacancies is (Figure 4.10 (d)) the greatest for the 5 u.c. conductive sample ($> 50\%$), (Figure 4.10 (f)) reduced to about $\sim 35\%$ for the 3 u.c. sample and (Figure 4.10 (e)) the lowest for the 5 u.c. insulating sample ($\sim 25\%$). If we evaluate the Ti/Sr stoichiometry ratio on the basis of the cation occupancy from the interface down to 10 nm below the surface, the 5 u.c. conductive sample exhibits the highest Ti/Sr ratio of 1.15, whereas the 3 u.c. and 5 u.c. insulating samples show reduced results of 1.09 and 1.06, respectively.

The discrepancies among the samples may be interpreted on the basis of both the LAO thickness- and p_{O_2}-dependent arguments. Taking into account that all the STO substrate were prepared in a similar way - i.e. TiO_2-terminated - and all the LAO film were grown by the same deposition technique (PLD), it is reasonable to assume that similar Ti/Sr stoichiometry ratios occur for all the samples. However the discrepancies above estimated suggest that:

I. the lowest Ti/Sr out-of-stoichiometry ratio for the 5 u.c. insulating sample could be ascribed either to (i) the formation of Sr- and Ti-vacancies during the PLD growth (for both the STO substrate and LAO film deposition), as reported in Ref. [246, 248], or to (ii) the pre-treatment of the STO substrate to create well-defined TiO_2-terminated surface [251,252]. In the

[19] For example, if 10 u.c. below the nominal interface are considered in the model, the final results would be modified in the Sr-occupancy in such a way to provide equivalent effective AR-XPS profiles, similarly as obtained in the case of the terrace roughness models.

latter procedure, indeed, different steps are needed to achieve the preferential surface termination, among which the ultrasonically immersion of the STO substrates in demineralized water in order to form Sr-hydroxide complexes at the topmost layer of SrO-terminated domains, which are subsequently etched by a short dip in a NH_4F buffered HF solution (BHF). Thereby, our opinion is that the BHF acid etching treatment may not only remove the surface SrO-domains but even a limited amount of SrO-complexes below the resulting TiO_2-terminated surface.

II. The discrepancy of the Ti/Sr stoichiometry ratios between the couple of the 5 u.c. conductive (1.15) and 3 u.c. samples (1.09) with respect to the 5 u.c. insulating sample (1.06) may be attributed to the different growth conditions (i.e., $p_{O_2} = 10^{-3}$ and 10^{-1} $mbar$, respectively),

III. whereas the difference between the 5 u.c. conductive (Ti/Sr= 1.15) and 3 u.c. sample (1.09) may be differently ascribed to an additional La-Sr interdiffusion process, dependent on the LAO thickness. In this way, the larger amount of Sr-vacancies ($> 50\%$ for 5 u.c. sample and $\sim 35\%$ for the 3 u.c. sample) may be partially compensated by the $La_xSr_{1-1.5x}O$ exchange process, leading to a more stable structure for the same amount of cation vacancies.

4.6 Conclusions

In this chapter, the LAO/STO interface has been studied by AR-XPS in order to reconstruct the cation distribution across the junction. Different models, based on the effective transport of photoelectrons in the oxide heterojunction, have been taken into account and both the abrupt interface and multiple cation disorder effects have alternatively been included in the calculations. In summary, considering the LAO/STO interface as abrupt, we can conclude that:

I. on the basis of a stoichiometric (film and bulk) layered structure model and a nominal film thickness for the effective calculations, the AR-XPS analysis evidences an overestimation of the experimental Sr 3d profile and a slight mismatch with theory for the Al 2s core level. These are signatures of a LAO film thickness greater than the nominal values and of a modified La/Al stoichiometry ratio in the film (see paragraph 4.2);

II. using the La/Al stoichiometry correction in the model, as well as the nominal film thicknesses, the overall result remains almost unchanged with respect to point I (see paragraph 4.3 and 4.3.1);

III. by adding the Ti 2p AR-XPS profile and considering the La/Al stoichiometry correction in the model, a good match of the Ti 2p profile between theory and experiment is found, at odds with the overestimation of the Sr 3d profile. This is a signature that the interface may be non-abrupt and other structural interface/bulk modifications may be taken into account (see paragraph 4.3.2).

Taking into account the possibility of cation disorder across the LAO/STO heterojunction, in terms of La-Sr and Al-Ti interdiffusion, as well as La- and Al-vacancies, we have obtained that:

IV. the La-Sr and Al-Ti cation interdiffusion are present for all the samples;

V. the La-Sr interdiffusion depth is more pronounced for the 5 u.c. conductive with respect to the other cases;

VI. the 5 u.c. insulating sample, grown at high oxygen partial pressure (10^{-1} $mbar$) shows a greater cation disorder across the junction with respect to the samples grown at lower $p_{O_2} = 10^{-3}$ $mbar$;

VII. the La-Sr exchange appears to be at a larger depth with respect to the Al-Ti interdiffusion, at odds with Ref. [191];

VIII. the overall interdiffusion depth is within 3-4 u.c., in agreement with other investigations [185, 190, 191];

VIII. a Sr-deficient interfacial layer is present for all the samples.

Finally, considering the LAO/STO interface as abrupt and allowing the La/Al and Ti/Sr correction of stoichiometry, we have obtained that:

IX. the 5 u.c. conductive shows a larger amount of Sr-vacancies ($> 50\%$) at the interface with respect to the 3 u.c. sample ($\sim 35\%$) and the 5 u.c. insulating sample ($\sim 25\%$);

X. the low amount of Sr-vacancies ($\sim 25\%$) in the 5 u.c. insulating sample may be anyhow ascribed to the pre-treatment of the substrate carried out to TiO_2-terminate the STO surface;

XI. whereas the increasing Sr-vacancy concentrations for the 5 u.c. conductive and 3 u.c. sample may be explained invoking an additional LAO thickness-dependent mechanism, such as the $La_xSr_{1-1.5x}O$ interdiffusion process. This assumption appears to be corroborated by the independent result of point VIII, suggesting the combined effect of interdiffusion and Sr-vacancies as a possible explanation for the present LAO/STO heterojunctions.

Our final conclusion is that the AR-XPS analysis based on the effective modeling, which is here provided by the BriXias code (see paragraph 1.6), has proved to be suitable for the investigation of the cation distribution across the interface of LAO/STO heterostructures. When supported by a different experimental technique which can provide additional information about the interface chemistry and structure - for instance, the film and bulk stoichiometry, or the abruptness of the interface, or the surface roughness - the results of the model could more specifically address the prevalent role of one feature with respect to others - e.g. terrace (Figure 4.7) vs. LAO stoichiometry gradient (Figure 4.5), or interdiffusion (Figure 4.9) vs. Sr-vacancies (Figure 4.10).

Appendix A

A.1 Determination of the uncertainty in the band offset analysis

On the basis of Ref. [119], the precision of the VBM extrapolation is evaluated by linear regressions of different sets of data points along the linear part of the leading edge of the VB spectrum. Then the resulting E_{VBM} values obtained from the different intersections with the fit-line of the baseline are shown in Figure A.1. The average E_{VBM} for TiO_2 and CTO are 2.99 eV and 2.71 eV respectively, with an uncertainty equal to the standard deviation of ± 0.04 eV for both the cases.

In Figure A.2 the core level peaks of Cd 4d and Ti 3p for the bare CTO and TiO_2 respectively are fitted by a double-Voigt function which properly takes into account the relative intensity ratio between the two spin-orbit contributions, i.e. $(1:2)$ for Ti $3p_{1/2}$ and Ti $3p_{3/2}$ and $(2:3)$ for Cd $4d_{3/2}$ and Cd $4d_{5/2}$. The uncertainty of the center position resulting from the fitting procedure is equal to $\Delta x_c = \pm 0.005$ eV for both cases.

According to the preceding results, the maximum error related to the energy distance between two core level peaks ΔE_{CL}(CTO-TO) can be estimated as the sum of two Δx_c contributions, equal to ± 0.01 eV in agreement with Ref. [67, 68]. Similarly, the uncertainty for the energy distance between a shallow core level and the VBM in a bare substrate $\Delta E_{\mathrm{CL\text{-}VBM}}$(CTO or TiO_2) results to be ± 0.045 eV and thereby, on the basis of the equation (2.3), the error for the valence band offset ΔE_V is ± 0.1 eV, in agreement with Ref. [116, 119].

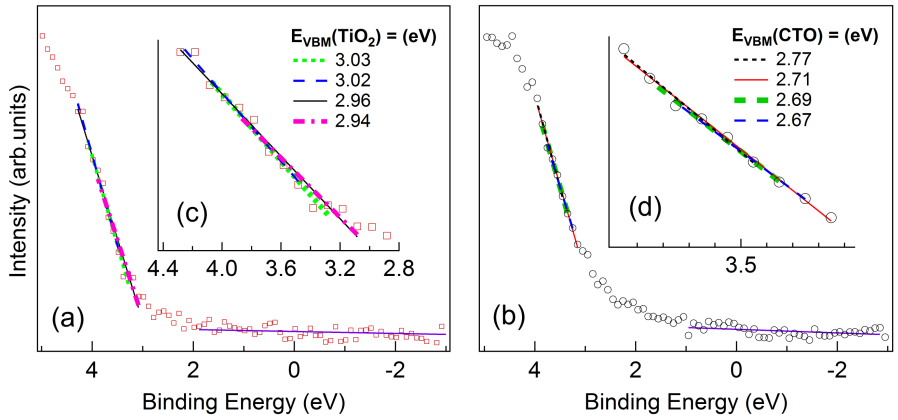

Figure A.1: *Maximum of the VB spectra for the bare TiO_2 (a) and CTO (b). Fitting lines for different energy range within the leading edge of the VB are displayed. E_{VBM} values resulting from the intersection with the linear regression for the background (violet solid line) are shown in the enlargements (c) and (d).*

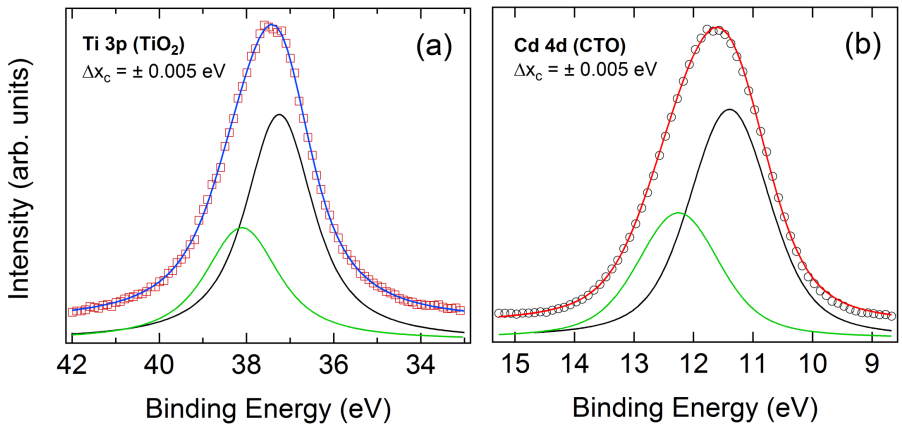

Figure A.2: *(a) Ti 3p and (b) Cd 4d core level peaks for the bare TiO_2 and CTO respectively. For both cases a double-Voigt function is used for the fitting procedure (blue and red solid lines) considering the two spin-orbit contributions: green solid line for Ti $3p_{1/2}$ and Cd $4d_{3/2}$ and black solid line for Ti $3p_{3/2}$ and Cd $4d_{5/2}$.*

A.2 Reliability of the band offset analysis

The major uncertainty which is introduced in the band offset analysis of an heterojunction originates in the valence band maximum (VBM) determination. In facts, the precision of the curve-fitting procedure used to evaluate the energy position of a core level peak can be assessed less than $\pm 0.01\ eV$ (see Appendix A.1) and similar uncertainties can be verified for the energy shift due to the background-subtraction, as well as the energy difference between two core level peaks [68].

Generally, the method for the VBM extrapolation consists of the fitting of the experimental VB spectrum by a Gaussian broadened theoretical VB density of states - i.e. the so called Kraut's method [67,68]. However, for different oxide materials the latter procedure has been shown to be affected by an error within $0.4 - 0.6\ eV$ [119] and a reliable alternative is the intersection of the linear regression of the leading edge of the VB and the background between the VBM and Fermi energy. Nevertheless the reliability of a correct E_{VBM} determination depends on the instrumental resolution which has to be lower than the energy range ($\Delta E_{10\%-90\%}$) within which the leading edge of the VB rises from 10% to 90% of its value above the baseline [119]. The assessments of $\Delta E_{10\%-90\%}$ for the bare CTO and TiO_2 are displayed in Figure A.3 (a) and result $1.87 \pm 0.01\ eV$ and $1.88 \pm 0.01\ eV$ respectively.

To find out the instrumental resolution, the XPS spectrum of the Au 4f core level is used. Taking into account the intrinsic line shape of Au $4f_{7/2}$ peak [130] - i.e. a Doniach-Sunjić with a FWHM $= 0.32 \pm 0.01\ eV$ and an asymmetry of 0.052 ± 0.01 - we have convolved the latter with a Gaussian function. The best fit of the experimental data was achieved for a $\mathrm{FWHM_{Gauss}} = 1.03 \pm 0.01\ eV$ (see Figure A.3 (b)). However, this may be even an overestimation of our real energy resolution, because the measurement was carried out on a non-epitaxial thin film of gold without any cleaning procedure before the experiment. Thus, defining R_{eff} the ratio between $\Delta E_{10\%-90\%}$ and the Gaussian FWHM, we have obtained values > 1 both for CTO and TiO_2 (see Figure A.3 (a)), thereby verifying the reliability of the band offset analysis for our case.

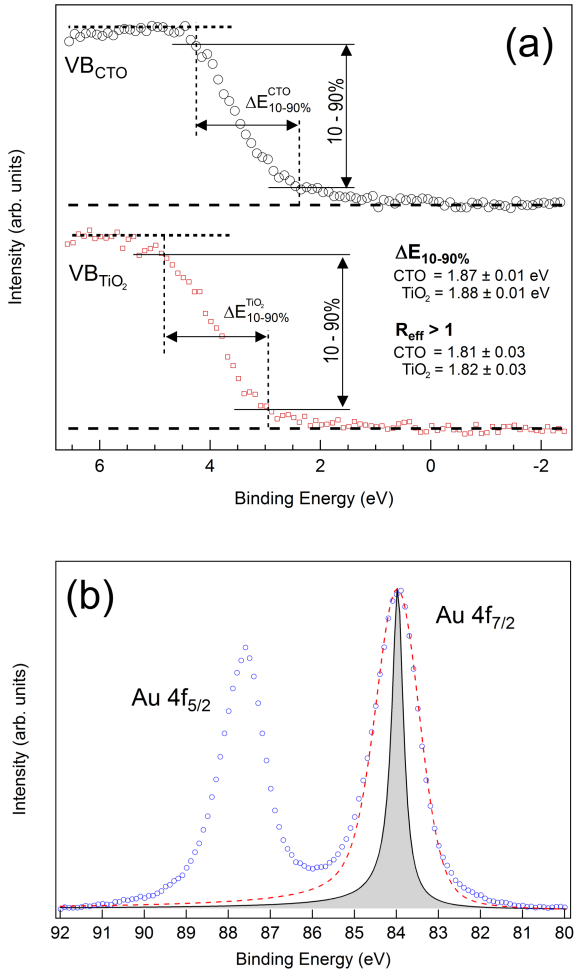

Figure A.3: *(a) Determination of the energy range ($\Delta E_{10\%-90\%}$) for the valence band spectra of the bare CTO (top) and TiO_2 (bottom). R_{eff} represents the ratio between $\Delta E_{10\%-90\%}$ and the instrumental resolution. (b) XPS spectrum for Au 4f core level (blue open-circles), intrinsic Doniach-Sunjić line shape for Au $4f_{7/2}$ (shaded area) and the convolution of the latter with a Gaussian function (red-dashed line).*

A.3 Remark on the bare CTO energy gap

The VBM for the bare CTO is $2.71 \pm 0.04\ eV$ as displayed in Figure A.4 (a) and justified in the Appendix A.1. Since the bare CTO was proved to be conductive [61, 98, 102] it follows that the energy gap has to be less than 2.71 eV. Nevertheless, for a bare CTO 650 nm thick film grown on a glass substrate (simultaneously with respect to our bare CTO/Si specimen) the optical bandgap was obtained to be $2.83\ eV$ from a transmittance measurement, as reported in Ref. [102] and shown in Figure A.4 (b) and (c). In this case the bandgap was determined by extrapolating the straight line portion to the energy axis from the plot of $(\alpha h\nu)^2$ versus $h\nu$, where α is the absorption coefficient related to the transmittance T as:

$$T = (1 - R)^2 \exp(-\alpha t) \tag{A.1}$$

with R reflectance and t film thickness. For the bare CTO, the transmittance measurement from 300 nm to 1100 nm of wavelength is shown in Figure A.4 (c) and adapted from Ref. [102]. In Figure A.4 (b) the extrapolation of the optical bandgap is displayed where the black line is the fit of the linear portion of data while the blue parabola underlines the region in which the linear regime is lost.

The discrepancy between the energy gap evaluations from XPS ($E_g \leq 2.71\ eV$) and from the optical extrapolation analysis ($E_g = 2.83\ eV$) lies in the differences of the two techniques considered - in terms of probing depth - and the chemical properties of the present CTO - which exhibits a Sn/Cd surface gradient. In facts:

I. XPS is a surface sensitive technique and for the physical properties of the sample a probing depth of at most 7 nm can be estimated (taking into account the 99% of the area of the DDF obtained by MC calculations on the basis of the two-layer model represented in the inset of Figure 2.5),

II. while a transmittance measurement stems from the optical properties of the whole film thickness;

III. in addition, a Sn/Cd stoichiometry variation of 0.4 has been evidenced in the surface of the bare CTO from the AR-XPS analysis, as shown in Figure A.4 (d)

IV. and a linear dependence of the optical bandgap respect to the Sn/Cd stoichiometry has been evidenced for crystalline and amorphous CTOs by a recent work of T. Meng *et al.* [122], as adapted in Figure A.4 (e).

Therefore, we can conclude that the two energy gap evaluations ($\leq 2.71\ eV$ and $2.83\ eV$) must be necessarily different. Particularly, according to point IV, the XPS result - which is related to the sample surface ($\leq 7\ nm$) and to a lower Sn/Cd ratio ($2.0 - 1.6$) - is indeed lower than the gap assessment obtained from the optical analysis ($2.71\ eV < 2.83\ eV$) which instead originates from the whole film thickness ($650\ nm$) and from a greater Sn/Cd ratio (> 2).

A.4 Evaluation of the bare CTO energy gap

Considering the conclusions of the preceding paragraph A.3, in this section the energy gap for the bare CTO is determined in order to be consistent with all the other XPS data so far presented. To achieve this goal, the following conditions must be taken into account:

I. VBM $= 2.71 \pm 0.04\ eV$ is extrapolated from an XPS spectrum taken in normal emission ($\theta = 0°$);

II. Sn/Cd is 1.92 ± 0.08 for $\theta = 0°$(see Table 2.1);

III. $E_g^{CTO} \leq 2.71\ eV$ for conductivity.

Then, it follows that the highest possible energy gap can be expected in the orange area in Figure A.4 (e). Even though the latter region is out of the linear expectation deduced by T. Meng *et al.* [122] - but still within the amorphous CTO bandgap range of $2.7 - 3.1\ eV$ [120] - such a discrepancy may be ascribed to the different experimental setup and conditions used during the film growth. Nonetheless, we assume the same linear dependence of the gap as a function of the Sn/Cd ratio. Then, the fitting black-dotted line of Figure A.4 (e) is shifted to cross our expectation value and considering the Sn/Cd surface variation of 0.4 evidenced by AR-XPS data in Figure A.4 (d) a bandgap uncertainty equal to $0.1\ eV$ is deduced. According to point III, the energy gap is obtained as $2.66 \pm 0.05\ eV$.

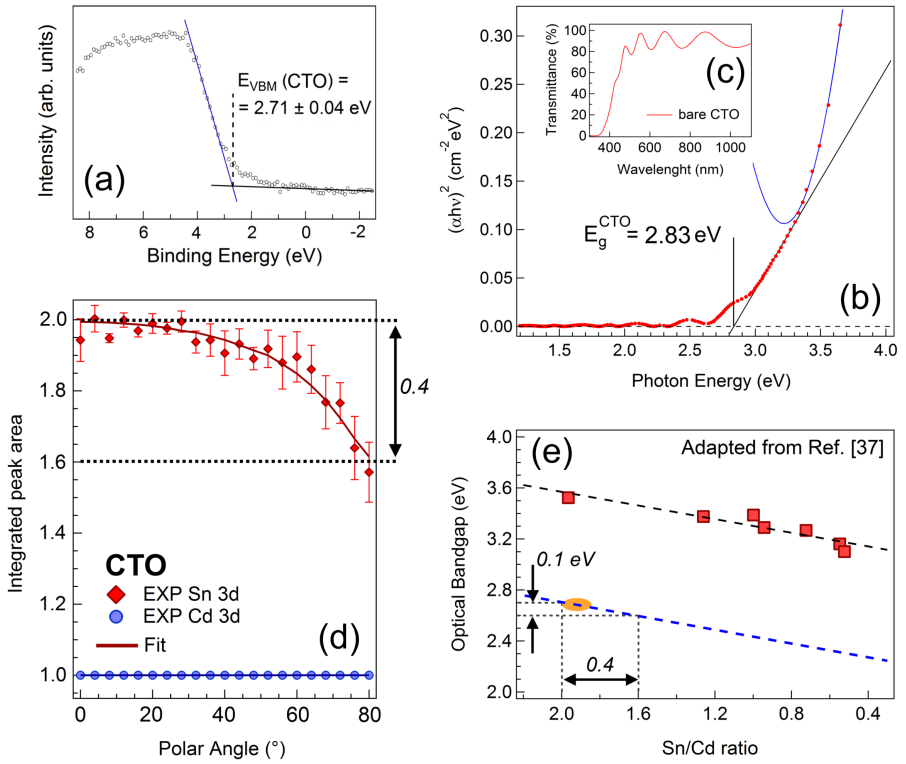

Figure A.4: *(a) XPS measurement of the VB for the bare CTO. The VBM evaluation is displayed. (b) Extrapolation of the optical bandgap to the energy axis (solid black line) for the bare CTO from the plot of $(\alpha h\nu)^2$ vs $h\nu$ obtained from (c) the transmittance measurement taken from Ref. [102]. (d) AR-XPS data for the bare CTO, first displayed in Figure 2.5. (e) Variation of the optical bandgap with respect to the Sn/Cd stoichiometry ratio, adapted from Fig.5 (b) in Ref. [122]. Black-dotted line is the fit for the experimental data which include crystalline and amorphous cadmium stannates, while the blue-dotted line represents the same behavior but crossing the VBM value for the bare CTO (orange area) taken from panel (a).*

Bibliography

[1] I. Osborne, M. Lavine, and R. Coontz, Looking Beyond Silicon. *Science*, **327**, 1595 (2010).

[2] J. Mannhart, and D. G. Schlom, Oxide Interfaces - An Opportunity for Electronics. *Science*, **327**, 1607-1611 (2010).

[3] H. Takagi and H.Y. Hwang, An Emergent Change of Phase for Electronics. *Science*, **327**, 1601 (2010).

[4] J Heber, Enter the oxides. *Nature*, **459**, 28-30 (2009).

[5] A. Ohtomo, H. Y. Hwang, A high-mobility electron gas at the $LaAlO_3/SrTiO_3$ heterointerface. *Nature*, **427**, 423 (2004).

[6] A. Ohtomo, D. A. Muller, J. L. Grazul, and H. Y. Hwang, Artificial charge-modulation in atomic-scale perovskite titanate superlattices. *Nature*, **419**, 378-380 (2002).

[7] H. Y. Hwang, Y. Iwasa, M. Kawasaki, B. Keimer, N. Nagaosa, and Y. Tokura, Emergent phenomena at oxide interfaces. *Nat. Mater.*, **11**, 103 (2012).

[8] E. Assmann, P. Blaha, R. Laskowski, K. Held, S. Okamoto, and G. Sangiovanni, Oxide Heterostructures for Efficient Solar Cells. *Phys. Rev. Lett.*, **110**, 078701 (2013).

[9] H. Liang, L. Cheng, X. Zhai, N. Pan, H. Guo, J. Zhao, H. Zhang, L. Li, X. Zhang, X. Wang, C. Zeng, Z. Zhang, and J. G. Hou, Giant photovoltaic

effects driven by residual polar field within unit-cell-scale $LaAlO_3$ films on $SrTiO_3$. *Sci. Rep.*, **3**, 1975 (2013).

[10] S. Wu, X. Luo, S. Turner, H. Peng, W. Lin, J. Ding, A. David, B. Wang, G. Van Tendeloo, J. Wang, and T. Wu, Nonvolatile Resistive Switching in $Pt/LaAlO_3/SrTiO_3$ Heterostructures. *Phys. Rev. X*, **3**, 041027 (2013).

[11] C. W. Bark, P. Sharma, Y. Wang, S. H. Baek, S. Lee, S. Ryu, C. M. Folkman, T. R. Paudel, A. Kumar, S. V. Kalinin, A. Sokolov, E. Y. Tsymbal, M. S. Rzchowski, A. Gruverman, and C. B. Eom, Switchable Induced Polarization in $LaAlO_3/SrTiO_3$ Heterostructures. *Nano Lett.*, **12**, 1765 (2012).

[12] A. Kumar, T. M. Arruda, Y. Kim, I. N. Ivanov, S. Jesse, C. W. Bark, N. C. Bristowe, E. Artacho, P. B. Littlewood, C. B. Eom, and S. V. Kalinin, Probing Surface and Bulk Electrochemical Processes on the $LaAlO_3$-$SrTiO_3$ Interface. *ACS Nano*, **6**, 3841 (2012).

[13] A. Einstein, *Ann. Phys.*, **17**, 132 (1905).

[14] C. S. Fadley, X-ray photoelectron spectroscopy: Progress and perspectives. *J. Electron Spectrosc. Relat. Phenom.*, **178-179**, 2-32, (2010).

[15] J. Cazaux, About the charge compensation of insulating samples in XPS. *J. Electron Spectrosc. Relat. Phenom.*, **113**, 15-33 (2000).

[16] C. S. Fadley: Basic Concepts of X-ray Photoelectron Spectroscopy, Electron Spectroscopy, Theory, Thechniques and Applications. Ed. by C. R. Brundle, and A. D. Baker, *Academic Press*, London, (1978).

[17] M. P. Seah, and W. A. Dench, Quantitative electron spectroscopy of surfaces: A standard data base for electron inelastic mean free paths in solids. *Surf. Interface Anal.*, **1**, 2-11 (1979).

[18] Y. Takataa, M. Yabashi, K. Tamasaku, Y. Nishino, D. Miwa, T. Ishikawa, E. Ikenaga, K. Horiba, S. Shin, M. Arita, K. Shimada, H. Namatame, M. Taniguchi, H. Nohira, T. Hattori, S. Södergren, B. Wannberg, K. Kobayashi, Development of hard X-ray photoelectron spectroscopy at BL29XU in SPring-8. *Nucl. Instrum. Methods Phys. Res. A*, **547**, 50-55 (2005).

[19] S. Tanuma, C. J. Powell, and D. R. Penn, Calculation of electron inelastic mean free paths (IMFPs) VII. Reliability of the TPP-2M IMFP predictive equation. *Surf. Interf. Anal.*, **35**, 268-275 (2003).

[20] P. Y. Yu, and M. Cardona: Fundamentals of Semiconductors: Physics and Materials Properties, 3rd edition, Springer (2005).

[21] W. E. Spicer, Photoemissive, Photoconductive, and Optical Absorption Studies of Alkali-Antimony Compounds. *Phys. Rev.*, **112**, 114 (1958).

[22] C. N. Berglund, and W. E. Spicer, Photoemission Studies of Copper and Silver: Theory. *Phys. Rev.*, **136**, A1030-1044 (1964).

[23] J. J. Yeh, I. Lindau, Atomic Subshell Photoionization Cross Sections and Asymmetry Parameters: $1 \leq Z \leq 103$. *At. Data Nucl. Data Tables*, **32**, 1-155 (1985).

[24] M.B. Trzhaskovskaya, V.I. Nefedov, V.G. Yarzhemsky, Photoelectron angular distribution parameters for elements Z=1 to Z=54 in the photoelectron energy range $100 - 5000\ eV$. *Atom. Data Nucl. DataTables*, **77**, 97 (2001).

[25] A. Damascelli, Z. Hussain, and Z. X. Shen, Angle-resolved photoemission studies of the cuprate superconductors. *Rev. Mod. Phys.*, **75**, 473-541 (2003).

[26] F. de Groot, and A. Kotani, Core level spectroscopy of solids. *CRC Press*, London, (2008).

[27] M. Magnuson, Electronic Structure Studies Using Resonant X-Ray and Photoemission Spectroscopy, *Acta Universitatis Upsaliensis*, Uppsala, (1999).

[28] P. A. Brüuhwiler, O. Karis, and N. Mårtennson, Charge-transfer dynamics studied using resonant core spectroscopies. *Rev. Mod. Phys.*, **74**, 703 (2002).

[29] G. Drera, G. Salvinelli, F. Bondino, E. Magnano, M. Huijben, A. Brinkman, and L. Sangaletti, Intrinsic origin of interface states and band-offset profiling of nanostructured $LaAlO_3/SrTiO_3$ heterojunctions probed by element-specific resonant spectroscopies. *Phys. Rev. B*, **90**, 035124 (2014).

[30] C. O. Almbladh, and L. Hedin, Handbook on Synchrotron Radiation, E. E. Koch, eds., *North-Holland Publishing Company*, Amsterdam, (1983), vol. 1B, pp. 607

[31] U. Fano, Effects of Configuration Interaction on Intensities and Phase Shifts. *Phys. Rev.*, **124**, 1866-1878 (1961).

[32] N. Mårtennson, M. Weinelt, O. Karis, M. Magnuson, N. Wassdahl, A. Nilsson, J. Stöhr, and M. Samant, Coherent and incoherent processes in resonant photoemission. *Appl. Phys A*, **65**, 159 (1997).

[33] K. Okada and A. Kotani, Theory of core level X-ray photoemission and photoabsorption in Ti compounds. *J. Electron Spectrosc. Relat. Phenom.*, **62**, 131 (1993).

[34] L. H. Tjeng, C. T. Chen, J. Ghijsen, P. Rudolf, and F. Sette, Giant Cu $2p$ resonances in CuO valence-band photoemission. *Phys. Rev. Lett.*, **67**, 501 (1991).

[35] S. Pagliara, L. Sangaletti, A. Goldoni, C. Kim, Z. X. Shen, A. Revcolevschi, G. Dhalenne, and F. Parmigiani, Coexistence of interfering and noninterfering channels in resonant photoemission spectra across the Cu $2\vec{p}3d$ threshold. *Phys. Rev. B*, **65**, 205107 (2002).

[36] M. F. Sunding, K. Hadidi, S. Diplas, O. M. Løvvik, T. E. Norby, A. E. Gunnaes, XPS characterisation of in situ treated lanthanum oxide and hydroxide using tailored charge referencing and peak fitting procedures. *J. Electron Spectrosc. Relat. Phenom.*, **184**, 399 (2011).

[37] C. Dallera, K. Giarda, G. Ghiringhelli, A. Tagliaferri, L. Braicovich, and N. B. Brookes, Charge-transfer excitations in lanthanum compounds measured by resonant inelastic x-ray scattering at the M_5 edge. *Phys. Rev. B*, **64**, 153104 (2001).

[38] S. Günther, B. Kaulich, L. Gregoratti, M. Kiskinova, Photoelectron microscopy and applications in surface and materials science. *Prog. Surf. Sci.*, **70**, 187-260 (2002).

[39] E. Bauer, Photoelectron spectromicroscopy: present and future. *J. Electron Spectrosc. Relat. Phenom.*, **114-116**, 975-987 (2001).

[40] T. O. Mente, M. A. Niño, and A. Locatelli, Spectromicroscopy with Low-Energy Electrons: LEEM and XPEEM Studies at the Nanoscale. *e-J. Surf. Sci. Nanotech.*, **9**, 72-79 (2011).

[41] E. Bauer, Low energy electron microscopy. *Rep. Prog. Phys.*, **57**, 895-938 (1994).

[42] J. C. Dupuy, A. Sibai, and B. Vilotitch, Mirror electron microscopy (MEM): work function and imaging of an electron beam biased junction of silicon (100). *Surf. Sci.*, **147**, 191-202 (1984).

[43] G. F. Rempfer, and O. H. Griffith, Emission microscopy and related techniques: resolution in photoelectron microscopy, low energy electron microscopy and mirror electron microscopy. *Ultramicroscopy*, **47**, 35-54 (1992).

[44] G. Drera, G. Salvinelli, J. Åhlund, P. Karlsson, B. Wannberg, E. Magnano, L. Sangaletti, Transmission function calibration of an angular resolved analyzer for X-ray photoemission spectroscopy: Theory vs experiment. *J. Electron Spectrosc. Relat. Phenom.*, **195**, 109-116 (2014).

[45] M. P. Seah, I. S. Gilmore, S. J. Spencer, Quantitative XPS: I. Analysis of X-ray photoelectron intensities from elemental data in a digital photoelectron database. *J. Electron Spectrosc. Relat. Phenom.*, **120**, 93-111 (2001).

[46] J. Végh, The Shirley-equivalent electron inelastic scattering cross-section function, *Surf. Sci.*, **563**, 183-190 (2004).

[47] S. Tougaard, Universality Classes of Inelastic Electron Scattering Cross-sections. *Surface And Interface Analysis*, **25**, 137-154 (1997).

[48] W. S. M. Werner, Electron Transport in Solids for Quantitative Surface Analysis. *Surf. Interface Anal.*, **31**, 141-176 (2001).

[49] I. S. Tilinin, A. Jablonski, J. Zemek, S. Hucek, Escape Probability of Signal Photoelectrons From Noncrystalline Solids: Influence of Anisotropy of Photoemission. *J. Electron Spectrosc. Relat. Phenom.*, **97**, 127-140 (1997).

[50] A. Jablonski, and H. Ebel, Comparison of electron attenuation lengths and escape depths with inelastic mean free paths. *Surf. Inter. Anal.*, **11**, 627-632 (1988).

[51] A. Jablonski, J. Zernek, Angular distribution of photoemission from amorphous and polycrystalline solids. *Phys. Rev. B*, **48**, 4799-4805 (1993)

[52] A. Jablonski, Transport Cross Section for Electrons at Energies of Surface-Sensitive Spectroscopies. *Phys. Rev. B*, **58**, 16470-16480 (1998).

[53] A. Jablonski, and S. Tougaard, Escape probability of electrons from solids. Influence of elastic electron scattering. *Surf. Sci.*, **432**, 211-227 (1999).

[54] C. Pintossi, G. Salvinelli, G. Drera, S. Pagliara, L. Sangaletti, S. Del Gobbo, M. Morbidoni, M. Scarselli, M. De Crescenzi, and P. Castrucci, Direct Evidence of Chemically Inhomogeneous, Nanostructured, Si-O Buried Interfaces and Their Effect on the Efficiency of Carbon Nanotube/Si Photovoltaic Heterojunctions. *J. Phys. Chem. C*, **117**, 18688-18696 (2013).

[55] E. M. J. Johansson, R. Lindblad, H. Siegbahn, A. Hagfeldt, H. Rensmo, Atomic and Electronic Structures of Interfaces in Dye-Sensitized, Nanostructured Solar Cells. *ChemPhysChem*, **15**, 1006-1017 (2014).

[56] I. Mora-Seró, S. Gimnez, F. Fabregat-Santiago, E. Azaceta, R. Tena-Zaera, J. Bisquert, Modeling and characterization of extremely thin absorber (eta) solar cells based on ZnO nanowires. *Phys. Chem. Chem. Phys.*, **13**, 7162-7169 (2011).

[57] B. E. Hardin, H. J. Snaith, M. D. McGehee, The renaissance of dye-sensitized solar cells. *Nature Photonics*, **6**, 162-169 (2012).

[58] D. Jiang, Y. Hao, R. Shen, S. Ghazarian, R. Angela, F. Zhou, Effective Blockage of the Interfacial Recombination Process at TiO_2 Nanowire Array Electrodes in Dye-Sensitized Solar Cells. *ACS Applied Materials & Interfaces*, **5**, 11906-11912 (2013).

[59] Y. Zheng, S. Klankowski, Y. Yang, Y. Li, Preparation and Characterization of TiO_2 Barrier Layers for Dye-Sensitized Solar Cells. *ACS Applied Materials & Interfaces*, **6**, 10679-10686 (2014).

[60] Z. Yang, S. Gao, T. Li, F. Q. Liu, Y. Ren, T. Xou, Enhanced Electron Extraction from Template-Free 3D Nanoparticulate Transparent Conducting Oxide (TCO) Electrodes for Dye-Sensitized Solar Cells. *ACS Applied Materials & Interfaces*, **4**, 4419-4427 (2012).

[61] A. Braga, C. Baratto, P. Colombi, E. Bontempi, G. Salvinelli, G. Drera, L. Sangaletti, An ultrathin TiO_2 blocking layer on Cd stannate as highly efficient front contact for dye-sensitized solar cells. *Phys. Chem. Chem. Phys.*, **15**, 16812-16818 (2013).

[62] A. Kay, M. Grätzel, Dye-Sensitized Core-Shell Nanocrystals: Improved Efficiency of Mesoporous Tin Oxide Electrodes Coated with a Thin Layer of an Insulating Oxide. *Chem. Mater.*, **14**, 2930-2935 (2002).

[63] B. Yoo, K. Kim, D. K. Lee, M. J. Ko, H. Lee, Y. H. Kim, W. M. Kim, N. G. Park, Enhanced charge collection efficiency by thin-TiO_2 film deposition on FTO-coated ITO conductive oxide in dye-sensitized solar cells. *J. Mater. Chem.*, **20**, 4392-4398 (2010).

[64] H. Yu, S. Zhang, H. Zhao, G. Will, P. Liu, An efficient and low-cost TiO_2 compact layer for performance improvement of dye-sensitized solar cells. *Electrochimica Acta*, **54**, 1319-1324 (2009).

[65] P. J. Cameron, L. M. Peter, Characterization of Titanium Dioxide Blocking Layers in Dye-Sensitized Nanocrystalline Solar Cells. *J. Phys. Chem. B*, **107**, 14394-14400 (2003).

[66] C. H. Lee, W. H. Chiu, K. M. Lee, W. F. Hsiehb, J. M. Wu, Improved performance of flexible dye-sensitized solar cells by introducing an interfacial layer on Ti substrates. *J. Mater. Chem.*, **21**, 5114-5119 (2011).

[67] E. A. Kraut, R. W. Grant, J. R. Waldrop, S. P. Eowalczyk, Precise Determination of the Valence-Band Edge in X-Ray Photoemission Spectra: Application to Measurement of Semiconductor Interface Potentials. *Physical Review Letters*, **44**, 1620-1623 (1980).

[68] E. A. Kraut, R. W. Grant, J. R. Waldrop, S. P. Kowalczyk, Semiconductor core-level to valence-band maximum binding-energy differences. Precise

determination by x-ray photoelectron spectroscopy. *Physical Review B*, **28**, 1965-1977 (1983).

[69] G. Salvinelli, G. Drera, C. Baratto, A. Braga, and L. Sangaletti, Stoichiometry Gradient, Cation Interdiffusion, and Band Alignment between a Nanosized TiO_2 Blocking Layer and a Transparent Conductive Oxide in Dye-Sensitized Solar Cell Front Contacts. *ACS Appl. Mater. Interfaces*, *ACS Appl. Mater. Interfaces*, **7**, 765-773 (2015).

[70] B. O'Regan, M. Grätzel, A low-cost, high-efficiey solar cell based on dye-sensitized colloidal TiO_2 films, *Nature*, **353**, 737-740 (1991).

[71] S. Ito, N. L. C. Ha, G. Rotherberger, P. Liska, P. Compte, Z. M. Zakeeruddin , P. Pechy , M. K. Nazeeruddin , M. Grätzel, High-efficiency (7.2%) flexible dye-sensitized solar cells with Ti-metal substrate for nanocrystalline-TiO_2 photoanode. *Chem. Commun.*, **38** , 4004-4006 (2006).

[72] V. Galstyan, A. Vomiero, I. Concina , A. Braga, M. Brisotto, E. Bontempi, G. Faglia, G. Sberveglieri, Vertically Aligned TiO_2 Nanotubes on Plastic Substrates for Flexible Solar Cells. *Small*, **7**, 2437-2442 (2011).

[73] M. Grätzel, Photoelectrochemical cells, *Nature*, **414**, 338-344 (2001).

[74] A. Hagfeldt, G. Boschloo, L. Sun, L. Kloo, H. Pettersson, Dye-Sensitized Solar Cells. *Chem. Rev.*, **110**, 6595-6663 (2010).

[75] J. B. Baxter, A. M. Walker, K. van Ommering, E. S. Aydil, Synthesis and characterization of ZnO nanowires and their integration into dye-sensitized solar cells. *Nanotechnology*, **17**, S304-S312 (2006).

[76] K. Tennakone, J. Bandara, P. K. M. Bandaranayake, G. R. A. Kumara and A. Konno, Enhanced Efficiency of a Dye-Sensitized Solar Cell Made from MgO-Coated Nanocrystalline SnO_2. *Jpn. J. Appl. Phys.*, **40**, 732-734 (2001).

[77] K. Sayama, H. Suguhara, H. Arakawa, Photoelectrochemical Properties of a Porous Nb_2O_5 Electrode Sensitized by a Ruthenium Dye. *Chem. Mater.*, **10**, 3825 (1998).

[78] R. Jose, V. Thavasi, and S. Ramakrishna, Metal Oxides for Dye-Sensitized Solar Cells. *J. Am. Ceram. Soc.*, **92**, 289-301 (2009).

[79] T. W. Hamann, R. A. Jensen, A. B. F. Martinson, H. Van Ryswyk, and J. T. Hupp, Advancing beyond current generation dye-sensitized solar cell. *Energy Environ. Sci.*, **1**, 66-78 (2008).

[80] J. Bisquert, Physical electrochemistry of nanostructured devices. *Phys. Chem. Chem. Phys.*, **10**, 49-72 (2008).

[81] V. Thavasi, V. Renugopalakrishnan, R. Jose, S. Ramakrishna, Controlled electron injection and transport at materials interfaces in dye-sensitized solar cells. *Mater. Sci. Eng. R*, **63**, 81 (2009).

[82] K. Park, Q. Zhang, D. Myers, G. Cao, Charge Transport Properties in TiO_2 Network with Different Particle Sizes for Dye-Sensitized Solar Cells. *ACS Appl. Mater. Interfaces*, **5**, 1044-1052 (2013).

[83] J. B. Baxter, E. S. Aydila, Nanowire-based dye-sensitized solar cells. *Appl. Phys. Lett.*, **86**, 053114, (2005).

[84] K. T. Dembele, G. S. Selopal, C. Soldano, R. Nechache, J. C. Rimada, I. Concina, G. Sberveglieri, F. Rosei, A. Vomiero, Hybrid Carbon Nanotubes-TiO_2 Photoanodes for High Efficiency Dye-Sensitized Solar Cells. *J. Phys. Chem. C*, **117**, 14510-14517 (2013).

[85] A. Yella, H. W. Lee, H. N. Tsao, C. Yi, A. K. Chandiran, M. K. Nazeeruddin, E. W. G. Diau, C. Y. Yeh, S. M. Zakeeruddin, M. Grätzel, Porphyrin-Sensitized Solar Cells with Cobalt (II/III)-Based Redox Electrolyte Exceed 12 Percent Efficiency. *Science*, **334**, 629 (2011).

[86] M. D. McGehee, Paradigm Shifts in Dye-Sensitized Solar Cells. *Science*, **334**, 607 (2011).

[87] L. Que, Z. Lan, W. Wu, J. Wu, J. Lin, M. Huang, Titanium dioxide quantum dots: Magic materials for high performance underlayers inserted into dye-sensitized solar cells. *Journal of Power Sources*, **268**, 670-676 (2014).

[88] A. K. Chandiran , M. K. Nazeeruddin , M. Grätzel, The Role of Insulating Oxides in Blocking the Charge Carrier Recombination in Dye-Sensitized Solar Cells. *Adv. Funct. Mater.*, **24**, 1615-1623 (2014).

[89] S. A. Haque, Y. Tachibana, R. L. Willis, J. E. Moser, M. Grätzel, D. R. Klug, and J. R. Durrant, Parameters Influencing Charge Recombination Kinetics in Dye-Sensitized Nanocrystalline Titanium Dioxide Films. *J. Phys. Chem. B*, **104**, 538-547 (2000).

[90] A. Zaban, S. G. Chen, S. Chappel and B. A. Gregg, Bilayer nanoporous electrodes for dye sensitized solar cells. *Chem. Commun.*, **22**, 2231 (2000).

[91] H. J. Son, X. Wang, C. Prasittichai, N. C. Jeong, T. Aaltonen, R. G. Gordon, and J. T. Hupp, Glass-Encapsulated Light Harvesters: More Efficient Dye-Sensitized Solar Cells by Deposition of Self-Aligned, Conformal, and Self-Limited Silica Layers. *J. Am. Chem. Soc.*, **134**, 9537-9540 (2012).

[92] T. C. Li, M. S. Ges, F. Fabregat-Santiago, J. Bisquert, P. R. Bueno, C. Prasittichai, J. T. Hupp, and T. J. Marks, Surface Passivation of Nanoporous TiO_2 via Atomic Layer Deposition of ZrO_2 for Solid-State Dye-Sensitized Solar Cell Applications. *J. Phys. Chem. C*, **113**, 18385-18390 (2009).

[93] E. Palomares, J. N. Clifford, S. A. Haque, T. Lutz, and J. R. Durrant, Control of Charge Recombination Dynamics in Dye Sensitized Solar Cells by the Use of Conformally Deposited Metal Oxide Blocking Layers. *J. Am. Chem. Soc.*, **125**, 475-482 (2003).

[94] Y. J. Kim, Y. H. Lee, M. H. Lee, H. J. Kim, J. H. Pan, G. Lim, Y. S. Choi, K. Kim, N. G. Park, C. Lee, and W. I. Lee, Formation of Efficient Dye-Sensitized Solar Cells by Introducing an Interfacial Layer of Long-Range Ordered Mesoporous TiO_2 Thin Film. *Langmuir*, **24**, 13225-13230 (2008).

[95] Kim, M. H.; Kwon, Y. U. Semiconducting Divalent Metal Oxides as Blocking Layer Material for SnO_2-Based Dye-Sensitized Solar Cells. *J. Phys. Chem. C*, **115**, 23120-23125 (2011).

[96] J. N. Hart, D. Menzies, Y. B. Cheng, G. P. Simon, L. Spiccia, TiO_2 sol-gel blocking layers for dye-sensitized solar cells. *C. R. Chim.*, **9**, 622-626 (2006).

[97] J. Xia, N. Masaki, K. Jiang, Y. Wata, S. Yanagida, Importance of Blocking Layers at Conducting Glass/TiO_2 Interfaces in Dye-sensitized Ionic-liquid Solar Cells. *Chem. Lett.*, **35**, 252-253 (2006).

[98] C. Baratto, A. Ponzoni, M. Ferroni, L. Borgese, E. Bontempi, and G. Sberveglieri, Sputtering deposition of amorphous cadmium stannate as transparent conducting oxide. *Thin Solid Films*, **520**, 2739 (2012).

[99] H. Kim, C. M. Gilmore, A. Piqu, J. S. Horwitz, H. Mattoussi, H. Murata, Z. H. Kafafi, and D. B. Chrisey, Electrical, optical, and structural properties of indium-tin-oxide thin films for organic light-emitting devices. *J. Appl. Phys.*, **86**, 6451 (1999).

[100] X. Wu, T. J. Coutts, and W. P. Mulligan, Properties of transparent conducting oxides formed from CdO and ZnO alloyed with SnO_2 and In_2O_3. *J. Vac. Sci. Technol. A*, **15**, 1057 (1997).

[101] A. E. Rakhshani, Y. Makdisi, and H. A. Ramazaniyan, Electronic and optical properties of fluorine-doped tin oxide films. *J. Appl. Phys.* **83**, 1049-1057 (1997).

[102] A. Braga, C. Baratto, E. Bontempi, P. Colombi, G. Sberveglieri, Transparent front contact optimization in dye sensitized solar cells: use of cadmium stannate and titanium oxide by sputtering. *Thin Solid Films*, **555**, 18-20 (2014).

[103] Bädeker, *K. Ann. Phys. (Leipzig)*, **22**, 749-766 (1907).

[104] R. G. Gordon, Criteria for Choosing Transparent Conductors. *MRS Bull.*, **8**, 52-57 (2000).

[105] M. Godlewski, E. Guziewicz, G. Luka, T. Krajewski, M. Lukasiewicz, L. Wachnicki, A. Wachnicka, K. Kopalko, A. Sarem, B. Dalati, ZnO layers grown by Atomic Layer Deposition: A new material for transparent conductive oxide. *Thin Solid Films*, **518**, 1145-1148 (2009).

[106] P. M. Gorley, V. V. Khomyak, S. V. Bilichuk, I. G. Orletsky, P. P. Horley, V. O. Grechko, SnO_2 films: formation, electrical and optical properties. *Materials Science and Engineering B*, **118**, 160-163 (2005).

[107] C. A. Pan and T. P. Ma, Highquality transparent conductive indium oxide films prepared by thermal Evaporation. *Applied Physics Letters*, **37**, 163 (1980).

[108] B. J. Lokhande, P. S. Patil, M. D. Uplane, Studies on cadmium oxide sprayed thin films deposited through non-aqueous medium. *Materials Chemistry and Physics*, **84**, 238-242 (2004).

[109] C. G. Granqvist, A. Hultaker, Transparent and conducting ITO films: new developments and applications. *Thin Solid Films*, **411**, 1-5 (2002) .

[110] S. Jäger, B. Szyszka, J. Szczyrbowski, G. Bräuer, Comparison of transparent conductive oxide thin films prepared by a.c. and d.c. reactive magnetron sputtering. *Surface and Coatings Technology*, **98**, 1304-1314 (1998).

[111] Y. Sato, J. Kiyohara, A. Hasegawa, T. Hattori, M. Ishida, N. Hamada, N. Oka, Y. Shigesato, Study on inverse spinel zinc stannate, Zn_2SnO_4, as transparent conductive films deposited by rf magnetron sputtering. *Thin Solid Films*, **518**, 1304-1308 (2009).

[112] T. Minami, H. Sonohara, T. Kakumu and S. Takata, Highly Transparent and Conductive $Zn_2In_2O_5$ Thin Films Prepared by RF Magnetron Sputtering. *Jpn. J. Appl. Phys.*, **34**, 971 (1995).

[113] X. Wu, T. J. Coutts, W. P. Mulligan, Properties of transparent conducting oxides formed from CdO and ZnO alloyed with SnO_2 and In_2O_3. *J. Vac. Sci. Technol. A*, **15** 1057-1062 (1997).

[114] A. J. Nozik, Optical and Electrical Properties of Cd_2SnO_4: A Defect Semiconductor. *Phys. Rev. B*, **6**, 453-459 (1972).

[115] H. Hosono, M. Yasukawa, K. Kawazoe, Novel oxide amorphous semiconductors: transparent conducting amorphous oxides. *J. Non-Cryst. Solids*, **203**, 334-344 (1996).

[116] I. Goldfarb, D. A. A. Ohlberg, J. P. Strachan, W. D. Pickett, J. J. Yang, G. Medeiros-Ribeiro, R. S. Williams, Band offsets in transition-metal oxide heterostructures. *J. Phys. D: Appl. Phys.*, **46**, 295303-295309 (2013).

[117] R. J. Bird, P. Swift, Energy calibration in electron spectroscopy and the re-determination of some reference electron binding energies. *J. Electron Spectrosc. Relat. Phenom.*, **21**, 227-240 (1980).

[118] NIST X-Ray Photoelectron Spectroscopy Database, *http://srdata.nist.gov/xps/*

[119] S. A. Chambers, T. Droubay, T. C. Kaspar, M. Gutowski, Experimental determination of valence band maxima for $SrTiO_3$, TiO_2, and SrO and the associated valence band offsets with Si(001). *Journal of Vacuum Science & Technology B*, **22**, 2205-2215 (2004).

[120] D. Raviendra, J. K. Sharma, Electroless deposition of cadmium stannate, zinc oxide, and aluminumdoped zinc oxide films. *J. Appl. Phys.* **58**, 838-844 (1985).

[121] Y. Dou, R. G. Egdell, Surface properties of indium-doped Cd_2SnO_4 ceramics studied by EELS and photoemission spectroscopy. *Surface Science*, **372**, 289-299 (1997).

[122] T. Meng, B. McCandless, W. Buchanan, E. Kimberly, R. Birkmire, Cadmium tin oxide thin films deposited by RF magnetron sputtering for photovoltaic applications. J*ournal of Alloys and Compounds*, **556**, 39-44 (2013).

[123] D. O. Scanlon, C. W. Dunnill, J. Buckeridge, S. A. Shevlin, A. J. Logsdail, S. M. Woodley, C. Richard, A. Catlow, M. J. Powell, R. G. Palgrave, I. P. Parkin, G. W. Watson, T. W. Keal, P. Sherwood, A. Walsh, A. A. Sokol, Band alignment of rutile and anatase TiO_2. *Nature Materials*, **12**, 798-801 (2013).

[124] K. Jang, E. Hong, J. H. Kim, Effect of an electrodeposited TiO_2 blocking layer on efficiency improvement of dye-sensitized solar cell. *Korean J. Chem. Eng.*, **29**, 356-361 (2012).

[125] S. M. Waita, B. O. Aduda, J. M. Mwabora, G. A. Niklasson, C. G. Granqvist, G. Boschloo, Electrochemical characterization of TiO2 blocking layers prepared by reactive DC magnetron sputtering. *Journal of Electroanalytical Chemistry*, **637**, 79-83 (2009).

[126] L. Meng, C. Li, Blocking Layer Effect on Dye-Sensitized Solar Cells Assembled with TiO_2 Nanorods Prepared by dc Reactive Magnetron Sputtering. *Nanoscience and Nanotechnology Letters*, **3**, 181-185 (2011).

[127] S. Hore, R. Kern, Implication of device functioning due to back reaction of electrons via the conducting glass substrate in dye sensitized solar cells. *Applied Physics Letters*, **87**, 263504-263507 (2005).

[128] B. Peng, G. Jungmann, C. Jäger, D. Haarer, H. W. Schmidt, M. Thelakkat, Systematic investigation of the role of compact TiO_2 layer in solid state dye-sensitized TiO_2 solar cells. *Coordination Chemistry Reviews*, **248**, 1479-1489 (2004).

[129] M. Law, L. E. Greene, A. Radenovic, T. Kuykendall, J. Liphardt, P. Yang, ZnO-Al_2O_3 and ZnO-TiO_2 Core-Shell Nanowire Dye-Sensitized Solar Cells. *J. Phys. Chem. B*, **110**, 22652-22663 (2006).

[130] P. H. Citrin, G. K. Wertheirn, and Y. Baer, *Physical Review Letters*, **41** 1425 (1978).

[131] N. Reyren, S. Thiel, A. D. Caviglia, L. F. Kourkoutis, G. Hammerl, C. Richter, C. W. Schneider, T. Kopp, A. S. Ruetschi, D. Jaccard, M. Gabay, D. A. Muller, J. M. Triscone, and J. Mannhart, Superconducting Interfaces Between Insulating Oxides. *Science*, **317**, 1196 (2007).

[132] A. Gozar, G. Logvenov, L. F. Kourkoutis, A. T. Bollinger, L. A. Giannuzzi, D. A. Muller, and I. Bozovic, High-temperature interface superconductivity between metallic and insulating copper oxides. *Nature*, **455**, 782 (2008).

[133] A. Brinkman, M. Huijben, M. Van Zalk, J. Huijben, U. Zeitler, J. C. Maan, W. G. van der Wiel, G. Rijnders, D. H. A. Blank and H. Hilgenkamp, Magnetic effects at the interface between non-magnetic oxides. *Nature Mater.*, **6**, 493-496 (2007).

[134] Y. Hotta, T. Susaki, and H. Y. Hwang, Polar discontinuity doping of the $LaVO_3/SrTiO_3$ interface. *Phys. Rev. Lett.*, **99**, 236805 (2007).

[135] A. Kalabukhov, R. Gunnarsson, T. Claeson, and D. Winkler, Electrical transport properties of polar heterointerface between $KTaO_3$ and $SrTiO_3$. *arXiv:0704.1050 [cond-mat.mtrl-sci]* (2007).

[136] J. A. Bert, B. Kalisky, C. Bell, M. Kim, Y. Hikita, H. Y. Hwang, and K. A. Moler, Direct imaging of the coexistence of ferromagnetism and superconductivity at the $LaAlO_3/SrTiO_3$ interface. *Nat. Physics*, **7**, 767 (2011).

[137] S. Thiel, G. Hammer, A. Schmehl, C. W. Schneider, and J. Mannhart, Tunable Quasi-Two-Dimensional Electron Gases in Oxide Heterostructures. *Science*, **313**, 1942 (2006).

[138] G. Drera, G. Salvinelli, A. Brinkman, M. Huijben, G. Koster, H. Hilgenkamp, G. Rijnders, D. Visentin, and L. Sangaletti, Band offsets and density of Ti^{3+} states probed by x-ray photoemission on $LaAlO_3/SrTiO_3$ heterointerfaces and their $LaAlO_3$ and $SrTiO_3$ bulk precursors. *Phys. Rev. B*, **87**, 075435 (2013).

[139] J. Goniakowski, F. Finocchi and C. Noguera, Polarity of oxide surfaces and nanostructures, *Rep. Prog. Phys.*, **71**, 016501 (2008).

[140] D. G. Schlom, L. Q. Chen, X. Pan, A. Schmehl, and M. A. Zurbuchen, A Thin Film Approach to Engineering Functionality into Oxides, *J. Am. Ceram. Soc.*, **91**, 2429-2454 (2008).

[141] V. M. Goldschmidt, *Naturwissenschaften*, **14**, 477 (1926).

[142] Y. Tokura and N. Nagaosa, Orbital Physics in Transition-Metal Oxides. *Science*, **288**, 462 (2000).

[143] S. G. Lim, S. Kriventsov, T. N. Jackson, J. H. Haeni, D. G. Schlom, A. M. Balbashov, R. Uecker, P. Reiche, J. L. Freeouf, and G. Lucovsky, Dielectric functions and optical bandgaps of high-K dielectrics for metal-oxide-semiconductor field-effect transistors by far ultraviolet spectroscopic ellipsometry. *J. Appl. Phys.*, **91**, 4500 (2002).

[144] Y. Y. Mi, Z. Yu, S. J. Wang, P. C. Lim, Y. L. Foo, A. C. H. Huan, and C. K. Ong, Epitaxial $LaAlO_3$ thin film on silicon: Structure and electronic properties. *Applied Physics Letters*, **90**, 181925 (2007).

[145] R. W. Simon, C. E. Platt, A. E. Lee, G. S. Lee, K. P. Daly, M. S. Wire, J. A. Luine, and M. Urbanik, Lowloss substrate for epitaxial growth of hightemperature superconductor thin films. *Applied Physics Letters*, **53**, 2677 (1988).

[146] C. J. Howard, B. J. Kennedy, and B. C. Chakoumakos, Neutron powder diffraction study of rhombohedral rare-earth aluminates and the rhombohedral to cubic phase transition. *J. Phys.: Condens. Matter*, **12**, 349 (2000).

[147] B. E. Park and H. Ishiwara, Formation of $LaAlO_3$ films on Si (100) substrates using molecular beam deposition. *Appl. Phys. Lett.*, **82**, 1197 (2003).

[148] D. O. Klenov, D. G. Schlom, H. Li, and S. Stemmer, The Interface between Single Crystalline (001) $LaAlO_3$ and (001) Silicon. *Jpn. J. Appl. Phys.*, - *Part 2*, **44**, L617 (2005).

[149] D. Kan, T. Terashima, R. Kanda, A. Masuno, K. Tanaka, S. Chu, H. Kan, A. Ishizumi, Y. Kanemitsu, Y. Shimakawa, and M. Takano, Blue-light emission at room temperature from Ar^+-irradiated $SrTiO_3$. *Nat. Mater.*, **4**, 816 (2005).

[150] K. Zhao, K. J. Jin, Y. H. Huang, S. Q. Zhao, H. B. Lu, M. He, Z. H. Chen, Y. L. Zhou, and G. Z. Yang, Ultraviolet fast-response photoelectric effect in tilted orientation $SrTiO_3$ single crystals. *Appl. Phys. Lett.*, **89**, 173507 (2006).

[151] K. van Benthem, C. Elsässer and R. H. French, Bulk electronic structure of $SrTiO_3$: Experiment and theory. *Journal of Applied Physics*, **90**, 6156 (2001).

[152] M. Cardona. Optical properties and band structure of $SrTiO_3$ and $BaTiO_3$. *Phys. Rev.*, **140**, A651-A655 (1965).

[153] F. W. Lytle, X-Ray Diffractometry of Low-Temperature Phase Transformations in Strontium Titanate, *Journal of Applied Physics*, **35**, 2212-2215 (1964).

[154] H. Unoki and T. Sakudo, Electron Spin Resonance of Fe^{3+} in $SrTiO_3$ with Special Reference to the 110 K Phase Transition. *J. Phys. Soc. Jap.*, **23**, 546 (1967).

[155] K.A. Müller, W. Berlinger, and F. Waldner. Characteristic Structural Phase Transition in Perovskite-type Compounds. *Phys. Rev. Lett.*, **21**, 814, (1968).

[156] J. A. Sulpizio, S. Ilani, P. Irvin, and J. Levy, Nanoscale Phenomena in Oxide Heterostructures. *Annu. Rev. Mater. Res.*, **44**, 117-149 (2014).

[157] R. Werner, C. Raisch, A. Ruosi, B. A. Davidson, P. Nagel, M. Merz, S. Schuppler, M. Glaser, J. Fujii, T. Chassé, R. Kleiner, and D. Koelle, $YBa_2Cu_3O_7/La_{0.7}Ca_{0.3}MnO_3$ bilayers: Interface coupling and electric transport properties. *Phys. Rev. B*, **82**, 224509 (2010).

[158] R. Werner, C. Raisch, V. Leca, V. Ion, S. Bals, G. Van Tendeloo, T. Chassé, R. Kleiner, and D. Koelle, Transport, magnetic, and structural properties of $La_{0.7}Ce_{0.3}MnO_3$ thin films: Evidence for hole-doping. *Phys. Rev. B*, **79**, 054416 (2009).

[159] J. G. Mavroides, J. A. Kafalas, and D. F. Kolesar, Photoelectrolysis of water in cells with $SrTiO_3$ anodes. *Appl. Phys. Lett.*, **28**, 241 (1976).

[160] Y. Matsumoto, T. Ohsawa, R. Takahashi, and H. Koinuma, Surface termination effect on the photocatalysis on atomically controlled $SrTiO_3(001)$ surface. *Thin Solid Films*, **486**, 11 (2005).

[161] D. Fuchs, C. W. Schneider, R. Schneider, and H. Rietschel, High dielectric constant and tunability of epitaxial $SrTiO_3$ thin film capacitors. *J. Appl. Phys.*, **85**, 7362 (1999).

[162] J. H. Haeni, P. Irvin, W. Chang, R. Uecker, P. Reiche, Y. L. Li, S. Choudhury, W. Tian, M. E. Hawley, B. Craigo, A. K. Tagantsev, X. Q. Pan, S. K. Streiffer, L. Q. Chen, S.W. Kirchoefer, J. Levy, and D.G. Schlom, Room-temperature ferroelectricity in strained $SrTiO_3$. *Nature*, **430**, 758, (2004).

[163] K.A. Müller and H. Burkard, $SrTiO_3$: An intrinsic quantum paraelectric below 4 K". *Phys. Rev. B*, **19**, 3593, (1979).

[164] D. Olaya, F. Pan, C. T. Rogers and J. C. Price. Electrical properties of La-doped strontium titanate thin films. *Applied Physics Letters*, **80**, 2928 (2002).

[165] T. Tomio, H. Miki, H. Tabata, T. Kawai and S. Kawai. Control of electrical conductivity in laser deposited $SrTiO_3$ thin films with Nb doping. *Journal of Applied Physics*, **76**, 5886 (1994).

[166] A. Leitner, C. T. Rogers, J. C. Price, D. A. Rudman and D. R. Herman. Pulsed laser deposition of superconducting Nb-doped strontium titanate thin flms. *Applied Physics Letters*, **72**, 3065 (1998).

[167] W. Luo, W. Duan, S. G. Louie, and M. L. Cohen. Structural and electronic properties of n-doped and p-doped $SrTiO_3$. *Phys. Rev. B*, **70**, 214109 (2004).

[168] V. E. Henrich, G. Dresselhaus, H. J. Zeiger, Surface defects and the electronic structure of $SrTiO_3$ surfaces. *Phys. Rev. B*, **17**, 4908-4921 (1978).

[169] J. F. Schooley, W. R. Hosler and M. L. Cohen. Superconductivity in semiconducting $SrTiO_3$. *Phys. Rev. Lett.*, **12**, 474-475 (1964).

[170] G. Binnig, A. Baratoff, H. E. Hoenig, and J. G. Bednorz, Two-Band Superconductivity in Nb-Doped $SrTiO_3$. *Phys. Rev. Lett.*, **45**, 1352 (1980).

[171] K. Ueno, S. Nakamura, H. Shimotani, A. Ohtomo, N. Kimura, T. Nojima, H. Aoki, Y. Iwasa and M. Kawasaki, Electric-feld-induced superconductivity in an insulator. *Nature Materials*, **7**, 855-858 (2008).

[172] A. F. Santander-Syro, O. Copie, T. Kondo, F. Fortuna, S. Pailhès, R. Weht, X. G. Qiu, F. Bertran, A. Nicolaou, A. Taleb-Ibrahimi, P. Le Fèvre, G. Herranz, M. Bibes, N. Reyren, Y. Apertet, P. Lecoeur, A. Barthélémy, and M. J. Rozenberg, Two-dimensional electron gas with universal subbands at the surface of $SrTiO_3$. *Nature*, **469**, 189-194 (2011).

[173] L. F. Mattheis, Energy Bands for $KNiF_3$, $SrTiO_3$, $KMoO_3$, and $KTaO_3$. Phys. Rev. B, **6**, 4718-4740 (1972).

[174] D. A. Dikin, M. Mehta, C. W. Bark, C. M. Folkman, C. B. Eom, and V. Chandrasekhar, Coexistence of superconductivity and ferromagnetism in two dimensions. *Phys. Rev. Lett.*, **107**, 056802 (2011).

[175] A. D. Caviglia, S. Gariglio, N. Reyren, D. Jaccard, T. Schneider, M. Gabay, S. Thiel, G. Hammerl, J. Mannhart, and J. M. Triscone, Electric field control of the $LaAlO_3/SrTiO_3$ interface ground state. *Nature*, **456**, 624-627 (2008).

[176] S. Thiel, G. Hammerl, A. Schmehl, C. W. Schneider, and J. Mannhart, Tunable quasi-two-dimensional electron gases in oxide heterostructures. *Science*, **313**, 1942-1945 (2006).

[177] C. Cen, S. Thiel, G. Hammerl, C. W. Schneider, K. E. Andersen, C. S. Hellberg, J. Mannhart, and J. Levy, Nanoscale control of an interfacial metal-insulator transition at room temperature. *Nature Mater.*, **7**, 298-302 (2008).

[178] Ariando, X. Wang, G. Baskaran, Z. Q. Liu, J. Huijben, J. B. Yi, A. Annadi, A. Roy Barman, A. Rusydi, S. Dhar, Y. P. Feng, J. Ding, H. Hilgenkamp, and T. Venkatesan, Electronic phase separation at the $LaAlO_3/SrTiO_3$ interface, *Nat. Comm.*, **2**, 188 (2011).

[179] N. Nakagawa, H. Y. Hwang, and D. A. Muller, Why some interfaces cannot be sharp. *Nat. Mater.*, **5**, 204 (2006).

[180] G. Drera, F. Banfi, F. Federici Canova, P. Borghetti, L. Sangaletti, F. Bondino, E. Magnano, J. Huijben, M. Huijben, G. Rijnders, D. H. A. Blank, H. Hilgenkamp, and A. Brinkman, Spectroscopic evidence of in-gap states at the $SrTiO_3/LaAlO_3$ ultrathin interfaces. *Appl. Phys. Lett.*, **98**, 1 (2011).

[181] A. Koitzsch, J. Ocker, M. Knupfer, M. C. Dekker, K. Dörr, B. Buchner, and P. Hoffmann, In-gap electronic structure of $LaAlO_3$-$SrTiO_3$ heterointerfaces investigated by soft x-ray spectroscopy. *Phys. Rev. B*, **84**, 245121 (2011).

[182] M. Takizawa, S. Tsuda, T. Susaki, H. Y. Hwang, and A. Fujimori, Electronic charges and electric potential at $LaAlO_3/SrTiO_3$ interfaces studied by core-level photoemission spectroscopy. *Phys. Rev. B*, **84**, 245124 (2011).

[183] M. Sing, G. Berner, K. Goss, A. Müller, A. Ruff, A. Wetscherek, S. Thiel, J. Mannhart, S. A. Pauli, C. W. Schneider, P. R. Willmott, M. Gorgoi, F. Schäfers, and R. Claessen, Profiling the Interface Electron Gas of $LaAlO_3/SrTiO_3$ Heterostructures with Hard X-Ray Photoelectron Spectroscopy. *Phys. Rev. Lett.*, **102**, 176805 (2009).

[184] E. Slooten, Z. Zhong, H. J. A. Molegraaf, P. D. Eerkes, S. de Jong, F. Massee, E. van Heumen, M. K. Kruize, S. Wenderich, J. E. Kleibeuker, M. Gorgoi, H. Hilgenkamp, A. Brinkman, M. Huijben, G. Rijnders, D. H. A. Blank, G. Koster, P. J. Kelly, and M. S. Golden, *Phys. Rev. B*, **87**, 085128 (2013).

[185] S. A. Chambers, M. H. Englehard, V. Shutthanandan, Z. Zhu, T. C. Droubay, T. Feng, H. D. Lee, T. Gustafsson, E. Garfunkel, A. Shah, J. M. Zuo, and Q. M. Ramasse, Instability, intermixing and electronic structure at the epitaxial $LaAlO_3/SrTiO_3$ (001) heterojunction. *Surf. Sci. Rep.*, **65**, 317 (2010).

[186] K. Yoshimatsu, R. Yasuhara, H. Kumigashira, and M. Oshima, Origin of Metallic States at the Heterointerface between the Band Insulators $LaAlO_3$ and $SrTiO_3$. *Phys. Rev. Lett.*, **101**, 026802 (2008).

[187] R. Pentcheva and W. E. Pickett, Avoiding the Polarization Catastrophe in $LaAlO_3$ Overlayers on $SrTiO_3$ (001) through Polar Distortion. *Phys. Rev. Lett.*, **102**, 107602 (2009).

[188] Y. Segal, J. H. Ngai, J. W. Reiner, F. J. Walker, and C. H. Ahn, X-ray photoemission studies of the metal-insulator transition in $LaAlO_3/SrTiO_3$ structures grown by molecular beam epitaxy. *Phys. Rev. B*, **80**, 241107 (2009).

[189] G. Berner, A. Müller, F. Pfaff, J. Walde, C. Richter, J. Mannhart, S. Thiess, A. Gloskovskii, W. Drube, M. Sing, and R. Claessen, Band alignment in $LaAlO_3/SrTiO_3$ oxide heterostructures inferred from hard x-ray photoelectron spectroscopy. *Phys. Rev. B*, **88**, 115111 (2013).

[190] V. Vonk, J. Huijben, D. Kukuruznyak, A. Stierle, H. Hilgenkamp, A. Brinkman, and S. Harkema, Polar-discontinuity-retaining A-site intermixing and vacancies at $SrTiO_3/LaAlO_3$ interfaces. *Phys. Rev. B*, **85**, 045401 (2012).

[191] P. R. Willmott, S. A. Pauli, R. Herger, C. M. Schleputz, D. Martoccia, B. D. Patterson, B. Delley, R. Clarke, D. Kumah, C. Cionca, and Y. Yacoby, Structural Basis for the Conducting Interface between $LaAlO_3$ and $SrTiO_3$. *Phys. Rev. Lett.*, **99**, 155502 (2007).

[192] G. Herranz, M. Basletić, M. Bibes, C. Carrétéro, E. Tafra, E. Jacquet, K. Bouzehouane, C. Deranlot, A. Hamzić, J. M. Broto, A. Barthélémy, and A. Fert, High Mobility in $LaAlO_3/SrTiO_3$ Heterostructures: Origin, Dimensionality, and Perspectives. *Phys. Rev. Lett.*, **98**, 216803 (2007).

[193] W. Siemons, G. Koster, H. Yamamoto, W. A. Harrison, G. Lucovsky, T. H. Geballe, D. H. A. Blank, and M. R. Beasley, Origin of Charge Density at $LaAlO_3$ on $SrTiO_3$ Heterointerfaces: Possibility of Intrinsic Doping. *Phys. Rev. Lett.*, **98**, 196802 (2007).

[194] G. Rijnders and D. H. A. Blank, An atomic force pencil and eraser. *Nat. Mater.*, **7**, 270 (2008).

[195] A. E. Paladino, L. G. Rubin, J. S. Waugh, Oxygen ion diffusion in single crystal $SrTiO_3$. *Journal of Physics and Chemistry of Solids*, **26**, 391- 397 (1965).

[196] J. M. Pan, B. L. Maschhoff, U. Diebold, and T. E. Madey, Interaction of water, oxygen, and hydrogen with TiO_2 (110) suerfaces having different defect densities. *J. Vac. Sci. Technol. A*, **10**, 2470-2476 (1992).

[197] F. D. Auret, S. A. Goodman, G. Myburg, and W. E. Meyer, Electrical characteristics of Arion sputter induced defects in epitaxially grown nGaAs. *Journal of Vacuum Science & Technology B*, **10**, 2366 (1992)

[198] M. M. Lucchese, F. Stavale, E. H. Martins Ferreira, C. Vilani, M. V. O. Moutinho, R. B. Capaz, C. A. Achete, A. Jorio, Quantifying ion-induced defects and Raman relaxation length in graphene. *Carbon*, **48**, 1592-1597 (2010).

[199] K. Sugiyama, H. Ishii, Y. Ouchi, and K. Seki, Dependence of indium-tin-oxide work function on surface cleaning method as studied by ultraviolet and x-ray photoemission spectroscopies. *J. Appl. Phys.*, **87**, 295 (2000).

[200] L. Qiao, T. C. Droubay, T. Varga, M. E. Bowden, V. Shutthanandan, Z. Zhu, T. C. Kaspar, and S. A. Chambers, Epitaxial growth, structure, and intermixing at the $LaAlO_3/SrTiO_3$ interface as the film stoichiometry is varied. *Phys. Rev. B*, **83**, 085408 (2011).

[201] NIST X-ray Photoelectron Spectroscopy Database, *http://srdata.nist.gov/xps/Default.aspx*

[202] M. P. Warusawithana, C. Richter, J. A. Mundy, P. Roy, J. Ludwig, S. Paetel, T. Heeg, A. A. Pawlicki, L. F. Kourkoutis, M. Zheng, M. Lee, B. Mulcahy, W. Zander, Y. Zhu, J. Schubert, J. N. Eckstein, D. A. Muller, C. Stephen Hellberg, J. Mannhart and D. G. Schlom, $LaAlO_3$ stoichiometry is key to electron liquid formation at $LaAlO_3/SrTiO_3$ interfaces. *Nat. Comm.*, **4**, 2351 (2013).

[203] L. Sangaletti, M. C. Mozzati, G. Drera, P. Galinetto, C. B. Azzoni, A. Speghini, and M. Bettinelli, Ferromagnetism and local electronic properties of rutile $Ti_{1-x}Fe_xO_2$ single crystals. *Phys. Rev. B*, **78**, 075210 (2008).

[204] W. Siemons, G. Koster, H. Yamamoto, T. H. Geballe, D. H. A. Blank, and M. R. Beasley, Experimental investigation of electronic properties of buried heterointerfaces of $LaAlO_3$ on $SrTiO_3$. *Phys. Rev. B*, **76**, 155111 (2007).

[205] S. S. A. Seo, Z. Marton, W. S. Choi, G. W. J. Hassink, D. H. A. Blank, H. Y. Hwang, T. W. Noh, T. Egami, and H. N. Lee, Multiple conducting carriers generated in $LaAlO_3/SrTiO_3$ heterostructures. *Appl. Phys. Lett.*, **95**, 082107 (2009).

[206] M. C. Tarun, F. A. Selim, and M. D. McCluskey, Persistent Photoconductivity in Strontium Titanate. *Phys. Rev. Lett.*, **111**, 187403 (2013).

[207] R. Claessen, M. Sing, M. Paul, G. Berner, A. Wetscherek, A. Müller, and W. Drube, Hard x-ray photoelectron spectroscopy of oxide hybrid and heterostructures: a new method for the study of buried interfaces. *New Journal of Physics*, **11**, 125007 (2009).

[208] Z. S. Popović, S. Satpathy, and R. M. Martin, Origin of the Two-Dimensional Electron Gas Carrier Density at the $LaAlO_3$ on $SrTiO_3$ Interface. *Phys. Rev. Lett.*, **101**, 256801 (2008).

[209] M. Huijben, G. Rijnders, D. H. A. Blank, S. Bals, S. V. Aert, J. Verbeeck, G. V. Tendeloo, A. Brinkman, and H. Hilgenkamp, Electronically coupled

complementary interfaces between perovskite band insulators. *Nat. Mater.*, **5**, 556 (2006).

[210] A. Rastogi, J. J. Pulikkotil, S. Auluck, Z. Hossain, and R. C. Budhani, Enhanced persistent photoconductivity in δ-doped $LaAlO_3/SrTiO_3$ heterostructures. *Phys. Rev. B*, **86**, 075127 (2012).

[211] R. Pentcheva, and W. E. Pickett, Ionic relaxation contribution to the electronic reconstruction at the n-type $LaAlO_3/SrTiO_3$ interface. *Phys. Rev. B*, **78**, 205106 (2008).

[212] Z. S. Popović, S. Satpathy, R. M. Martin, Origin of the Two-Dimensional Electron Gas Carrier Density at the $LaAlO_3$ on $SrTiO_3$ Interface. *Phys. Rev. Lett.*, **101**, 256801 (2008).

[213] L. Qiao, T. C. Droubay, T. C. Kaspar, P. V. Sushko, S. A. Chambers, Cation mixing, band offsets and electric fields at $LaAlO_3/SrTiO_3$ (001) heterojunctions with variable La:Al atom ratio. *Surface Science*, **605**, 1381-1387 (2011).

[214] W. Siemons, G. Koster, H. Yamamoto, T. H. Geballe, D. H. A. Blank, and M. R. Beasley, Experimental investigation of electronic properties of buried heterointerfaces of $LaAlO_3$ on $SrTiO_3$. *Phys. Rev. B*, **76**, 155111 (2007).

[215] A. Kalabukhov, R. Gunnarsson, J. Börjesson, E. Olsson, T. Claeson, and D. Winkler, Effect of oxygen vacancies in the SrTiO3 substrate on the electrical properties of the $LaAlO_3/SrTiO_3$ interface. *Phys. Rev. B*, **75**, 121404(R) (2007).

[216] Y. Li, and J. Yu, Polarization screening and induced carrier density at the interface of $LaAlO_3$ overlayer on $SrTiO_3$ (001). *J. Appl. Phys.*, **108**, 013701 (2010).

[217] L. Weston, X. Y. Cui, S. P. Ringer, and C. Stampfl, Density-Functional Prediction of a Surface Magnetic Phase in $SrTiO_3/LaAlO_3$ Heterostructures Induced by Al Vacancies. *Phys. Rev. Lett.*, **113**, 186401 (2014).

[218] J. Lee and A. A. Demkov, Charge origin and localization at the n-type $SrTiO_3/LaAlO_3$ interface. *Phys. Rev. B*, **78**, 193104 (2008).

[219] B. C. Huang, Y. P. Chiu, P. C. Huang, W. C. Wang, V. T. Tra, J. C. Yang, Q. He, J. Y. Lin, C. S. Chang, and Y. H. Chu, Mapping Band Alignment across Complex Oxide Heterointerfaces. *Phys. Rev. Lett.*, **109**, 246807 (2012).

[220] C. Cancellieri, M. L. Reinle-Schmitt, M. Kobayashi, V. N. Strocov, T. Schmitt, P. R. Willmott, S. Gariglio, and J. M. Triscone, Interface Fermi States of $LaAlO_3/SrTiO_3$ and Related Heterostructures. *Phys. Rev. Lett.*, **110**, 137601 (2013).

[221] G. Berner, M. Sing, H. Fujiwara, A. Yasui, Y. Saitoh, A. Yamasaki, Y. Nishitani, A. Sekiyama, N. Pavlenko, T. Kopp, C. Richter, J. Mannhart, S. Suga, and R. Claessen, Direct k-Space Mapping of the Electronic Structure in an Oxide-Oxide Interface. *Phys. Rev. Lett.*, **110**, 247601 (2013).

[222] M. Huijben, A. Brinkman, G. Koster, G. Rijnders, H. Hilgenkamp, and D. H. A. Blank, Structure-Property Relation of $SrTiO_3/LaAlO_3$ Interfaces. *Adv. Mater.*, **21**, 1665 (2009).

[223] M. Salluzzo, J. C. Cezar, N. B. Brookes, V. Bisogni, G. M. De Luca, C. Richter, S. Thiel, J. Mannhart, M. Huijben, A. Brinkman, G. Rijnders, and G. Ghiringhelli, Orbital Reconstruction and the Two-Dimensional Electron Gas at the $LaAlO_3/SrTiO_3$ Interface. *Phys. Rev. Lett.*, **102**, 166804 (2009).

[224] F. Iori, M. Gatti, and A. Rubio, Role of nonlocal exchange in the electronic structure of correlated oxides. *Phys. Rev. B*, **85**, 115129 (2012).

[225] Y. Li, S. Na Phattalung, S. Limpijummong, J. Kim, and J. Yu, Formation of oxygen vacancies and charge carriers induced in the n-type interface of a $LaAlO_3$ overlayer on $SrTiO_3$(001). *Phys. Rev. B*, **84**, 245307 (2011).

[226] C. Cancellieri, M. L. Reinle-Schmitt, M. Kobayashi, V. N. Strocov, P. R. Willmott, D. Fontaine, Ph. Ghosez, A. Filippetti, P. Delugas, and V. Fiorentini, Doping-dependent band structure of $LaAlO_3/SrTiO_3$ interfaces by soft x-ray polarization-controlled resonant angle-resolved photoemission. *Phys. Rev. B*, **89**, 121412(R) (2014).

[227] P. Delugas, A. Filippetti, V. Fiorentini, D. I. Bilc, D. Fontaine, and P. Ghosez, Spontaneous 2-Dimensional Carrier Confinement at the n-Type $SrTiO_3/LaAlO_3$ Interface. *Phys. Rev. Lett.*, **106**, 166807 (2011).

[228] U. Scotti di Uccio, C. Aruta, C. Cantoni, E. Di Gennaro, A. Gadaleta, A. R. Lupini, D. Maccariello, D. Marré, I. Pallecchi, D. Paparo, P. Perna, M. Riaz, F. Miletto Granozio, Reversible and Persistent Photoconductivity at the $NdGaO_3/SrTiO_3$ Conducting Interface. *arXiv:1206.5083 [cond-mat.mtrl-sci]* (2012).

[229] A. Tebano, E. Fabbri, D. Pergolesi, G. Balestrino, E. Traversa, Room-Temperature Giant Persistent Photoconductivity in $SrTiO_3/LaAlO_3$ Heterostructures. *ACS Nano*, **6**, 1278-1283 (2012).

[230] N. C. Plumb, M. Kobayashi, M. Salluzzo, E. Razzoli, C. E. Matt, V. N. Strocov, K. J. Zhou, C. Monney, T. Schmitt, M. Shi, J. Mesot, L. Patthey, and M. Radovic, From the $SrTiO_3$ surface to the $LaAlO_3/SrTiO_3$ interface: How thickness is critical. *arXiv:1304.5948v1 [cond-mat.mtrl-sci]* (2013).

[231] G. Drera, L. Sangaletti, F. Bondino, M. Malvestuto, L.Malavasi, Y. Diaz-Fernandez, S. Dash, M. C. Mozzati and P. Galinetto, Labeling interacting configurations through an analysis of excitation dynamics in a resonant photoemission experiment: the case of rutile TiO_2. *J. Phys.: Condens. Matter*, **25**, 075502 (2013).

[232] G. Drera, G. Salvinelli, C. Pintossi, A. Cossaro, A. Verdini, L. Floreano, and L. Sangaletti, in preparation (2015).

[233] A. Fujimori, I. Hase, M. Nakamura, H. Namatame,Y. Fujishima, Y. Tokura, M. Abbate, F. M. F. de Groot, M. T. Czyzyk, J. C. Fuggle, O. Strebel, F. Lopez, M. Domke, and G. Kaindl, Doping-induced changes in the electronic structure of $La_xSr_{1-x}TiO_3$: Limitation of the one-electron rigid-band model and the Hubbard model. *Phys. Rev. B*, **46**, 9841(R) (1992).

[234] Y. Ishida, R. Eguchi, M. Matsunami, K. Horiba, M. Taguchi, A. Chainani, Y. Senba, H. Ohashi, H. Ohta, and S. Shin, Coherent and Incoherent Excitations of Electron-Doped $SrTiO_3$. *Phys. Rev. Lett.*, **100**, 056401 (2008).

[235] C. Cancellieri, N. Reyren, S. Gariglio, A. D. Caviglia, A. Fete, and J. M. Triscone, Influence of the growth conditions on the $LaAlO_3/SrTiO_3$ interface electronic properties. *Europhys. Lett.*, **91**, 17004 (2010).

[236] M. W. Haverkort, Z. Hu, A. Tanaka, G. Ghiringhelli, H. Roth, M. Cwik, T. Lorenz, C. Schüssler-Langeheine, S. V. Streltsov, A. S. Mylnikova, V. I. Anisimov, C. de Nadai, N. B. Brookes, H. H. Hsieh, H. J. Lin, C. T. Chen, T. Mizokawa, Y. Taguchi, Y. Tokura, D. I. Khomskii, and L. H. Tjeng, Determination of the Orbital Moment and Crystal-Field Splitting in $LaTiO_3$. *Phys. Rev. Lett.*, **94**, 056401 (2005).

[237] K. Boller, R. P. Haelbich, H. Hogrefe, W. Jark, C. Kunz, Investigation of carbon contamination of mirror surfaces exposed to synchrotron radiation. *Nucl. Instr. and Meth.*, **208**, 273 (1983).

[238] N. Pavlenko, T. Kopp, E.Y. Tsymbal, J. Mannhart, and G. A. Sawatzky, Oxygen vacancies at titanate interfaces: Two-dimensional magnetism and orbital reconstruction. *Phys. Rev. B*, **86**, 064431 (2012).

[239] Z. Zhong, P. X. Xu, and P. J. Kelly, Polarity-induced oxygen vacancies at $LaAlO_3/SrTiO_3$ interfaces. *Phys. Rev. B*, **82**, 165127 (2010).

[240] N. C. Bristowe, P. B. Littlewood, and E. Artacho, Surface defects and conduction in polar oxide heterostructures. *Phys. Rev. B*, **83**, 205405 (2011).

[241] A. Kalabukhov, Yu. A. Boikov, I. T. Serenkov, V. I. Sakharov, J. Börjesson, N. Ljustina, E. Olsson, D. Winkler, and T. Claeson, Improved cationic stoichiometry and insulating behavior at the interface of $LaAlO_3/SrTiO_3$ formed at high oxygen pressure during pulsed-laser deposition. *Europhys. Lett.*, **93**, 37001 (2011).

[242] A. S. Kalabukhov, Yu. A. Boikov, I. T. Serenkov, V. I. Sakharov, V. N. Popok, R. Gunnarsson, J. Börjesson, N. Ljustina, E. Olsson, D. Winkler, and T. Claeson, Cationic Disorder and Phase Segregation in $LaAlO_3/SrTiO_3$ Heterointerfaces Evidenced by Medium-Energy Ion Spectroscopy. *Phys. Rev. Lett.*, **103**, 146101 (2009).

[243] F. J. García de Abajo, M. A. Van Hove, and C. S. Fadley, Multiple scattering of electrons in solids and molecules: A cluster-model approach. *Phys. Rev. B*, **63**, 075404 (2001).

[244] T. Ohnishi and M. Lippmaa, Improved stoichiometry and misfit control in perovskite thin film formation at a critical fluence by pulsed laser deposition. *Appl. Phys. Lett.*, **87**, 241919 (2005).

[245] C. M. Brooks, L. Fitting Kourkoutis, T. Heeg, J. Schubert, D. A. Muller, and D. G. Schlom, *Appl. Phys. Lett.*, Growth of homoepitaxial SrTiO3 thin films by molecular-beam epitaxy. **94**, 162905 (2009).

[246] D. J. Keeble, S. Wicklein, R. Dittmann, L. Ravelli, R. A. Mackie, and W. Egger, Identification of A- and B-Site Cation Vacancy Defects in Perovskite Oxide Thin Films. *Phys. Rev. Lett.*, **105**, 226102 (2010).

[247] R. Krause-Rehberg and H. S. Leipner, Positron Annihilation in Semiconductors, Springer-Verlag, Berlin, (1999).

[248] D. J. Keeble, R. A. Mackie, W. Egger, B. Löwe, P. Pikart, C. Hugenschmidt, and T. J. Jackson, Identification of vacancy defects in a thin film perovskite oxide. *Phys. Rev. B*, **81**, 064102 (2010).

[249] M. C. Tarun and M. D. McCluskey, Infrared absorption of hydrogen-related defects in strontium titanate. *J. Appl. Phys.*, **109**, 063706 (2011).

[250] J. T. Thienprasert, I. Fongkaew, D. J. Singh, M.H. Du, and S. Limpijumnong, Identification of hydrogen defects in SrTiO3 by first-principles local vibration mode calculations. *Phys. Rev. B*, **85**, 125205 (2012).

[251] M. Kawasaki, K. Takahashi, T. Maeda, R. Tsuchiya, M. Shinohara, O. Ishiyama, T. Yonezawa, M. Yoshimoto, H. Koinuma, Atomic Control of the $SrTiO_3$ Crystal Surface. *Science*, **266**, 1540-1542 (1994).

[252] G. Koster, B. L. Kropman, G. J. H. M. Rijnders, D. H. A. Blank, and H. Rogalla, Quasi-ideal strontium titanate crystal surfaces through formation of strontium hydroxide. *Appl. Phys. Lett.*, **73**, 2920 (1998).

Acknowledgements

I would like to express my gratitude to my supervisor Prof. Luigi Sangaletti, who gave me the opportunity to perform a PhD thesis in his working group and guided me into the everyday problematic novelties which characterize the physics research.

A special thank to Dr. Giovanni Drera, who assisted me during all the PhD experience in the experiments, beamtimes, analysis, programming and conferences, sharing with me some of his outstanding knowledge and revealing himself as a friend.

I wish to acknowledge all the people who contributed to the work presented in this thesis:

- A. Brinkmann, M. Huijben and co-workers of the University of Twente for the growth of the $LaAlO_3/SrTiO_3$ interfaces;
- A. Braga for the preparation of the CTO/TiO_2 heterojunctions;
- F. Bondino, E. Magnano and S. Nappini at the BACH beamline;
- A. Locatelli and T.O. Mentes at the NANOSPECTROSCOPY beamline;
- A. Verdini, L. Floreano, A. Cossaro at the ALOISA beamline.

Furthermore, I wish to express a special acknowledgement to Prof. Mark Golden for his refereeing work.

Finally, I would like to thank all the friends of the ILAMP laboratories who shared with me many difficulties but also unforgettable moments of joy and happiness. In alphabetic order: Alessio Giampietri, Chiara Pintossi, Emanuele

Cavaliere, Federica Rigoni, Gianluca Galimberti, Silvia Tognolini and Stefano Ponzoni. *Grazie a tutti!*

Da ultimo i ringraziamenti più importanti, ovvero ai miei genitori, che hanno ben compreso durante gli anni il peso di questo lavoro dalle innumerevoli rinunce fatte, mi hanno sempre sostenuto e appoggiato nelle mie scelte. Un grazie di cuore a tutti quegli amici di cui non occorre fare i nomi, perchè sono incisi nel mio cuore ed il mio nel loro. Ma il grazie più grande va a mia moglie Gloria, che giorno dopo giorno ha saputo amarmi nella paziente attesa della fine di questo dottorato, condividendo ogni mia fatica e gioia.

Publications and Activities

List of publications related to the PhD thesis:

- G. Drera, **G. Salvinelli**, A. Brinkman, M. Huijben, G. Koster, H. Hilgenkamp, G. Rijnders, D. Visentin, and L. Sangaletti, Band offsets and density of Ti^{3+} states probed by x-ray photoemission on $LaAlO_3/SrTiO_3$ heterointerfaces and their $LaAlO_3$ and $SrTiO_3$ bulk precursors. *Phys. Rev. B*, **87**, 075435 (2013).

- C. Pintossi, **G. Salvinelli**, G. Drera, S. Pagliara, L. Sangaletti, S. Del Gobbo, M. Morbidoni, M. Scarselli, M. De Crescenzi, and P. Castrucci, Direct Evidence of Chemically Inhomogeneous, Nanostructured, Si-O Buried Interfaces and Their Effect on the Efficiency of Carbon Nanotube/Si Photovoltaic Heterojunctions. *J. Phys. Chem. C*, **117**, 18688-18696 (2013).

- A. Braga, C. Baratto, P. Colombi, E. Bontempi, **G. Salvinelli**, G. Drera, L. Sangaletti, An ultrathin TiO_2 blocking layer on Cd stannate as highly efficient front contact for dye-sensitized solar cells. *Phys. Chem. Chem. Phys.*, **15**, 16812-16818 (2013).

- G. Drera, **G. Salvinelli**, J. Åhlund, P. Karlsson, B. Wannberg, E. Magnano, L. Sangaletti, Transmission function calibration of an angular resolved analyzer for X-ray photoemission spectroscopy: Theory vs experiment.
  J. Electron Spectrosc. Relat. Phenom., **195**, 109-116 (2014).

- G. Drera, **G. Salvinelli**, F. Bondino, E. Magnano, M. Huijben, A. Brinkman, and L. Sangaletti, Intrinsic origin of interface states and band-offset profil-

ing of nanostructured $LaAlO_3/SrTiO_3$ heterojunctions probed by element-specific resonant spectroscopies. *Phys. Rev. B*, **90**, 035124 (2014).

- G. Drera, **G. Salvinelli**, F. Bondino, E. Magnano, M. Huijben, A. Brinkman, and L. Sangaletti, Band offset profiling of oxide heterostructures probed by resonant electron spectroscopies. *Elettra Highlights 2013-2014*, 16-17.

- **G. Salvinelli**, G. Drera, C. Baratto, A. Braga, and L. Sangaletti, Stoichiometry Gradient, Cation Interdiffusion, and Band Alignment between a Nanosized TiO_2 Blocking Layer and a Transparent Conductive Oxide in Dye-Sensitized Solar Cell Front Contacts. *ACS Appl. Mater. Interfaces*, **7**, 765-773 (2015).

Other publications not directly related to the PhD thesis:

- G. Drera, M. C. Mozzati, P. Colombi, **G. Salvinelli**, S. Pagliara, D. Visentin, and L. Sangaletti, Amorphous Si layers co-doped with B and Mn: thin film growth and steering of magnetic properties. submitted to *Thin Solid Films*, Nov. 2014.

- S. Dash, G. Drera, E. Magnano, F. Bondino, P. Galinetto, M.C. Mozzati, **G. Salvinelli**, V. Aguekian, and L. Sangaletti Cation diffusion and hybridization effects at the Mn-GaSe(0001) interface probed by soft X-ray electron spectroscopies. *arXiv:1303.1984*, 8 March 2013.

Works during the PhD activity in preparation for a submission:

- **G. Salvinelli**, G. Drera, A. Giampietri, A. Brinkman, M. Huijben, L. Sangaletti, Exploring the $LaAlO_3$-$SrTiO_3$ interface with angle-resolved X-ray photoemission spectroscopy: experiments and modelling of cation interdiffusion and substitution effects.

- **G. Salvinelli**, G. Drera, A. Locatelli, T. O. Mentes, and L. Sangaletti, High-flux resonant μ-probe X-ray photoelectron spectroscopy investigation on a conductive $LaAlO_3/SrTiO_3$ heterostructure in low-oxygen pressure: Ti^{3+} reduction and regeneration evidences.

- G. Drera, **G. Salvinelli**, C. Pintossi, A. Verdini, L. Floreano, A. Cossaro, L. Sangaletti, Defect states in $SrTiO_{3-\delta}$ probed by resonant photoemission spectroscopy.

Participation in research activities at synchrotron radiation facilities:

- *Magnetic proximity effects in weakly ferromagnetic $Ti_{1-x}Mn_xO_2$ rutile single crystals and in non-magnetic $Cd_{1-x}Mn_xTe$ single crystals.* ELETTRA Sincrotrone Trieste, beamline BACH, Proposal Number 20120337 (September 2012), **Proposer: L. Sangaletti**.

- *Resonant photoelectron diffraction from non-stoichiometric $SrTiO_3$ surfaces and $LaAlO_3/SrTiO_3$ heterointerfaces.* ELETTRA Sincrotrone Trieste, beamline ALOISA, Proposal Number 20130272 (November 2013), **Proposer: L. Sangaletti.**

- *Resonant angle resolved photoelectron spectroscopy of buried interface in $LaAlO_3/SrTiO_3$ heterostructures.* ELETTRA Sincrotrone Trieste, beamline BACH, Proposal Number 20135418 (April 2014), **Proposer: G. Drera**.

- *Probing interface effects in TiO_2 based magnetic oxides with dichroic X-ray absorption spectroscopies.* ELETTRA Sincrotrone Trieste, beamline BACH, Proposal Number 20135432 (May 2014), **Proposer: L. Sangaletti**.

- *Search for electronic phase separation in a quasi-2D electron gas at the ultrathin $LaAlO_3$ and $SrTiO_3$ interface by XPEEM and LEEM.* ELETTRA Sincrotrone Trieste, beamline NANOSPECTROSCOPY, Proposal Number 20140154 (September 2014), **Proposer: G. Salvinelli**.

Participation in international/national conferences:

- **G. Salvinelli**, G. Drera, A. Giampietri, A. Brinkman, M. Huijben, L. Sangaletti, Exploring the $LaAlO_3$-$SrTiO_3$ interface with angle-resolved X-ray photoemission spectroscopy: experiments and modelling of cation interdiffusion and substitution effects. *SuperFOX 2014 - Second Conference on*

Superconductivity and Functional Oxides, Rome (Italy); 24-26 September 2014. (Poster)

- **G. Salvinelli**, G. Drera, A. Braga, C. Baratto, L. Sangaletti, Stoichiometry gradients and cation interdiffusion effects in the CdSnO-TiO_2 front contact of a dye-sensitized solar cell probed by angle resolved X-ray photoelectron spectroscopy. *ECOSS30 - European Conference on Surface Science*, Antalya (Turkey); 31 August - 5 September 2014. (Oral presentation)

- **G. Salvinelli**, G. Drera, C. Pintossi, L. Sangaletti, A. Braga, S. Del Gobbo and P. Castrucci, Profiling nanostructured interfaces and buried layers for photovoltaic applications by Angle-Resolved X-ray Photoelectron Spectroscopy. *FisMat 2013 - Italian National Conference on Condensed Matter Physics*, Milan (Italy); 9-13 September (2013). (Poster)

Contribution in international/national conferences:

- G. Drera, **G. Salvinelli**, A. Giampietri, M. Huijben, A. Brinkman, and L. Sangaletti, Interface states and band offset profiling of $LaAlO_3/SrTiO_3$ conductive heterojunctions probed by element-specific resonant spectroscopies. *SuperFOX 2014 - Second Conference on Superconductivity and Functional Oxides*, Rome (Italy); 24-26 September 2014.

- G. Drera, **G. Salvinelli**, A. Verdini, L. Floreano, A. Cossaro, L. Sangaletti, Defect states in $SrTiO_{3-\delta}$ gap probed by resonant photoemission spectroscopy. *SuperFOX 2014 - Second Conference on Superconductivity and Functional Oxides*, Rome (Italy); 24-26 September 2014.

- G. Drera, **G. Salvinelli**, L. Sangaletti, M. Huijben, A. Brinkman, Band profiling at the conducting $LaAlO_3$-$SrTiO_3$ interface. New insights from resonant photoemission spectroscopies. *ECOSS30 - European Conference on Surface Science*, Antalya (Turkey); 31 August - 5 September 2014.

- **G. Salvinelli**, G. Drera, A. Braga, C. Baratto, L. Sangaletti, Front contact CdSnO-TiO_2 Stoichiometry Gradients and Cation Interdiffusion effects in dye-Sensitized Solar Cells probed by Angle Resolved X-Ray Photo-

electron Spectroscopy. *E-MRS 2014 Spring Meeting*, Lille (France); 27-29 May 2014.

- P. Colombi, A. Borgese, L. Medici, G. Drera, **G. Salvinelli**, L. Sangaletti, Structural and electrical properties of highly boron-doped microcrystalline silicon prepared by RF magnetron sputtering. *XVII AISEM - Annual Conference*, Brescia (Italy); 5-7 February 2013.

- G. Drera, M. C. Mozzati, P. Galinetto, Y. A. Diaz-Fernandez, L. Malavasi, F. Bondino, M. Malvestuto, **G. Salvinelli**, L. Sangaletti, Towards a control over the electronic properties and magnetism in formally $3d^0$ compounds: the case of rutile TiO_2. *SuperFOX 2012 - First Conference on Superconductivity and Functional Oxides*, Como (Italy); 19-22 June 2012.